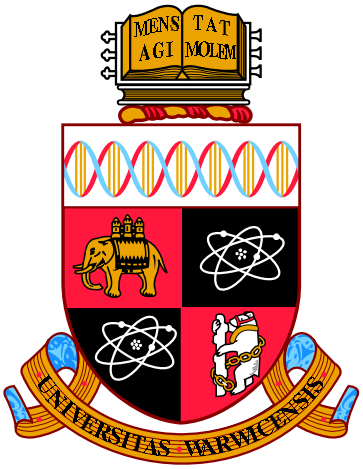

Stationary and rotational axisymmetric granular column collapse

by

Jason Warnett

Thesis

Submitted to the University of Warwick

for the degree of

Doctor of Philosophy

School of Engineering

June 2014

THE UNIVERSITY OF WARWICK

Contents

List of Tables

List of Figures

Acknowledgments

Firstly I would like to thank my supervisors Dr Petr Denissenko and Prof. Peter Thomas for their academic support throughout my PhD. They have been readily available and participated in many fruitful discussions to aid in the direction of my work. The guidance from these two academics has moulded me into the confident researcher I am now. It was Peter who convinced me to enter research after a successful MSc project and aided in securing funding for the venture, without which I wouldn't be here now. The experiences I have had with them has shaped my future and ultimately defined my career in research.

Mark Williams and his team at Warwick Manufacturing Group were extremely accomodating in allowing use of their equipment for the investigations presented. Being able to use such high end technology has produced results which other groups would have been unable to obtain, and has hugely enriched my research. In particular I offer my gratitude to Erichan Kirachi, Dan Norman and John Thornby for their assistance and training in using the laser scanning and CT technologies.

My parents and sister have been great in offering their emotional support over the last three and a half years. Sometimes just having someone to vent at when things haven't quite worked has been just what I needed! I know they are extremely proud of me, and will continue to make them so with what ever comes next.

I would also like to thank my housemates Richard Sugden, Anna Hilarious and Scott Ferry for lending a similar ear and their support while I worked on 'a PhD in sandcastles'. This jest frequently echoed throughout my group of friends to include Oli Coe, Dom Selby and Emily Dixon whom have been a welcome relief for when things have got tough with work or otherwise.

Taking up a new sport through joining WarwickSquash has also kept my san-

ity, while becoming somewhat of an obsession - the club has been much of a second home to me and would particularly like to thank my coach Chris Hall. Working on unique projects such as 'UV Squash' with Jen Emeny has been a highlight of my extra-curricular activities and look forward to continue to develop them.

All these people have been a great help in a variety of ways, and I'm not sure if I would have made it here without them.

With gratitude,

Jason Warnett June 2014

Declarations

The work contained in this thesis was conducted by the author, except where stated otherwise, in the School of Engineering and Warwick Manufacturing Group, University of Warwick in the academic years 2010–2013. The author is aware of the University's regulations regarding proper academic practice. No Part of this work has been previously submitted to the University of Warwick or any other academic institution for admission to a higher degree. All sources of the work are clearly referenced. Details of the work presented here are/will attempt to be published in the following articles/conference proceedings:

Warnett J. M., Denissenko P., Thomas P. J., Norman D., Williams M. A. (2014) "Internal characteristics of granular column collapse", Powder Technology (*'Under preparation'*)

Warnett J. M., Denissenko P., Thomas P. J., Williams M. A. (2014) "Collapse of a granular column under rotation", Powder Technology

Warnett J. M., Denissenko P., Thomas P. J., Kiraci E., Williams M. A. (2014) "Scalings of axisymmetric granular column collapse", Granular Matter, vol. 16, no. 1, pp. 115–124

Warnett J. M., Denissenko P., Thomas P. J. (2013) "Granular collapse in a rotational environment". Program of the 2nd IMA Dense Granular Flows, Cambridge, UK, 1–4 July 2013

Warnett J. M., Denissenko, P., Thomas P. J. (2012) "Axisymmetric column collapse in a rotating system". Abstract in Bulletin of the American Physical Society, vol. 57, no. 17, pp. 242–243, Program of the 65th Annual Meeting of the Division of Fluid Dynamics, San Diego, California, USA, 18-20 November 2012, ISSN 0003-0503

Jason Warnett June 2014

Abstract

The experiments presented investigate the collapse of a granular column on a stationary surface and a rotating table. A cylinder of radius r_0 was positioned on the surface and filled with particulate to a height h_0, giving an aspect ratio $a = h_0/r_0$. The cylinder was quickly removed and the resultant pile investigated. Spatial and geometric data obtained pre and post collapse were used to derive empirical relations. A high speed camera collected temporal data of the collapse in both cases.

In the stationary case a 3D laser scanner quantified measurements of the resultant pile from which scalings involving aspect ratio were derived. The spatial data revealed that the final runout of the pile is not only dependent on the aspect ratio of the initial geometry as previously thought [Lube et al., 2004; Lajeunesse et al., 2004] but also the initial column radius. This was also observed to be true for the angle at the base of the deposit. Theoretical considerations and obtained data allowed the summital angle to be described by material parameters and aspect ratio. X-ray computer tomography allowed observation and quantification of the internal phenomenology to include the granular packing and the failure surface over which the collapse occurs.

Consideration was given to the effect of rotation on previously obtained spatial and temporal scalings. Increasing the rotation rate encourages growth in the final pile radius until a critical frequency is reached where material loss begins to occur. Any further increase for fixed a results in further material loss and a decrease in the final pile radius. Initial results from DEM (discrete element method) simulations of granular collapse on a rotating table are presented for the case of spherical particles. In these simulations a spiral pattern evolves where all particles have left the central pile. Laboratory experiments have yet to demonstrate this exact patterning, but comparison to similar investigations suggests its existence.

Nomenclature

Here a full list of the different notation used is given in order of first appearance

r_0	initial column radius
h_0	initial column height
a	column aspect ratio $a = h_0/r_0$
ϕ	mean packing density
ρ	bulk density
m_0	initial mass
d	grain diameter
θ_r	angle of repose
θ_μ	internal angle of friction
s	system size $s = r_0/d$
t_r	time to raise cylinder
t_m	time for mass to set into motion
v_{lift}	average cylinder lifting speed
r_f	final pile radius
r_*	normalised final pile radius
h_f	final pile height
h_*	normalised final pile height

t_f	total time for collapse
t_*	normalised total time for collapse
r_a	radius of second discontinuity
α_s	angle at summit
α_b	angle at base
l_0	initial channel length (2D)
w	channel width
l_f	final channel runout
ω	angular rotation speed
μ	static rotation
R	tank radius
δ	dynamic friction
e	coefficient of restitution
k_n, k_t	spring constants
c_n, c_t	damper constants
F	force
F_r	centripetal force
F_μ	frictional force
M	moment
I	intertia
a_{cone}	aspect ratio for onset of full cone shape
Λ	slope for r_* vs a
Λ_*	normalised slope for r_* vs a

f	frequency of rotation
f_*	normalised frequency
m_*	fractional mass loss

Chapter 1

Introduction

The study of granular flows is important to gain an understanding of environmental particulate movements. Natural deluges such as avalanches, landslides (seen in Figure 1.1 (a)) and pyroclastic flows have been well described by a number of authors through analysis of granular flows [Savage and Hutter, 1991; Cleary and Sawley, 2004; Forterre and Pouliquen, 2008]. Granular flows are also important to civil engineering projects, predominantly in the storage of grains and powders in silos and other retaining walls. Apart from a fixed mass, man-made granular flows are frequently initiated by deposition from a hopper. Coupling this with deposition onto a centrifuging disk provides a way to spread granular medium such as in the spreading of seeds and fertilisers on fields as shown in Figure 1.1 (b). This has been a recent subject of investigation, both experimentally and computationally [Borovikov et al., 2002; Rioual et al., 2007; Shinbrot et al., 2007; Liedekerke et al., 2009].

Granular column collapse is a fundamental experimental setup studied by numerous previous authors that is useful to undertand gravity-driven granular flows [Lube et al., 2004; Lajeunesse et al., 2004; Staron and Hinch, 2005; Zenit, 2005;

(a) (b)

Figure 1.1: Granular flows can be observed in natural circumstances and utilised in many man-made processes. (a) Landslide at a copper mine in Utah, USA [Daily-Mail]. (b) A tractor using a hopper and certrifuging disc arrangement to distribute seeds in a field [PowerFarming].

Kerswell, 2005; Cleary and Frank, 2006; Thompson and Huppert, 2007; Lube et al., 2005; Balmforth and Kerswell, 2005; Siavoshi and Kudrolli, 2005]. The system leads to a number of empirical scalings based on the aspect ratio of the column to describe characteristic geometric measurements of the resultant pile.

Given the simplicity of the flows, they are ideal to verify theoretical models that often utilise combinations of continuum approximations. A common approach is to apply a shallow water model as has been performed by authors in the description of the flow down a slope [Savage and Hutter, 1989; Mangeney et al., 2000; Doyle et al., 2007]. A recent investigation has found validity in using a combination of Navier-Stokes and $\mu(I)$ rheology to model granular column collapse [Lagrée et al., 2011]. This is the currently accepted best approximation but has its own weaknesses and to date has only been applied to 2D flows. Without a satisfactory universally agreed set of equations to directly apply to granular flows, the primary investigations are frequently experimental.

The difficulty arises from the very nature of granular flows; they exhibit properties of all material states [Jop et al., 2006]. Granular material can behave as a solid as in a sand pile, a liquid when being poured from a silo, and even as a gas when strong agitation causes saltation causing some of the granular media to leave the main granular flow. Solid and gas phenomena displayed in granular flows have been modelled on kinetic theory, but the liquid regime is far from an agreed model and is the topic of debate among researchers.

For this reason DEM (discrete element method) simulations are used as they are based on pure newtonian mechanics and have a direct implementation of friction and particle interactions. Granular column collapse has been simulated frequently in 2D using DEM [Zenit, 2005; Staron and Hinch, 2005] but only one study has performed the collapse in 3D [Cleary and Frank, 2006].

1.1 Research objectives

Consideration of the collapse of a granular column is the central theme to the work presented. With the availability of laser scanning metrology equipment more precise measurement of the deposit has been made possible, resulting in publication [Warnett et al., 2014a]. Previously internal dynamics of this collapse have not been investigated due to the difficulty of its observation. In this study X-ray CT is employed to visualise the internal structure of the column pre and post collapse and obtain internal measurements. While this particular methodology is devoid of a temporal scale, resultant measurements provide clues as to the internal compaction and rearrangement within the column.

Inspired by the agricultural spreading of seeds and fertilisers the column col-

lapse experimental setup was then mounted on a rotating table. No previous authors have investigated this experimental arrangement and while it currently has no direct application, the empirical relations derived may find use in the future for examination of different granular rheologies. For this reason the work has been accepted for publication [Warnett et al., 2014b]. This experimental setup was duplicated computationally but with the use of spherical particles. This has led pattern-formation processes and while needing further verification, initial physical experiments are suggestive of its existence.

The thesis is structured into eight chapters. Chapter 1 introduces the topic and provides a general overview of granular flows. Chapter 2 covers the literature associated with granular column collapse and flows on centrifuging disks, presenting previous results. In addition the operation of X-ray CT is discussed and how it has recently been applied to a few granular setups, in preparation for experiments outlined in Chapter 5. Chapter 3 discusses the design and manufacture of the equipment used throughout this thesis. Chapter 4 covers investigations of granular column collapse using laser scanning. Chapter 5 examines the application of X-ray CT to the collapse of the column, investigating density variations. Chapter 6 presents granular column collapse on a rotating table. Chapter 7 explores initial computational simulations using of rotational collapse with spherical particles. This is achieved through DEM (discrete element method) where each particle is modelled individually. Chapter 8 concludes the thesis with evaluation of observed results and potential ways in which this research could be extended.

Chapter 2

Literature review

In this section literature relevant to the research presented is outlined. Where applicable, results given here are compared with achieved data throughout this thesis.

2.1 Experimental granular column collapse

Granular column collapse has been investigated over the last 20 years both experimentally and computationally with varying degrees of success. The results of this research could be used in further understanding natural granular flows such as avalanches and landslides and to improve industrial processes in handling grains and powders. This particular experimental arrangement is similar to a 'dam break' situation and is more applicable to the storage of granular particulates in silos and other retaining walls. This thesis explores axisymmetric column collapse through a variety of methodologies, including a variation where the effect of rotation on the collapse is considered. The collapse of axisymmetric and 2D granular columns are discussed here.

2.1.1 Axisymmetric experimental setup

Figure 2.1 shows the typical experimental setup for investigations into granular column collapse as performed by Lajeunesse et al. [2004]; Lube et al. [2004]; Thompson and Huppert [2007]. Cylindrical columns of radius r_0 are prepared by filling with granular material by a funnel to a height h_0, with the top surface gently flattened. From this, non dimensional parameters can be defined as the aspect ratio of the column, a, and the mean packing density, ϕ, given by

$$a = h_0/r_0 \tag{2.1}$$

and

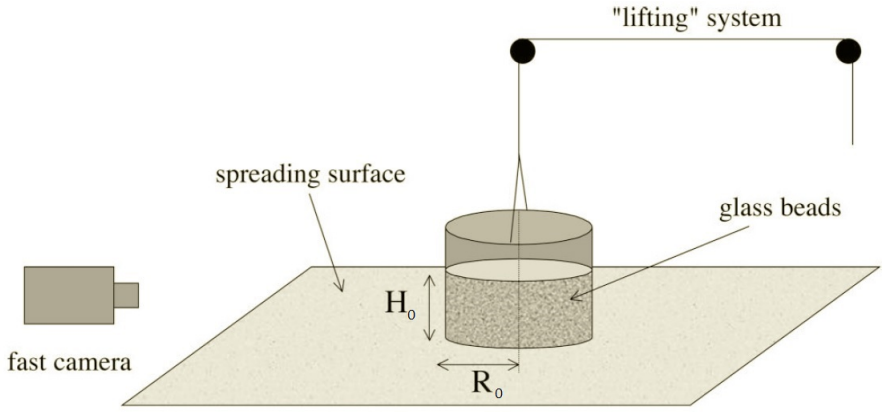

Figure 2.1: Experimental setup for axisymmetric granular column collapse [Lajeunesse et al., 2004].

$$\phi = \frac{m_0}{\rho \pi r_0^2 h_0} \tag{2.2}$$

respectively, where m_0 is the mass and ρ is the density of the material.

The granular material predominantly used across experiments by Lube et al. [2004] and Lajeunesse et al. [2004] was sand, although other materials were trialled in addition to different collapse surfaces as shown in Table 2.1. Associated with the granular material is the mean particle diameter d, density, ρ, angle of repose, θ_r, and angle of friction, θ_μ. The angle of repose is defined as the steepest angle of slope when material on the slope face is on the verge of sliding. The angle of friction is defined as the angle between the normal and resultant force when a limiting shear stress is applied close to the onset of failure of the surface [Mehta and Barker, 1994]. The authors have not given a sphericity associated with their particulate, although it is known that spherical particles and irregular shaped grit-like particles result in slightly different resultant scalings. This is discussed throughout the literature review.

Also shown in Table 2.1 is a system size parameter, $s = r_0/d$, the number of particle diameters per initial radius of the column. While in these experiments no system size dependence is discussed, it is found in Chapter 4 that such a dependence exists based on this parameter. Size dependence occurs in a variety of granular systems from the formation of microstructures in granular gases where they use the ratio of number density to the average density [Goldhirsch et al., 1993; Goldhirsch and Zanetti, 1993], to sphere dispersion in a fluid under shear where they use a size is incorporated into a ratio of grain intertia to maximum viscous stress [Bagnold, 1954]. The particular parameter used here is the same as typically used when considering flows down inclined planes [Silbert et al., 2001].

To initiate the collapse, the cylinder is raised vertically with speed. The

Particle Type	d (mm)	r_0 (mm)	a range	s	Surfaces
		Lajeunesse	2004		
ballotini	0.35	13.0	0.45–12	37	sandpaper, erodible bed, smooth wood
	0.35	28.0	0.21–5.5	80	sandpaper, erodible bed, smooth wood
	0.35	40.0	0.17–2.5	114	sandpaper, erodible bed, smooth wood
	0.35	70.5	0.18–5	201	sandpaper, erodible bed, smooth wood
	1.15	70.5	0.4–10	61	sandpaper
		Lube	2004		
sugar	1.00	25.5	4.23–25	26	smooth wood
	1.00	57.5	1.86–3.69	58	smooth wood
	1.00	73.0	0.37–1.84	73	smooth wood
rice	7.00x2.00	25.5	5.22–25.3	4–13	smooth wood
	7.00x2.00	57.5	0.49–8.54	8–29	smooth wood
	7.00x2.00	73.0	0.44–1.99	10–37	smooth wood
cous cous	2.00	25.5	9.10–25.1	12	smooth wood
	2.00	57.5	1.91–4.76	29	smooth wood
	2.00	73.0	0.31–1.89	36	smooth wood
salt	0.30	16.9	4.8–42.9	56	smooth wood
	0.30	22.5	2.0–35	75	smooth wood
	0.30	26.0	2.7–31.4	87	smooth wood
	0.30	31.9	1.09–17.7	106	smooth wood
	0.30	57.5	0.25–5.22	192	smooth wood
sand	0.32	29.2	1.5–13.8	91	smooth wood
	0.32	74.5	0.44–4.62	233	smooth wood
	0.32	97.0	0.19–4.8	303	smooth wood

Table 2.1: Particle types and surfaces used in experiments by Lajeunesse et al. [2004] and Lube et al. [2004]. d is grain diameter, r_0 is initial column radius, a is aspect ratio and s is system size.

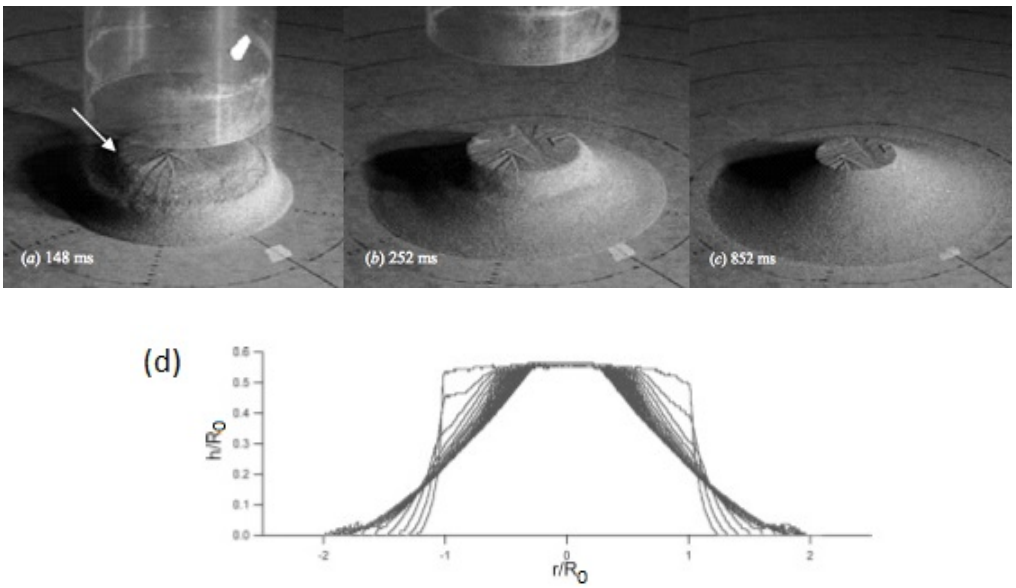

Figure 2.2: For $a < 0.74$ the final deposit results in a truncated cone. (a)–(c) Photographs of the collapse for $a = 0.55$ [Lube et al., 2004]. (d) Graphical representation of the collapse for $a = 0.56$. Time lapse between each profile is 20 ms [Lajeunesse et al., 2004].

cylinder must be raised in a time t_r much smaller than the time taken for the mass to set into motion t_m. This can be evaluated by comparing

$$t_r = h_0/v_{\text{lift}} \tag{2.3}$$

with

$$t_m = \sqrt{\frac{2h_0}{g}} \tag{2.4}$$

where v_{lift} is the average speed at which the cylinder is lifted [Lajeunesse et al., 2004; Lube et al., 2004].

Using the above setup scalings were derived for the final runout radius, r_f, final height, h_f, and runout time based on the initial aspect ratio of the column. Measurements obtained by Lube et al. [2004] were procured using a laser pointer on a sliding ruler which had an estimated accuracy of ± 0.1 mm. Lajeunesse et al. [2004] used a camera with a spatial resolution of 0.4 mm. Lube states that the final radius of the pile was repeatable within ± 5 mm, while offering no reasoning for the figure.

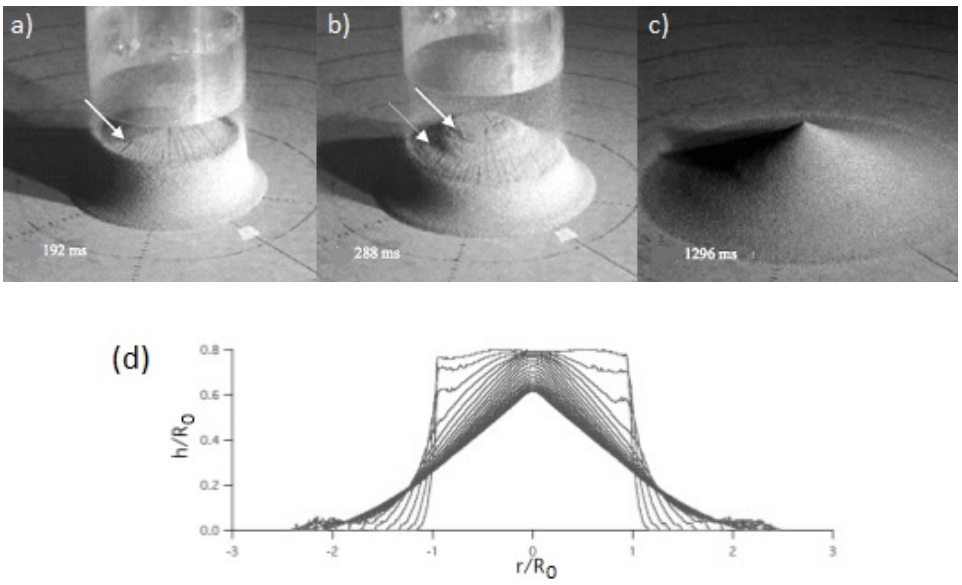

Figure 2.3: For $a > 0.74$ the final deposit results in a full conical shape. (a)–(c) Photographs of the collapse for $a = 0.90$ [Lube et al., 2004]. (d) Graphical representation of the collapse for $a = 0.80$. Time lapse between each profile is 20 ms [Lajeunesse et al., 2004].

2.1.2 Qualitative results

Qualitative observations of the flow were made using a high speed camera, in particular how the flow mechanics evolved with aspect ratio. It has been observed that there are two different regimes of collapse dependent on aspect ratio resulting in different morphologies of sandpile as shown in Figure 2.2 and 2.3.

It is universally agreed that for $a < 0.74$ the collapse initiates with edges of the granular column beginning to move under free fall developing a front flow at the foot of the pile that propagates outwards. This value appears to have little dependence on the properties of the granular material such as the angle of repose and angle of internal friction, but analysis of the variation of these characterisitics has not been performed. A singular circular discontinuity was observed during the collapse by Lube et al. [2004] that seperates the outer slumping regions from a non deformed inner region. At these aspect ratios, the appearance of the resulting sand pile resembles a truncated cone, where a region of the upper surface of the column remains undisturbed. This motion can be observed in Figure 2.2 (a)-(c), and the development of the profile can be seen in Figure 2.2 (d).

For $a > 0.74$, the entirety of the upper surface is consumed by the granular avalanche, but still evolves in the same manner as the lower aspect ratios, whereby the edges of the granular column develop a front flow at the foot of the pile. This can be seen in Figure 2.3 (a)-(c). Huppert et al. [2003] and Lube et al. [2004] claim

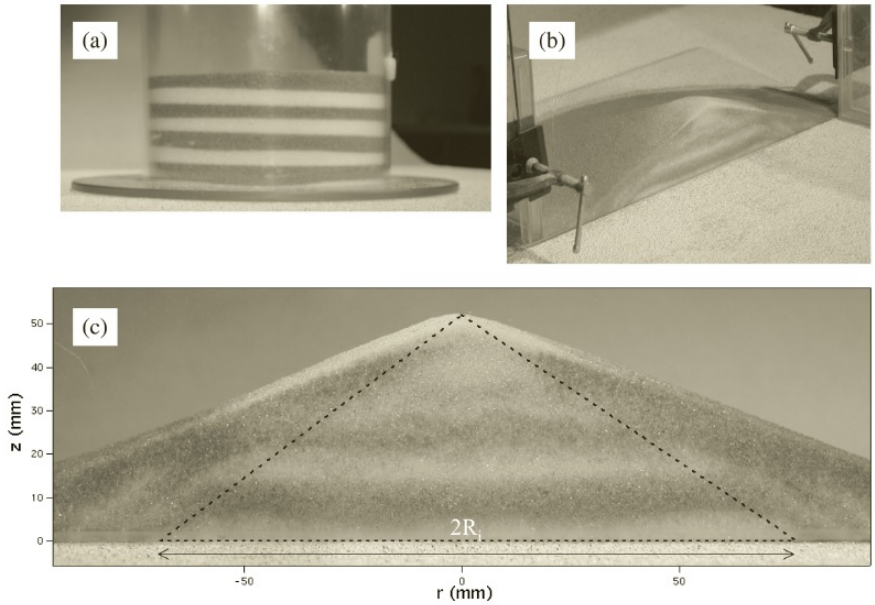

Figure 2.4: Collapse with $a = 1$ and layers of sand alternately coloured. (a) Initial preparation. (b) Splitting the resultant pile with a glass pane. (c) Internal region with no movement shown by dotted line with inclination between 35° and 37° [Lajeunesse et al., 2004].

this occurs for $0.74 < a < 1.7$, whereas Lajeunesse et al. [2004] gives $0.74 < a < 3$. Lube et al. [2004] describes the appearance of a second discontinuity propagating towards the centre for the collapse in this aspect ratio range as indicated in Figure 2.3 (b). The second discontinuity is seen to separate an outer static region from an inner region of flowing grains propogating over the surface.

Lube et al. [2004] compares the radius of this second discontinuity upon its first appearance r_a with the initial height and demonstrates the relation

$$r_a = 9.6 - 0.585 h_0 \tag{2.5}$$

consistent with an inner static body within the cone geometry. Interpretation of this relation gives an inclination of 59.4° of the cone. This is approximately equal to the internal angle of friction θ_μ with the aspect ratio of the cone equal to $\tan^{-1} 59.4° = 1.7$. For $a > 1.7$ the discontinuity is no longer observed but cites that the relaxation to a cone shape suggests a static interior to the pile.

Lajeunesse et al. [2004] demonstrates the existence of the static cone experimentally by splitting the sandpile, accepting that there will be some minor disturbances with this technique as shown in Figure 2.4. The difference in angular variation between the two authors can be attributed to the material properties; Lajeunesse et al. [2004] states $\theta_\mu \approx 36.5°$. This experiment also demonstrates that

there is no/little interaction between the layers during the collapse.

Daerr and Douady [1999] observes the existence of a failure surface in a similar experimental setup where the angle of incidence equates to θ_μ. The difference with this experimental setup is that the material is released on a disc with the same radius as the column. It is discussed that this is due to a process known as active Coulomb yielding where the combination of compression and tensile stresses within the material define the surface over which subsequent material avalanches. While the failure surface has previously been observed, there has been no prior mention of the inner region remaining static as claimed by Lajeunesse et al. [2004].

Both authors note that in all cases the steepest inclination of the resultant pile is approximately equal to θ_r as would be expected from its definition. For $a > 1.7$, Lube et al. [2004] records the steepest inclination of the resultant pile to be much less than θ_r.

For larger aspect ratios where $a > 3$ a different flow regime emerges where the whole upper surface of the column is seen to move intantaneously, initially conserving its shape while the frontal flow is developing at the foot of the pile [Lube et al., 2004; Lajeunesse et al., 2004]. Before the central body ceases to flow two stationary bulges are observed at the surface that dissapate as the frontal flow continues to propogate [Lube et al., 2004]. The resultant deposit is described as a 'mexican hat' shape due the shallow deposit with the exception of a relatively sharp peak towards the centre as observed in Figure 2.5.

2.1.3 Scalings of the collapse

In both experiments by Lube et al. [2004] and Lajeunesse et al. [2004] a number of particle sizes and surfaces were trialled as indicated in Table 2.1. In both studies the scalings were found to be independent of system size, $s = r_0/d$. Lajeunesse et al. [2004] found there to be a weak dependence of the surface type on the shape of the initial deposit.

Geometrical features of interest are the final runout, r_f, final height, h_f, and angular values at the summit, α_s, and base α_b. Non-dimensionalisation of the final runout and height against the initial radius r_0 leads to expressions $r_* = (r_f - r_0)/r_0$ and $h_* = h_f/r_0$ respectively. Following the discussion of collapse dynamics the resultant profiles of the deposit are shown in Figure 2.6.

Final runout

There is a disagreement in the scaling for the final runout of the pile r_f between the two authors, while both providing logical arguments.

While $a < 1.7$ Lube et al. [2004] argues by dimensional analysis and the observation that only grains beyond r_a contribute to the final runout, that the

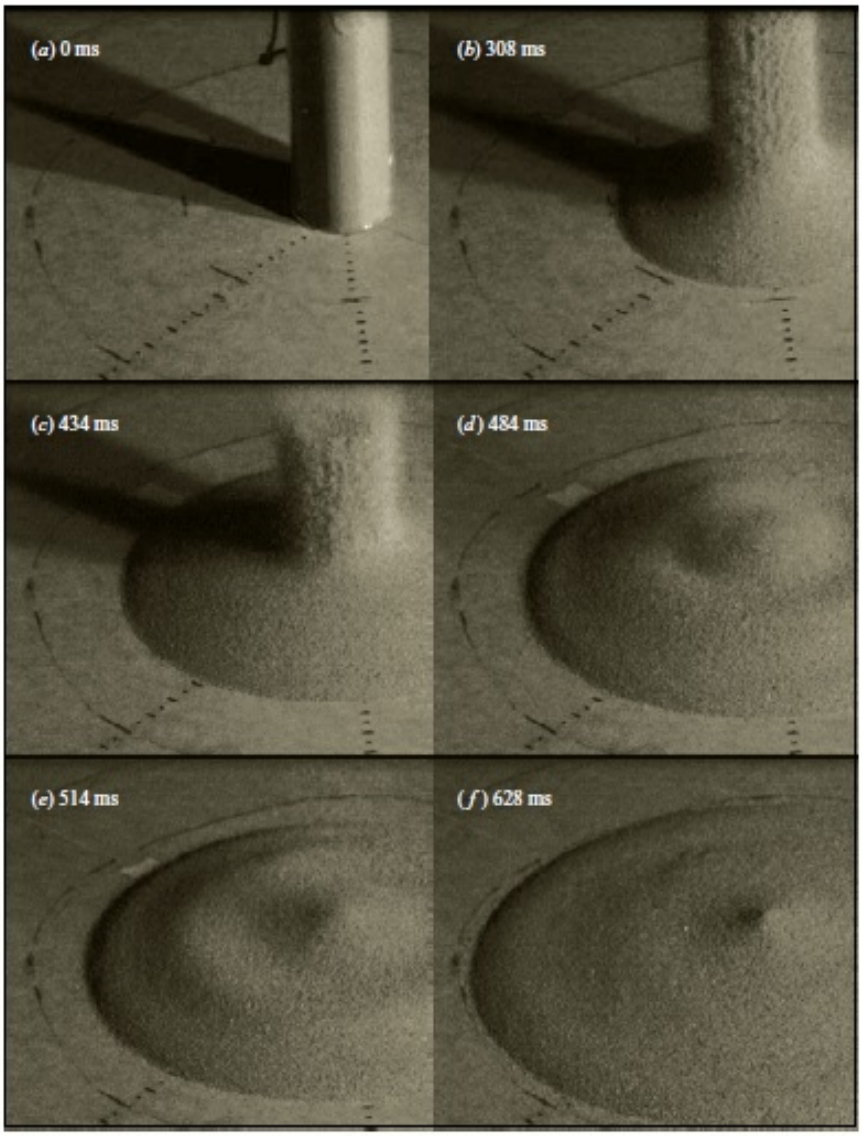

Figure 2.5: Photographs of the collapse for $a = 13.8$ [Lube et al., 2004]. The upper surface initially retains its shape before doming causing the development of two bulges within the deposit. These all but dissipate leaving a 'mexican hat' shaped deposit.

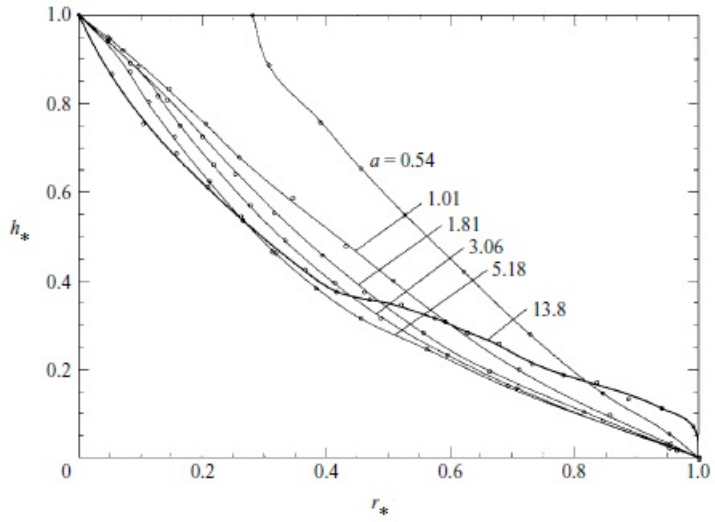

Figure 2.6: Comparison of resultant profiles with varying aspect ratio [Lube et al., 2004].

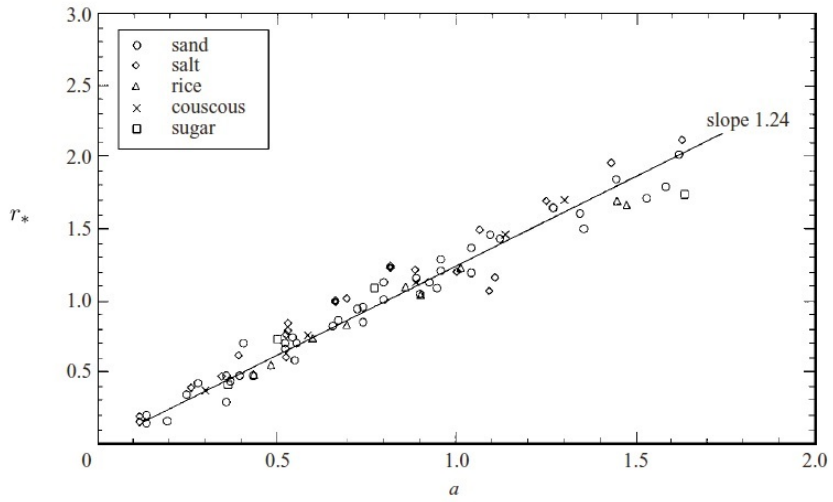

Figure 2.7: Linear fit of dependence of final runout on aspect ratio to data as given by Lube et al. [2004].

relation must be of the form

$$r_* = ca \tag{2.6}$$

for some constant c. By directly fitting the linear relation to experimental data Lube finds that $c = 1.24$ with a regression coefficient of 0.975 for all materials as shown in Figure 2.7. Lajeunesse et al. [2004] reasons by approximate volume comparison of the initial column to the truncated cone that exists for $a < 0.74$ that

$$r_* = \frac{1}{2\tan\theta_r}\left(a + \sqrt{4(\tan\theta_r)^2 - \frac{a^2}{3}}\right) - 1 \tag{2.7}$$

Beyond $a > 0.74$ a full conical shape emerges and Lajeunesse et al. [2004] again uses an approximate volume comparison to find that

$$r_* = \sqrt{\frac{3a}{0.74}} - 1 \tag{2.8}$$

Figure 2.8 (a) shows that both volume derivations fit well with the data, although note that the relations arise from an approximation of the profile shape. Lube et al. [2004] is in agreement that for $a > 1.7$ a square root power-law is appropriate giving

$$r_* = 1.6\sqrt{a} \tag{2.9}$$

but is unable to provide theoretical derivation and the relation emerges from data fitting as in Figure 2.8 b). It has been shown by Jop et al. [2006] and G.D.R-Midi [2004] that in certain granular surface flow geometries the distance from bounding walls has an effect on the scalings. In this particular case both Lube et al. [2004] and Lajeunesse et al. [2004] show that there is no dependence on particle size/system size or the surface onto which it collapses. It is reasoned that the surface has little implication on this scaling as there is an initially deposited layer of granules over which the rest of the collapse occurs. The flow is then dominated by inertial forces until near the end of the collapse where it comes to an abrupt halt due to inter-granular friction [Lube et al., 2004].

Final height

While in the truncated cone regime the final height of the deposit, h_f, equals the initial height. Lajeunesse et al. [2004] reports that the height stagnates upon leaving this geometric regime and so for $a > 0.74$

$$h_* = 0.74 \tag{2.10}$$

where $h_* = h_f/r_0$ is the non-dimensional height. Lube et al. [2004] however reports

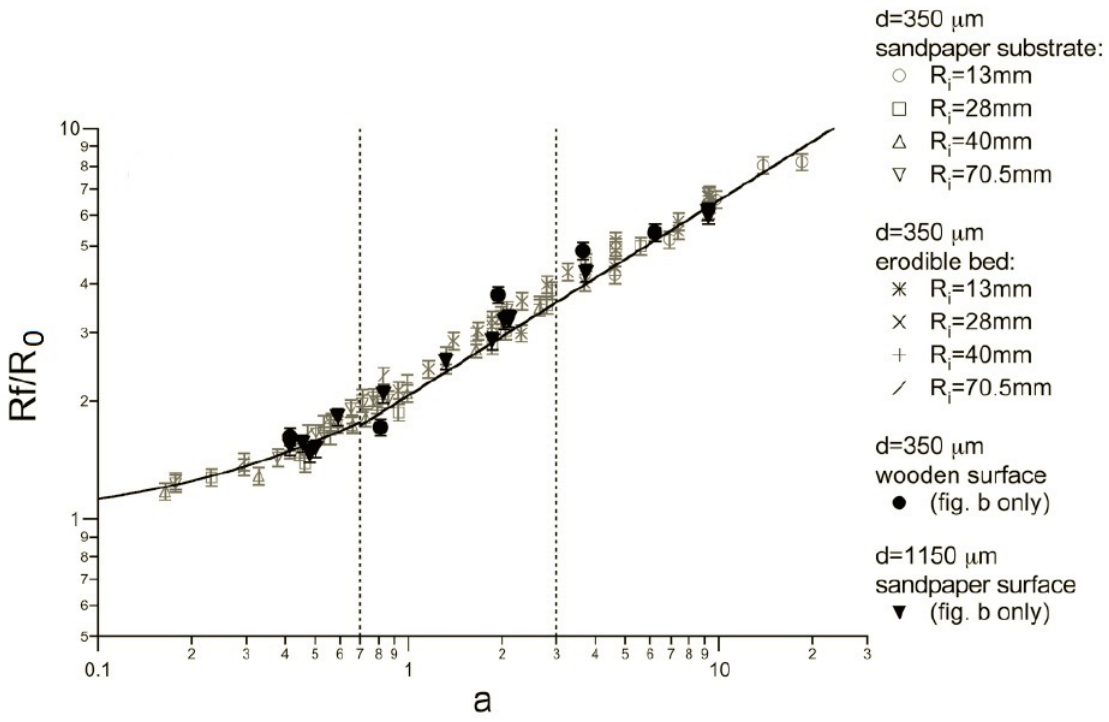

(a)

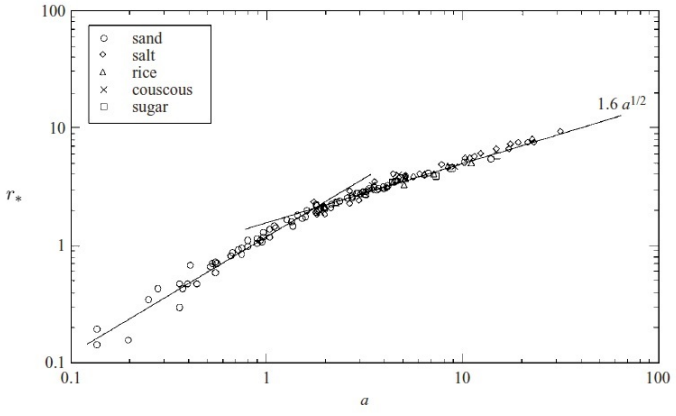

(b)

Figure 2.8: Dependence of r_* on a as given by (a) Lajeunesse et al. [2004] (b) Lube et al. [2004].

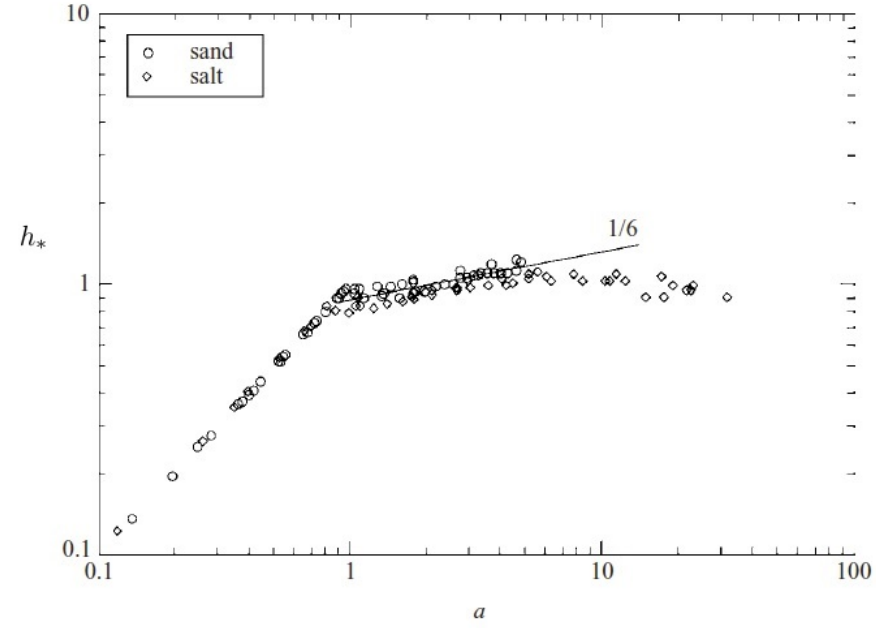

(a)

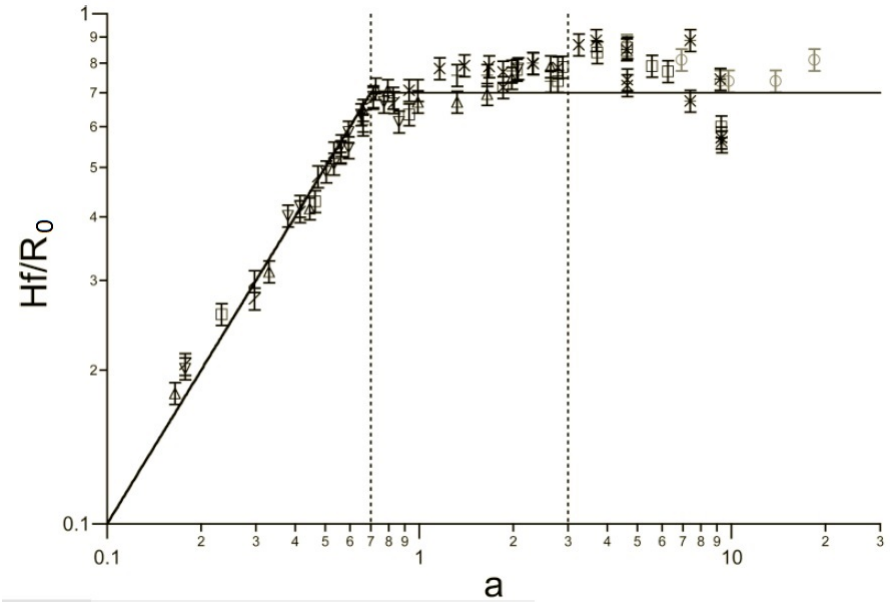

(b)

Figure 2.9: Dependence of h_f on a as given by (a) Lube et al. [2004] (b) Lajeunesse et al. [2004]. Legend as in Figure 2.8 (b).

that there is a moderate increase in h_f for $a > 1$, fitting

$$h_* = 0.88a^{1/6} \tag{2.11}$$

to obtained data as seen in Figure 2.9 (a). It is then argued that there is a slight decrease in h_f for $a > 10$. Both arguments provided by Lube et al. [2004] could be applied to data provided by Lajeunesse et al. [2004] as seen in Figure 2.9 (b), but without existing theory able to support either claim both possbilities are entertained.

Angular quantities

In addition to the final height and runout, Lajeunesse et al. [2004] measures the angle at the base, α_b and summit, α_s of the resultant pile as seen in Figure 2.10. In both cases the angle is less than the angle of repose as would be expected from its definition. While the angle at the summit continues to decrease on a logarithmic scale for the range of aspect ratios trialled, the angle at the base saturates at 5° at approximately $a = 1.7$, coinciding with the change in flow regime.

Time evolution

Both Lube et al. [2004] and Lajeunesse et al. [2004] considered the propagation of the pile radius with time and found that it followed a logistic shaped curve as shown in Figure 2.11. This indicates that there is an initial period of acceleration, followed by a period of constant velocity and finally a period of deceleration before all movement ceases. The period of constant velocity is small, and arguably non existent for $a < 1.7$ because the overall flow time is too short. The total period of acceleration decreases with increasing aspect ratio. This can be attributed to the dynamic of collapse changing from crumbling at the periphery to the entirety of the upper surface collapsing.

The total time for collapse increases with aspect ratio, and follows a relation of the form

$$t_f = (r_0/g)^{1/2} f(a) \tag{2.12}$$

as indicated by dimensional analysis by Lube et al. [2004]. With the requirement that t_f must be independent of r_0 it follows that $f(a) = Ka^{1/2}$ for some constant K. Curve fitting to the data finds that

$$\frac{t_f}{\sqrt{(r_0/g)}} = 3\sqrt{a} \tag{2.13}$$

as shown in Figure 2.12.

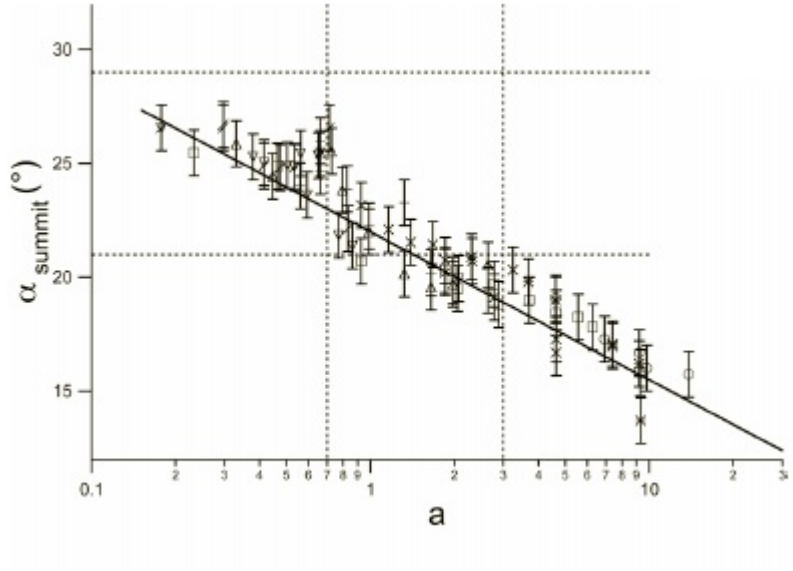

(a)

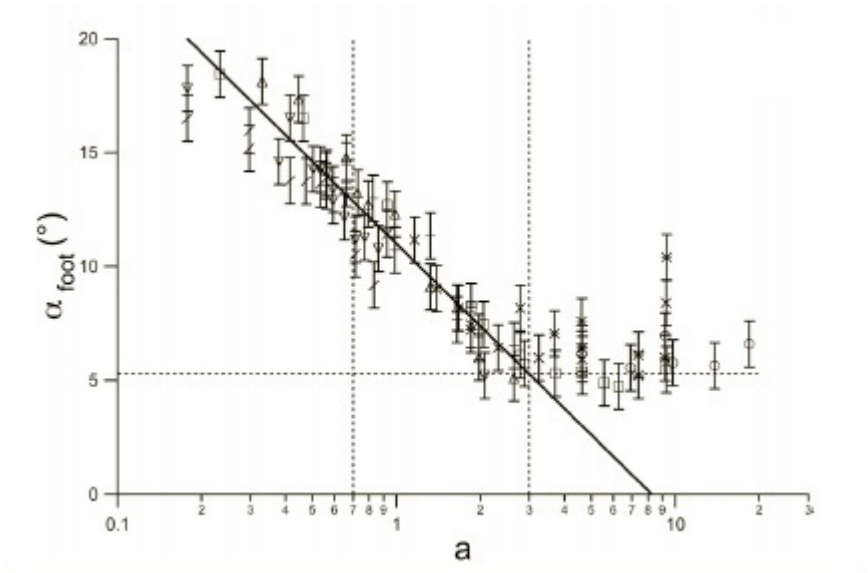

(b)

Figure 2.10: Angular evolution with aspect ratio after collapse (a) Angle at the summit. (b) Angle at the the foot of the pile Lajeunesse et al. [2004].

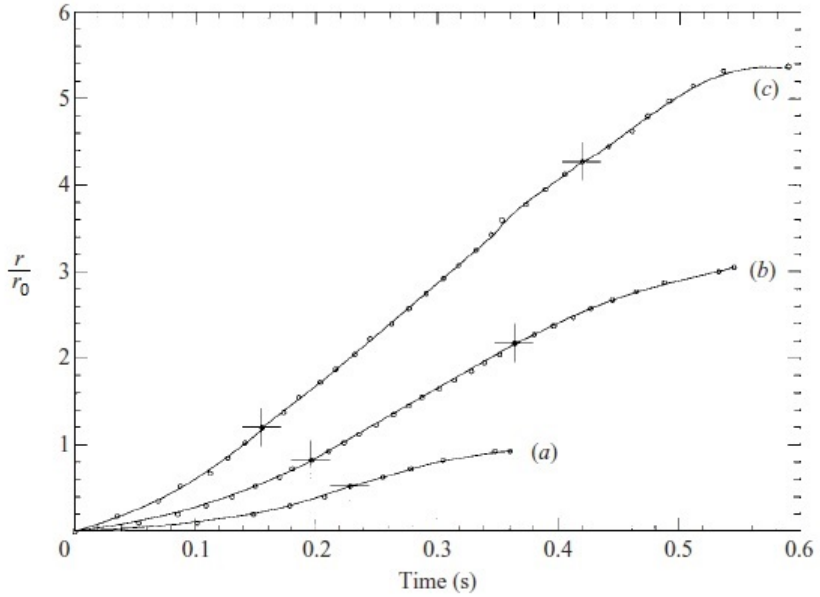

Figure 2.11: Evolution of the pile radius, r, with time for different aspect ratios. (a) $a < 1.7$. (b) $1.7 < a < 10$. c) $a > 10$ [Lube et al., 2004].

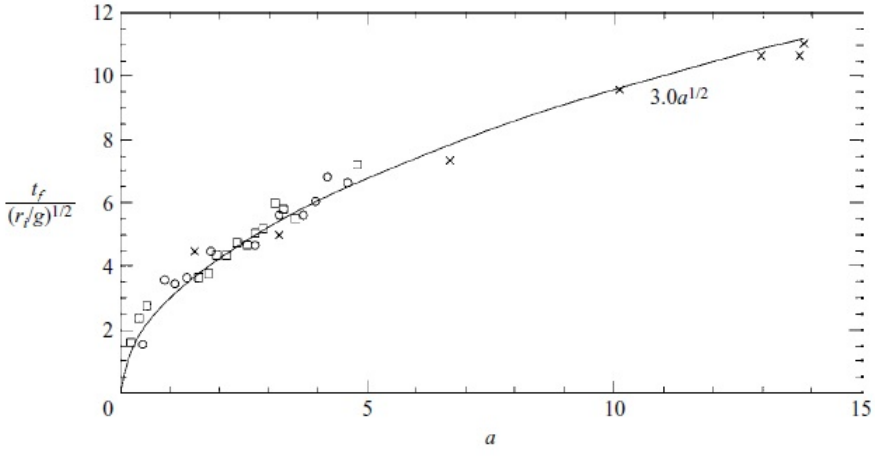

Figure 2.12: Total time t_f for collapse against aspect ratio a [Lube et al., 2004].

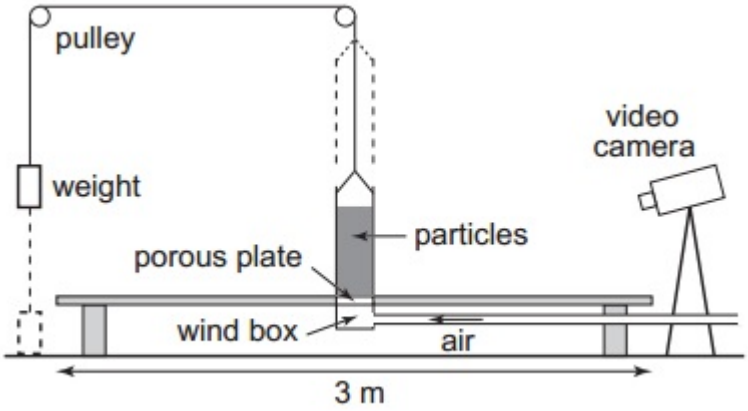

Figure 2.13: Experimental setup for fluidized axisymmetric granular column collapse [Roche et al., 2011].

2.2 Fluidized axisymmetric column collapse

The previous section has highlighted that the collapse scales well with the non-dimensional parameter aspect ratio. Due to the difficulty in isolating material properties it has been difficult for previous authors to identify which coefficients and exponents are dependent on such parameters. By initially fluidizing the column the initial dependence on friction is removed exposing not only a new dynamic of the collapse, but where material properties fit with the scalings in the dry (non-fluidized) case.

2.2.1 Experimental setup

An adaptation of experiments in the previous section is the initial fluidization of axisymmetric granular column as performed by [Roche et al., 2011]. The setup is as before but with small pores in the table confined to region of the initial position of the column as shown in Figure 2.13. An constant air flow at 10^5 Pa is passed through the porous region to fluidize the column, kept on for the duration of the collapse. This results in essentially binary contacts between grains making internal friction negligible at the initiation of the collapse. This then increases as pore pressure diffuses throughout the collapse.

Here the author uses initial column radii $r_0 = 21 - 46\,\text{mm}$ with aspect ratios in the range $a = 0.24 - 30.7$. Two grades of glass beads are used throughout the experiment; 'fine' with $d \approx 0.075\,\text{mm}$ and 'coarse' with $d \approx 0.330\,\text{mm}$. No further information is given on the properties of the particulate.

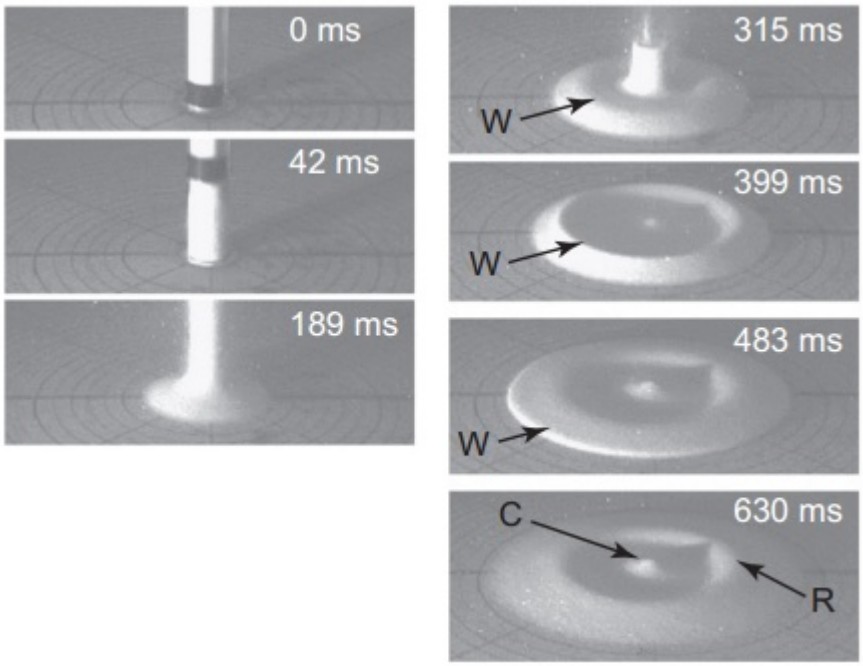

Figure 2.14: Collapse of a 'dry' column of coarse particles with $a = 16.7$ evolving over time. W marks the wave propagating outwards, resulting in the cone (marked C) and ridge (marked R) morphology. [Roche et al., 2011].

2.2.2 Qualitative results

Experiments involving a fluidized column of coarse particles showed little qualitative difference with the column collapse of the 'dry' coarse particles (to mean non-fluidized in the context of this section). The major difference between the two cases is that the front flow propogrates with a greater acceleration at high aspect ratios ($a > 10$) for the fluidized column. The resultant morphology for $a \approx 7 - 8$ is a central cone with an outer ridge as seen in Figure 2.14, formed by a travelling wave throughout the collapse. This was only weakly observed by Lube et al. [2004]; Lajeunesse et al. [2004].

Experiments with the fluidized column of fine particles reveal the travelling wave occurs at a smaller aspect ratio of $a \approx 4-5$ with the ridge forming at $a \approx 6-7$. As a increases, a greater number of travelling waves occur resulting in the formation of a number of ridges as observed in Figure 2.15. The front flow in this case is subject to variations in acceleration and deceleration as each wave begins and a new one overtakes.

2.2.3 Quantitative results and friction dependence

The resultant geometric scalings of the collapse are given in Table 2.2. In the case of the normalised final runout, $r_* = (r_f - r_0)/r_0$, the fluidization causes an increase in

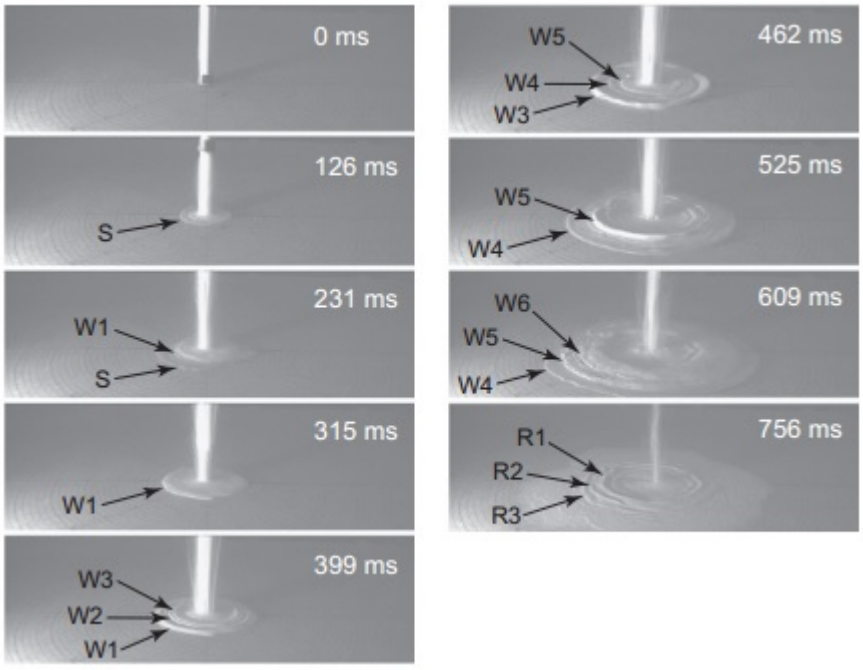

Figure 2.15: Collapse of a fludized column of fine particles with $a = 30.4$ evolving over time. W marks the wave propagating outwards, resulting in the cone (marked C) and ridge (marked R) morphology. [Roche et al., 2011].

Scaling	Coarse Dry	Coarse Fluidized	Fine Dry	Fine Fluidized
r_*	$1.40a\,(a < 1.6)$ $1.82a^{0.5}\,(a > 1.6)$	$1.48a\,(a < 1.6)$ $1.99a^{0.5}\,(a > 1.6)$	$1.61a\,(a < 1.6)$ $1.84a^{0.67}\,(a > 1.6)$	$2.49a\,(a < 1.1)$ $2.53a^{0.5}\,(1.1 < a < 17)$ $1.68a^{0.69}\,(a > 17)$
h_*	$a\,(a < 0.7)$ $0.7\,(0.7 < a < 7)$ $\propto a^{-0.5}\,(a > 7)$	$0.26a^{0.33}\,(a < 5)$ $a^{-0.5}\,(a > 5)$	$0.84a\,(a < 1)$ $0.95\,(1 < a < 6)$ $\propto a^{-0.5}\,(a > 6)$	0.1–0.2

Table 2.2: Scalings for normalised runout r_* and normalised final height h_* for experiments by Roche et al. [2011].

the leading coefficient in all aspect ratios. It is important to note that the exponent decreasing from 1 to 0.5 (except in the case of a fine fluidized column for $a > 17$) is independent of fluidization. Given that fluidization removes the dependence on internal friction between particles, it can be concluded that the coefficient is subject to material dependence but the exponent is not.

The increase in the final runout from a dry column to a fluidized one, is less in the coarse particle case than the fine particle one. This is due to the coarse particles diffusing the pore pressure rapidly throughout the collapse, re-establishing the effect of internal friction almost instantaneously. Conversely for the fine particle case, the high pore pressure is maintained for a larger proportion of the flow resulting in a severely lower dependence on particle friction and hence slower energy dissipation.

The effect of diffusion of pore pressure is mirrored in the final height of the fluidized column. As expected the final height of the fluidized columns are significantly less than their dry counterparts. In the case of fluidized coarse particles the height increases initially with aspect ratio unlike the fine particles which remain stagnant. This illustrates the coarse particles establishing particle contacts throughout the collapse through diffusing pore pressure. The coarse particle final height start to decrease at $a > 5$ - an earlier onset than what the authors found for the dry columns, occuring for $a > 7$. Note that a decrease was not noticed in the dry case by Lajeunesse et al. [2004] and only minutely by Lube et al. [2004].

2.3 2D Channel collapse

While this thesis is concerned with axisymmetric collapse, attention is given to the experiment's 2D counterpart; column collapse in a channel. This simplified version gives rise to approximate numerical models discussed in Section 2.4 that have been recast to demonstrate axisymmetric flow. Studies discussed in this section have been completed by Balmforth and Kerswell [2005]; Lube et al. [2005]; Lajeunesse et al. [2005]; Siavoshi and Kudrolli [2005].

2.3.1 Experimental setup

Figure 2.16 shows the experimental setup for observing 2D collapse in a channel with experimental parameters for the studies by Lajeunesse et al. [2005], Lube et al. [2005] and Balmforth and Kerswell [2005] given in Table 2.3. The channel consists of a gate creating and enclosed area with length l_0 and width w. The enclosed area is filled with granular material to an initial height h_0. The gate is then quickly removed, faster than the speed of collapse, and the resulting flow observed and measured. As with the axisymmetric collapse there is an aspect ratio in the flowing direction $a = h_0/l_0$, but there is also a second aspect ratio based on the width of

Particle Type	d (mm)	w (mm)	l_0 (mm)	s_w	s_{l0}	a	b
		Balmforth		2005			
Grit	1.0	10	180	10	180	0.5–50.0	0.06
			300	10	300		0.03
		200	180	200	180		1.11
			300	200	300		0.67
Ballotini	0.8	10	180	12	225		0.06
			300	12	375		0.03
		200	180	250	225		1.11
			300	250	375		0.67
	3.0	10	180	3	60		0.06
			300	3	100		0.03
		200	180	66	60		1.11
			300	66	100		0.67
Polystyrene	0.75	10	180	13	240		0.06
			300	13	400		0.03
		200	180	266	240		1.11
			300	266	400		0.67
		Lube		2005			
Sand	1.5	200	45	133	30	0.2–18.0	4.44
			83	133	55		2.41
			125	133	83		1.6
		Lajeunesse		2005			
Ballotini	1.15	45	10–102	39	8–88	0.2-13.0	0.44–4.50
	3.0	45	10–102	15	3–34		0.44–4.50

Table 2.3: Particle types and system parameters in experiments by Lajeunesse et al. [2005], Lube et al. [2005] and Balmforth and Kerswell [2005]. d is grain diameter, w is channel width, l_0 is initial channel length, $a = h_0/l_0$ and $b = w/l_0$ are system aspect ratios and $s_w = w/d, s_{l0} = l_0/d$ are system size parameters.

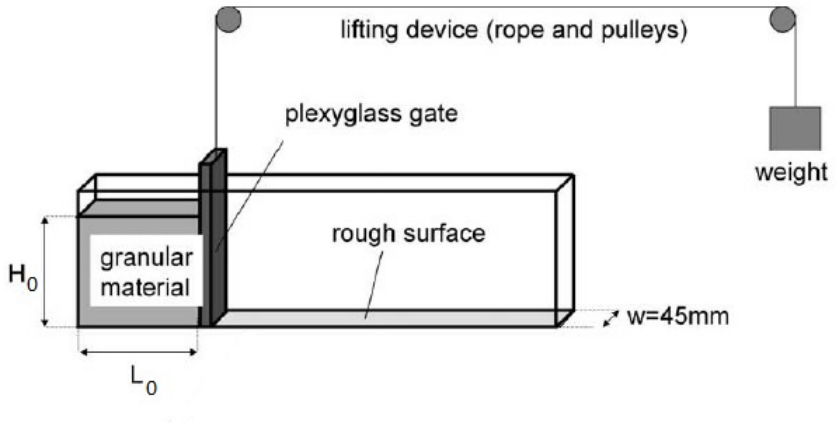

Figure 2.16: Experimental setup for collapse in a channel [Lajeunesse et al., 2005].

the channel $b = w/l_0$. Similarly the system size s can be given by two length scales, w and l_0, defined as $s_w = w/d$ and $s_{l0} = l_0/d$ respectively.

Both narrow and and wide channels have been considered by authors demonstrating a range of system sizes. Wall friction effects could affect the flow as found in other channel experiments discussed by Jop et al. [2006] and G.D.R-Midi [2004]. They find that where the system size perpendicular to the flow direction becomes large enough this effect becomes negligible. Quantification of this effect is dependent on the experimental setup, demonstrating the need for its consideration.

2.3.2 Flow description

Similar to the axisymmetric case there are two different flow regimes; for low aspect ratios the periphery of the column initially crumbles and begins to flow, and for high aspect ratios the entirety of the upper surface collapses and contributes to the flow [Lajeunesse et al., 2005; Lube et al., 2005; Balmforth and Kerswell, 2005]. Examples of these flows are shown in Figure 2.17. Both regimes begin in the same manner with an initial spreading phase. This initiates with a flowing layer that moves as a deforming bulk flow. There is a separation zone between a static region and a flowing layer that decreases in thickness as the flow propagates, observed in Figure 2.18. Particles on the upper free surface remain there or are deposited on the collapse surface over which the rest of the collapse occurs. When this separation zone reaches the free surface the flow ceases to spread. If the slope is steep enough towards the back of the initial step there is a second avalanching stage that occurs over the surface which doesn't increase the runout, but alters the surface shape. This avalanching stage predominantly occurs for low aspect ratios where the flow initiates at the periphery of the step [Lube et al., 2005].

Figure 2.19 shows scaled final deposits for wide slot (180mm) channel collapse

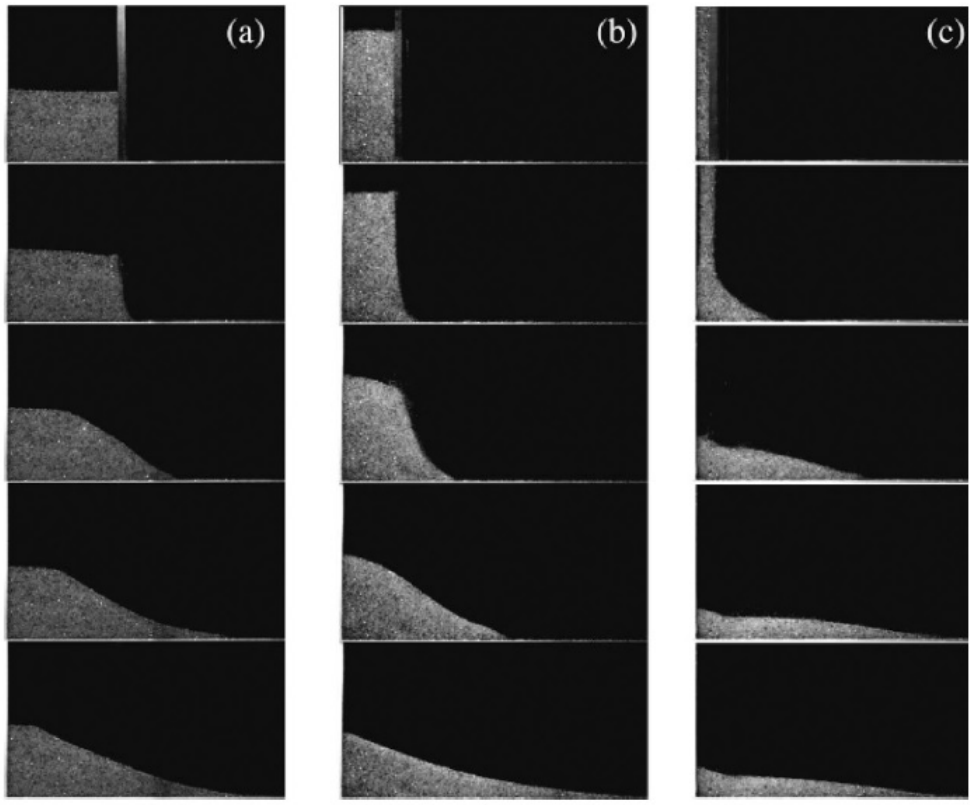

Figure 2.17: Evolution of the flow of a granular step for different aspect ratios as per Lajeunesse et al. [2005] experiments. In this case $w = 45\,\text{mm}$. (a) $a = 0.6$, $l_0 = 102\,\text{mm}$. (b) $a = 2.4$, $l_0 = 56\,\text{mm}$. (a) $a = 16.7$, $l_0 = 10\,\text{mm}$.

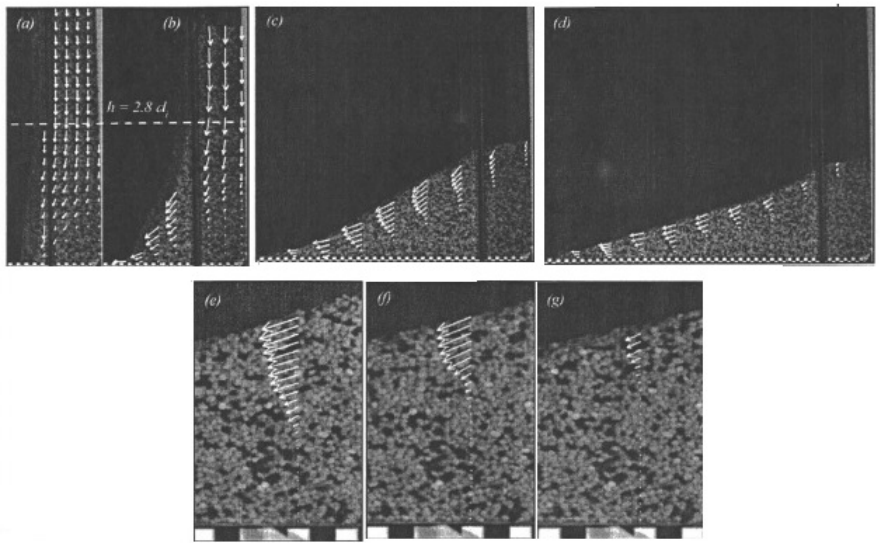

Figure 2.18: Velocity of individual layers throughout a collapse with $a = 7$ in a wide channel. The magnitude of the velocity is indicated by the length of arrows. (a)–(d) show the entire profile while (e)–(g) show a close up view at a distance $l_f/3$ [Lube et al., 2005].

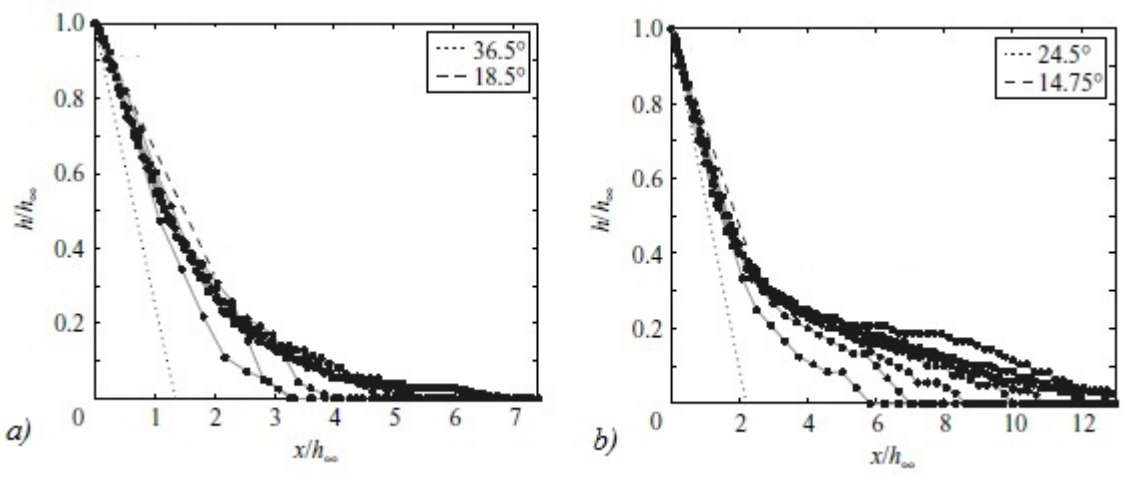

Figure 2.19: Scaled final deposits for different aspect ratios with a wide slot (180mm). (a) Irregular shaped grit. (b) Fine ballotini (spherical shaped media) [Balmforth and Kerswell, 2005].

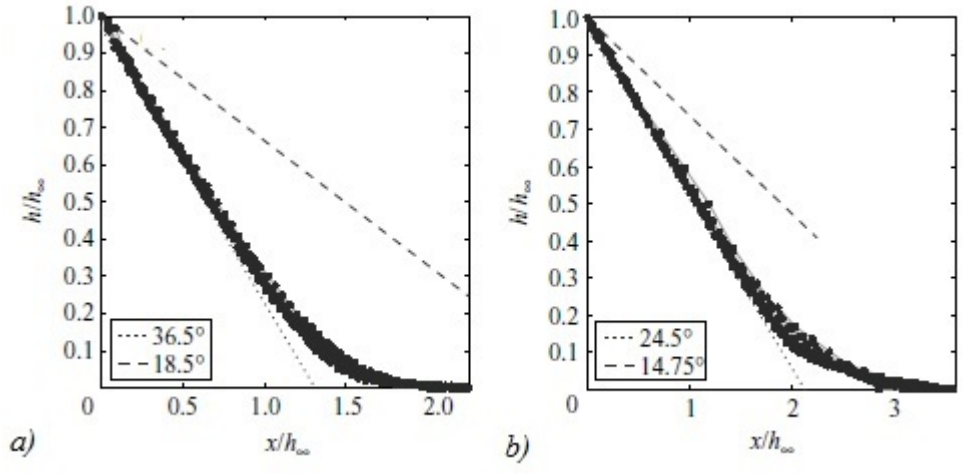

Figure 2.20: Scaled final deposits for different aspect ratios with a narrow slot (10mm). (a) Irregular shaped grit. (b) Fine ballotini (spherical shaped media) [Balmforth and Kerswell, 2005].

Channel width (mm)	Author	α		β	
10	Balmforth	0.65	$a > 3$	1.00	$a < 1$
				0.50	$a > 1$
45	Lajeunesse	1.00	$a < 3$	1.00	$a < 0.7$
		0.67	$a > 3$	0.33	$a > 0.7$
180	Balmforth	0.90	$a > 1.5$	1.00	$a < 2$
				0.60	$a > 2$
200	Lube	1.00	$a < 1.8$	1.00	$a < 1.15$
		0.66	$a > 2.8$	0.40	$a > 1.15$

Table 2.4: Exponents for length and height scalings as per equations 2.14 and 2.15 from studies by Balmforth and Kerswell [2005]; Lajeunesse et al. [2004]; Lube et al. [2004]

performed by Balmforth and Kerswell [2005]. Interestingly the curves collapse quite well for the irregular shaped grit media unlike spherical ballotini, likely due to slipping that is more likely to occur with spherical particles. This scales significantly better than the axisymmetric case shown in Figure 2.6. In the case of the narrow slot (10mm) the scaling is extremely strong, once again with a slightly better result in the grit case as shown in Figure 2.20.

2.3.3 Collapse scalings

Similar to the axisymmetric case appropriate scaling laws can be derived for the final runout l_f and the final height h_f,

$$\frac{l_f - l_0}{l_0} = \lambda a^{\alpha} \tag{2.14}$$

$$\frac{h_f}{l_0} = \lambda a^{\beta} \tag{2.15}$$

Dependence on the width of the channel is evident as each study finds different exponents and validity ranges for the power laws. Notice in this case that the height of the resultant profile increases with aspect ratio where as in the axisymmetric case it ceases to grow/minutely increases at the end of the first flow regime. In addition, Balmforth and Kerswell [2005] demonstrate a strong dependence on the material properties on the proportional constant. A summary of the constants can be found in Table 2.4.

2.3.4 Time evolution

Time characteristics of the flow are similar to the axisymmetric case. Lube et al. [2005] show that the runout of the column again follows a logistic shape curve as in

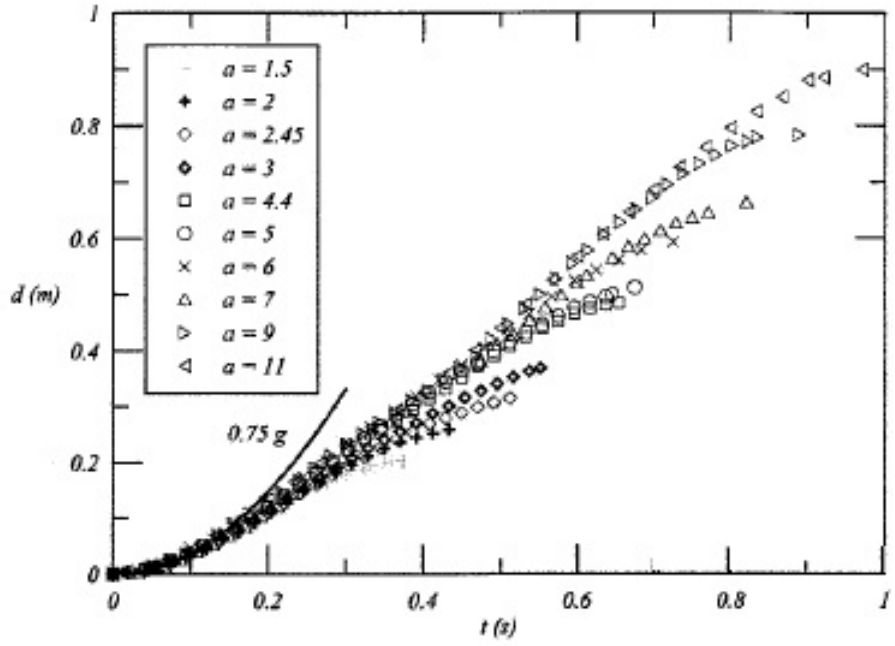

(a)

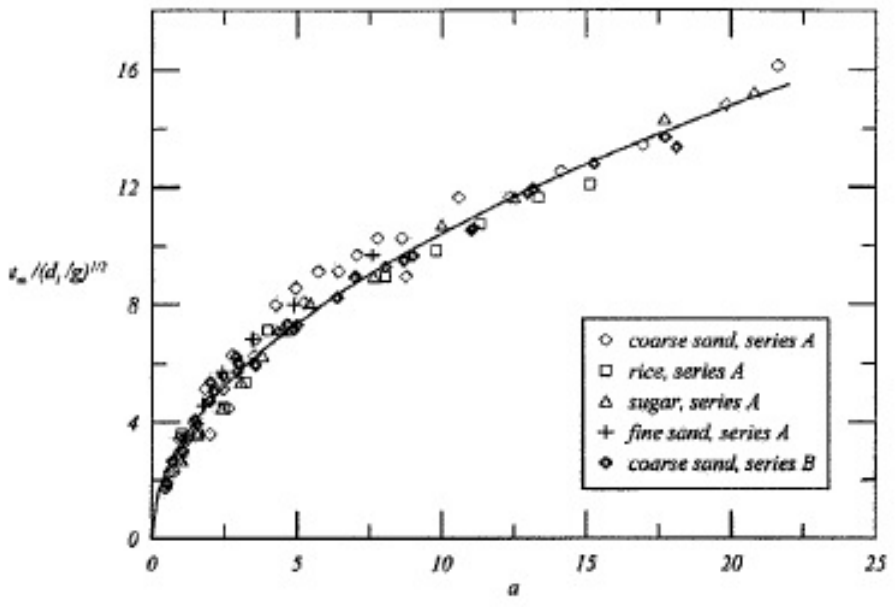

(b)

Figure 2.21: Time characteristics of the flow for experiments by Lube et al. [2005] in a wide slot (200 mm). Series A refers to a dual gate symmetric channel collapse and series B refers to a single gate. (a) Runout against time (single gate only). (b) Total time for collapse against aspect ratio.

Figure 2.21 (a). There is an initial acceleration owing to the deposition of a basal layer over the surface, followed by a period of constant velocity and decelerating as the avalanching begins to cease. The total time for collapse is shown in Figure 2.21 (b) with all values approximately falling to the same curve given by

$$\frac{t_f}{\sqrt{l_0/g}} = 3.3\sqrt{a} \tag{2.16}$$

This is exactly the same relation as seen in the axisymmetric case given in Equation 2.13 with the constant of proportionality only 10% higher.

2.3.5 Similarities with axisymmetric collapse

The literature review has shown that there are extremely strong similarities of the channel collapse with the axisymmetric case. The exception lies with the values of exponents and proportional constants, while the kinematics of the flows seem largely the same. The main difference with the axisymmetric case is the existence of a bounding wall for the duration of the collapse. All the above cited authors have found different values of exponents for channel collapse, demonstrating a strong dependence on the ratio of channel width to granule size as noted by Jop et al. [2006]. The axisymmetric case removes the constant bounding wall with the radial collapse only constricted by neighbouring material. Lube et al. [2004]; Lajeunesse et al. [2004] both find that there is no such system size dependence in this case, and without any direct discussion have discounted this for the aforementioned reason.

2.4 Granular flows on rotating disks

The most commonly investigated rotational granular flow is the rotating drum, popularised by analogies that can be drawn with avalanching behaviours and in industrial rotary kilns. Spreading of material using a disk spinning in the horizontal plane is employed by industry as discussed in the introduction, but the dynamics have less frequently been explored. Chapter 6 of this thesis considers axisymmetric column collapse on a rotating surface, motivated by the centrifuging granular flows discussed here.

2.4.1 Centrifuging granular heaps

Shinbrot et al. [2007] considered the idea of granular media being deposited on a disk rotating at a speed ω to investigate the growth of piles under reduced gravity. Solid glass beads of diameter 75–106 μm were continuously deposited onto a 100 mm rotating acrylic disk via a hopper arrangement fed by a slanted reservoir of grains allowing modification of the flow rate as shown in Figure 2.22.

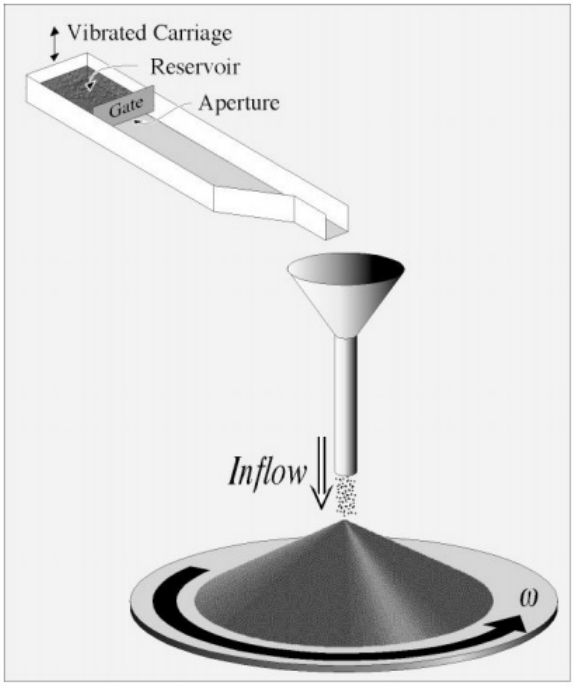

Figure 2.22: Experimental arrangement for centrifuging granular heaps as performed by Shinbrot et al. [2007]. A slanted reservoir that is vibrated at different rates controls the mass flow into the funnel and onto the spinning disk.

The experimental setup imitates a reduced gravity situation where normal and tangential accelerations at the surface are given by

$$a_n = g\cos\theta - \omega^2 r\sin\theta \tag{2.17}$$

$$a_t = g\sin\theta + \omega^2 r\cos\theta - \mu a_n \tag{2.18}$$

respectively. A central radial value $r = 50\,\text{mm}$ is taken to estimate the angle of repose for each rotation rate. Combining the above two equations and taking $\mu = 0.55$ (found from experiments at $\omega = 0$) the angle of repose is found to vary like

$$\tan\theta_r = \frac{\mu g - \omega^2 r}{g - \mu\omega^2 r} \tag{2.19}$$

in good agreement with experimental values as shown in Figure 2.23 (b). The decrease in the angle of repose with rotation rate implies the reduction of compressive stress and an increased outwards acceleration under reduced gravity situations.

The different rotation rates resulted in a variety of well defined surface features with a sharp transition between them. As the rotation rate increases this evolves from channels, to droplets, and eventually to spirals after a period without

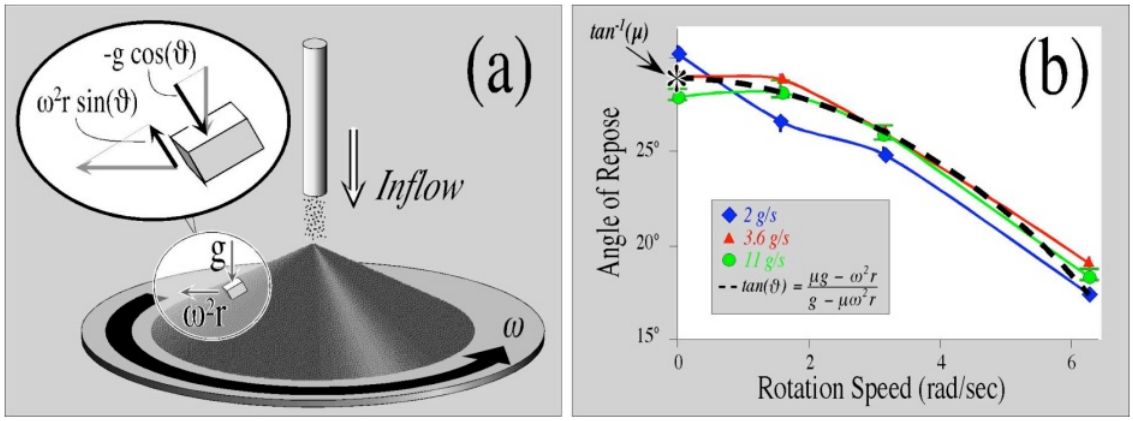

Figure 2.23: (a) Evaluation of forces on a granular element at the surface. (b) Estimations of the angle of repose at different rotation rates compared against a theoretical value [Shinbrot et al., 2007].

any features as shown in Figure 2.24. These patterns were observed using glass beads whereas trials with sand, crushed glass and hollow beads only allowed the formation of channels or irregular landscapes.

Cohesive forces were found to have an impact in the formation of contours. To increase the cohesiveness of the particles the humidity of the environment was increased. This led to the transition of features to occur earlier but no reasoning is given to this counter intuitive effect. The authors best understanding of this observation is that cohesive grains appear to solidify into channel boundaries or droplets more readily than freely flowing grains.

2.4.2 Ripple formation in centrifuging granular beds

While this study concentrates on collapse of granular columns, the effect of rotation on granular beds as performed by Zoueshtiagh and Thomas [2000] [Zoueshtiagh and Thomas, 2003; Thomas and Zoueshtiagh, 2005] could provide information on rotational collapse. The experimental setup is shown in Figure 2.25 consisting of tank of radius $R = 0.5\,\mathrm{m}$ filled evenly with select granular media of $0.11 < d < 3.17\,\mathrm{mm}$ to a thickness of $3 - -30\,\mathrm{mm}$, and the tank then filled with water. The tank is spun up to a rotation rate ω_0 slow enough so granules are not set into motion. The granules and fluid are then allowed to reach solid body rotation before being instantaneously spun up to a speed ω_1 such that $0 < \Delta\omega = \omega_1 - \omega_0 < 5\,\mathrm{rad\ s^{-1}}$. The shear force at the fluid/granule boundary mobilised the grains and allowed the formation of ripples.

For their experimental parameters $7 \leq n \leq 110$ spiral arms were formed with a centrally undisturbed patch of radius r_0 as shown in Figure 2.26. Both the number of spiral arms and the radius of the undisturbed patch were inversely proportional

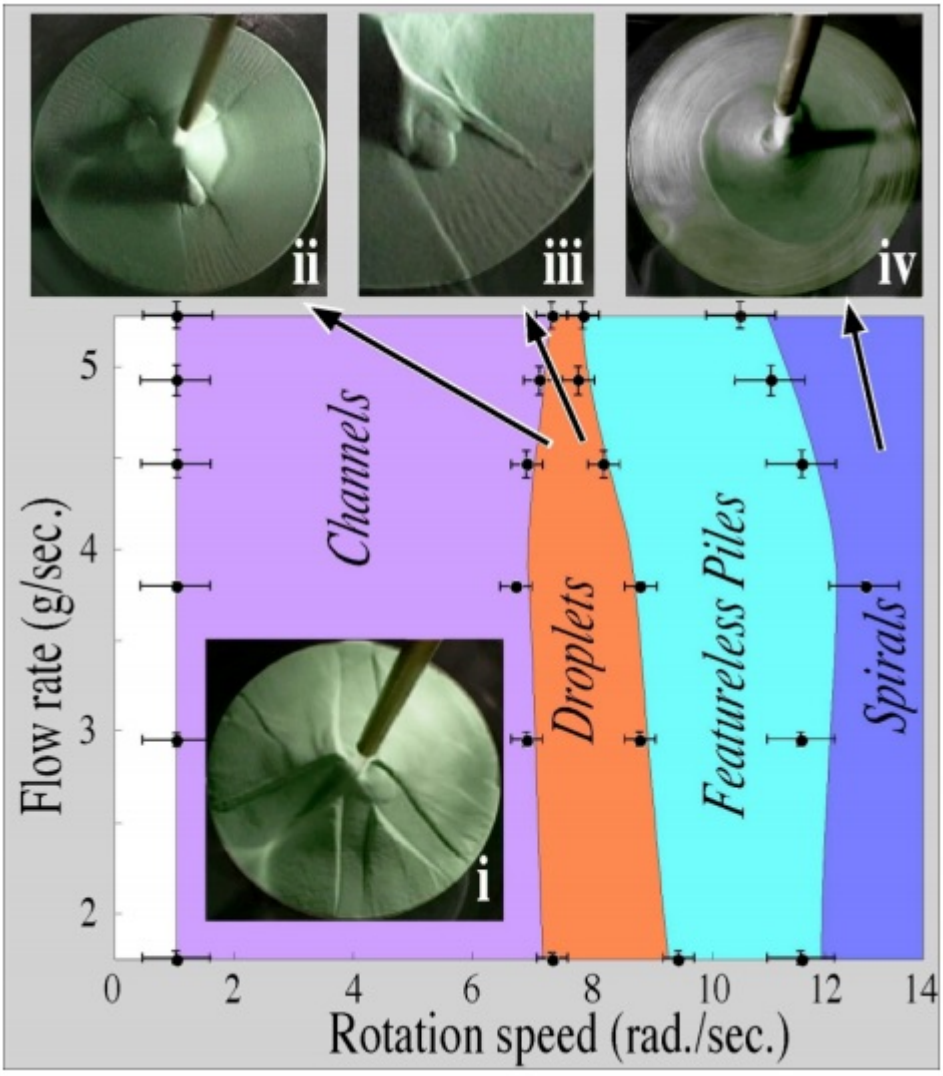

Figure 2.24: Different geometrical patterns are observed on the surface of the deposit with the geometry being strongly dependent on rotation rate [Shinbrot et al., 2007].

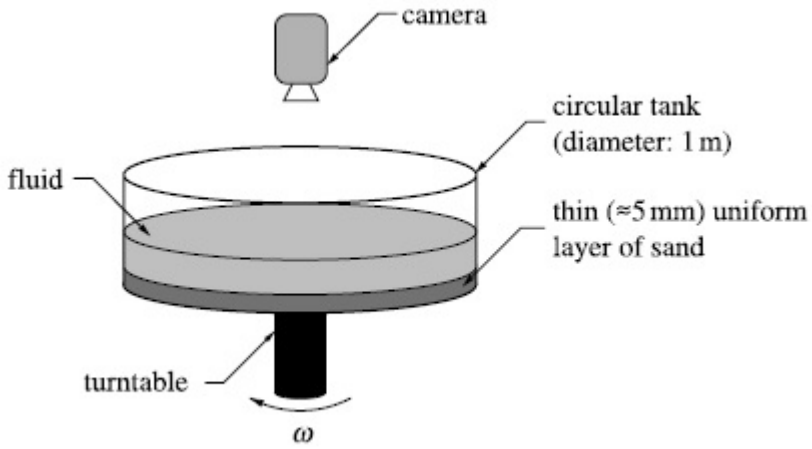

Figure 2.25: Setup for the observation of granular ripples in a granular bed immersed in a fluid [Thomas and Zoueshtiagh, 2005].

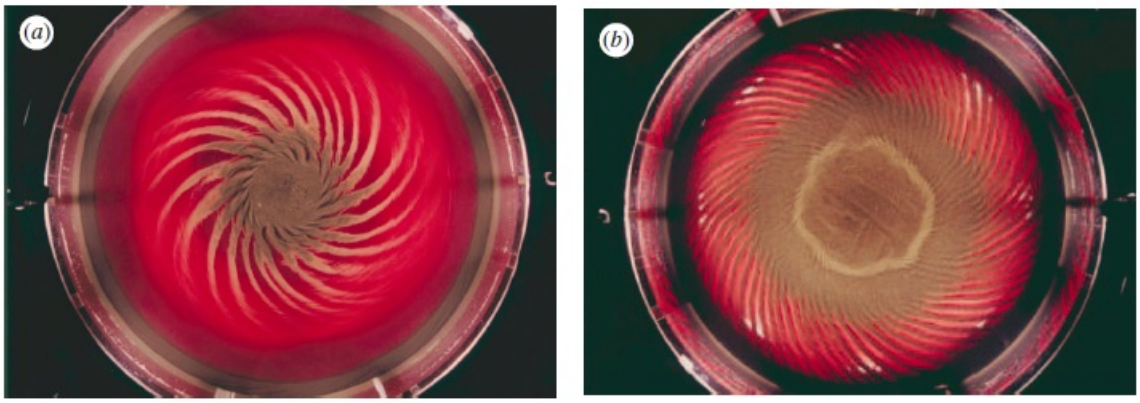

Figure 2.26: Examples of granular ripples obtained by Zoueshtiagh and Thomas [2000] by experimental setup shown in Figure 2.25. (a) $\Delta\omega = 2.15\,\text{rad s}^{-1}$, $\omega_1 = 3.16\,\text{rad s}^{-1}$. (b) $\Delta\omega = 1.30\,\text{rad s}^{-1}$, $\omega_1 = 4.00\,\text{rads}^{-1}$. [Thomas and Zoueshtiagh, 2005].

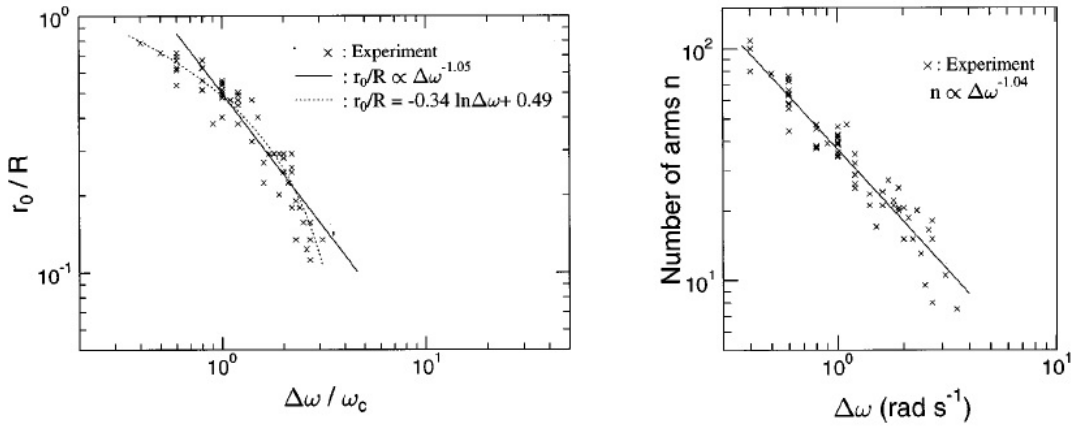

Figure 2.27: Scalings of characteristic ripple patterns. Left: $r_0 \propto \Delta\omega^{-1}$. Right: $n \propto \Delta\omega^{-1}$ (Figure adapted from Zoueshtiagh and Thomas [2000]).

to the spin up rate $\Delta\omega$ as illustrated in Figure 2.27. Where the initial layer was thin enough there were occasions where the gaps between spiral arms exposed the bottom of the tank completely.

Further quantification of the phenomena is given by defining a wavelength $\lambda = 2\pi r_0/n$ and a mobility parameter Θ:

$$\Theta = \frac{\rho_G U}{g(\rho_G - \rho_F)d} \tag{2.20}$$

where U is some charateristic velocity with $U = \Delta\omega r_0$. This is similar to a Shields parameter which is a non dimensionalisation of shear stress of sediment in fluid flow which has been used in seemlingly different experiments such as oscillating and non oscillating annular flows and straight channel flows. The data from the presented work follows the same law as in the other experiments as shown in Figure 2.28 with

$$\frac{\lambda}{d} \propto \Theta^{0.52} \tag{2.21}$$

This is in agreement with the results of the dimensional analysis for the setup of Zoueshtiagh et al. [2008] where an exponent of 0.5 was found.

It is a suprise that the scaling which held for non-rotational granular systems also holds for the rotational case. This means that the background rotation doesn't affect the scaling, and potentially scalings from the rotational system can give analogous results to non-rotating ones with an equivalent characteristic velocity.

2.5 Theoretical models

Fluid flows are subject to a set of constitutive laws described by Navier-Stokes, but granular flows do not have such fundamental equations associated with them.

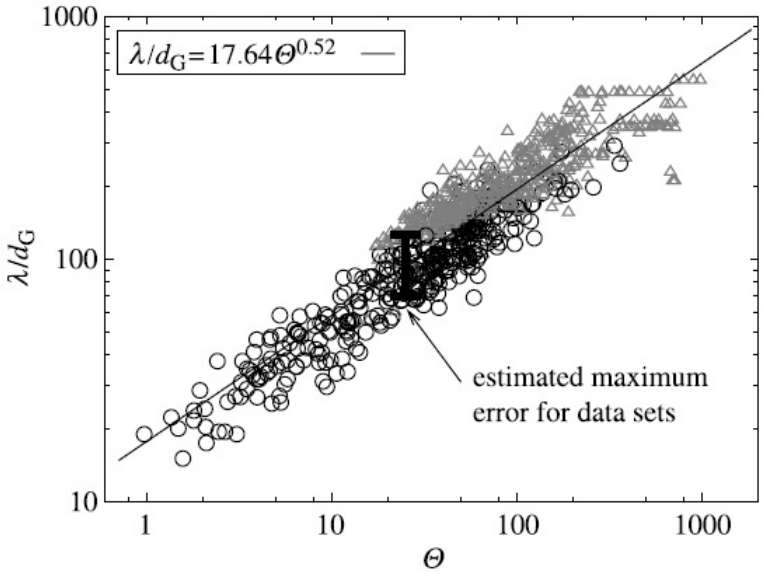

Figure 2.28: Wavelength of the ripples are proportional to the mobility parameter defined by other non-rotating granular flows. Data from rotating tank shown by circles and other non-rotating experiments shown by triangles [Thomas and Zoueshtiagh, 2005].

The difficulty in establishing such a description lies with the unsteady flow nature where systems often consist of areas that behave concurrently like a solid (plastic deformation), liquid (non newtonian fluid) and gas (saltation of grains). There have been several attempts to model granular systems with flud-like rheologies with varied degrees of success and often has resulted in application to specific situations.

2.5.1 Surface flows

The earliest model applied by Savage and Hutter [1989] uses an inviscid shallow water model to describe the flow down a rough inclined surface. They assume a constant velocity profile with a sliding layer on the bottom providing a Coulomb friction force. The equations are derived from standard incompressibility and momentum laws and given by

$$\frac{\partial H}{\partial t} + \epsilon \frac{\partial}{\partial x}(HU) = 0 \tag{2.22}$$

$$\frac{\partial H}{\partial t} + \epsilon U \frac{\partial U}{\partial x} = [\sin(\theta) - \tan(\delta)\cos(\theta)] - \beta \frac{\partial H}{\partial x} \tag{2.23}$$

where H is the flow height, U is the velocity, θ is the slope angle and δ is dynamic basal friction angle. The driving term is a combination of pressure variation in the layer depth and the Coulomb friction force.

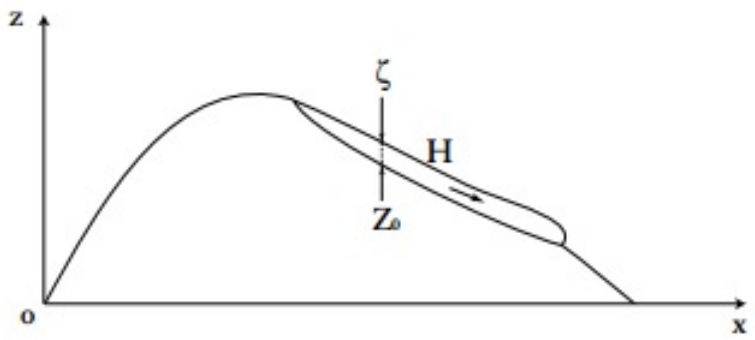

Figure 2.29: Sketch of a granular avalanche over a static pile. The flow is divided into an upper profile $\Gamma(x,t)$ and a static/flowing profile $Z_0(x,t)$ with a flow height $H(x,t)$ [Douady et al., 1999].

An extention provided by Douady et al. [1999] again uses the same laws, but uses depth-averaging with a fixed basal condition giving:

$$\frac{\partial H}{\partial t} + \epsilon \Gamma H \frac{\partial H}{\partial x} = 0 \tag{2.24}$$

$$\frac{\partial H}{\partial t} + \epsilon \Gamma H \frac{\partial H}{\partial x} = \frac{g}{\Gamma} \left[\sin(\theta) - (\mu(H) + \delta\mu(H,\theta)) \cos(\theta) \right] \tag{2.25}$$

for variables shown in Figure 2.29 and Γ is the velocity gradient, μ is the friction coefficient. This model has successfully been applied to decribe surface flows down a mountain face [Mangeney-Castelnau et al., 2003] in good agreement with experimental data.

Further it has been applied to axisymmetric column collapse [Mangeney-Castelnau et al., 2005], retrieving scalings proposed by Lajeunesse et al. [2004] at least for $a < 1$. Beyond this aspect ratio the runout significantly overshoots the experimental results and the relaxation near the summit becomes too great. This is observed in Figure 2.30 for a low and a high aspect ratio where the numerical results are shown with a solid line, and the experimental by a dashed line. The disagreement can be attributed to shallow water equations assuming variation in the horizontal directions that occur over scales much greater than depth, which is not consistent with a high aspect ratio.

2.5.2 Adaptation of shallow water equations

Shallow water equations have shown a promising start to modelling the column collapse as a continuum, but struggles to recover the behaviour of the collapse at high aspect ratio columns. It was observed experimentally that while a thin layer of the material spreads horizontally, the collapsing central region feeds the flow.

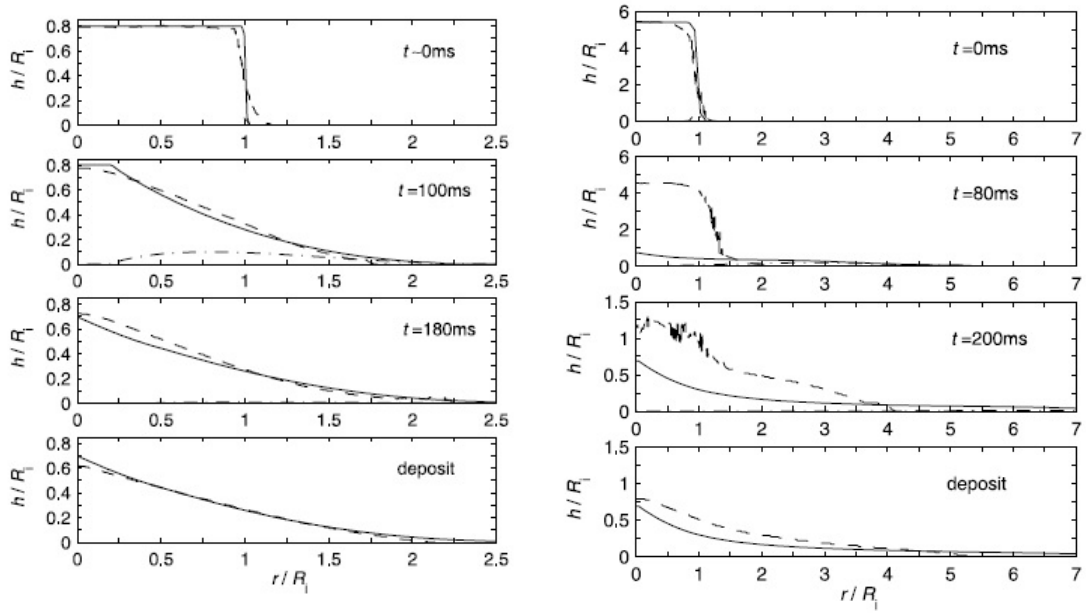

(a) (b)

Figure 2.30: Shallow water depth averaged equations are applied to axisymmetric collapse. There is good agreement for $a < 1$ but the runout overshoots and the pile over-relaxes where $a > 1$. Solid line indicates numerical result and dashed line indicates experimental result. (a) $a = 0.8$. (b) $a = 5.6$ [Mangeney-Castelnau et al., 2005].

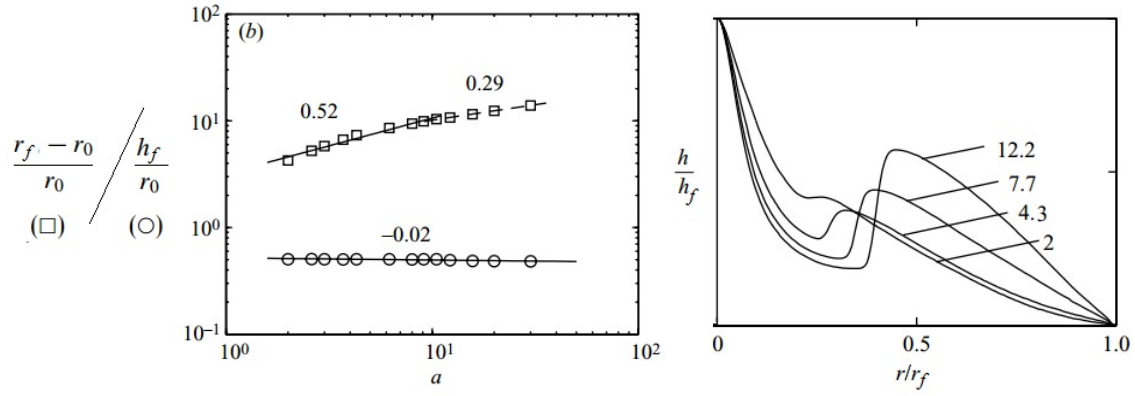

(a) (b)

Figure 2.31: Results from continuum with granular 'rain' modelling by Larrieu et al. [2006]. (a) Scaling of the resultant deposit for both height and final runout. (b) Normalised shape of the resultant deposit.

Larrieu et al. [2006] used this knowledge to adapt the shallow water equations to mimic this behaviour.

The initial setup consists of a short cylinder such that $a = 0.1$ with the increase in mass flow performed by adding a volume flux per unit area for the duration of the free-fall of the column:

$$q(r,t) = \begin{cases} gt & 0 \leq r \leq r_0 \\ 0 & \text{otherwise} \end{cases} \tag{2.26}$$

i.e. for $0 \leq t \leq \sqrt{2(h_0 - 0.1r_0)/g}$. Shallow water depth-averaged equations are applied to the horizontal flowing layer of material, but the additional volume is assumed to have no horizontal momentum. The equations for mass conservation and momentum are then given (in polar coordinates):

$$\frac{\partial H}{\partial t} + \frac{1}{r}\frac{\partial (rHU)}{\partial r} = q \tag{2.27}$$

$$\frac{\partial (HU)}{\partial t} + \frac{1}{r}\frac{\partial (rHU^2)}{\partial r} = -\frac{1}{2}Kg\frac{\partial (H^2)}{\partial r} - \mu gH \tag{2.28}$$

In the momentum equation the first term on the right hand side is a spreading term proportional to the material slope. K is the earth pressure coefficient; the ratio between horizontal and vertical normal stress related to internal friction. As per results from Pouliquen and Forterre [2002] the hydraulic assumption value $K = 1$ is used. The second term is the shear stress at the base where μ is the frictional coefficient between the plane and the granular material. No $-qu$ term appears due to the added volume having no horizontal momentum.

This model produces scalings for the final runout and final height as in Figure 2.31 (a). The equations for the final runout are given

$$\frac{r_f - r_0}{r_0} = \begin{cases} 3.2a^{0.52} & 2 \leq a \leq 10 \\ 5.2a^{0.29} & a \geq 10 \end{cases} \tag{2.29}$$

which are in good agreement with both Lube et al. [2004] and Lajeunesse et al. [2004] who found an exponent of 0.5. The coefficients of 3.2 and 5.2 arise from their selection of basal friction ($\mu = 0.45$) which is approximately double observed experimentally. To obtain a coefficient of 1.6 as Lube et al. [2004] did, the basal friction (between the surface and granular material) would have to be set at $\mu = 0.8$ which is extremely high. This value could represent the vertical velocity variations which are not included in this plug flow model. Larrieu et al. [2006] finds a stagnation in the final height with increasing aspect ratio seen in Figure 2.31 (a). This is in agreement with experimental results by Lajeunesse et al. [2004].

While the scalings show good agreement, the resultant profiles of the deposit are not as compatible with experimental results as shown in Figure 2.31 (b). This demonstrates a strong secondary maximum, which while experimental authors agree with its existence, report that it is only a slight bump. The model's runout propagation showed a logistic 'S' shaped curve in agreement with experiments but the total time for collapse was severely underestimated, finding an exponent of 0.33 as opposed to 0.5 as reported by Lube et al. [2004].

2.5.3 Shallow water equations with static/flowing interface

The model proposed by Larrieu et al. [2006] was further developed by Doyle et al. [2007] in 2D by introducing an interfacing approximation between the static and flowing regions of the collapse. This was made possible by confirmation of the interfacing surface over time shown in experiments by Lube et al. [2005]. The equations show a resemblance to Larrieu et al. [2006] (given above in polar coordinates) with some additional terms to manage the interface:

$$\frac{\partial H}{\partial t} + \frac{\partial (HU)}{\partial x} = q - k_1 L_s - k_2 \frac{W_s(x)}{\Delta t_{rw}} \tag{2.30}$$

$$\begin{aligned} &\frac{\partial (HU)}{\partial t} + \frac{\partial}{\partial x}(HU^2 + 0.5g\cos\theta H^2) \\ &\quad = gH\sin\theta - gH\cos\theta\tan\delta - \frac{\partial z_b}{\partial x} g\cos\theta h + U\left[q - k_1 L_s - k_2 \frac{W_s(x)}{\Delta t_{rw}}\right] \end{aligned} \tag{2.31}$$

where L_s defines a sedimentation rate, $W_s(x)$ is an additional mass loss term de-

scribing the initial static wedge seen after lock release, Δt_{rw} time for the wedge to be deposited and z_b is the deposit surface. k_1, k_2 are constants to manage the sedimentation and mass loss rate based on experimental observations.

Through numerical simulation of the above equations, scalings of the final collapse for $a > 3$ were found to be:

$$\frac{l_f - l_0}{l_0} = 2.14a^{0.67} \tag{2.32}$$

$$\frac{h_f}{l_0} = 1.66a^{0.21} \tag{2.33}$$

$$\frac{t_f}{\sqrt{2l_0/g}} = 2.14a^{0.46} \tag{2.34}$$

The first equation for the final runout finds extremely good agreement with the exponent given by Lube et al. [2005] in a narrow channel, but again over estimates the leading coefficient found to be 1.9. This model is significantly closer to the experiment than Larrieu et al. [2006], who found the leading coefficient to be 4.4, unless they used extremely high basal friction. The second equation for the final height under-estimates the exponent given by Lube et al. [2005] who finds a value of 0.4 and is attributed to the additional mass loss term being too large. The third equation for total time for collapse is in much stronger agreement with experimental results by Lube et al. [2005] who found an exponent of 0.5, than the model proposed by Larrieu et al. [2006] who found an exponent of 0.33.

Results for $a < 3$ were not comparable to the experimental results possibly due to the static wedge occupying a proportionally larger amount of the final deposit. In summary, this model has provided stronger results for high aspect ratios without requiring unrealistic basal friction as per Larrieu et al. [2006], while now finding weaknesses with the lower aspect ratios. This model was possible in 2D because of observation of static wedges and the movement of the interfacing surface which is clearly not possible in an axisymmetric case. Importantly this model has demonstrated where there is a strong and a weak dependence on the initial wedge, indicating the effect throughout the flow.

2.5.4 μ(I) rheology

The most recent model currently accepted as the best continuum approximation is the $\mu(I)$ rheology proposed by Lagrée et al. [2011] which uses the Navier Stokes equations in combination with shear rates and pressures experienced within the media. Its has only been applied to 2D columns but it is presupposed that it equally extends to the axisymmetric case.

Coulomb based friction laws as used in previous models are based on the ratio of tangential to normal stresses. The $\mu(I)$ model, instead of using a fixed value of friction, uses a dependence on inertial number, the ratio of shear deformation and inertial time scales as defined by da Cruz [2004]:

$$I = d\frac{\partial u/\partial y}{\sqrt{p/\rho}} \tag{2.35}$$

where d is grain diameter, ρ is material density, p is pressure and $\partial u/\partial y$ is the shear rate. The dependence is then given as proposed by Jop et al. [2005]:

$$\mu(I) = \mu_s + \frac{\Delta\mu}{I_0/I + 1} \tag{2.36}$$

Inclusion of this dependence was previously not incorporated due to the difficulty of coupling it with the free surface condition, but Lagrée et al. [2011] overcame this by use of a Gerris flow solver (for details of discretization of finite volume/volume of fluid method see reference). The two phase Navier-Stokes flow equations are given:

$$\nabla \cdot \mathbf{u} = 0 \tag{2.37}$$

$$\rho\left(\frac{\partial \mathbf{u}}{\partial t} + \mathbf{u}\cdot\nabla\mathbf{u}\right) = -\nabla p + \nabla\cdot(2\eta\mathbf{D}) + \rho\mathbf{g} \tag{2.38}$$

$$\frac{\partial c}{\partial t} + \nabla\cdot(c\mathbf{u}) = 0 \tag{2.39}$$

$$\rho = c\rho_1 + (1-c)\rho_2 \tag{2.40}$$

$$\eta = \frac{1}{c/\eta_1 + (1-c)/\eta_2} \tag{2.41}$$

where $\mathbf{D}$ is the strain tensor $(\nabla\mathbf{u} + \nabla\mathbf{u}^T)/2$, $c(x,y,t)$ is the volume fraction and η is kinematic viscosity. Lagrée et al. [2011] implements the $\mu(I)$ viscosity in the second invariant $D_2 = \sqrt{D_{ij}D_{ij}}$ defining

$$\eta = \max\left(\frac{\mu(I)}{\sqrt{2}D_2}p, 0\right) \tag{2.42}$$

$$I = \frac{d\sqrt{2}D_2}{\sqrt{|p|/\rho}} \tag{2.43}$$

The results for profile evolution are far more convincing than previous models as shown in Figure 2.32 without any excessive bumps as found with numerics by Larrieu et al. [2006]. The recovered scalings are given

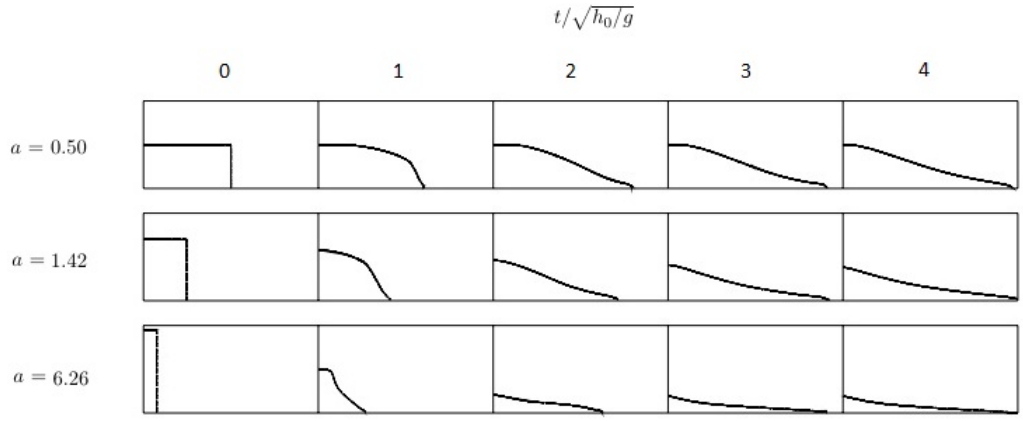

Figure 2.32: Profile evolution for column collapse with aspect ratios $a = 0.50, a = 1.42, a = 6.26$ (top to bottom) at times $t/\sqrt{h_0/g} = 0, 1, 2, 3, 4$ [Lagrée et al., 2011].

$$\frac{l_f - l_0}{l_0} = \begin{cases} 2.2a & a \leq 7 \\ 3.9a^{0.7} & a > 7 \end{cases} \tag{2.44}$$

$$\frac{h_f}{l_0} = \begin{cases} a & a \leq 0.5 \\ 0.67a^{0.4} & 0.5 < a < 6 \\ 1.4 & a \geq 6 \end{cases} \tag{2.45}$$

The exponent of the runout scaling is in agreement with Lube et al. [2005] for a wide channel but the bounding aspect ratio found experimentally was $a = 1.8$; nearly four times smaller than the shallow water model. Similarly the exponents for the final height scaling are in good agreement for a wide channel, but the aspect ratio bound for the transition from linearity was found to be $a = 1.15$ experimentally. The stagnation for $a > 6$ was observered exactly as Lajeunesse et al. [2005]. The reason for these bounding differences is not obvious, but comparison with contact dynamics simulations (the setup of which is discussed in the next section) offers some insight. As seen in Figure 2.33 the runout of the pile becomes progressively underestimated as the aspect ratio increases. At the periphery of the pile the granular material behaviour is more saltating than liquid which means the inertial number would be over estimated, leading to the under-estimation of the runout.

These first results are the most promising yet and with some further tweaking of the strain tensor at the periphery of the collapse to mimic the saltating behaviour, even stronger agreement could be found. While the results presented are in two dimensions, there is no obvious reason to why this result would not extend to three dimensions as presupposed by the authors.

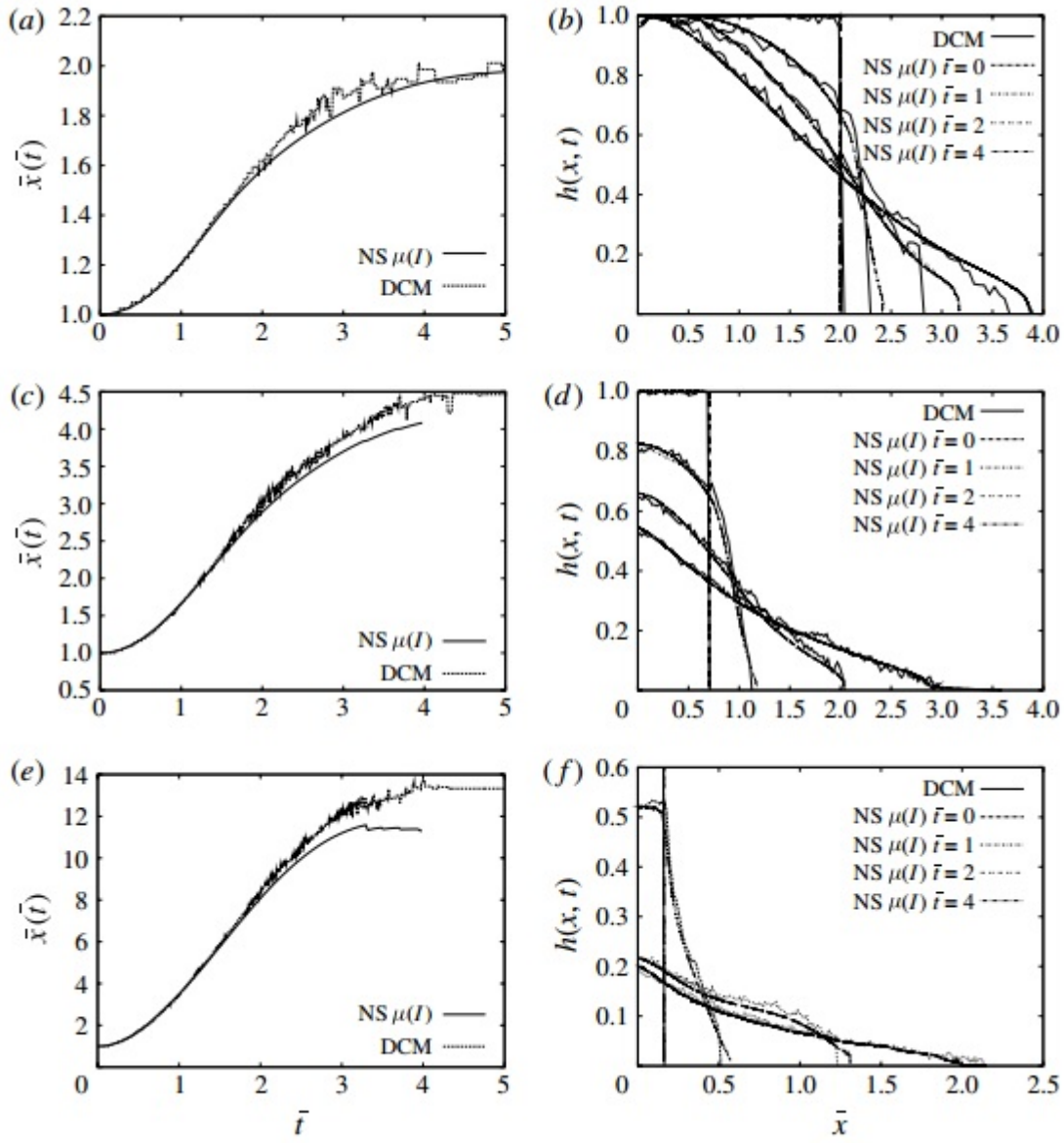

Figure 2.33: Comparison of numerical model (NS $\mu(I)$, solid line) with contact dynamics simulation (DCM, dashed line) [Lagrée et al., 2011]. Left is the normalised position of the front flow against normalised time, and right shows profile evolution. (a,b) $a = 0.5$, (c,d) $a = 1.42$, (e,f) $a = 6.26$.

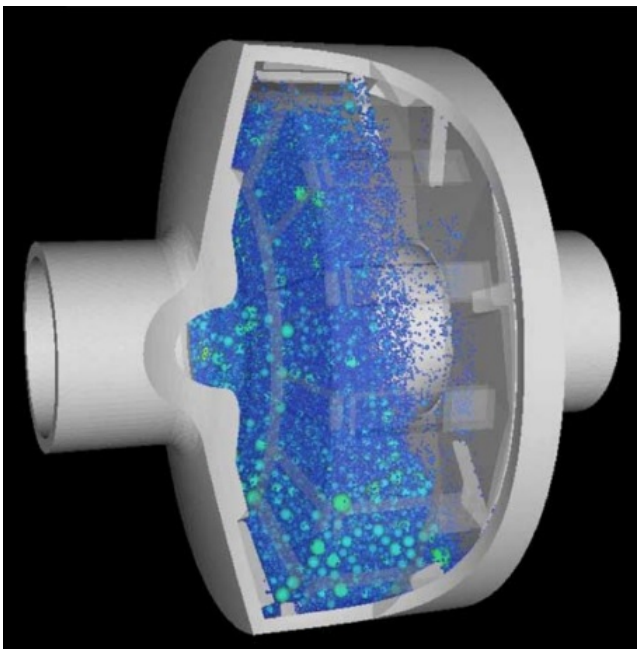

Figure 2.34: DEM of the milling technique using a polydisperse mixture of 425,000 particles as performed by Morrison and Cleary [2004].

2.6 Discrete Element Method (DEM)

Discrete Element Method (DEM) models granular flows using individual particles by evaluation of the standard laws of motion and forces at the contact points of granules at discrete time steps [Cundall and Strack, 1979b]. DEM can be coupled with a fluid flow, but discussed here is the pure granule interaction. This simulation methodology has been used widely across granular flows from avalanches to milling (pictured in Figure 2.34) to the particle interaction in an iron blast furnace, and is quickly overtaking the use of theoretical models for simulation given the strength of assumptions required for a theoretical model to be tractable. An initial exploration into rotational column collapse modelled through DEM is given in Chapter 7, with the following discussion serving as a preface to the modelling techniques employed.

The grains can be represented in two or three dimensions with the shape of the grains often assumed to be circular/spherical to avoid further computational complexities but immediately includes an assumption in the model. Several methodologies being applied to include non circular/spherical particles in simulations are discussed by Dziugys and Peters [2001] to include ellipsoids, super/hyper quadrics, composite particles (several spheres overlapping 'glued' together) and archimedean solids. Modelling of a particles shape can be important in many granular problems involving dense packings as the densest possible packing will vary dependent upon shape. While 'Newton's kissing problem' for spheres shows the greatest number

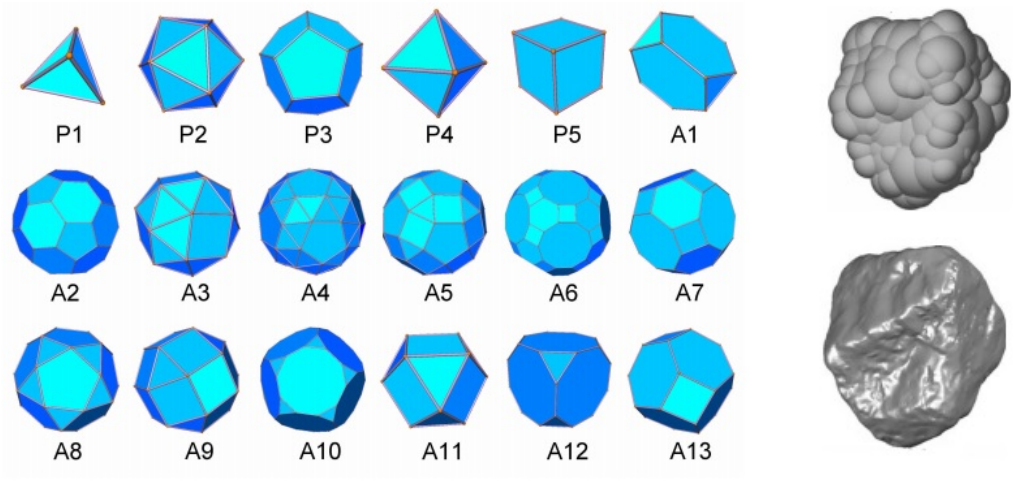

(a) (b)

Figure 2.35: Variations on spherical particle DEM may involve (a) Archimedean/Platonic solids [Torquato and Jiao, 2009] or (b) composite particles - 73 different sized sphere are used to model ballast [Ferellec and McDowell, 2010].

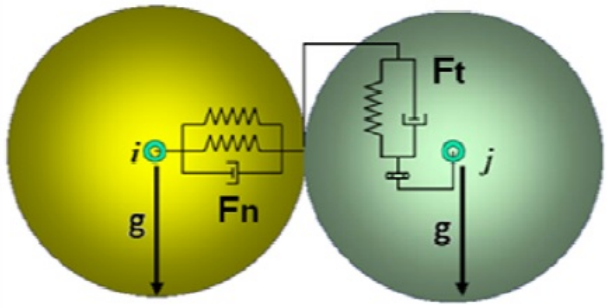

Figure 2.36: The theoretical arrangement of 'springs' in soft contact model of DEM [Goniva et al., 2012]

of spheres touching is 12, the densest packing is provided by a lattice model which Torquato and Jiao [2009] investigates for the set of Platonic and Archimedean solids depicted in Figure 2.35 (a). When modelling particle shape by cylinders or ellipsoids is not sufficient, the most common method is the composite particle method with an example of ballast multi-sphere description shown in Figure 2.35 (b).

Parameters of individual grains can be set to include grain diameter d, density ρ, particle-particle/particle-surface friction, and coefficient of restitution e. DEM is then further divided into soft (molecular dynamics) and hard (contact dynamics) particle interactions.

2.6.1 Molecular dynamics

The soft-particle model assumes that the particles can overlap at which point a linear or non-linear spring model forces the particles apart. The stiffness of the springs associated with loading and unloading of the particles indicated in Figure 2.36 set how much they can overlap which is desirable to keep at 0.1–1%, and additionally sets the coefficient of restitution of the particles [Zenit, 2005]. Such soft-particle models were suggested as early as 1979 [Cundall and Strack, 1979a] but realistic systems with thousands, even millions of particles would have to wait for computational speeds to improve. The simplest linear springs model gives the normal and tangential forces as:

$$\boldsymbol{F_n} = -k_n \Delta \boldsymbol{x_p} + c_n \Delta \boldsymbol{u_{p,n}} \tag{2.46}$$

$$\boldsymbol{F_t} = min \left\{ \left| k_t \int_{t_{c,0}}^{t} \Delta \boldsymbol{u_{p,t}}\, dt + c_t \Delta \boldsymbol{u_{p,t}} \right|, \mu_c \boldsymbol{F_n} \right\} \tag{2.47}$$

where k_n, k_t are spring constants, c_n, c_t are damper constants, $\Delta \boldsymbol{x_p}$ is the overlap distance and $\Delta \boldsymbol{u_{p,n}}$ is the relative tangential velocity [Goniva et al., 2012]. The damping coefficient defined by

$$c_n = 2\gamma \sqrt{\frac{k_n m_0 m_j}{m_0 + m_j}} \tag{2.48}$$

where

$$\gamma = -\frac{\ln e}{\sqrt{\pi^2 + \ln^2 e}} \tag{2.49}$$

is set to give the coefficient of restitution e.

With this model and an appropriate time step, first a list of near-neighbours to each particle is constructed to reduce the number of calculations. The collisional force is then calculated at each particle considering the newly constructed list using the above model (or another spring model). Appropriate equations of motion and intertia for particle i are given

$$\ddot{\boldsymbol{x}}_{\boldsymbol{i}} m_0 = \boldsymbol{F_i} + m_0 \boldsymbol{g} \tag{2.50}$$

$$\boldsymbol{I_i} \boldsymbol{\omega_i} = \boldsymbol{m_0} \tag{2.51}$$

where $\boldsymbol{m_0}$ is the moment and ω_i is the angular velocity. These equations are then integrated over discrete timesteps.

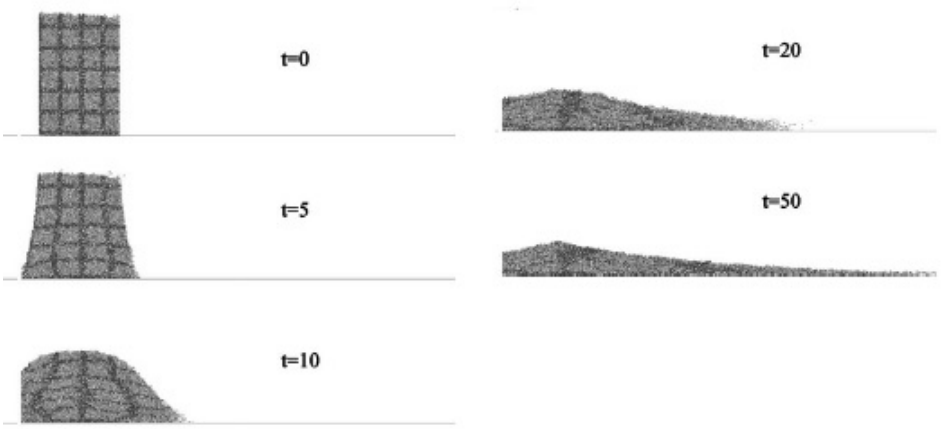

Figure 2.37: Collapse of a column as modelled by Zenit [2005] using soft-particle DEM. $N = 5000$, $a = 2.98$, $\mu = 0.30$.

2.6.2 Contact dynamics

A hard-particle model assumes that two particles do not induce a force on one another until in contact, after which no overlap can occur and repulsive forces cause the particles to move away from one another [Moreau, 1994]. This requires the time step to be irregular and simultaneously small enough so no overlap occurs but interaction is observed between some particles. The advantage of this system is that there is no need to consider where particles overlap and applying a method to keep this small. For each particle interaction only direct forces need to be considered with no compensation term for the integration step. The difficulty in predicting the time scales is what makes the codes complex in their exposition and intensive in computational power [Donze et al., 2009].

2.6.3 Column collapse

2D

Due the number of particles required and additional complexity of computation in an additional dimension, a large number of early DEM studies were completed in 2D. To further simplify the computation only circular particles were considered - non-spherical shaped particles have not been used to model the collapse to date.

The first such study for a 2D column was completed by Zenit [2005] who used a soft-particle model. Details of particle size and density are not recorded in this publication nor covergence of the time step, but a coefficient of restitution of $e = 0.75$ is given and two different friction coefficients $\mu = 0.30, 0.57$. The number of particles varies with $100 < N < 10000$ to achieve a variety of aspect ratios with different initial column radii.

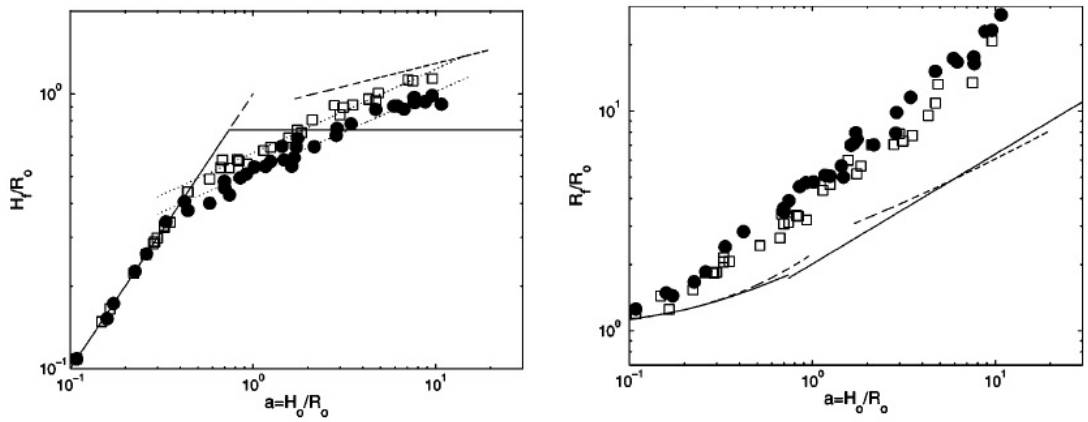

(a) (b)

Figure 2.38: Scalings of the collapse of a column as modelled by Zenit [2005] using soft-particle DEM. Solid circles $\mu = 0.30$, squares $\mu = 0.57$, solid line scaling by Lajeunesse et al. [2005], dashed line scaling by Lube et al. [2005].(a) Final height with aspect ratio. (b) Final pile radius with aspect ratio.

Time lapse of a collapse for 5000 particles is shown in Figure 2.37. The DEM model recovers the qualitative dynamics extremely well, and while the scalings display the right characteristics as observed in Figure 2.38 the runout is severely overestimated. Potential reasons can lie with the correct selection of friction or the aforementioned system size. Another difference with experimental studies by Lube et al. [2005]; Lajeunesse et al. [2005] is the particle shape - random shapes such as that found in quartz sand can lead to significantly more jamming and less rolling and hence a shorter final runout.

Another study also performed in 2D by Staron and Hinch [2005] made use of the contact dynamics algorithm [Moreau, 1994], with an example of a collapse shown in Figure 2.39 (a). The number of particles was varied $1000 < N < 8000$ with some polydispersity such that the smallest particle was at least 2/3 of the size of the largest one. This allowed column aspect ratios $0.21 < a < 17$ with a mean packing density $\phi = 0.82$. The system size was investigated with $s = r_0/d = 10, 20, 30, 40$ but was found to have little effect. Their simulations found that:

$$\frac{r_f - r_0}{r_0} = \begin{cases} 2.5a & a \leq 2 \\ 3.25a^{0.75} & a > 2 \end{cases} \tag{2.52}$$

$$\frac{h_f}{t_0} = \begin{cases} a & a \leq 1 \\ 0.65a^{0.35} & 1 < a < 10 \\ 1.45 & a \geq 10 \end{cases} \tag{2.53}$$

both in close agreements with experiments by Lube et al. [2005]. The coefficients

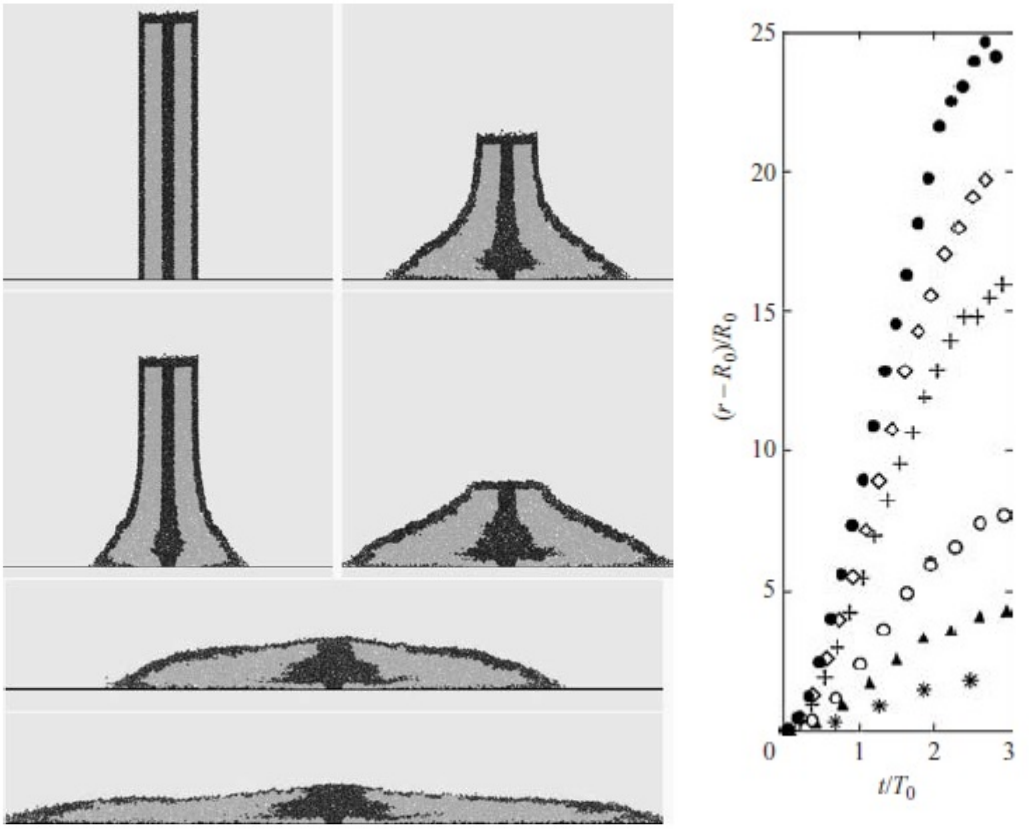

(a) (b)

Figure 2.39: Collapse of a column as modelled by Staron and Hinch [2005] using hard-particle DEM. (a) Example of collapse with $a = 9.1$, $\mu = 1$, $e = 0.9$. (b) Normalised runout scaling.

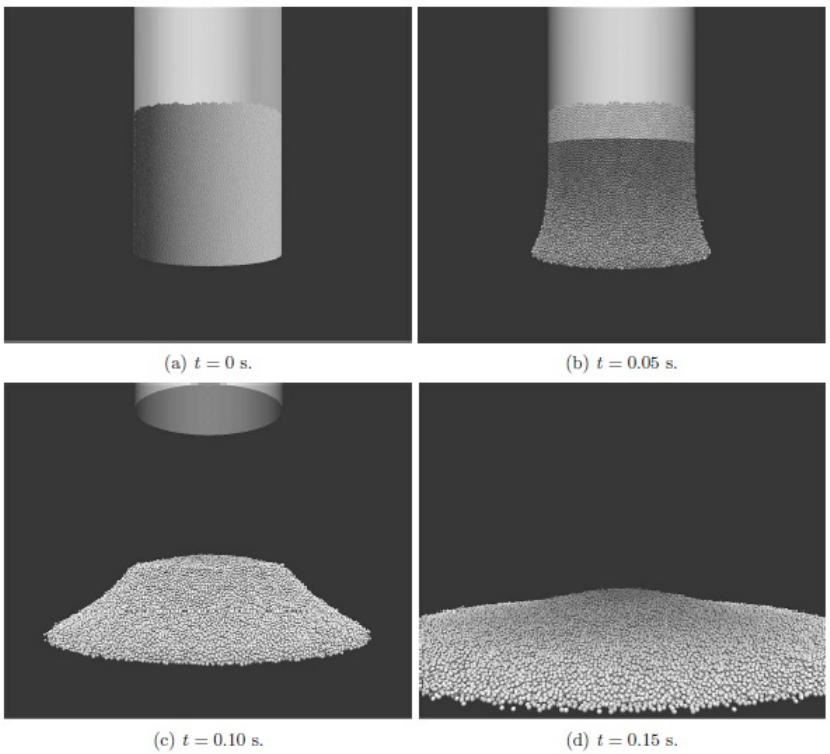

Figure 2.40: DEM simulation of axisymmetric collapse as performed by Cleary and Frank [2006]. The column shown consists of 165,000 particles with $a = 1.91$.

for the runout are significantly higher which is likely due to the choice of friction and the circular shape particles enhancing the movement. The stagnation of the height was not found to occur in experiments, and while no reason was given by the author it is thought that this might be a combination of the circular nature of the particles and small system size. Staron and Hinch [2005] also found the correct square root proportionality of collapse duration with aspect ratio, but as shown in Figure 2.39 (b) the initial acceleration phase was not well captured.

Axisymmetric

The only axisymmetric column collapse DEM simulation recorded is in a preprint by Cleary and Frank [2006] who use a soft-particle model. Here the authors use spherical particles with $1.9 < d < 2.1$ mm and a physical column of radius $r_0 = 57.5\,\text{mm}$ (a system size of $s = 28$) to mimic experiments by Lube et al. [2004]; Lajeunesse et al. [2004]. 165,000 particles are used for a single column height of $h_0 = 110\,\text{mm}$ resulting in $a = 1.91$ with a typical collapse shown in Figure 2.40. The investigation aimed to relate DEM parameters to that physically observed in real systems. It is noted in its generality that using spherical particles results in a large over-estimation of the final runout and under-estimation of the final height. This is

due to the spherical particles causing failure within the pile too easily generating a greater spread, although it could be argued that this might be overcome at larger system sizes. Unlike in the experiments, no centrally undisturbed cone is observed and is attributed to the great amount of failure within the pile due to sphericity.

Under the best case scenario where $\mu = 0.3$, $\mu_s = 0.65$, $\mu_r = 0.025$, $k_n = 1000$, $e = 0.4$ the final scalings were $r_f = 292\,\text{mm}$ $h_f = 243\,\text{mm}$ which is a significant difference from that observed by Lube et al. [2004]; Lajeunesse et al. [2004]. There has been no discussion on system size here which could notably play a large role - particularly when comparing to real experiments. When considering spherical particles it would be right to assume that a larger system size will result in a more stable pile. Its influence has been shown throughout the 2D channel experiments, but its emergence is yet to be shown in the axisymmetric case although it most likely exists. Outcomes from the study show the necessity of rolling friction in soft-sphere models where possible and to not overestimate friction between particles and the cylinder wall.

2.7 Principals of X-ray computed tomography

2.7.1 Introduction

X-ray Computed Tomography (XCT) is the process of generating a 3D volume represenatation of an object for interior inspection by reconstructing a number of 2D images or 'tomographs'. Uni-directional radiographs have been used in medicine as early as 1895, but observation of a singular plane through an object was not made possible until 1975 where advancements in computer processing power allowed for more complex reconstruction techniques of multiple radiographs [Copley et al., 1994]. Its value to industrial processes was quickly recognised as it provided a method to non-destructively investigate components in terms of internal cracks and voids, delamination and porosity. The high cost of a CT system slowed its implementation but saw steady growth in the 1990's to the present day where its use is highly sought after in high value manufacturing applications. Its use in fundamental research is still limited, predominantly due to access to such a system.

The ability to 'see inside' granular systems opens numerous possibilities for further quantification. This could include, but is not limited to: grain centres, orientation, size, sphericity, and packing fraction. There have already been a few studies using XCT investigating packing of granular materials, usually dealing with particle arrangement and structure [Fu et al., 2006; Al-Raoush, 2007; Caulkin et al., 2008] with only a couple considering dynamically evolving materials..

In Chapter 5 this technique is exploited to evaluate the packing within the initial column and resultant pile of axisymmetric collapse. To better understand the

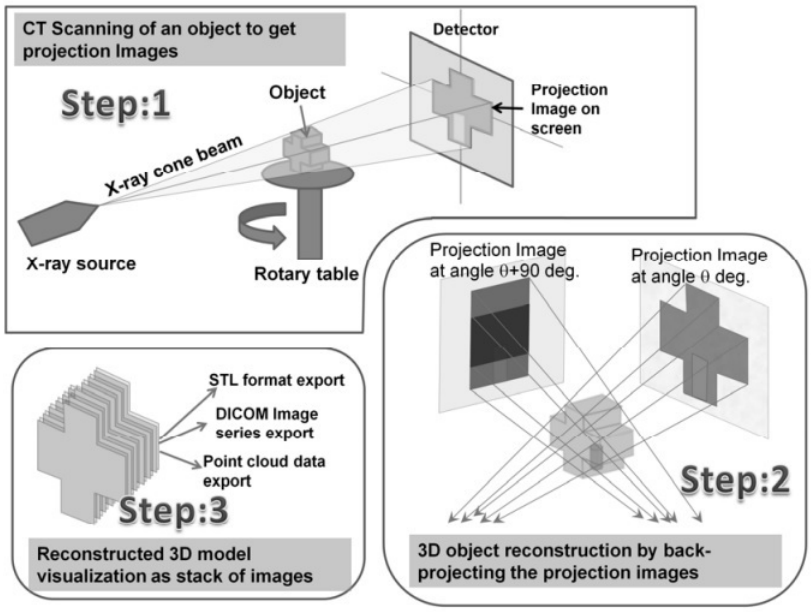

Figure 2.41: Process of 3D volume generation by XCT [Warwick Manufacturing Group 2011].

methodology applied, the technology and its operation is described here.

2.7.2 Scanner operation

X-rays are produced at the source by firing electrons at high speed onto a metal target. When they hit the metal target the sudden deceleration results in the production of heat and X-rays. They are emitted from the source as a cone beam which then may pass through the object before being absorbed by a detector comprised of light sensitive diodes as shown in Figure 2.41. Emitted X-rays belong to a spectrum of energies dependent on source parameters with an example given in Figure 2.42.

X-rays that encouter the object are either attenuated or pass straight through. The number of X-rays received by a diode on the detector in a beam path is represented by a grey scale value on the 2D image of the object. The diodes receiving the greatest number of X-rays display the whitest colour, while the diodes receiving the least due to the greatest attentuation by material within the object are the darkest in colour [Copley et al., 1994; Ketcham and Carlson, 2001]. This is shown in Figure 2.41 step 1 where the plus shaped cuboid has a cylindrical hole. The image produced on the detector has a lighter patch where the cylindrical hole exists.

Images are taken at a variety of angles through 360° by rotation of the object. These images are then subject to a process called filtered back projection [Feldkamp et al., 1984] as shown in Figure 2.41 step 2 to produce a 3D volume. The reconstruction consists of a cube sub-divided into a large number of smaller cubes

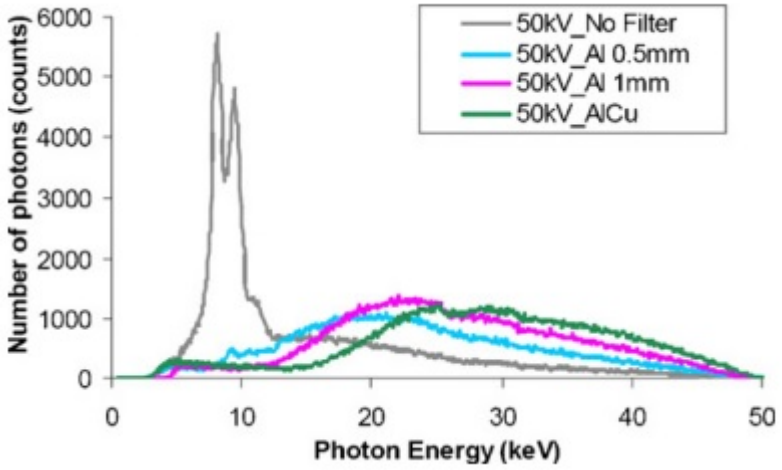

Figure 2.42: Example of beam energy spectra emitted from an X-ray source. Shown also are the spectra for the same beam but with physical filtering applied [Kruth et al., 2011].

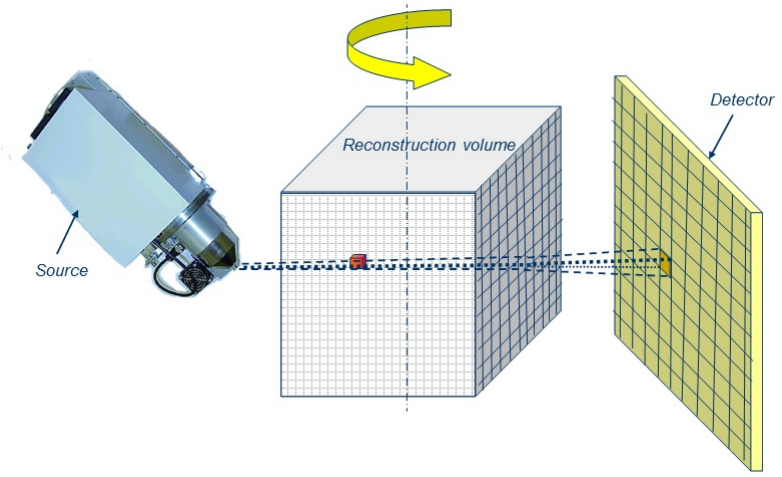

Figure 2.43: A particular voxel is reconstructed from numerous scans at different angles by analysis of the intensity of X-rays detected at the relevant pixel on the detector [Nikon Metrology Seminar 2013, Warwick Manufacturing Group].

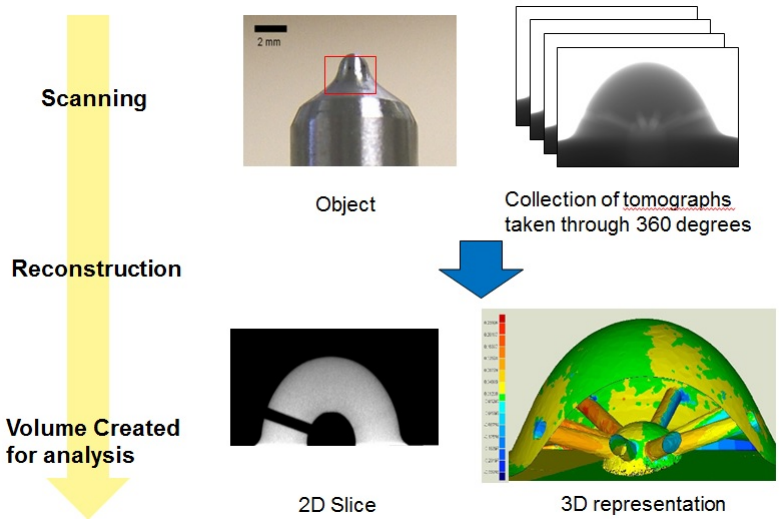

Figure 2.44: From part to 3D volume. In the scanning stage, the relevant volume is selected and scanned to obtain a collection of 2D tomographs. Using filtered back projection these are then reconstructed as a 3D volume. From this 2D slices of the object and a full 3D representation can be obtained [adapted from Nikon Metrology Seminar 2013, Warwick Manufacturing Group].

based on the number of pixels of the detector called voxels as seen in Figure 2.43. Each voxel can be traced to a pixel in every image which has an associated grey value. The average of the contributions in each image then provides a grey value for that particular voxel. With the grey value of each voxel calculated, a full 3D volume is then produced which can be exported for evaluation [Copley et al., 1994; Ketcham and Carlson, 2001]. An example of an object with resultant tomographs and the final reconstruction is shown in Figure 2.44.

2.7.3 Scanning parameters

When setting up a scan of an object several parameters must be set to include voltage, power, exposure and magnification. This is down to operator experience as there are no industrial standards that outline a general work flow to achieve the best results [Ketcham and Carlson, 2001].

Grey scale range

The detector had a grey scale range of 0–65000 where the lowest values are the darkest and the largest are the whitest. The creation of a grey scale value associated with a particular pixel is determined by the intensity of X-rays received by the detector. This can be visualised in a preview before the scan commences and is shown as a histogram displaying the frequency of the different values. Since this is only in one particular view and the histogram will vary for different rotations of the

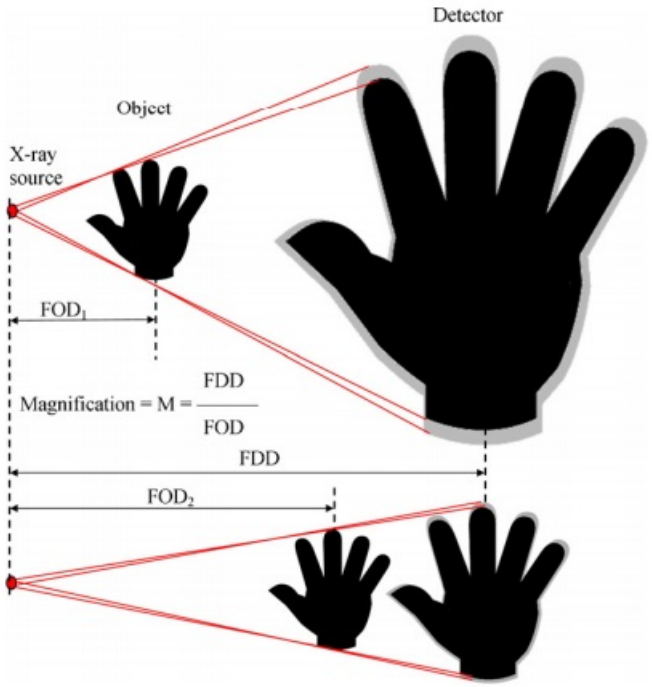

Figure 2.45: Geometric blurring occurs with higher magnification for a fixed spot size [Kruth et al., 2011].

object, it is advised to keep values in the range 10000–60000. To achieve the best contrast between different materials and areas within the image it is desired to use as much of this range as possible.

Magnification

When setting up a scan the first parameter that is selected is the magnification. The table upon which the object rests is moved to a position between the source and detector such that the object reaches the horizontal edge of the detector image. Assuming the object is centralised on the table it will remain entirely in view of the detector at all rotation angles. It is undesirable for part of the object to go out of view in the rotational plane otherwise calculated grey value contributions to different voxels during the reconstruction process will be false.

Magnification is calculated as the the source to detector distance divided by the source to object distance. Dividing a known pixel size at the detector by the magnification gives the size of the voxels in the reconstruction - the resolution of the scan. It is clear that for the best possible resolution the object must occupy as much of the detector width as possible.

The X-ray source is a spot with an associated size as opposed to a point. Basic optics informs that for a fixed spot size higher magnification results in a

greater amount of blurring at the edges as shown in Figure 2.45. The spot size is controllable by the beam power as discussed in the next section.

Voltage and power

In the most general terms an increase in voltage increases the energy of the X-rays and so the lowest emmitted energy is higher. The result is that a lower amount of X-rays are directly absorbed and causes a shift in the histogram in the positive direction. For thicker objects with a higher attenuation coefficient, a higher voltage is required.

Increasing the power increases the number of X-rays passing through the object resulting in an expansion in frequency range observed in the histogram. The power controls the spot size of the X-ray source where an increase in 1 W increases the spot size by 1 μm, with the smallest possible spot size of 3 μm achieved at 3 W in the system used for this investigation. It is therefore desirable to keep the beam power as low as possible to minimise geometric blurring as discussed in the previous section. The geometric unsharpness can be calculated:

$$R = \sqrt{\left(\frac{p}{M+1}\right)^2 + \left(x\frac{M}{M+1}\right)^2} \tag{2.54}$$

where p is pixel size (200 μm for this system), M is magnification and x is spot size.

Exposure

The exposure time at each rotation value can also alter the accuracy of the scan. Typically this varies from 0.25–4.00 seconds and is set prior to the scan. The longer the object is exposed to X-rays, the longer the detector has to notice minute variations in the received intensities. This will then result in a greater resolution of the 2D image and hence less artefacts, but at the cost of an increase in scan time.

An increase in exposure also causes an upward shift in the current grey scale frequency histogram. So an increase in exposure allows for the beam power to be decreased and therefore a lower unsharpness.

Physical filtering

If altering the voltage and power of the emitted X-rays is still not permitting an even spread of values between 10000–60000 then a physical filter can be used. The filter is placed infront of the cone beam source which in effect 'hardens' the beam by removing lower energy X-rays prior to reaching the object as shown in Figure 2.42. This results in a shift downwards of the grey scale frequency histogram of the tomograph, and so an increase in beam power is required to compensate.

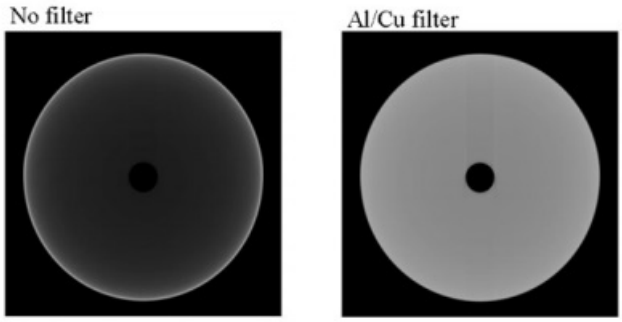

Figure 2.46: A scan of a hollow cylinder with 0.6 mm inner diameter and 6 mm outer diameter with and without filtering. Without filtering the low-energy X-rays are in abundance in the beam and attenutated quickly at the periphery of the object. By using a combination of aluminium and copper filter the beam in hardened generating more high energy X-rays that are less easily attenuated [Kruth et al., 2011].

In the case of non-metallic objects (often of significantly lower attenuation values) only a thin filter is considered as hardening the beam too much may result in the image becoming too white and losing contrast. Metallic objects however have a high attenuation rate so by using a thicker filter pre-emptively absorbs the low energy x-rays and allows for a stronger penetrative beam. In addition metallic objects often cause lower energy X-rays to scatter and blur the image further - see beam hardening in the next section.

2.7.4 Artefacts

X-ray CT images are not perfect and suffer peturbations and imperfections which are generally called artefacts. Some occur due to parameters of the system and scan setup whereas others exist due to improper reconstruction. Being able to handle them in the correct manner is a necessary skill and is something to consider when evaluating the accuracy of measurements. Common artefacts include:

- Internal noise where a single material object is represented by several grey values. This is predominantly due to the reconstruction method, but normally with the differences being small it is easy to compensate for when selecting the correct isosurface.
- External noise is the 'halo-ing' of boundaries of a physical object and is caused by a variety of factors. This could be where the geometric sharpness becomes large due to a beam spot size or if the object moved during the scan. It can also occur during reconstruction where the centre of rotation is poorly determined.
- Scatter where X-rays are deflected by the object and arrive at the detector

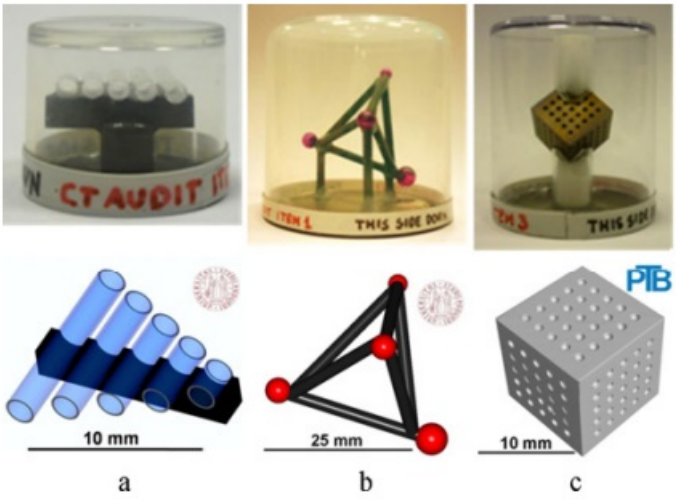

Figure 2.47: Reference geometries with known measurements can be scanned under the same conditions as an object to determine a scaling applied to voxel. Shown are three examples of reference objects: (a) pan flute (known cylinder lengths), (b) sphere tetrahedra (known centre to centre distances), (c) cube with known drill hole sizes [Carmignato, 2012]

producing false readings.

- Beam hardening is an effect where the inside of a solid object appears darker than the periphery as shown in Figure 2.46. This happens due to low energy X-rays being attenuated quicker than high energy ones and is most severely experienced in metallic objects due to their high attenuation rate. This can be overcome by 'hardening' the beam by physical filtering discussed in the previous section. The impact such filtering can have is shown in Figure 2.46. This can also be further overcome at the reconstruction stage by pre filtering tomographs [Copley et al., 1994].

- Cone beam artefacts are where the central region of the tomographs appear marginally lighter than the exterior and are due to the manner in which X-rays are produced at the source. While globally there is a variation in grey values for a material (even if small), locally the difference between material and background are still proportional i.e. this is not a blurring artefact. This can be problematic for direct surface determinations but can be overcome with a variety of filters or local isosurfacing in reconstruction.

2.7.5 Analysis and accuracy

The resultant 3D volume of a scan consists of number of voxels of a given size dependent upon the magnification. Innaccuracies can occur in the voxel size (while often

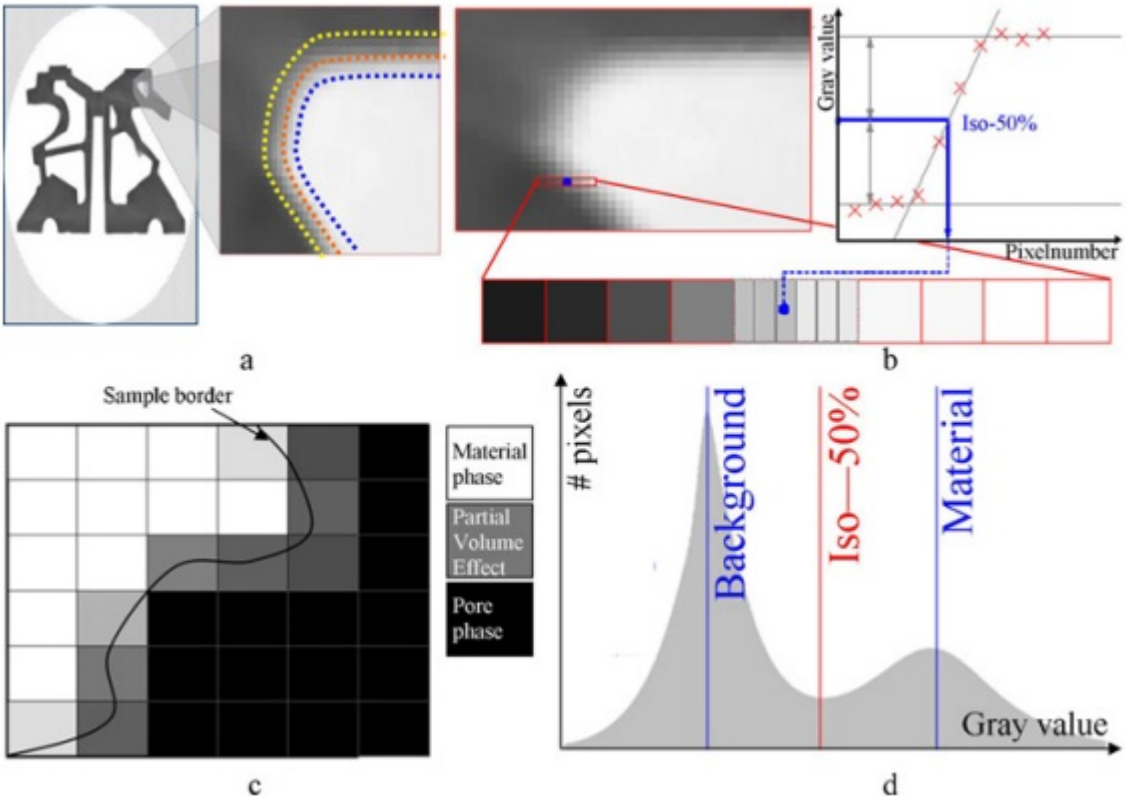

Figure 2.48: Surface determinations are performed by selecting an isosurface where every grey value above the threshold is considered to be material. With appropriate voxel size for the feature to be measured and low geometric unsharpness, the edge effect is minimal - to the order of a few voxels [Kruth et al., 2011].

minute) due to errors in the calculated source to detector/source to object distance which can be as high as 1% in a calibrated machine. In turn this can affect the accuracy of any measurement. To overcome this a reference geometry with known distances can be scanned under the same parameters. The reconstructed geometry is then measured and compared against known measurments, providing a scaling for the voxels. Various examples of trialled reference geometries are shown in Figure 2.47. It has been shown that this method can reduce measurement inaccuracies to $< 0.2\%$ [Lifton et al., 2013] which frequently can be sub-voxel size [Carmignato et al., 2009].

Volume and surface area measurements depends on threshold measurements which are subject to their own errors. From the reconstructed 3D data the user selects which grey values can be considered material, and what can be considered as background. This process known as surface determination is performed by selecting an isosurface in the grey scale range above which all values are considered to be material. With the edges of surfaces always subject to some degree of blurring, if

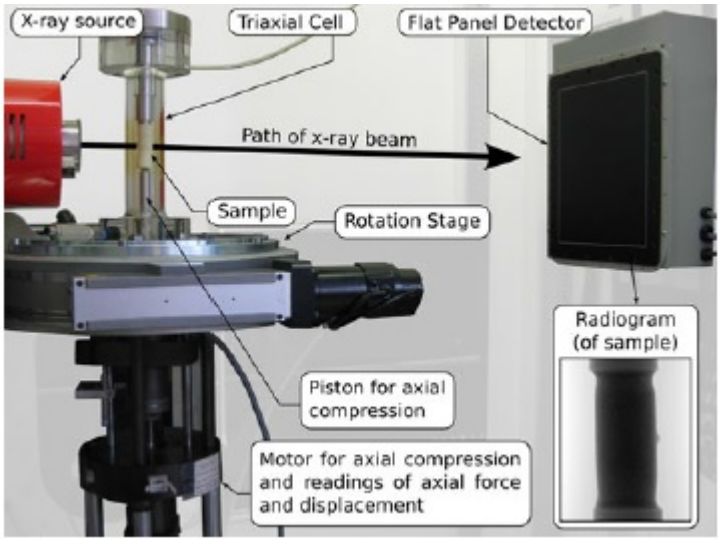

Figure 2.49: Synchotron source setup for XCT of a granular packing undergoing compaction where the triaxial cell is loaded from the bottom [Andò et al., 2012].

only a voxel or two, care must be taken to apply the same process of isosurface selection when comparing between scans so any perceived error is systematic. A study comparing volumes of pores in foams based on reasonable isosurface selection shows that in a worst case scenario the actual volume can vary by up to 5% dependent on this parameter choice [Kumar et al., 2011]. This error can be significantly reduced if the rare situation arises where the volume of the object is already known.

2.7.6 Application to granular materials

The first study of granular materials using XCT by [Richard et al., 2003] and several subsequent studies [Forsberg and Siviour, 2009; Andò et al., 2012] have related to granular materials undergoing compaction. In studies by Richard et al. [2003]; Andò et al. [2012] they use synchotron based XCT which is similar in setup to the lab source discussed throughout this section with the exception that the X-ray source is monochromatic (produces X-rays of a single energy as opposed to a spectrum) and the detector is of higher quality allowing a spatial resolution of 1μm. The more coherent source also enables a shorter exposure and hence a quicker scan time. The experimental setup for Andò et al. [2012] can be seen in Figure 2.49 where the triaxial cell contains granular material where the loading is applied by a ceramic cap at the bottom. The first study by Richard et al. [2003] differs where the compaction is applied by vertical vibrations. To observe the internal dynamic deformation the load was applied at interval timesteps, either a vibration cycle or an upwards force. After the loading has been applied the scan is completed before the next incremental load is applied.

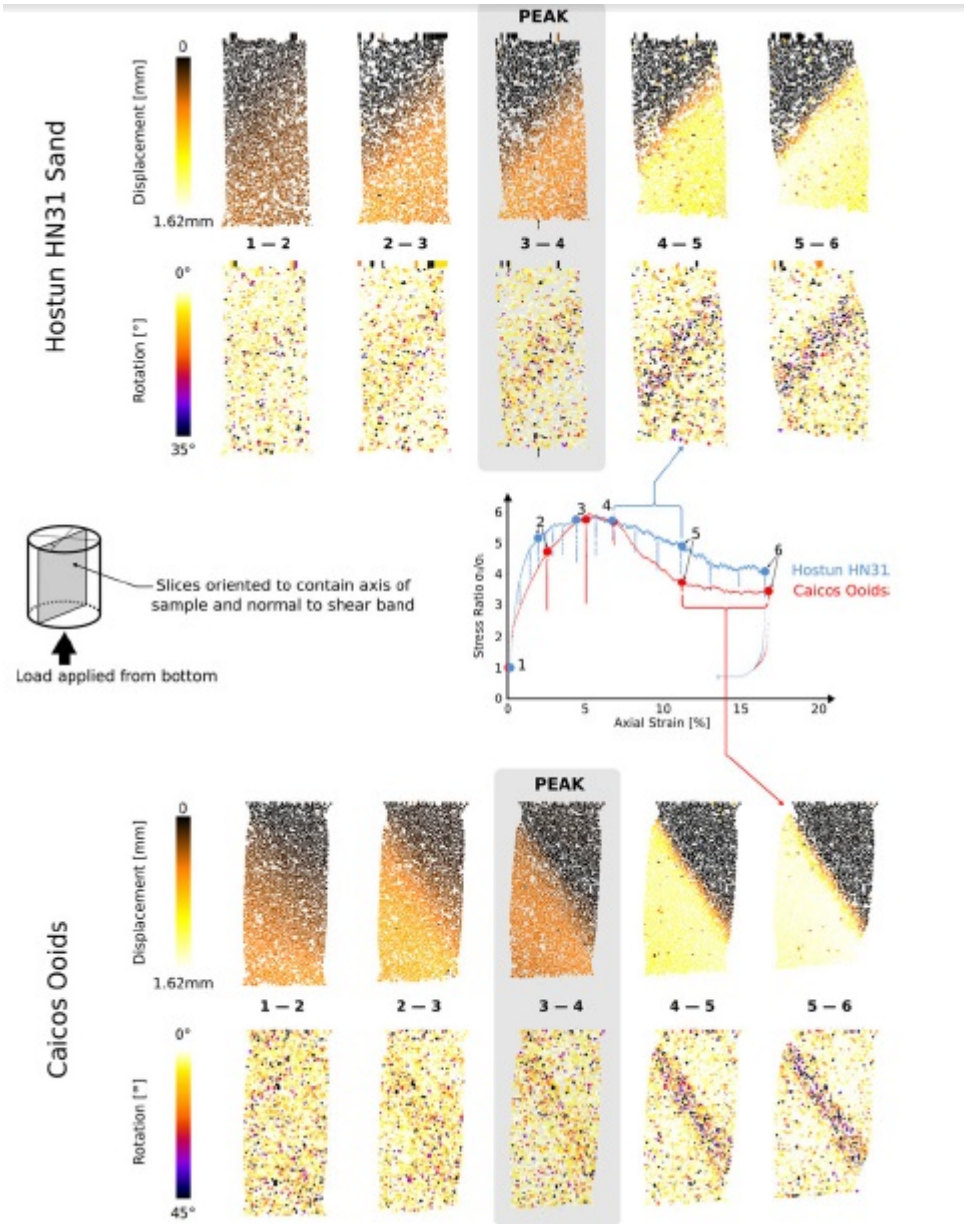

Figure 2.50: Results of displacement, rotation and stress ratio on particles from experiments by Andò et al. [2012]. Note that particles are coloured by absolute magnitude as opposed to a vector quantity.

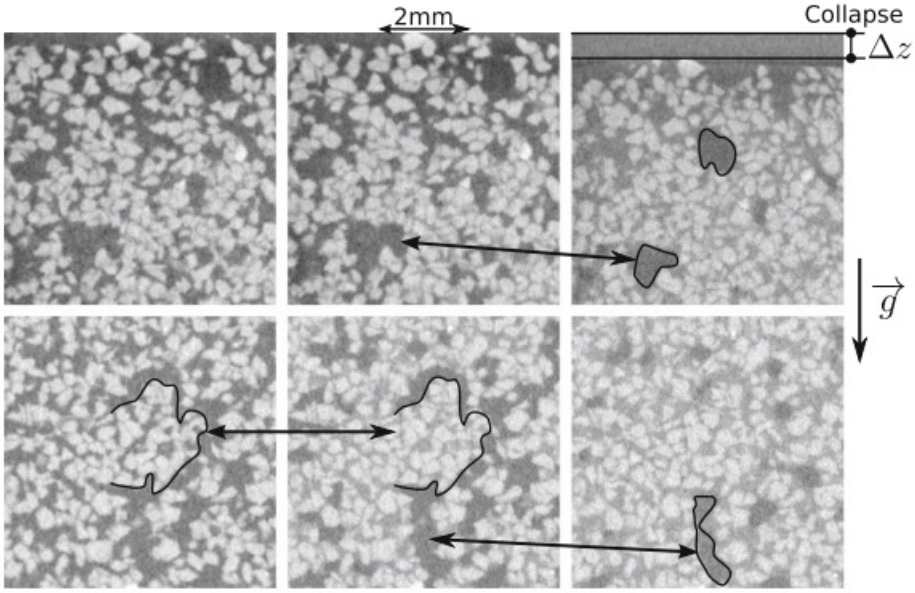

Figure 2.51: Propogating pores and deformation within a granular cell undergoing water imbibition as in experiments by Bruchon et al. [2013]. From left to right there is an increasing amount of saturation of the particulate, shown to cause deformation as highlighted by specific regions.

In each of these studies different information is extracted from the compaction; Richard et al. [2003] concentrates on the pairwise distribution function (density variation as a function of distance from a reference particle) and the volume of pores while Forsberg and Siviour [2009]; Andò et al. [2012] focus on displacement and strain through different image processing techniques (selected results from Andò et al. [2012] in Figure 2.50.

Another recent study by Bruchon et al. [2013] used XCT to investigate capillary collapse in granular media - this is the process where sudden deformation and collapse occurs within the medium due to wetting, often by water imbibition. Again staggered scanning was employed where after an initial scan was completed a fixed amount of water was allowed to infiltrate the granular cell before scanning for a second time, performed for a range of saturations. XCT has allowed the authors to observe the propagation of pores as shown in Figure 2.51 and the evolution of strain.

These studies demonstrate the potential of applying XCT in the field of granular flows, and is employed for the first time to further characterise the stationary axisymmetric column collapse in the Chapter 5.

Chapter 3

Equipment preparation

3.1 Introduction

To perform the experiments, a table to contain the collapse was required. For the rotational experiments this would need mounting to a rotating turntable already in existence within the department. The collapse itself was also recorded on a high speed camera, initiating a secondary requirement to manufacture an adjustable camera mount. To hold a cylinder in place containing the granular material that would then be removed vertically required a housing around the equipment so removal would not interfere with the rotating table.

The designed solution is outlined below with technical drawings found in Appendix A. Further items concerning system centering and the particulate are discussed here.

3.2 Apparatus manufacture

3.2.1 Perspex table and camera mount

A Perspex circle of diameter 900 mm and thickness 15 mm formed the base of the table with four circular holes of diameter 15 mm equally spaced around the periphery to allow mounting to the turntable. In the case of rotational collapse some material could be ejected from the pile and so a boundary was required to contain the ejection while not interfering with the collapse. An octagonal shape was selected as opposed to cylindrical due to costing reasons. The octagon was formed from 8 seperate pieces of Perspex, 10 mm in thickness, with the outside edge measuring 300 mm in width and 150 mm in height. To fit the pieces together each side was beveled by 22.5°. The pieces were aligned such that the centre of the octagon was coincident with the centre of the table. The pieces were fixed to each other and to the table using epoxy resin. The resultant octagon had a distance of 704.3 mm (to 1 d.p.) between the

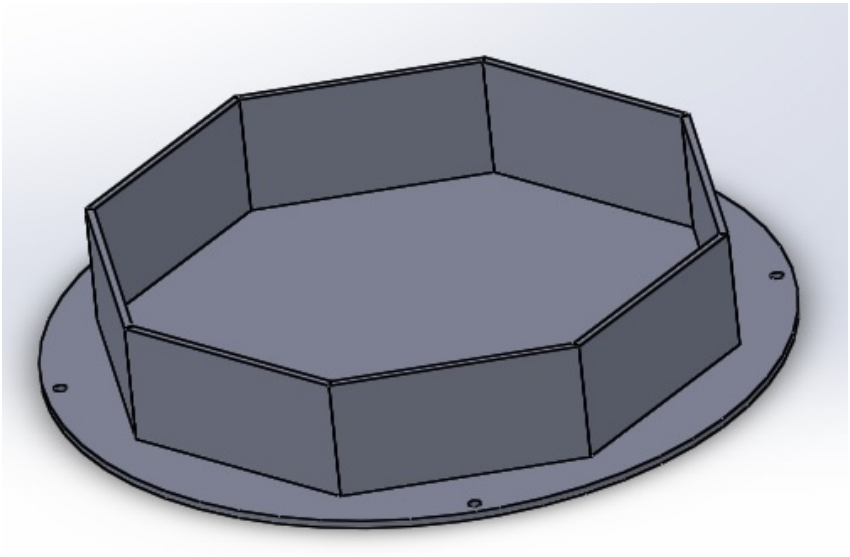

(a)

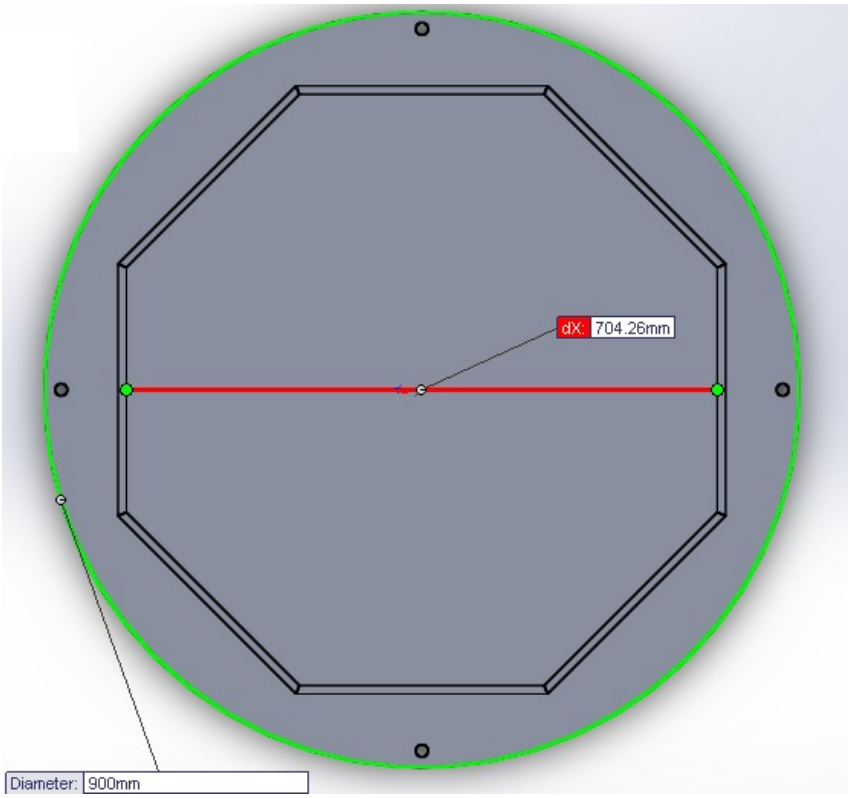

(b)

Figure 3.1: Circular Perspex table with octagonal boundary. (a) 3D view. (b) Top view.

(a)

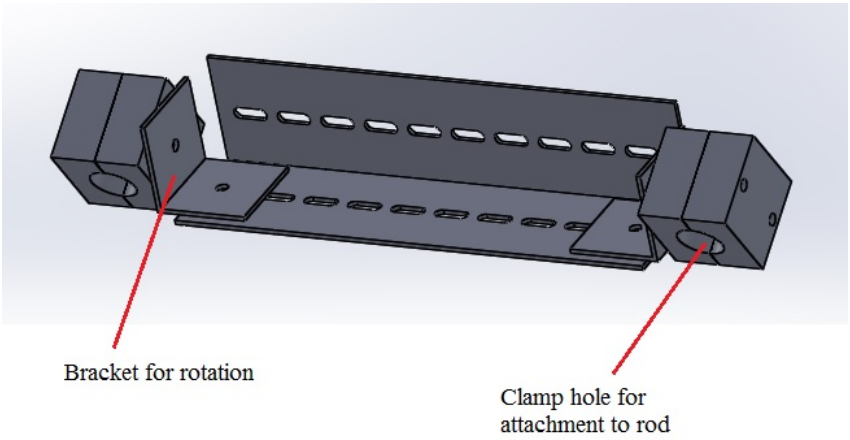

(b)

Figure 3.2: Camera support. (a) Series of rods to mount the camera bracket. (b) Camera bracket allowing rotation.

inside edges of two parallel sides as seen in Figure 3.1.

Where video capture was required the camera had to be placed close to collapse and within the rotating frame of reference. To achieve this an adjustable camera support was required. This was formed by a series of 8 rods of length 600 mm fixed to the table and held together at the top by a secondary annular piece of Perspex with an inner and outer radius of 720 mm and 800 mm respectively as shown in Figure 3.2 a). To hold the camera, a bracket was manufactured that could be fitted to two adjacent rods as shown in Figure 3.2 b). The bracket was able to be fixed vertically determined by its position along the rods with the bracket allowing rotation to move the view of the camera.

3.2.2 Housing and pulley system

To remove the cylinder vertically a pulley system was required that was separate from the table so it wouldn't interfere with the rotation. This was achieved with a square wooden base of side 1100 mm upon which the turntable sat, with bosch aluminum profile creating a cuboid shaped housing. The columns of the profile were 1400 mm in height and arranged to fit to the corners of the wooden base. A plinth was then placed across the top with a pulley in its centre to run the string down to the cylinder placed on the table. In this manner the string could be pulled sharply over the pulley to remove the cylinder.

3.2.3 Full assembly

The assembly of the above parts is shown in Figure 3.3 and further detailed in Appendix A. This was used as the experimental setup throughout the stationary and rotational experiments. In the case of CT scanning a 10:3 scaled version of the housing and pulley system was created with aluminum profile and the collapse was allowed to occur on a Perspex disk for transfer into the scanner.

3.2.4 System centing

First the table needed to be centrally aligned on the turntable. The centre of the table was coincident with the centre of the turntable before securing in place. The accuracy was then checked by using a fixed newton meter with the measuring point touching the edge table. Rotating the table slowly showed variations in force on the newton meter if the table was not aligned centrally as the edge of the table would trace an eccentric path. Where this occurred, a light tap to the edge of the table moved its position which was then checked with the newton meter again. This was repeated until the newton meter showed minimal amounts of variation. The

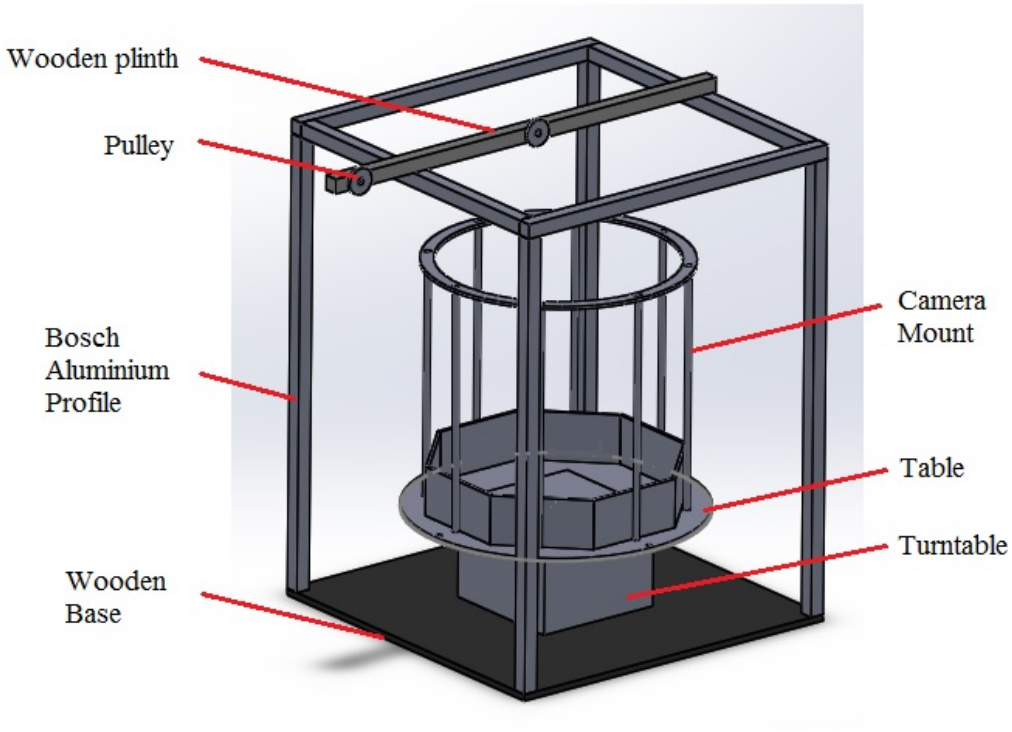

(a)

(b)

Figure 3.3: Full assembly of equipment used in experiments throughout this thesis. (a) CAD model. (b) Final construction.

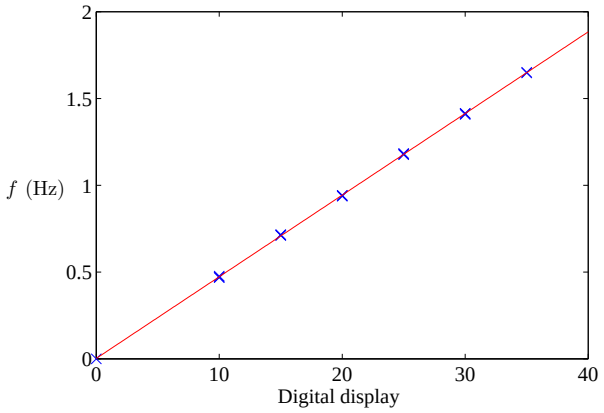

Figure 3.4: Calibration curve for frequency of rotation, f, against clock display. Follows a linear relation indicated by the red line as given in equation 3.1.

alignment method was thought to ensure concentricity to ±1mm and checked every 20 rotation experiments.

It was essential that the cylinder was raised as vertically as possible, and in the case of the rotational experiments it must also be placed centrally. The cylinder was attached to the string using a ring and cable ties passed through three equally spaced holes around the top of the cylinder. This ensured that the cylinder was level when being placed and small adjustments could be made by tightening the cable tie. The position of the plinth was altered so that a plumb line hung from the pulley matched the centre of the table. This ensured that when the cylinder was attached it would be aligned as centrally as possible with an accuracy of ±1 mm. Next the cylinder was lowered to just above the table and all swinging motion was stabilised. With all cylinder motion ceased it was then rested on the table. Column preparation for the experiment could then be performed.

3.2.5 Rotation rate calibration

The turntable was attached to a module where the rotation rate could be set by a dial and shown on a digital display. The scale of the display was arbitrary and so calibration was necessary. This was done by setting a clock display value and recording the rotation on a standard 30fps digital camcorder. The time taken for three complete rotations was determined using video editing software with an accuracy of ±0.033 s and averaged to find the time for one rotation with a mean absolute error of ±0.011 s. Hence, for the highest rotation rate of 1.65 Hz the error was ±0.03 Hz (1.8%), and for the lowest rotation rate the error was ±0.003 Hz (0.5%). This was performed three times for 6 different rotation rates, and the frequency calculated. From this a calibration curve was calculated, found to be linear, as in Figure 3.4 which shows negligible error in the measurement. For a given clock display value

Chapter	Experiment series	r_0 (mm)	a	s	# expts
4	Stationary collapse	20, 25, 30, 35, 40, 45, 75	0.20–8.69	28–107	240
5	CT stationary collapse	25	0.74–2.04	35	6
6	Rotating collapse	20, 25, 30, 36	0.20–1.75	28–50	657
7	DEM (simulations)	10, 30	2.80, 0.31	10, 30	5

Table 3.1: Experiments performed throughout this thesis with cylinder sizes used of radius r_0, range of aspect ratios trialled a, system size s and the number of experiments. Note that Chapter 7 relates to simulations that use computer generated cylinders.

the frequency of rotation can be calculated by

$$f_{actual} = 0.047 f_{display} \tag{3.1}$$

3.3 Cylinders

Throughout the presented experiments several different cylinder sizes were used. The available cylinders and in which experiments they were used are detailed in Table 3.1.

3.4 Granular particulate

In the presented experiments the granular medium used was a limestone particulate *'LG800'* supplied by *'Omya'* (Derbyshire, UK) with a bulk density of $\rho \approx 1.6\,\mathrm{g/cm^3}$. The angle of repose is the maximal angle to the horizontal sustained by a pile of granular material before the slope face begins to slide and was given by the manufacturer as $\theta_r \approx 30°$. The angle of internal friction is the angle between the direct stress and resultant stress where shear failure occurs and was given by the manufacturer as $\theta_\mu \approx 39°$. The angle of internal friction is assumed to be under a dense packing, and the angle of repose is essentially a limiting case of the angle of internal friction for an extremely loose packing. The shear strength of particles determine both these angles, which varies with the degree of non-sphericity of the particles (ability to interlock, though difficult to quantify) and the water content (due to cohesiveness). It is for these reasons that the values are approximate, but the particulate was dried in an oven at 130°C for 6 hours to remove any additional moisture in attempts to reduce variation between experiments.

The delivered particulate contained a range of particle diameters d as shown in Figure 3.5. Throughout experiments it was required to keep the particle diameter

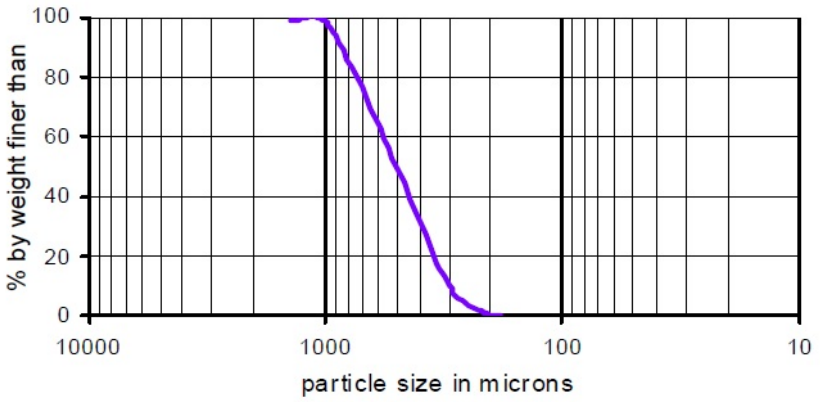

Figure 3.5: Particle size distribution of particulate *'LG800'* supplied by *'Omya'* [private communication (2010), Alan Simpson, Omya].

range small. To obtain the most amount of material from that supplied while having a small d, a particle diameter range of $600\,\mu\text{m} < d < 800\,\mu\text{m}$ was selected. This was obtained using a sieve shaker.

The sieve and shaker system used was the *'Endecotts Octagon D200'* as pictured in Figure 3.6. A $800\,\mu$m sieve was stacked on a $600\,\mu$m sieve and placed on a collector on the shaker system. Material was poured into the top sieve and the shaker started. This was allowed to run for a number hours after which the material left within the $600\,\mu$m sieve was transferred to a container for use in the experiments. The method was performed a number of times to sieve all the material.

The granular matter was reused throughout the experiments but entirely replaced every 40 runs before degradation could occur. This ensured the particle diameter range was maintained.

3.5 Experimental summary

In this thesis three experimental studies are discussed using the equipment and preparation detailed in this chapter. Each study uses the same particulate discussed in Section 3.4. Table 3.1 details the different cylinder sizes used, range of aspect ratios, system sizes and number of experiments performed. For completeness the DEM study found in Chapter 7 is also included in the table.

Chapter 4 investigates axisymmetric stationary column collapse in a similar vein to previous authors [Lube et al., 2004; Lajeunesse et al., 2004] as discussed in Section 2.1. Unique to this set of experiments is a new measurement approach using a laser scanner arm that has revealed a system size dependence on the scaling laws. Chapter 5 further explores axisymmetric stationary column collapse using X-ray CT, a methodology described in Section 2.6. This enables internal viewing of

Figure 3.6: Product photo of *'Endecotts Octagon D200'* sieve shaker system used to select particle size [http://www.endecotts.com/products/sieve-shakers/octagon-d200-digital.aspx, accessed June 2013].

the granular column and resultant pile and calculation of the distribution of packing fraction. This evaluation aids in identifying regions of compaction and dilation of the particulate, with non-destructive assessment of an internal static region proposed by previous authors [Lube et al., 2004; Lajeunesse et al., 2004]. Chapter 6 extends the stationary column collapse to a rotating case, where the initial column is placed on a rotating table. Here the scalings from Chapter 4 are reconstructed to include the centrifugal effect. Chapter 7 discusses a preliminary study using DEM to simulate the rotational collapse with spherical particles. The sphericity and ability to roll has led to the development of spiral patterns that have been previously unobserved experimentally. Steps towards verification have been made, but requires further attention.

Chapter 4

Stationary granular column collapse with laser scanning

4.1 Introduction

Several previous authors [Lube et al., 2004; Lajeunesse et al., 2004; Thompson and Huppert, 2007] have investigated the collapse of an axisymmetric column and have concluded several simple scaling laws based on the initial aspect ratio of the granular column. Lube et al. [2004] used a vernier scale and laser pointer technique with a stated accuracy of ± 0.1mm to measure the final column, where as Lajeunesse et al. [2004] used a camera imaging technique with a spatial resolution of 0.4mm. When investigating the rotational case outlined in Chapter 6 the scalings arising from different column sizes in the stationary case (no rotation) indicated that there might be some subtle differences across cylinder sizes, and hence the system size, which were not due to experimental error. To evaluate this hypothesis, a more accurate experimental technique was required than in previous studies. In the work presented a 3D laser scanner is employed for data acquisition with a substantially higher accuracy of ± 0.04mm. This methodology has the added benefit of digitizing the result for analysis and further interrogation. Experiments performed using this technique with similar initial system sizes to those of previous authors have revealed a variation of previously proposed scalings with a dependence on this initial system size. The experimental method has also allowed investigation into the angular profile of the deposit and the rate at which the summit is consumed with an increase in aspect ratio.

Data obtained from the experiments can be found in Appendix B. The key results of this section have been published as Warnett et al. [2014a]. A copy of the paper has been attached in Appendix F.

r_0 (mm)	s	a range
20	28	0.24–8.69
25	35	0.30–7.00
30	42	0.20–6.05
35	50	0.24–5.29
40	57	0.25–4.40
45	64	0.24–4.02
75	107	0.28–1.69

Table 4.1: Range of aspect ratios a trialled for each cylinder of radius r_0 and associated system size $s = r_0/d$.

4.2 Experimental setup

4.2.1 Apparatus

The apparatus was set up as in Figure 4.1. This consisted of the smooth perspex table housed in a Bosch Rexroth aluminium profile frame as described in Chapter 3. The purpose of the housing is to support a pulley system used to withdraw the cylinder vertically. The selected cylinder of radius r_0 was lowered to the table and allowed to axially stabalise before admitting to the surface. This ensured that the column rested in a position where it could be raised near perfectly vertically and not at an angle that would perturb the collapse of the granular mass. The cylinder needed to lie only approximately central on the table as all quantifications were made on the resultant scan.

4.2.2 Experimental method

A cylinder of radius r_0 was partially filled with granular material of mass m_0 to a specified height h_0. The aspect ratio, $a = h_0/r_0$, was varied for a single cylinder of radius r_0 by varying the mass of the particulate, m_0. A number of cylinder radii were used with a range of aspect ratios as outlined in Table 4.1. The selected cylinder size together with the particulate results in a non-dimensional system size parameter defined as $s = r_0/d$. The experiments were performed in a randomised order as outlined in Appendix B to prevent systematic errors from affecting the final results.

The granular material used and its preparation is described in Section 3.4. This was a limestone particulate with bulk density $\rho \approx 1.6\,\mathrm{g/cm^3}$, angle of repose $\theta_r \approx 30^\circ$ and angle of internal friction $\theta_\mu \approx 39^\circ$. Recall that the angle of internal friction is the angle between direct and resultant stress where shear failure occurs, defining a failure envelope. The angle of repose is the maximal angle to the horizontal sustained by a pile of granular material before the slope face begins to slide.

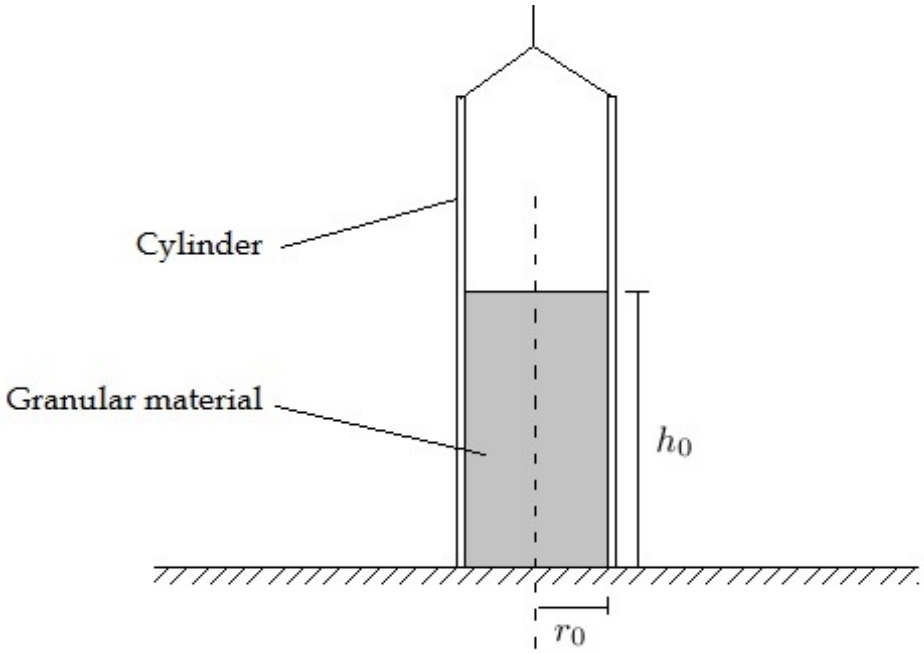

(a)

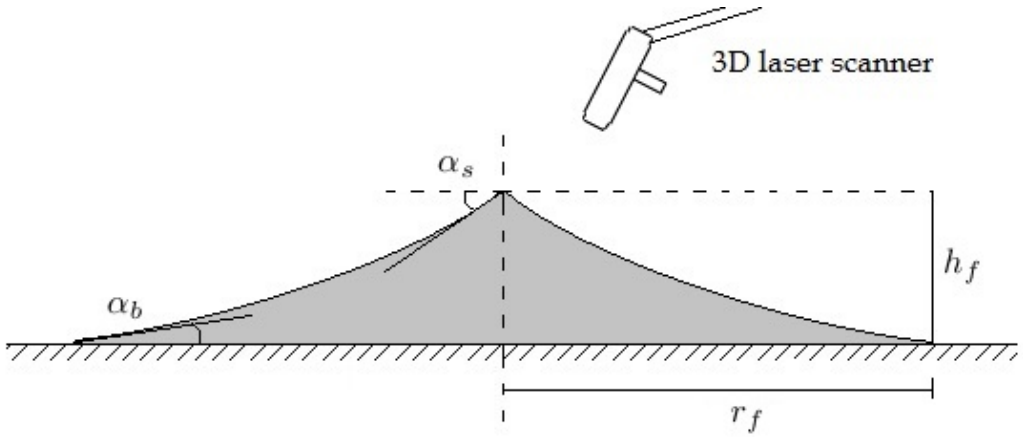

(b)

Figure 4.1: Experimental setup. (a) Initial setup of granular column on rotating table. (b) Column after collapse.

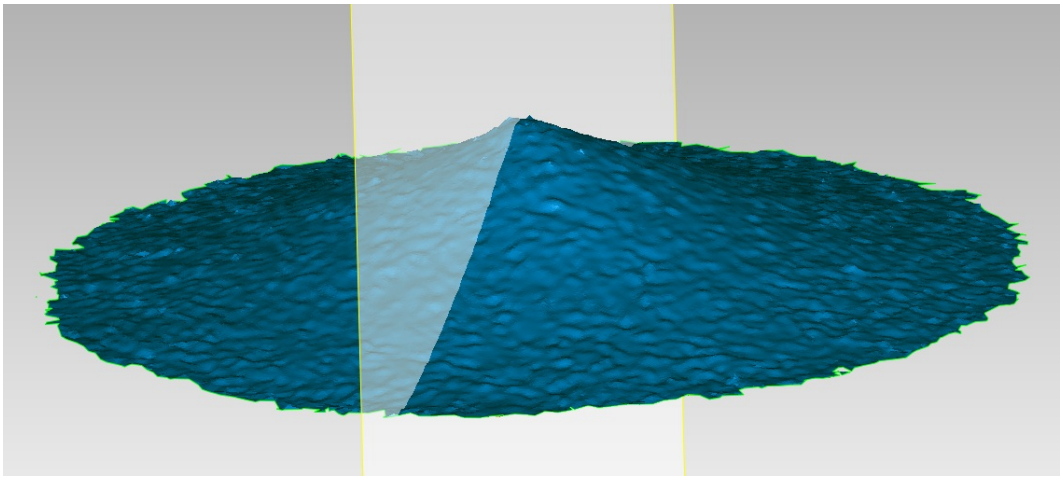

(a)

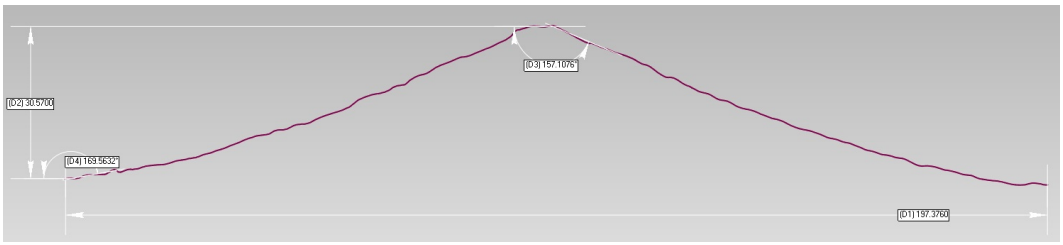

(b)

Figure 4.2: Mesh generation from scan of a collapsed column with $r_0 = 35\,\text{mm}$, $a = 1.64$. (a) Mesh view with plane of example cross section. (b) 2D cross section with example measurement.

Grains of diameter $d = 0.6 - -0.8\,\text{mm}$ were selected which were funnelled into the cylinder and the top gently flattened using a circular piece of card attached to a flexible rod. The mean packing density of the material in the cylinder was calculated to be $0.78 < \phi < 0.82$ as shown in Appendix B.

The cylinder was connected to rope over a series of pulleys that was mounted to the aluminum profile housing. The cylinder was removed quickly by pulling on the rope at a speed greater than the speed of collapse to ensure minimal interference with the collapse itself. An average speed of $1.8\,\text{ms}^{-1}$ was found to be sufficient as discussed by Lajeunesse et al. [2004] and presented in Section 2.2.1. After release, the material spreads across the table resulting in a final deposit.

A 3D laser scanner was then used to calculate the initial height and digitize the resulting deposit as shown in Figure 4.2 enabling precise measurement of the pile by use of the analysis software '*Geomagic Qualify*' (3D Digital 2002; Geomagic, Research Triangle Park, NC, USA). This enabled non-contact measurement with high accuracy and a greater possibility of interrogation in comparison to previous studies.

Figure 4.3: Nikon Metrology MCA 2400 M7 articulated arm used for laser scanning [http://www.nikonmetrology.com, accessed December 2012].

4.2.3 Scanning particulars

The 3D laser scanner used in this study was the '*Nikon Metrology MCA 2400 M7*' articulated arm as pictured in Figure 4.3. This equipment enabled complete detailed geometric scans of the sand piles which can then be stored as a digital library of the experiments performed.

The scanner head produced a laser stripe of thickness 0.543 mm that was programmed to traverse the deposit capturing surface data points collectively known as a point cloud. The measurement optics are based on the Foucault triangulation principle shown in Figure 4.4. The laser beam apeture is controlled by the Focault knife edge which is then focused into a thin strip by a lens for projection onto the desired surface. The reflected beam is split into two directions on its return: one way to an imaging sensor and the other to a differential diode. The imaging sensor calculates the position of the point with a correction applied based on the signal received by the differential diode [Hocken and Pereira, 2012].

The currently achieved point cloud was viewable in real time providing immediate feedback on the scanning pace, progress and scanned area. The scanner was able to scan areas up to 470 mm x 470 mm which was a limitation in terms of allowable aspect ratio ranges shown in Table 4.1. A typical scan path consisted of 1000 measurement points per stripe. To maintain a consistent number of measurement points per scan path and reduce the level of data noise it is critical to sustain the optimum distance between the scanning head and deposit. The scanner produced

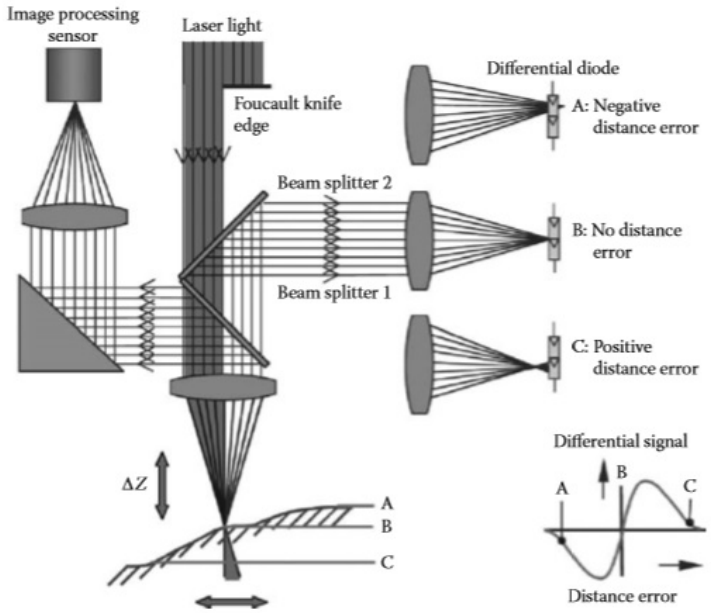

Figure 4.4: Foucault triangulation principle used by laser scanning arm for surface detection [Hocken and Pereira, 2012].

a laser guide with the stripe enabling the laser user to maintain this distance and obtain quality data. With this level of precision, the obtained point cloud contained 8–10 points per mm^2.

The laser intensity also has an impact on the quality of data achieved, and this is managed by the equipment itself to include adjustments according to lighting conditions. Once the system is fully calibrated the lighting levels were maintained and temperature controlled at $\pm 5°C$ relative to the temperature when calibrated. Single point and length accuracy of the scanner is 31 μm and 42 μm $\pm 2\sigma$ respectively. These values were determined by point repeatability and volumetric accuracy tests as outlined in the industrial standard ASME B89.4.22 [ASME, 2004; Kiraci et al., 2012].

When using the equipment to scan objects with defined edges, numerous scans can be easily amalgamated to produce the final object. The software was found to struggle performing this task with granular heaps due to the largely uneven surface and so all scans were completed in a single traversal of the articulated arm.

4.2.4 Post processing

The point cloud generated was interpreted as a surface mesh as in Figure 4.2 (a) using '*Geomagic Qualify*'; industrial standard software used for the inspection of scanned objects and materials. On occasion particles can be ejected out of the resultant pile. These were easily identifiable and removed from the final mesh for

a range	error in grain units d	absolute error (mm)
$a < 0.50$	3	± 1.1
$0.50 < a < 1.3$	4	± 1.4
$1.3 < a < 2$	5	± 1.8
$a > 2$	6	± 2.2

Table 4.2: Measurement error of r_f due to uneven periphery.

evaluation.

The global coordinate system of the mesh was altered so the table that the deposit rested on aligned with the $x-y$ plane. Four equally spaced 2D cross sections were taken of the resultant mesh through the centre of the pile. An example of such a cross section with measurements is given in Figure 4.2 (b). The ability to take several 2D cross sections of the final deposit allowed evaluation of the initial setup and cylinder removal. The cross sections made it easy to find where the cylinder had not been raised vertically as the resultant pile would be asymmetric, so adjustments could be made to the equipment in trials before the main experiments were run.

The achieved cross sections were then used to retrieve several measurements of the final deposit indicated in Figure 4.1; the final pile radius, r_f, the final pile height, h_f, the summital angle, α_s, the angle at the base, α_b, and in the case of a truncated cone, r_s, the summit radius. In the case of all these measurements with the exception of the final pile height, an average was taken across all four 2D cross sections where there is known to be variability due to an uneven periphery.

4.2.5 Repeatability and accuracy

Repeatability testing was performed on several initial aspect ratios and cylinder sizes to determine the maximal variation in quantities with results given in Appendix C. Three initial heights were randomly selected for each cylinder size and the collapse was performed three times with the resultant deposit scanned. From the mesh two reference circles were generated in the plane of collapse; one from three of the inner most points of the periphery and another from three of the outer most points, both with respect to the central peak. This gave a maximal and minimal radius of the resultant collapse and the difference could be measured as shown in Figure 4.5. The uneven periphery is a large source of error in the experiments, hence quantification is required for this high accuracy method. Differences in the maximal and minimal radius of a single deposit are shown in Figure 4.6 normalised against the grain size. The variation in the periphery of a single run is summarised in Table 4.2.

Averaging over four 2D cross-sections throughout experiments finds the mean periphery profile of the deposit and is likely subject to a slightly smaller error than that indicated above. Results from the repeatability testing and account-

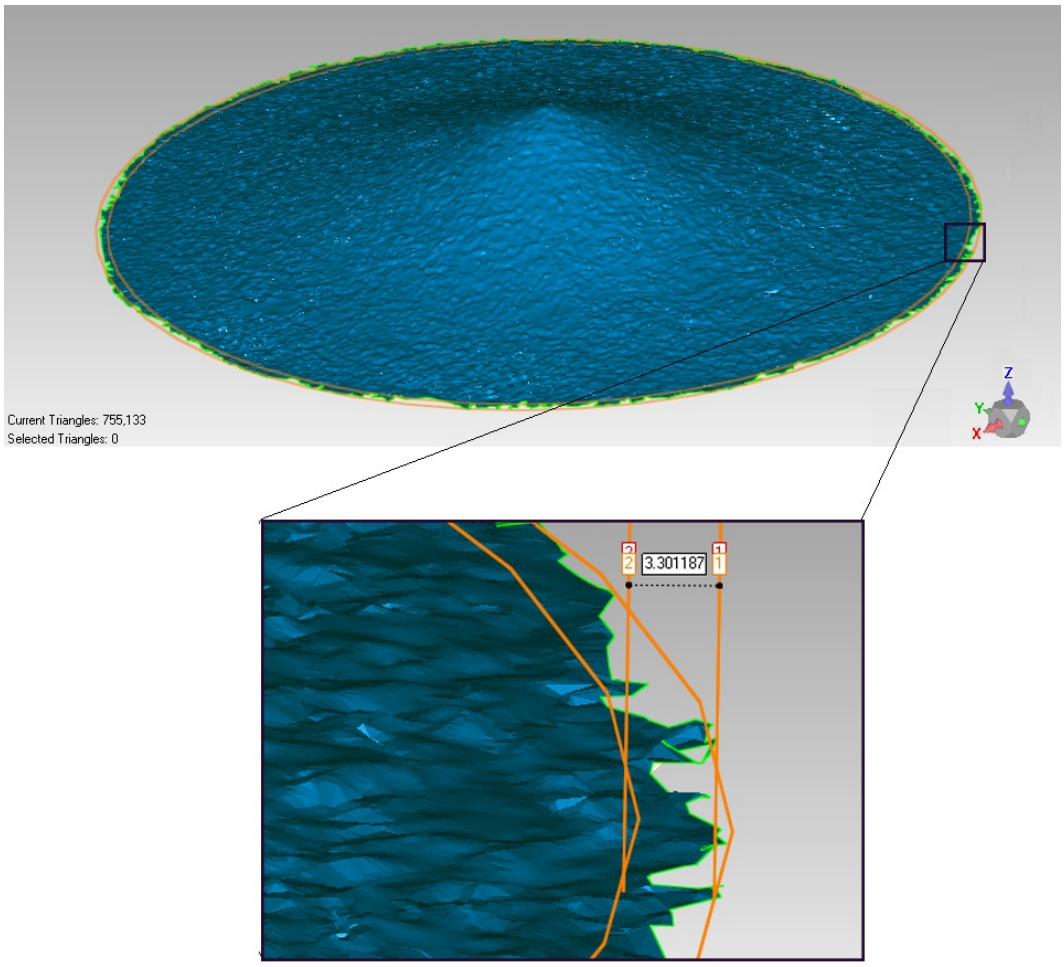

Figure 4.5: Example surface mesh for $r_0 = 45\,\text{mm}$ $a = 1.87$ produced from point cloud achieved with laser scanning of the resultant deposit. Boundary effect demonstrated by two orange periphery lines formed from the inner most and outer most points. The distance between these boundaries is 3.30 mm, approximately $4.7d$.

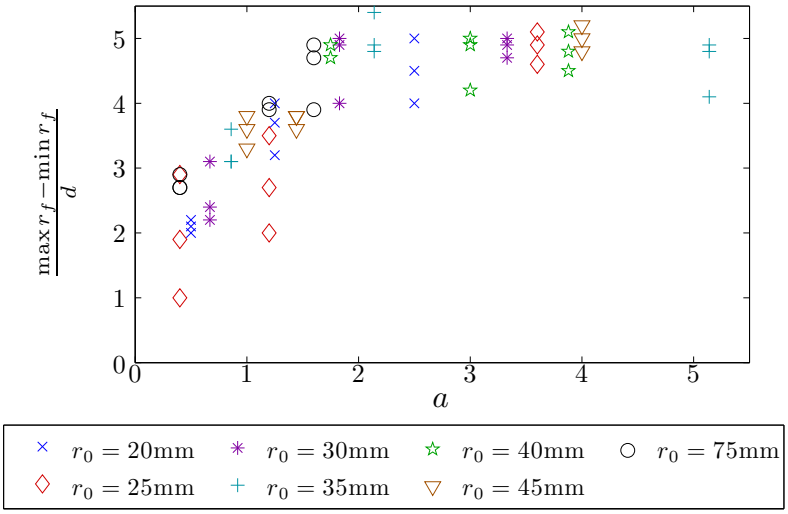

Figure 4.6: Difference between the maximal and minimal runout radius for a single trial normalised against grain size d.

ing for the error due to the uneven rim of the deposit indicated an accuracy of $r_f = \pm 1.6 - 2.2\,\text{mm}$ (aspect ratio dependent), $r_s = \pm 2.0\,\text{mm}$, $h_f = \pm 0.5\,\text{mm}$, and angular quantities $\pm 1°$. The material was measured to within $\pm 0.1\,\text{g}$, allowing only a variability in packing.

4.3 Flow description and morphology

Qualitative descriptions of the collapse have been previously studied by other authors [Lube et al., 2004; Lajeunesse et al., 2004] as discussed in Section 2.1.2, and illustrated in Figure 4.8. For $a \lesssim 3$ the periphery of the column crumbles vertically downwards resulting in a frontal flow developing at the foot of the column that propagates radially outwards. Subsequently collapsing layers flow over the surface of the deposit continuing the flow in the radial direction. This results in a secondary front which separates the frontal flow and the currently static summittal region, which propagates inwards. A circular discontinuity evolves between the two regions, which is eventually consumed by the avalanche and the flow continues until stability is achieved in the summital region of the deposit.

In this range the collapse depends strongly on the angle of internal friction, with the occurrence of two distinct morphological deposits seen in Figure 4.7. For shallow columns where $a < 0.90$ the summit is never completely consumed by the avalanche and results in a truncated cone. The failure envelope defined by the angle of internal friction provides a 'fracture' plane where material above slumps to form the deposit.

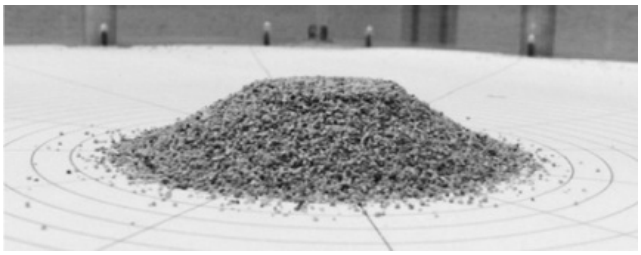

(a)

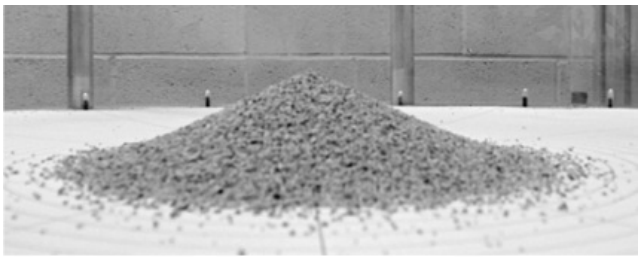

(b)

Figure 4.7: Two distinct morphologies arise dependent upon aspect ratio a. (a) Truncated cone when $a < 0.90$. (b) Sloping conical shape when $a > 0.90$.

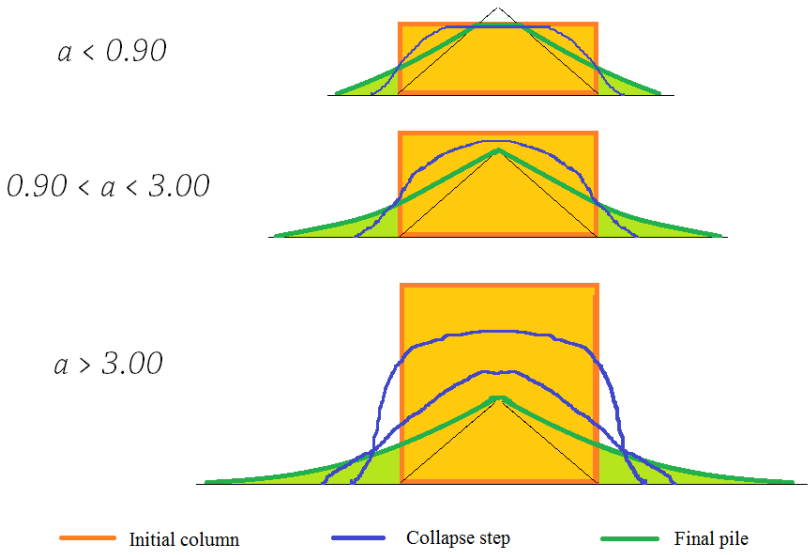

Figure 4.8: Collapse mechanism for different aspect ratios. The black triangle represents the failure envelope defined by the angle of internal friction, within which material is thought to remain static. For $a < 0.90$ a 'fracture' situation occurs with slumping over the failure envelope. For $0.90 < a < 3.00$ the periphery initially crumbles initiating the slumping over the failure envelope. For $a \gtrsim 3$ the entire upper surface remains horizontal as the collapse initiates with a frontal flow at the base.

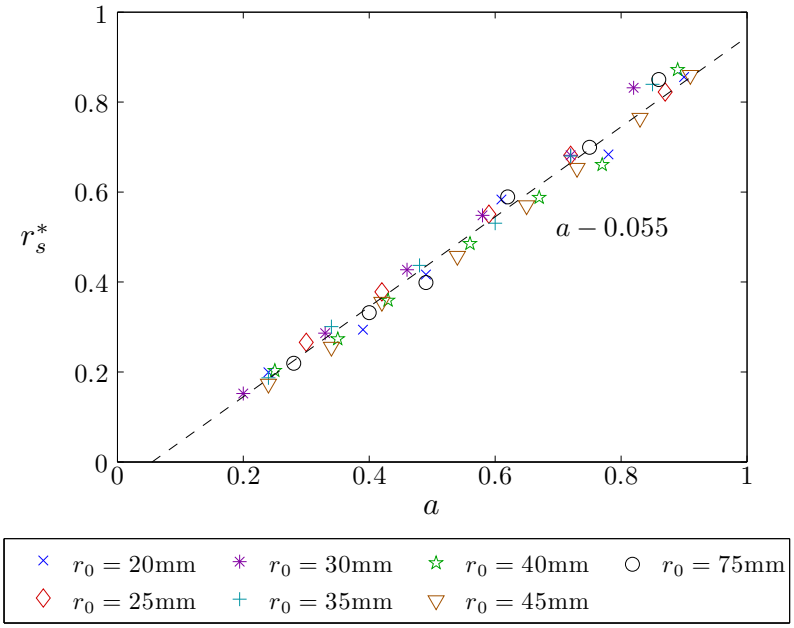

Figure 4.9: Variation of normalised summital radius $r_s^* = (r_0 - r_s)/r_0$ against aspect ratio. Dashed line (- -) indicates linear fit given in equation (4.2).

Upon exceeding this aspect ratio the summit is entirely consumed and a full conical shape is left. A similar slumping of the material is observed but with material above the failure envelope subject to avalanching, the angle at the summit must remain smaller than the angle of repose. This is because the angle of repose is the greatest angle sustainable by the medium by definition - a limiting case of the angle of internal friction under a loose packing.

Previous authors have found this critical aspect ratio to be $a = 0.74$ [Lube et al., 2004; Lajeunesse et al., 2004]. Without direct inspection with a 3D scanner, it can be difficult to determine where one geometric regime ends and the second begins as a summit may still exist but be small. It is for these reasons that a higher value is expected to be achieved although this maybe compounded with the difference in granular material.

With the non-intrusive and relatively accurate measurement techniques, the rate of consumption of the summital plateau was also observed. The variation of the summit radius, r_s, with aspect ratio is shown in Figure 4.9 where r_s is normalised against the initial radius as

$$r_s^* = \frac{r_0 - r_s}{r_0} \tag{4.1}$$

This shows a common linear relation across all cylinder sizes given by

$$r_s^* = a - 0.055 \tag{4.2}$$

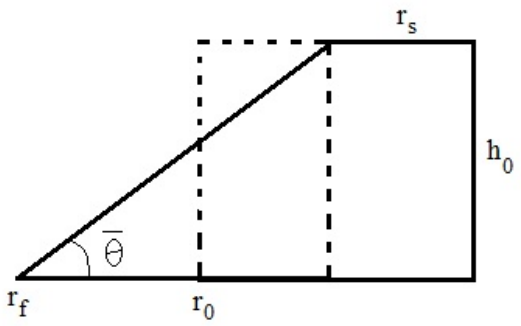

Figure 4.10: For consideration of geometric argument for direction proportionality of r_s with a.

valid for $a < 0.90$. Where $a > 0.90$ there is a sharp deceleration in the shrinking of the plateau with increasing aspect ratio as the peak becomes curved and the summital plateau becomes indistinguishable as it is of the order of a few grain sizes.

The direct proportionality observed is expected with consideration of geometric arguments as in Figure 4.10. Consider a 2D slice of the truncated cone. Assuming a constant area

$$A = r_0 h_0 \tag{4.3}$$

$$A = \frac{r_f + r_s}{2} h_0 \tag{4.4}$$

hence

$$r_f = 2r_0 - r_s \tag{4.5}$$

Given

$$\frac{h_0}{\tan\bar{\theta}} = r_f - r_s \tag{4.6}$$

for some mean angular profile of the slope of the deposit $\bar{\theta}$, then from equation 4.5

$$\frac{h_0}{\tan\bar{\theta}} = 2(r_0 - r_s) \tag{4.7}$$

Some rearrangement gives

$$r_s^* = \frac{a}{2\tan\bar{\theta}} \tag{4.8}$$

in agreement with the obtained data.

Where $a \gtrsim 3$ the collapse dynamic changes from that previously observed as seen in Figure 4.8 and described in the literature review in Section 2.1.2. In this

case the whole upper surface of the column moves, initially retaining its horizontal profile. A frontal flow then develops at the base of the pile as before, spreading radially outwards. Part way through the collapse the upper surface begins to dome while the frontal flow continues to spread. The end result is a deposit with a shallower angular profile than lower aspect ratios.

The evolution of the profile with increasing aspect ratio can be seen in Figure 4.11 (a) for $r_0 = 35\,\text{mm}$ obtained through averaging the profiles of four cross-sections. The height, $h(r)$, is given as a function of radius, r, and both values are normalised against r_0. It is evident that the angular profile not only becomes shallower with increasing a, but the nose of the deposit becomes less sharp and displays an increase in curvature. The relationship between defining measurement quantities and aspect ratio are discussed in detail below to include the final deposit radius, r_f, final height, h_f, and angles at the summit, α_s, and base, α_b. This has previously been investigated by Lube et al. [2004] and Lajeunesse et al. [2004] but a further dependence has emerged; a dependence on the initial system size r_0/d.

Similar system sizes were used as in previous experimental works with their values outlined in Table 2.1, but notable differences in the defining scaling relations were found and are presented in this study. An example of resultant deposit profiles for $a = 1.7$ is given in Figure 4.11 (b) for several cylinder sizes, again obtained through averaging four cross-sections. In this particular case the final height and angle at the summit is largely the same. The difference occurs at the nose of the deposit where larger system sizes result in a greater final deposit radius and a shallower angle at the base. The impact of r_0/d is considered for each of the quantities and frequently displays an arresting value of this effect. Meso-scale interactions are known to occur across granular systems but in this case it has been previously overlooked as both Lube et al. [2004]; Lajeunesse et al. [2004] used comparable system sizes.

4.4 Deposit scalings

4.4.1 Final pile radius

Previous results [Lube et al., 2004; Lajeunesse et al., 2004; Thompson and Huppert, 2007] suggested that the final deposit radius is independent of the initial system size. Final pile radius, r_f, against aspect ratio was considered for each cylinder radius, with r_f normalised against r_0 as

$$r_* = \frac{r_f - r_0}{r_0} \tag{4.9}$$

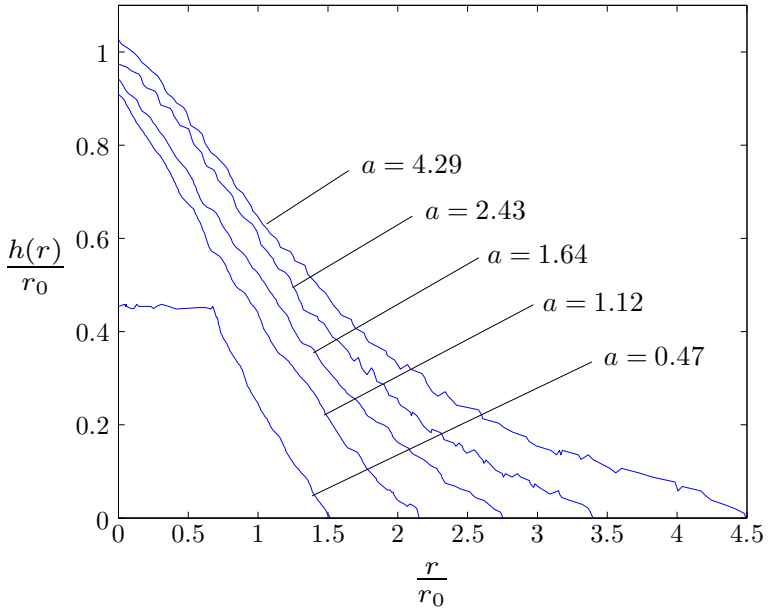

(a)

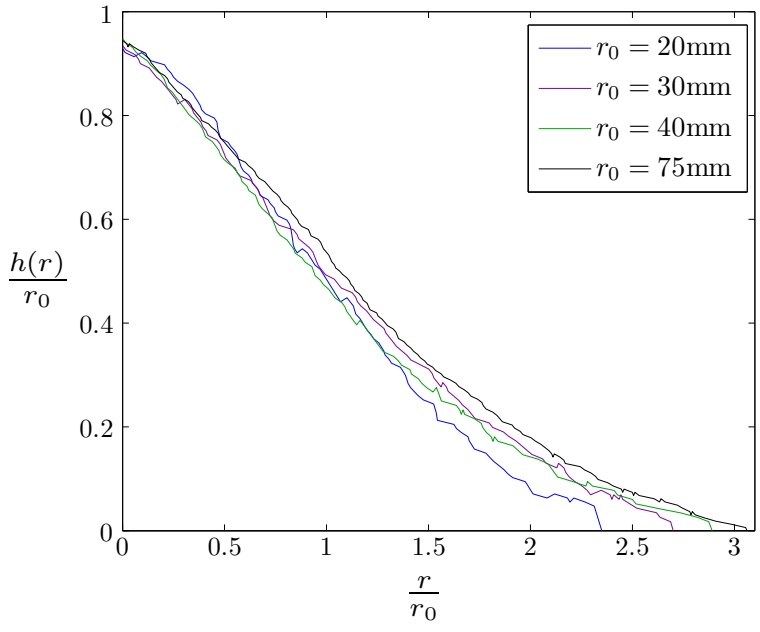

(b)

Figure 4.11: Deposit profiles normalised against the cylinder radius r_0. (a) Evolution of the profile with increasing aspect ratio a for $r_0 = 35\,\text{mm}$. (b) Difference in profiles for $a = 1.70$.

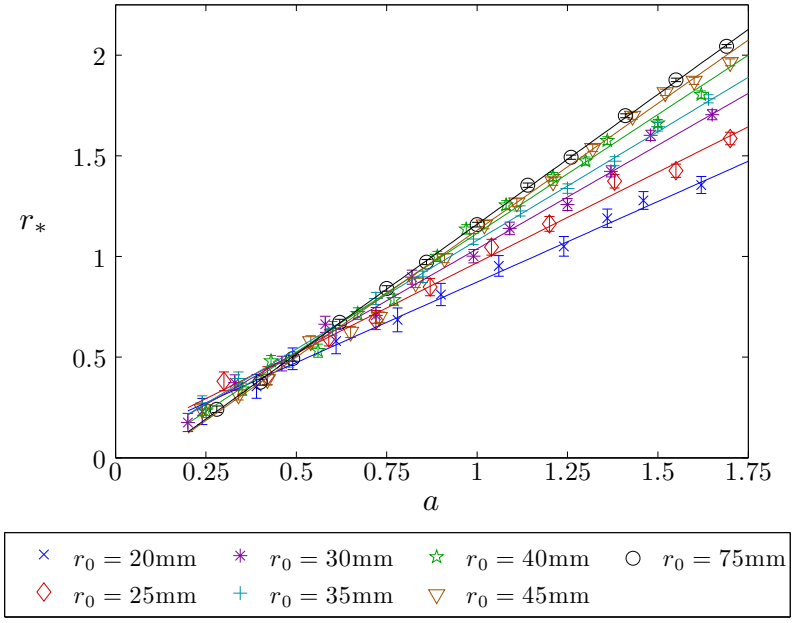

(a)

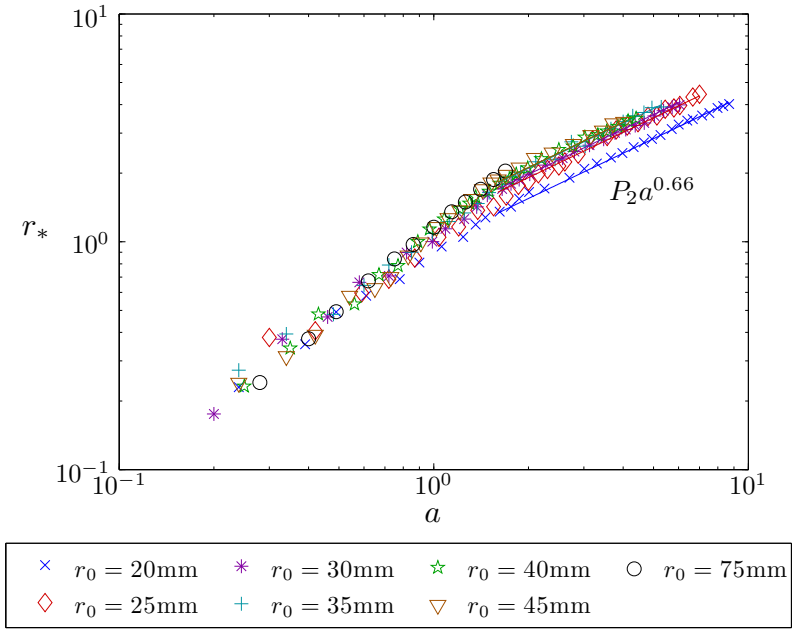

(b)

Figure 4.12: Relationship between r_* and a for varying cylinder radii r_0 with coefficients given in table 4.3. (a) $a < 1.7$ with errors displayed as discussed in section 4.2.5. Linear fits for each r_0 satisfying equation (4.10) are shown. (b) $a \gtrsim 1.7$ following a power law relation given in equation 4.13 as indicated by line fit.

r_0 (mm)	s	Λ_1	Λ_2
20	28	0.79	1.00
25	35	0.88	1.21
30	42	1.02	1.25
35	50	1.06	1.33
40	57	1.18	1.34
45	64	1.26	1.34
75	107	1.29	-

Table 4.3: Variation in proportional constants Λ_1 and Λ_2 for relationship between r_* and a given by equations (4.10) and (4.13) and respectively.

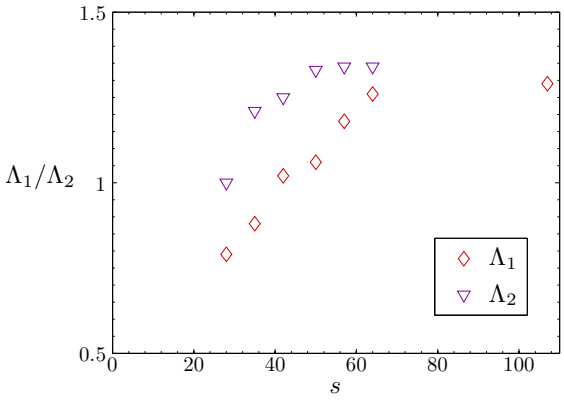

Figure 4.13: Data from Table 4.2. Variation in proportional constants Λ_1 and Λ_2 for relationship between r_* and a given by equations (4.10) and (4.13) and respectively.

Low aspect ratios

First consider where $a < 1.7$ as shown in Figure 4.12 (a). In this case error bars are given due to the proportionally smaller final radius. These have been calculated based on the repeatability testing in Section 4.2.5. In the repeatability testing three runs were performed with the final radius $r_{f,i}$ measured for each run $i = 1, 2, 3$. Given the variation in the periphery, the maximal and minimal radius was calculated based on the three inner-most and three outer-most points respectively on each run. The error bar length is then calculated as the difference between the largest maximum radius and the smallest minimum. This then not only accounts for the variation from one run to the next, but also the variation in the periphery at that aspect ratio.

For this aspect ratio rangle, the normalised final pile radius r_* is a linear relation of the form

$$r_* = \Lambda_1 a + \epsilon \tag{4.10}$$

where Λ_1 and ϵ are constants is observed, but there is a clear dependence of these coefficients on the initial cylinder size and inherently the system size. The gradient Λ_1 for each cylinder radius is given in Table 4.3. It evidently increases with cylinder radius although it indicates strong signs of arresting as can be seen in Figure 4.13. For $r_0 = 20 - -45\,\text{mm}$ it follows a linear relation given by:

$$\Lambda_1 = \frac{r_0}{80d} + 0.45 \tag{4.11}$$

and substituting this into equation 4.10 gives

$$r_* = \frac{h_0}{80d} + 0.45a + \epsilon \tag{4.12}$$

This reveals a secondary dependence on initial height h_0 while the system size $s \lesssim 70$. The increase in Λ_1 severely slows for the largest cylinder size and while limitations of the equipment prevent investigation of larger values of r_0/d due to the maximum possible scanning area, it is presupposed that this deceleration continues in strength with increases in Λ_1 becoming negligible. This disputes previous research by other authors Lube et al. [2004]; Lajeunesse et al. [2004]; Thompson and Huppert [2007] who conclude there is no such effect while investigating comparable system sizes, although the gradient for $r_0 = 75\,\text{mm}$, $\Lambda_1 = 1.29$ is close to the value of 1.24 achieved by Lube et al. [2004]. This is one of the key results of this section. With previous experiments subject to greater inaccuracies in their measurement methods, differences in achieved data have previously been assumed to be due to experimental error. The high spatial resolution in the presented results and strong variation in Λ_1 indicates the existence of this dependence to be correct. Reasoning for this difference in scaling can be given insight by consideration of the degree of mass flow and process of jamming and flowing layers as described by Cates et al. [1998].

Previous authors Lube et al. [2004]; Lajeunesse et al. [2004] theorise that the collapse contains an inner conical region that remains static throughout the collapse, with the base angle of this cone defined by the angle of internal friction. A larger system size will result in this conical region being more structurally stable than a smaller system size. When the system size is small enough there could be small amounts of plastic rearrangement of granules near the periphery of the conical region, significant enough to interfere with the flowing layer. This would lead to greater energy dissipation in the flowing layer resulting in a shorter runout.

Larger aspect ratios

When $a \gtrsim 1.7$ a new relation emerges fitting the power law

$$r_* = \Lambda_2 a^{0.66} \tag{4.13}$$

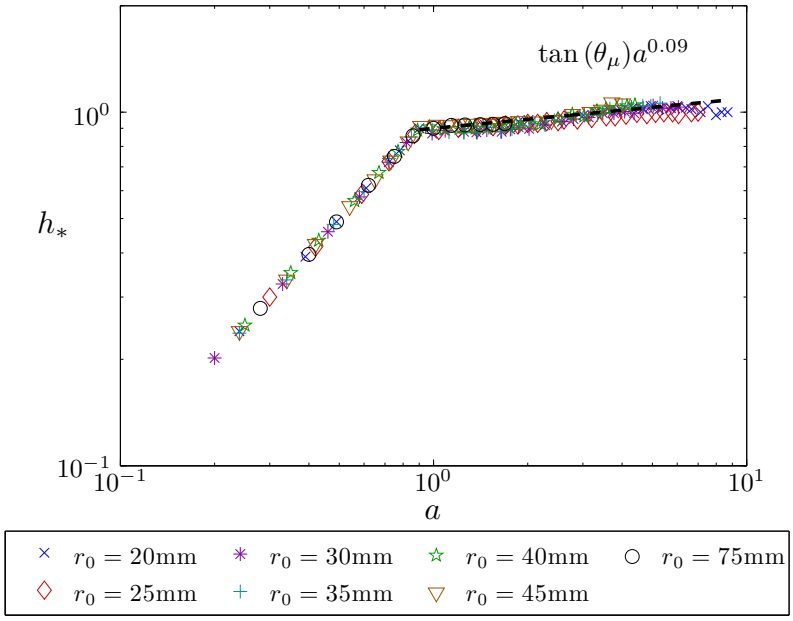

Figure 4.14: Evolution of normalised height h_* with aspect ratio a. Dashed line (- -) indicates power law relation given by equation (4.14).

as observed in Figure 4.12 (b) where Λ_2 varies with s as given in Table 4.3. Compared to the relation given in equation (4.10) this constant appears to arrest earlier having stagnated when $r_0 = 35\,\text{mm}$, $s = 50$. The difference in Λ_2 can be attributed to the earlier discussion on jamming with its quicker cessation likely to be due to the greater amount of material involved in the collapse. The data is in agreement with Lube et al. [2004] in terms of the onset of equation (4.13), but the power 0.66 is higher than both Lube et al. [2004]; Lajeunesse et al. [2004] who agree with a square root fit. The variation in the precise value of the power could be due to different granular materials used by the other authors, but again they negate the effect of r_0/d.

4.4.2 Final height

The final height was normalised as $h_* = h_f/r_0$ and compared against a in Figure 4.14. For $a < 0.90$ the deposit is a truncated cone and so $h_f = h_0$. This suggests that there is an internal conical surface over which the avalanche occurs, with the angle at the base of this internal cone to be $\theta = \tan^{-1}(0.90) = 42.0°$. This observation was concluded by Lajeunesse et al. [2004] where layers of coloured sand were used in the prepared column and the resultant deposit was split to reveal a conical zone where they suggest there has been no movement of material.

As aspect ratio increases beyond the point where the flat summit is entirely consumed and achieves a full conical shape, the particulate above a height $0.90r_0$

avalanches over the currently deposited matter and the height minutely continues to increase. It argued that this increase is marginally smaller for $r_0 = 20, 25\,\text{mm}$ with exponents of 0.05 and 0.07 respectively, while for all other cylinder radii the relation

$$h_* = 0.90a^{0.09} \tag{4.14}$$

holds. In this case the meso-scale effect is observed for $s \lesssim 40$, likely to be arresting faster than the radial coefficient Λ_1 due to the greater amount of material as presupposed for the radial coefficient Λ_2. Lube et al. [2004] agree that there is a minute increase in height at this onset, although proposing a higher exponent of 0.17, while Lajeunesse et al. [2004] argues a complete stagnation.

Mohr-Coulomb theory states that the development of surface failure is due to the inability to sustain its composition under shear stresses and occurs along an envelope projected at an angle equal to the internal friction angle θ_μ. The data provided for the limestone based particulate used indicated an internal friction angle $\theta_\mu \approx 39°$. This would imply that the onset of the second geometic regime would occur at an aspect ratio of $a = 0.89$ which is in good agreement with the experimental data. This allows description of the height with known material parameters:

$$\begin{array}{lll} h_* & = a & a < \tan\theta_\mu \\ h_* & = \tan(\theta_\mu)a^{0.09} & a > \tan\theta_\mu \end{array} \tag{4.15}$$

where 0.09 is exchanged for a lower value for the smallest system size. Obtaining scalings where constants are completely described by the material parameters is desirable for equivalence in other experimental setups with different granular materials. This is an encouraging step to a fuller description of the final deposit independent of seemingly arbitrary proportional constants.

4.4.3 Angular profiling

The surface of the deposit does not have a straight edge as a cone does, but it curved to some angular profile. Two characteristic angles of the profile are the angle at the summit, α_s, and the angle at the base, α_b. These values were obtained from the 3D meshes generated, so the method was not intrusive or destructive of the deposit. Where the first geometric regime exists and there is a flat summit, α_s was taken to be the angle of the slope directly below the flat surface.

For $a \lesssim 3$ the summital angle was found to vary with aspect ratio as in Figure 4.15 (a), following a power relation:

$$\alpha_s = 25.6a^{-0.33} \tag{4.16}$$

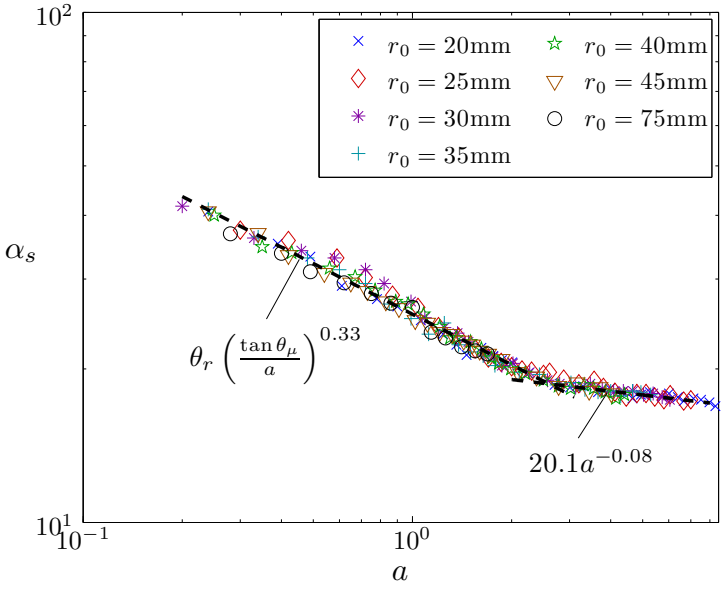

(a)

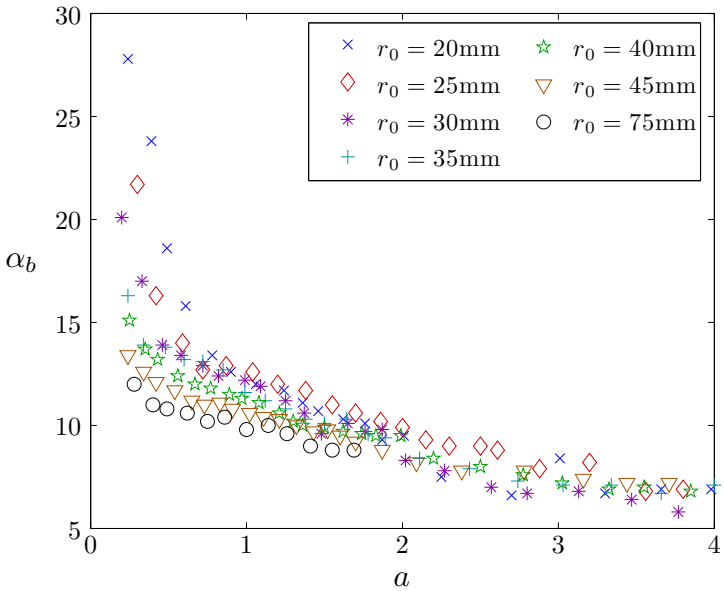

(b)

Figure 4.15: Variation in angle against aspect ratio for (a) summital angle (b) base angle.

While the aspect ratio is such that the resulting deposit is a truncated cone, the avalanching periphery is strongly dependent upon the internal friction angle rather than the angle of repose. This is due to the failure envelope initiating the motion with little avalanching over the deposited layers and so $\alpha_s > \theta_r$ as expected. The onset of the full conical shape where the entirety of the summit has been consumed corresponds to the aspect ratio where material exists above the conical failure envelope defined by the internal friction angle. At aspect ratios greater than this critical onset the greatest sustainable angle of a deposit with a sharp peak is exactly the angle of repose by definition, hence where this occurs $\alpha_s < \theta_r$. The continued decrease in the summital angle is due to increased avalanching over already deposited layers smoothing the steep sides.

Using the angular analysis of the onset of the full conical shape and assuming the summital angle to be a function of aspect ratio, $\alpha_s(a)$, we have the condition

$$\alpha_s(\tan\theta_\mu) = \theta_r \tag{4.17}$$

Applying this condition to equation (4.16) the coefficient can be expressed in terms of the internal parameters:

$$\alpha_s = \theta_r \left(\frac{\tan\theta_\mu}{a}\right)^{0.33} \tag{4.18}$$

Enabled by the previous analysis via interpretation of Mohr-Coulomb theory, this is the second scaling with constants given in terms of known material parameters.

When $a \gtrsim 3$ a different relationship emerges coinciding with the change in collapse regime where the entire upper surface of the initial column falls retaining its horizontal profile. The angle at the summit continues to decrease but at a severely slower rate following the power law

$$\alpha_s = 20.1a^{-0.08} \tag{4.19}$$

The variation in the angle at the base with aspect ratio was found to be more complex and dependent upon the r_0 and hence the initial system size as shown in Figure 4.15 (b). While $a \lesssim 3$ this follows a power law relation of the form

$$\alpha_b = Ea^{-F} \tag{4.20}$$

where E and F are constants dependent on system size s as given in Table 4.4. The dependence on r_0/d is initially linear up to $r_0 = 45\,\text{mm}$, giving relations

$$E = 14.7 - \frac{r_0}{15d} \tag{4.21}$$

r_0 (mm)	s	E	F
20	28	12.94	0.52
25	35	12.33	0.45
30	42	11.69	0.32
35	50	11.42	0.25
40	57	10.98	0.23
45	64	10.53	0.17
75	107	9.76	0.16

Table 4.4: Constants fitting power law relation $\alpha_b = Ea^{-F}$ for given initial cylinder size.

$$F = \frac{r_0}{100d} - 0.78 \tag{4.22}$$

For $r_0 = 75\,\text{mm}$ the F exponent evidently stagnates and it can be assumed that for $s > 100$ $F = 0.16$. With an error of $\pm 1^\circ$ it is presupposed that $E \approx 10$ for $s > 100$. For $a \gtrsim 3$, α_b stagnates with $6^\circ < \alpha_b < 8^\circ$.

For a fixed aspect ratio, smaller system sizes have a distinctly higher base angle at least while a truncated cone exists. This would be expected given a proportionally smaller radius of the deposit and equivalently low r_0/d as described in section 4.4.1. At the onset of a full conical shape the variation in angle between cylinder sizes becomes small and approaches the stagnation point. Here avalanching of the upper surface of the column flows over the already deposited layers stretching beyond $1.75r_0$ and are of similar thickness at the extremity. $\alpha_b < \theta_r$ for all aspect ratios as expected or further avalanching would occur as per the definition of the angle of repose.

4.5 Conclusions

The lase methodology used in the experiments have allowed a substantially greater degree of accuracy than any previous research on the subject. Given similar initial conditions to the previous studies, this analysis has shown that differences in data that were originally explained as experimental error are a demonstration of system size dependence $s = r_0/d$. Quantities r_f and α_b that result directly from material deposition depends strongly upon the initial system size r_0/d in addition to the aspect ratio and material parameters, whereas r_s, h_f and α_s have little or no secondary dependence and are subject only to aspect ratio and material parameters.

It is well known that the final deposit radius has a linear dependence on aspect ratio, but results showed that the coefficient of this proportionality increased linearly, at least for $s \lesssim 70$, with the system size. This behavior is mirrored in the angle at the base of the deposit, decreasing in magnitude with system size.

In the case of a truncated cone the summital plateau shrinks with increasing aspect ratio. The continued contraction was directly proportional to aspect ratio, but had no relation to system size or rate of increase of the final pile radius. During this phase the final height is exactly the initial height, but where $a > \tan\theta_\mu$ the height minutely increases of the order $a^{0.09}$. The angle at the summit follows a power law relation with aspect ratio, again independent of system size, and coupled with other analysis is shown to depend on the angle of repose and internal friction while $a \lesssim 1.7$.

The dependence of the parameters on system size is thought to occur due to the stability of the inner conical region. A smaller system size means this region is less structurally stable, further dissipating energy of the flowing region, resulting in a decreased runout and steeper base angle. This further fuels the necessity for any theoretical model of the collapse to incorporate internal dynamics such as those described by Cates et al. [1998], particularly where investigations could contain a meso-scale effect.

4.6 Acknowledgements

Training on the laser scanning equipment and software was provided by Mr Erichan Kiraci at Warwick Manufacturing Group. All data collected and analysed are my own work.

Chapter 5

Internal phenomenology of stationary granular column collapse

5.1 Introduction

Previously the description of the dynamic collapse has been limited to evaluation of what can be seen in time lapse videos and externally measured, rather than the changes within the sand pile. Lube et al. [2004]; Lajeunesse et al. [2004] theorise that the collapse occurs along a static failure surface defined by the angle of internal friction posed by Cates et al. [1998]. This assumption is made on the basis of apparently static coloured layers of sand where the pile has been split with a thin pane of glass as shown in Figure 2.4. To provide reliable quantitative data of the slip plane phenomenon, internal non destructive observation of the pile is required.

In this chapter the packing density within the initial column and resultant pile is investigated by computational reconstruction of the system using XCT, a technology outlined in Section 2.6 of the Literature review. This is the first time such a technique has been applied to this setup, and one of the few granular studies using this technique. By creating annular regions of interest in the reconstructed scan data the volume occupied by the granular material can be observed and the packing density calculated. This segmenting technique for density evaluation was applied by Hamel and Krumm [2008] physically when characterising fixed beds packed with wood chips. With the collapse being axisymmetric, the reasonable assumption is made that the packing is uniform in the aximuthal direction for a thin bounded annulus in the radial direction.

From the data a packing density map of a 2D slice through the centre of the column/pile was constructed. While the study lacks a temporal scale, the results

r_0 (mm)	h_0 (mm)	a	m_0 (g)
25	18.1	0.72	50.0
25	30.0	1.20	80.2
25	42.5	1.70	110.4
25	51.0	2.04	139.8

Table 5.1: Range of aspect ratios a trialled

indicate granular movement within what was previously thought to be a static region solely providing a failure envelope. This information could lead to improved theoretical models, in particular how the inertia should be modelled in the $\mu(I)$ rheology approximation given by Lagrée et al. [2011] previously discussed in Section 2.4.4.

All data relating to these experiments can be found in Appendix C, with a discussion on interpolation methods in Appendix D. A truncated version of these experiments are currently under consideration for publication in *'Physical Review Letters'* with a full paper in preparation for submission to *'Powder Technology'*.

5.2 Experimental method

5.2.1 Apparatus

The experiments were carried out using a 50 mm diameter cylinder and the granular material outlined in Chapter 3 consisting of particle diameters $d = 600$–800μ m. The column was prepared on a circular Perspex disk large enough to contain the collapse determined by experiments in Chapter 4. The collapse was performed within a housing as described in Appendix A used in Chapter 4, but was manufactured at a 10:3 scale. Prior to filling, the position of the cylinder and Perspex disk were marked in the housing such that the pulleys were in a position to raise the cylinder vertically. The aspect ratio and relevant initial parameters of the prepared columns are outlined in Table 5.1.

Scans were performed pre (contained within the cylinder) and post (after cylinder removal) collapse using the *'Nikon Metrology XT H 320 LC'* CT scanner. The collapse was performed outside of the scanner, after which it was sprayed with a fine mist of a strong adhesive before moving to prevent dislodging the pile in any manner. The orientation and position of the disk was maintained in pre and post collapse scans by marking its position on the loading table.

Ideally a smaller particle size or larger cylinder would have been used to negate any meso-scale effects as noted in Chapter 4. This was not possible as decreasing the particle size and hence increasing the system size r_0/d at the same magnifications would mean that fewer voxels would represent one particle and the

a	Voltage (kV)	Power (W)	Mag.	Filter (mm)	Voxel size (μm)	Unsharpness (μm)
0.72	215	7.0	3.15	0.5	70	49
1.20	200	10.0	2.28	1.0	87	61
1.70	220	12.0	2.21	1.0	91	63
2.04	200	14.0	1.99	1.0	100	68

Table 5.2: Scanner parameters for each aspect ratio.

geometric unsharpness would be proportionally larger. This could lead to clusters of particles being realised as one volume. Increasing the cylinder size while maintaining the aspect ratios would result in a greater runout. This means that a lower magnification would have to be used to keep the entire pile in view leading to the same problem.

5.2.2 Scanning parameters

Scans were performed using the *'ImpactX'* software package provided by *Nikon Metrology (UK)*. A preview image of the object under the current scan parameters is displayed with an associated greyscale profile in Figure 5.1 allowing real time configuration to find the optimal settings. The sample can be moved within the scanner by using a series of control nozzles; it can be moved parallel to the source, perpendicular to the source (increasing magnification) and rotated. The sample is moved into a position so it fills as much of the viewing area as possible, maximising magnification, while still being completely in view at all rotation angles. For a single aspect ratio scan parameters were recorded so the same conditions could be set for pre and post collapse scans.

With the specimen in place the grey scale values were altered to fit within the ideal zone of 10000–60000 as in Figure 5.1 (b). This was done by altering the voltage and power in addition to a small amount of filtering. A 2D image was collected at every 0.115° resulting in 3142 images to be used in the reconstruction; determined to be the optimal amount for the detector width. In all cases a 2 second exposure time was used to obtain the correct level of detail, while using the maximal scan time available. Details of the scan parameters for each specimen are given in Table 5.2 as well as the resultant voxel size and unsharpness. Notice that the unsharpness is below the voxel size indicating that the geometric blurring at the edges will be minimal - a voxel at most.

For each set of scanning conditions a ball bar known to have a centre-to-centre distance of 50 mm was scanned as a reference geometry for voxel scaling. This will further increase measurement accuracy as discussed in Section 2.6.5.

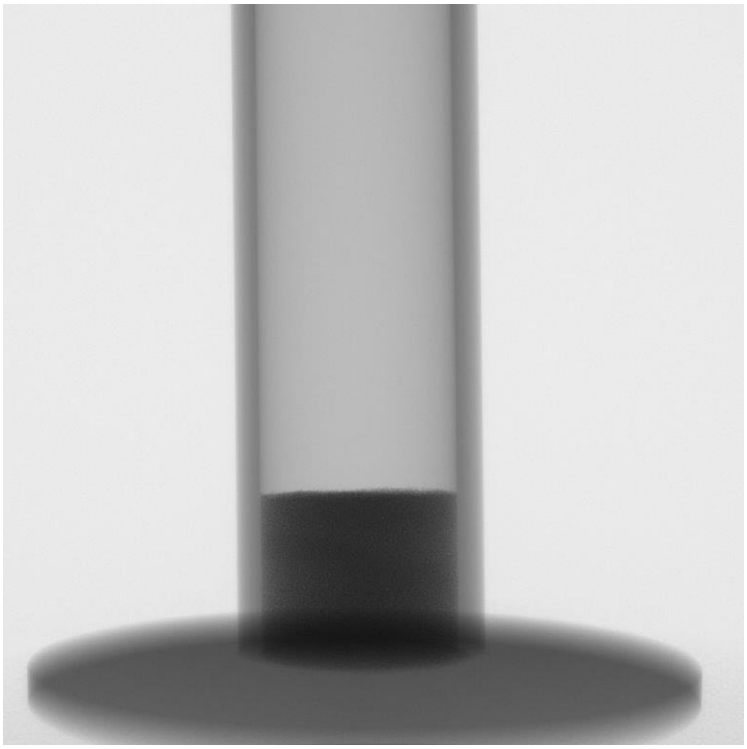

(a)

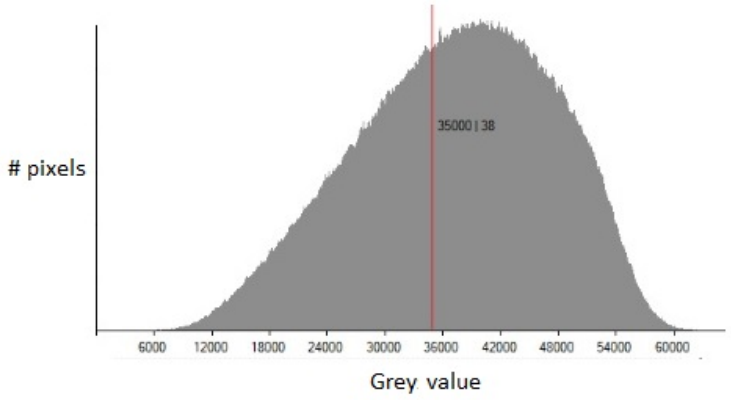

(b)

Figure 5.1: Setup of the scan of a granular column. (a) The preview image of the detector under the current X-ray conditions. (b) Histogram of greyscale values observed in the preview image.

a	Distance (mm)	Scaling
0.72	50.108	0.9978
1.20	50.147	0.9971
1.70	50.143	0.9971
2.04	50.132	0.9974

Table 5.3: Measured centre-to-centre distance of a scanned bar ball providing voxel scalings for increased accuracy.

5.2.3 Reconstruction

The projections were reconstructed using the software package *'CT Pro 3D'* (*Nikon Metrology (UK)*). First an algorithm was implemented to determine the axis of rotation using two slices through the medium. With this found, back projection was applied while using beam hardening and noise reduction algorithms to generate the volume file.

5.3 XCT results

The 3D reconstruction was loaded into the software package *'VG Studio Max'* (Volume Graphics; Heidelberg, Germany) for interrogation. An example of an imported collapse is shown in Figure 5.2 with the ability to scroll through slices in the three 2D planes and a 3D view for reference. The file generated retains voxel size data that was subsequently scaled based on the measurement of the 50mm ball bar reference geometry scanned for each set of scan conditions. The measured centre-to-centre distances and the voxel scaling applied can be seen in Table 5.3.

An example of a 2D cross section of the XCT images for $a = 0.72$ pre and post collapse can be seen in Figure 5.3 and Figure 5.4. Additional images of the other three aspect ratios trialled can be found in Appendix C. This is the raw data generated from reconstruction of the 2D images. Each voxel has been assigned a grey value based on the attenuation of X-rays by the material as discussed in Section 2.6.2. Observe that a grain can consist of a number of greyvalues as a result of the beam path through the sand pile and the subsequent reconstruction method with an example given in Figure 2.45. It is for this reason that thresholding must be applied to determine what is material and what is not. In this study a standard class seperability method is applied (locally) to set the threshold [Otsu, 1975], where the two classes are 'air' and 'granules', which is in standard use throughout CT.

In these figures it appears that some of the particles are 'free-floating', while in adjacent slices they will exhibit contacts with neighbouring particles. The white lines around particles are used for a 3D observation of the pile and are not con-

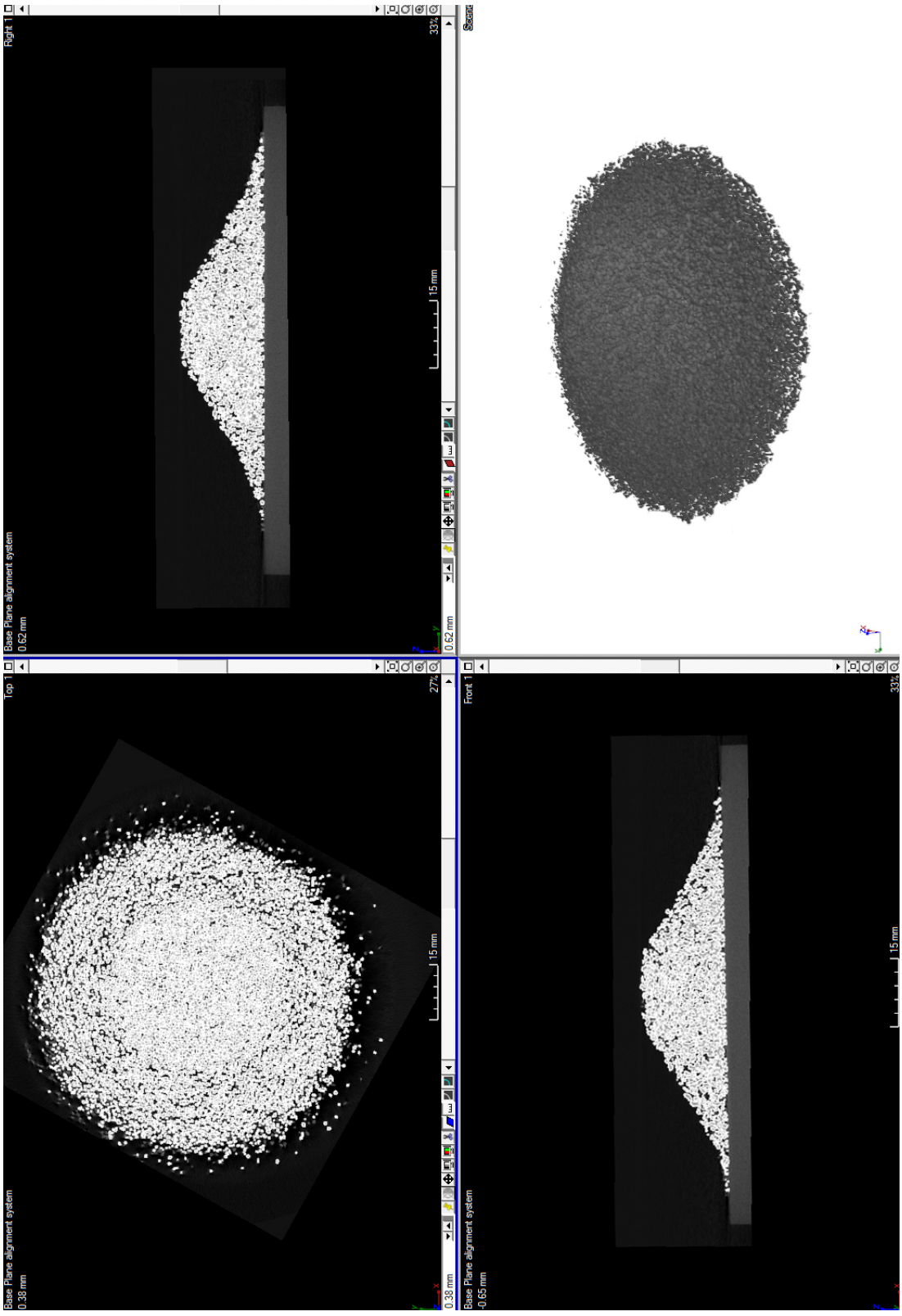

Figure 5.2: In software view of *'VG Studio Max'* displaying 3D reconstruction of $a = 0.72$ post collapse.

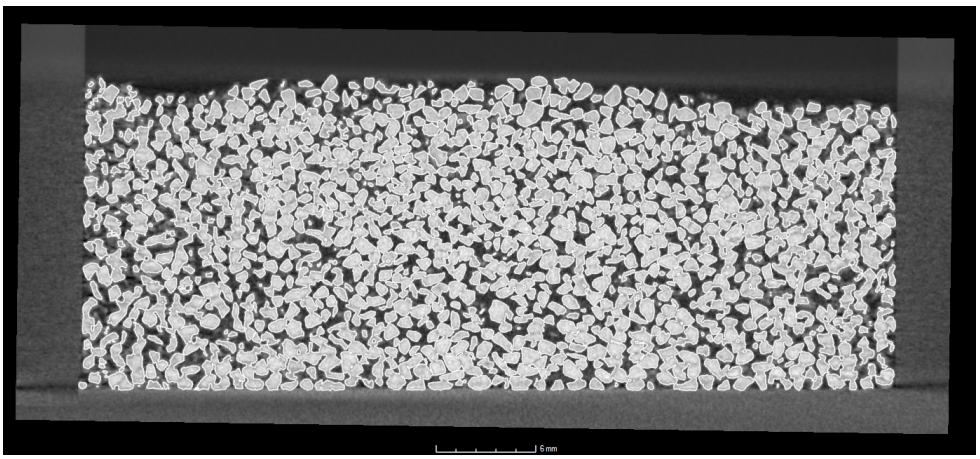

Figure 5.3: 2D slice through $a = 0.72$ pre collapse to depict grain position.

r_0 (mm)	h_0 (mm)	a	r_f (mm)	r_s (mm)	h_f (mm)
25.0	18.1	0.72	43.2	5.9	18.1
25.0	30.0	1.20	52.5	0.0	23.0
25.0	42.5	1.70	61.2	0.0	22.2
25.0	51.0	2.04	70.8	0.0	22.4

Table 5.4: Measurement data for the four collapses trialled as outlined in Table 5.1.

stituents of direct volume calculation, the method of which is explained in Section 6.6.

5.4 Measurement analysis

Quantifying measurements were made by observation of a 2D cross section through the centre of the column/pile. This image was imported into *'ImageJ'* (National Institutes of Health, Maryland, USA. http://rsbweb.nih.gov/) with the pixel scaling provided by *'VG Studio Max'* on export. Using the measure function the initial and final radii were found as given in Table 5.4. The final runout values are in good agreement with the scalings derived in Chapter 4:

$$r_* = 0.88a \qquad a < 1.7 \tag{5.1}$$

$$r_* = 1.21a^{0.66} \qquad a > 1.7 \tag{5.2}$$

The final height is similarly well represented with the final height equal to the initial for $a = 0.72$, and practically stagnating for higher aspect ratios.

Profiles of the final deposit were generated from a single 2D cross section by tracing the outline out the pile and exporting as $x - y$ coordinates with the assigned pixel scaling in *'ImageJ'*. The profiles obtained for the resultant deposits are given

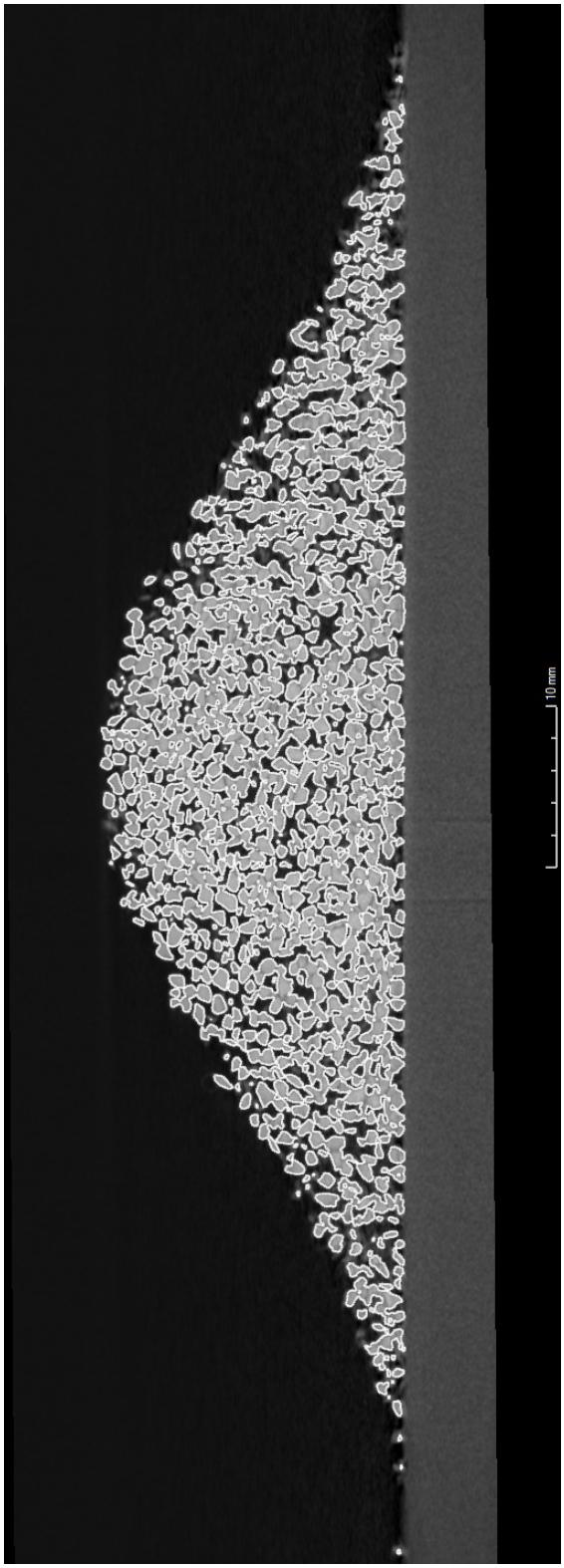

Figure 5.4: 2D slice through $a = 0.72$ post collapse to depict grain position.

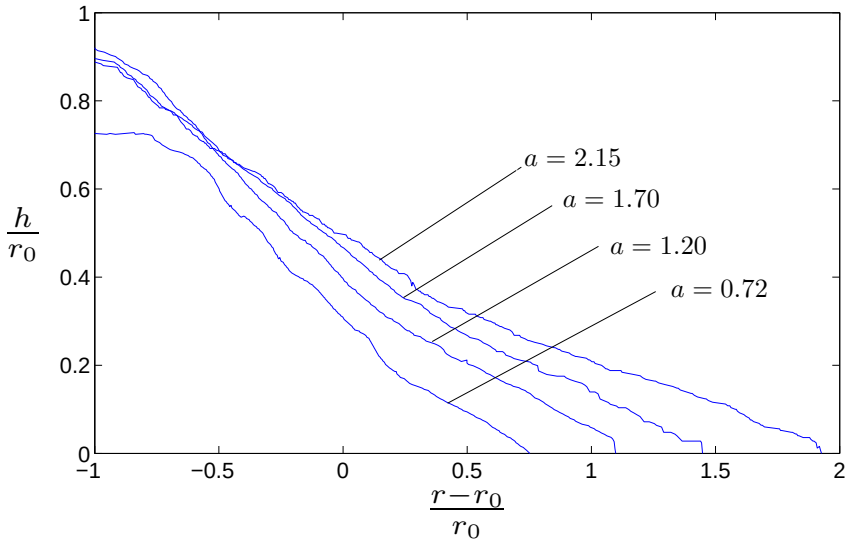

Figure 5.5: Profiles of the final deposit obtained using *'ImageJ'* with the height, h, and the radius, r, normalised against the initial cylinder size $r_0 = 25\,\text{mm}$.

in Figure 5.5, with the data given in Appendix C.

5.5 ROI generation

The 3D reconstructions were divided into regions of interest (ROI's) to investigate the volume of material and distribution of packing density throughout the column/pile. The software does not allow generation of ROI's for a selected shape with prescribed coordinates and must instead be created using an external template. The technical desciption of their creation is given below, with its intention to aid readers who wish to reproduce this segmentation.

Assuming that the collapse is axisymmetric and cylindrical in shape, annular ROI's were formed by the template shown in Figure 5.6 similar to the physical experiment carried out by [Hamel and Krumm, 2008]. Each ring (shown in white) is 2.4 mm thick in the horizontal plane with the central circle of the same radius (essentially an annulus with zero inner diameter). Gaps (shown in black) were $0.1\,mm$ thick and the template was stacked 2.4 mm high in the vertical direction. This allowed for 10 rings inclusive of the inner cylinder to fit within the width of the initial column. The size was chosen to be a tight fit within the cylinder itself and also to be four particles in width and height - large enough to obtain representative packing data but small enough to create a sufficient number of sub regions. The template could then be recursively translated 2.5 mm in a vertical direction to form new sets of ROI's for interrogation.

The ROI group was fitted centrally to the column/pile by aligning common geometries. A plane was fitted to the base of the ROI group and a line generated

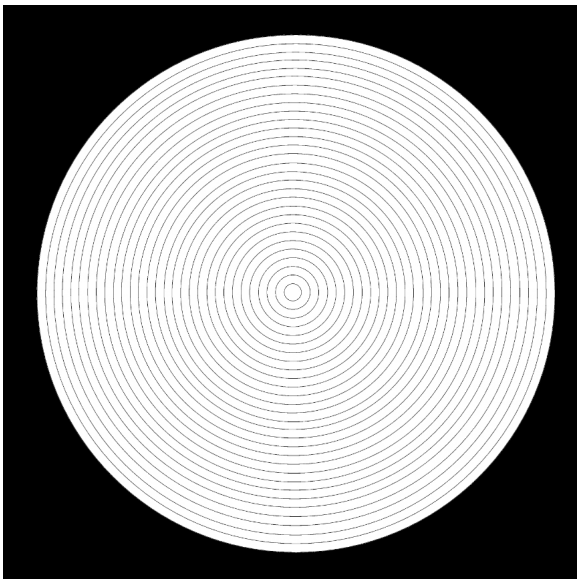

Figure 5.6: Template created for ROI generation consisting of annular rings of width 2.4 mm and a gap of 0.1 mm.

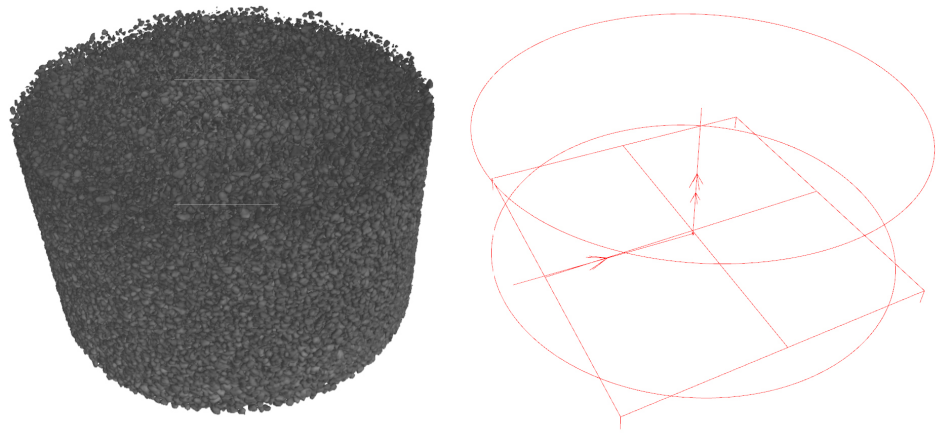

(a)

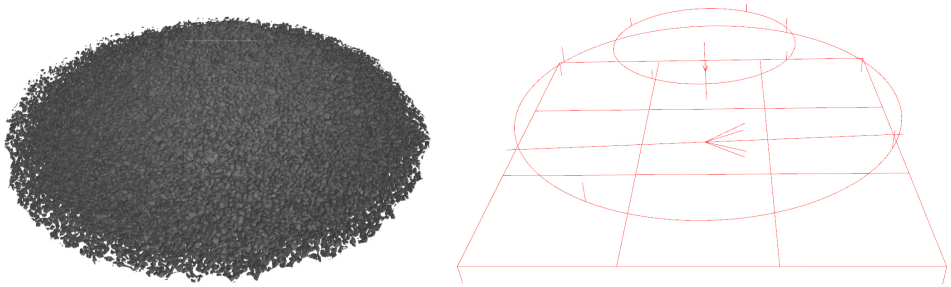

(b)

Figure 5.7: Reference geometry generation for 3D reconstruction of (a) column (b) pile.

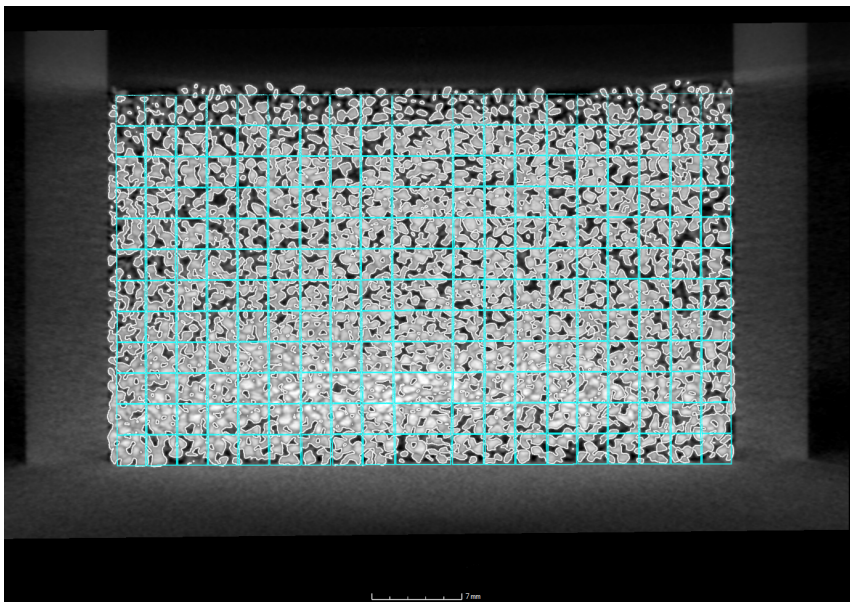

(a)

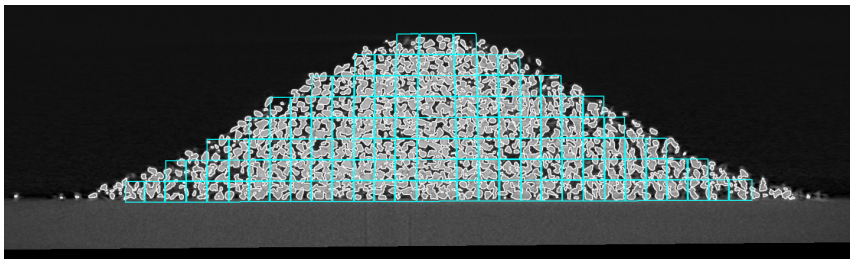

(b)

Figure 5.8: Placement of annular ROI's shown as a cross section. (a) Column. (b) Pile.

perpendicular to the plane fixed to the centre of the base. A similar method was applied to the 3D reconstruction but was more complex given that the reconstruction is not flat. A bottom plane was created by selecting approximately 50 points on the base of the reconstruction which were then averaged. Two circles were then fitted around the column/pile perpendicular to the plane. The centre of the two circles provided points to create a line that followed the centre axis of the pile. Examples of these constructions can be seen in Figure 5.7. With the relevant geometries constructed the planes and lines of the two sets are overlayed, ensuring the correct positioning of the 3D reconstruction with the template and allowing interrogation of each ROI.

5.6 Volume evaluation

For each reconstruction the volume of material in each ROI is recorded. When the current layer of ROI's has been evaluated the template is shifted by 2.5 mm in the positive z direction (perpendicular to the plane) and the process repeated, continuing until the entire column/pile is covered. ROI's are only evaluated where granular material fills the whole region. Examples of where the ROI's lie are shown in a 2D cross section in Figure 5.8. The volume of material in each ROI is then divided by the volume of the ROI giving the packing density, $\phi(x, y)$, for that region. The raw data is given in Appendix C.

An example of the volume selection in an ROI is shown in Figure 5.9. Here it can be seen that the unsharpness is negligible, making the volume selection simple. In areas of higher grain density slight grey areas become apparent between particles occuring due to the limitation of magnification where the distance between particles is of the order of a few microns. Auto-thresholding based on the Otsu method [Otsu, 1975] is applied locally within the ROI where voxels with a grey value above the mean of the background and particle grey value are counted towards the volume. Local thresholding in this manner negates any cone beam artefacts (where grey values may slightly vary from the top to the bottom of the detector) and applies a uniform selection criteria. In this way any subsequent measurement error is then systematic.

While normalised values (packing density) are considered from a systematic evaluation used throughout all scans providing a fair comparison, it is worth noting the potential error in the actual volume if it were for consideration. In a similar study of thresholding for porosity involving foam specimens by Kumar et al. [2011] this method was applied, and the effect of thresholding investigated. By moving 10% from the auto-threshold, which is a significant number of grey values, the overall volume calculated only varied by 5%.

5.7 Post processing

The details in this section deal with technical issues of acquired data and its interpretation for evaluation of results. This section can therefore be skipped by any reader only interested in the final results and how this relates to the collapse itself.

5.7.1 First visualisation

The symmetry of the concentric rings allows the density map of the column/pile to be viewed as a 2D cross section running from the centre to the extremity. Density is not a property that occurs at a point, but it can be inferred to occur at a particular

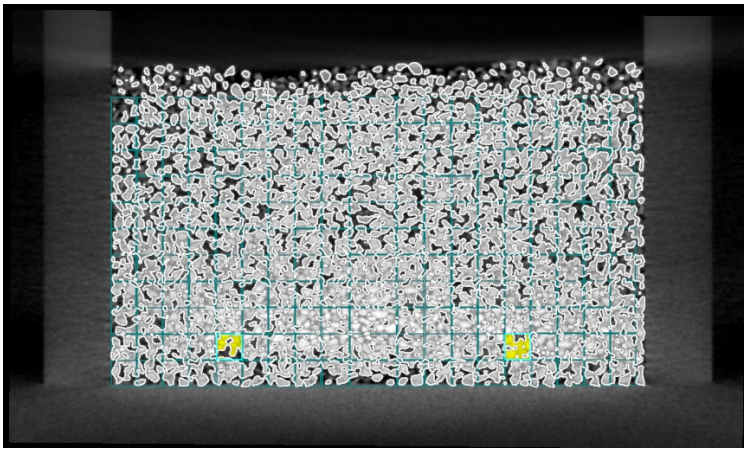

(a)

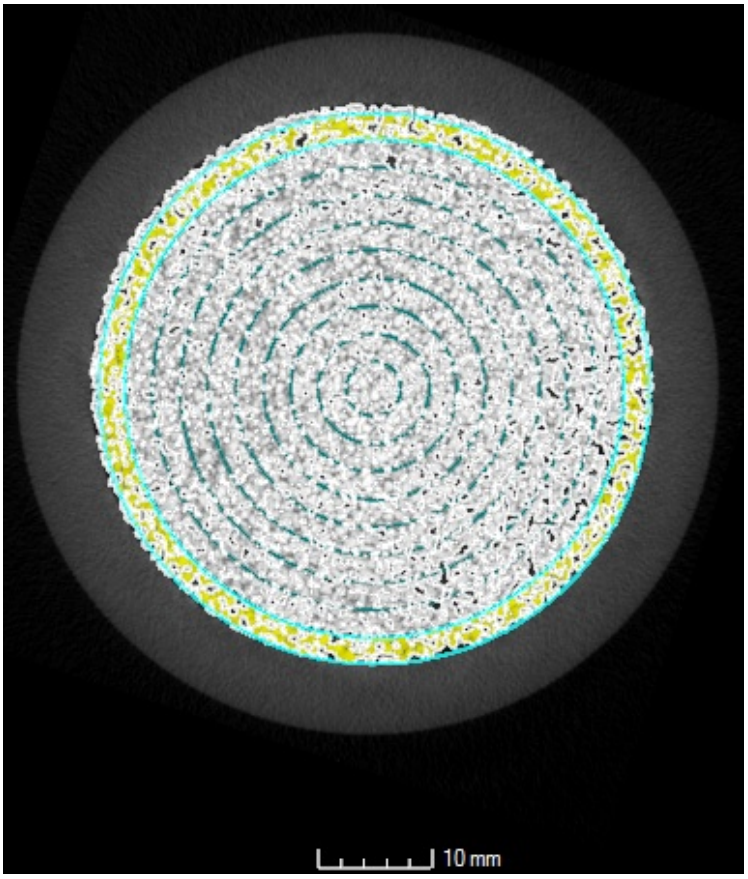

(b)

Figure 5.9: Selection of volume for evaluation within region of interest by selection of appopriate grey values for $a = 0.72$. (a) $x - z$ cross section. (b) $x - y$ cross section.

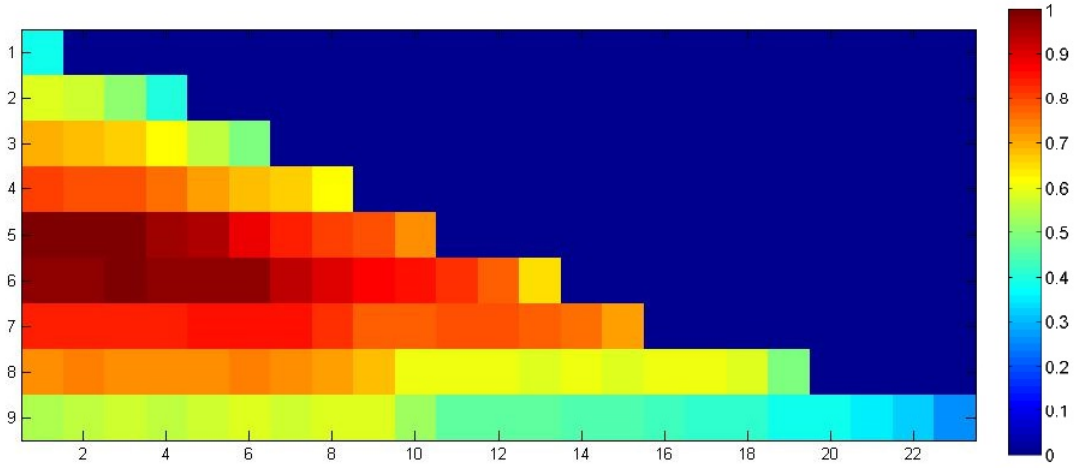

Figure 5.10: Example of nearest neighbour interpolation of data for $a = 1.70$. Data represented in ROI units.

point when averaged over a non-trival volume where that point is the centre. A non-trivial volume is one large enough such that a true reflection of the density is given as opposed to a volume so small that the value would tend to 0 or 1. With this definition of packing density at a point, we can take the density to occur at the centre of these squares.

The simplest interpretation of the data is to assign every element within the ROI the same $\phi(x, y)$ value, known as nearest neighbour interpolation, with an example given in Figure 5.10. To improve on this interpretation two other methods of interpolation are considered; bilinear and bicubic.

5.7.2 Interpolation

Throughout this section interpolation methods are applied to the obtained data. The bilinear and bicubic methods used were packaged with Matlab and directly applied. These methods are the same as their one-dimensional counterparts, linear and cubic interpolation, with an extension to be applied over a grid. Further details of these methods can be found within the documentation at http://www.mathworks.co.uk/help/vision/ug/interpolation-methods.html

Column

Centres of the squares are assigned values $\phi(x, y)$ as averaged over the ring. Where the material approaches a fixed boundary such as the cylinder wall or base the boundary is assigned a value by nearest neighbour interpolation. This similarly applies to the centre line of the column. The open top was assigned $\phi(x, y) = 0$, 1.2 mm above the boundary of the upper most ROI. This resulted in the data grid

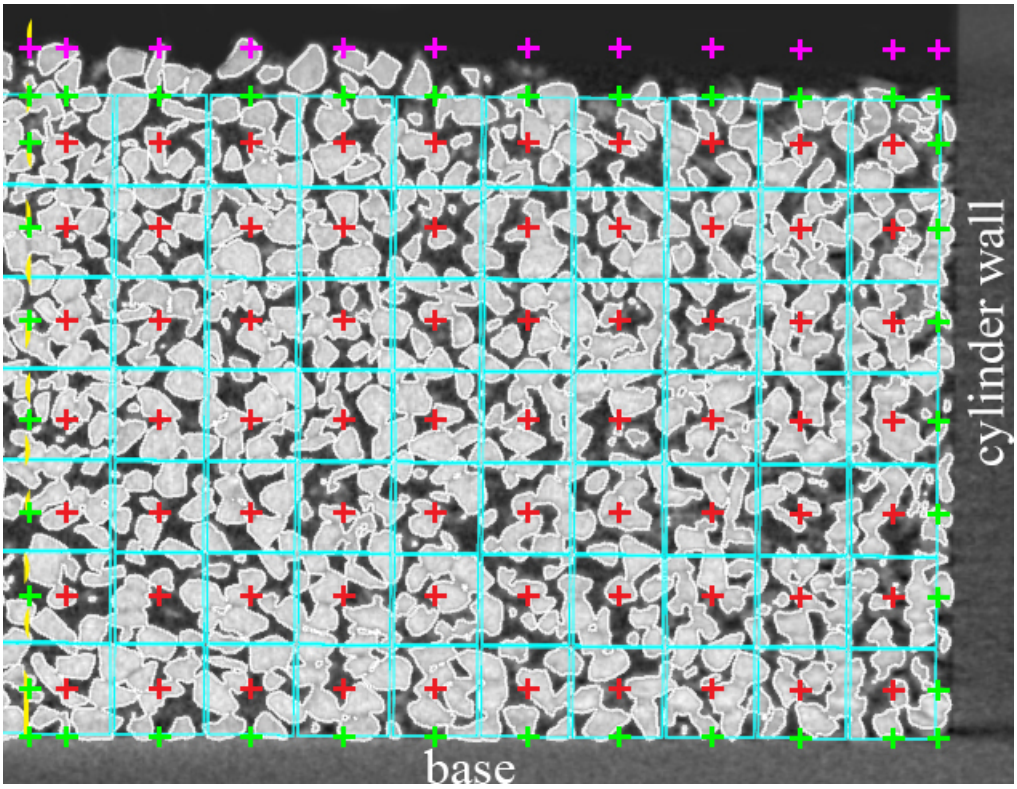

Figure 5.11: Arrangement of gridded data in column before bicubic interpolation. Yellow line indicates the centre and aqua represents ROIs. Red pluses indicate the raw data achieved from ROIs. Green pluses indicate points where nearest neighbour interpolation has been applied. Pink pluses indicate points where $\phi(x, y) = 0$.

as shown in Figure 5.11. The bicubic interpolation algorithm was then applied using *'Matlab'* (MathWorks; Massachusetts, USA), interpolating values within a grid the same width and height as the initial data set, but with regular spacing of 0.05 mm in both the x and y directions. The data is then trimmed using the calculated profile of the column, with all points above the boundary assigned $\phi(x, y) = 0$.

Pile

Where the profile of the resultant pile did not consist of a straight line this posed problems for direct bicubic interpolation. Where $\phi(x, y)$ has not been calculated it is assumed that the packing density is zero there, as shown by the initial gridded values represented by + signs in Figure 5.12.

The bicubic algorithms use of derivatives means that the smoothing is too intense at the boundary, resulting in a jagged edge and implying that $\phi(x, y) = 0$ for selected points within the boundary. To tackle this the interpolation is performed in two steps. Initially the resolution is doubled with bicubic interpolation performed everywhere onto a grid with regular spaces of 1.2 mm in both directions. Interpolated values near the boundary are then re-evaluated against the profile achieved from the 2D cross section with the following conditions:

- If the grid point (x, y) is above the boundary, then $\phi(x, y) = 0$
- If the grid point (x, y) is below the boundary, then $\phi(x, y)$ is linearly interpolated using nearby *raw* data

An example of how this is applied to the boundary is shown in Figure 5.12. This method prevents approximated derivatives becoming too large near the boundary, and hence over-smoothing by the bicubic algorithm.

A second pass of the bicubic algorithm at a resolution of 0.05mm grid points then results in a smoother boundary than a singular application of interpolation. This data is then trimmed using the calculated profile of the pile, with all points above the boundary assigned $\phi(x, y) = 0$.

5.8 Results

5.8.1 Repeatability

The results displayed are for a particular column packing and the resultant deposit from that particular preparation. It is impossible to repeat a particular column packing in a practical sense, even with precisely the same granules, and so the end deposit is unique to the column that was prepared. In particular the resultant deposit is likely to be sensitive to the initial packing density distribution. It is

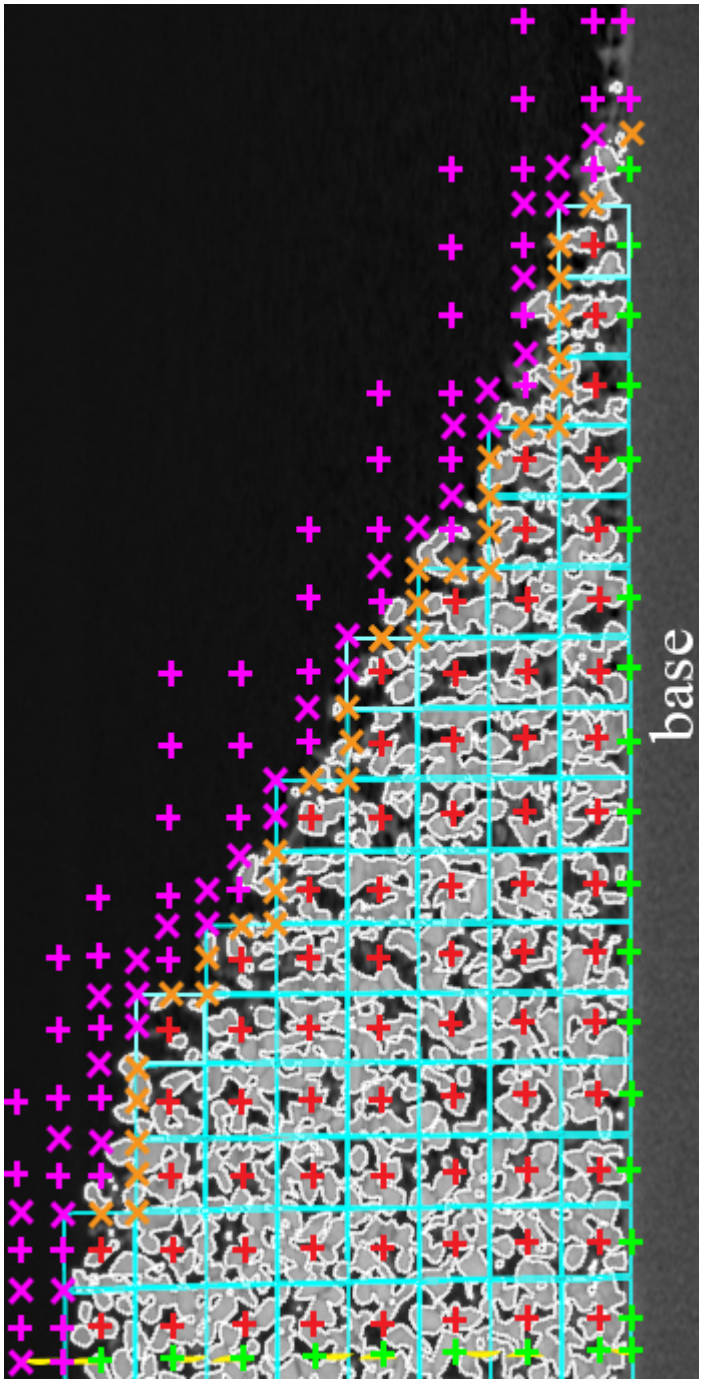

Figure 5.12: Arrangement of gridded data in column during bicubic interpolation. Yellow line indicates the centre and aqua represents ROIs. Red pluses indicate the raw data achieved from ROIs. Green pluses indicate points where nearest neighbour interpolation has been applied. Pink pluses indicate points where $\phi(x, y) = 0$. Then bicubic interpolation is applied for the first time. Then boundary values are modified with orange crosses indicating linear interpolation and pink crosses indicate $\phi(x, y) = 0$. Bicubic interpolation is then applied a second time.

a	pre/post	μ	σ^2	median	LQ	UQ	IQ range
0.72	pre	0.4930	0.0009	0.4925	0.4741	0.5109	0.0368
	post	0.5677	0.0315	0.6300	0.4573	0.7036	0.2463
1.20	pre	0.5013	0.0123	0.4901	0.4297	0.5693	0.1396
	post	0.7063	0.0342	0.7289	0.5960	0.8637	0.2677
1.70	pre	0.5755	0.0117	0.5643	0.5015	0.6074	0.1059
	post	0.5019	0.0397	0.5083	0.3520	0.6692	0.3172
2.04	pre	0.4842	0.0144	0.4915	0.3980	0.5439	0.1459
	post	0.4905	0.0516	0.4573	0.3055	0.6919	0.3864

Table 5.5: Measurement data for the four collapses trialled as outlined in Table 5.1.

shown in the following results that the method of preparation of the column results in similar initial packing density distributions. In this sense the global result will hold true for a similarly prepared column, with the spread of packing density post collapse displaying the same characteristics although the precise packing density at a particular point in space will vary.

5.8.2 Density attribution to volume

Shown in Figures 5.13, 5.14, 5.15 and 5.16 are the $\phi(x, y)$ distributions within the initial column and resultant pile for $a = 0.72$, $a = 1.20$, $a = 1.70$ and $a = 2.04$ respectively.

Each distribution has its own 'density signature' indicating the frequency of occurrence of each packing density value within the column or pile. Noting that the pile is a 3D construct as opposed to the 2D view shown, each point is assigned a weighting dependent upon the volume it represents. Given that every internal point is equally spaced by 0.05 mm, it represents a volume

$$V = \pi h(r_{outer}^2 - r_{inner}^2) \Rightarrow \tag{5.3}$$

$$V_{\text{internal}} = 0.05\pi([r + 0.025]^2 - [r - 0.025]^2) \tag{5.4}$$

$$V_{\text{base}} = 0.025\pi([r + 0.025]^2 - [r - 0.025]^2) \tag{5.5}$$

$$V_{\text{centre}} = 0.05\pi(0 + 0.025^2) \tag{5.6}$$

$$V_{\text{wall}} = 0.05\pi(r^2 - [r - 0.025]^2) \tag{5.7}$$

The base/centre join and base/wall join points have V_{centre} and V_{wall} with the exception that $h = 0.025$. ϕ groups were of size 0.001 for evalutation of the frequency density of packing fraction. The signature was normalised against the total volume with comparison of initial state and resultant pile signatures in Figures 5.13, 5.14, 5.15 and 5.16 (c) for $a = 0.72$, $a = 1.20$, $a = 1.70$ and $a = 2.04$ respectively.

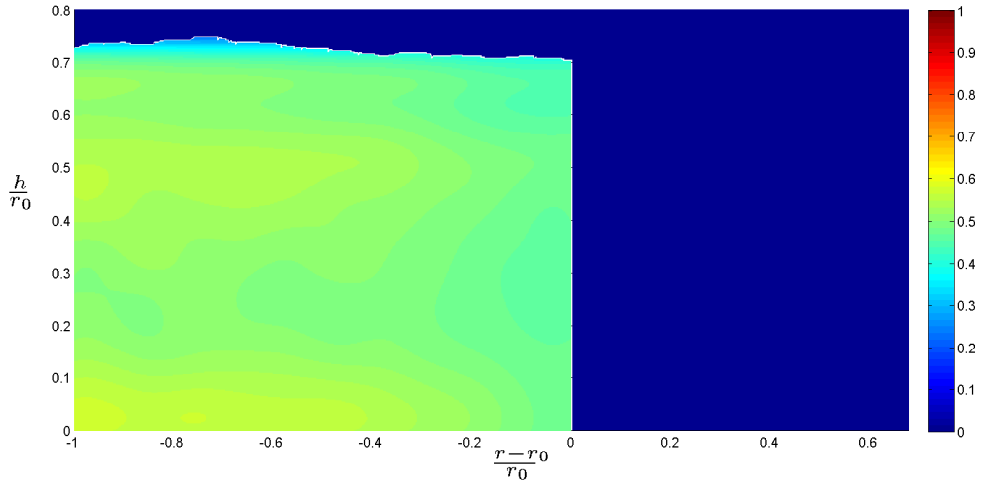

(a)

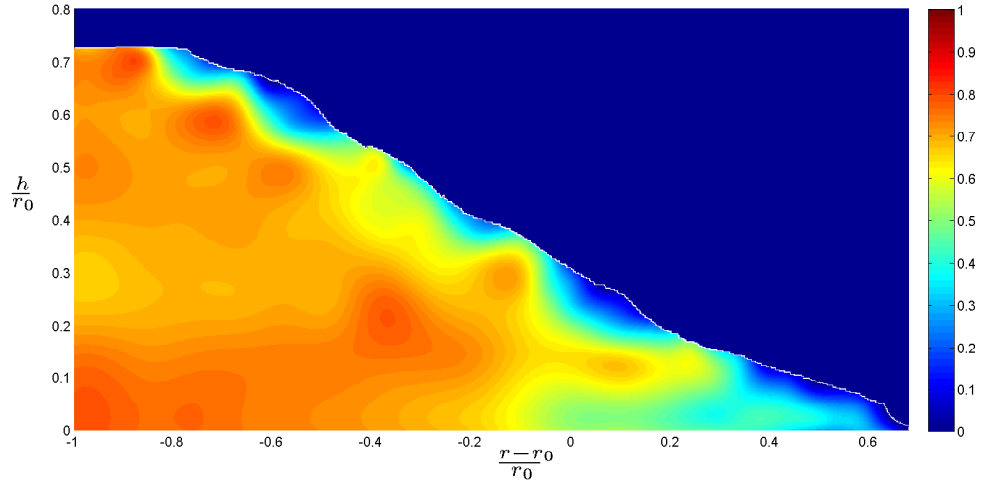

(b)

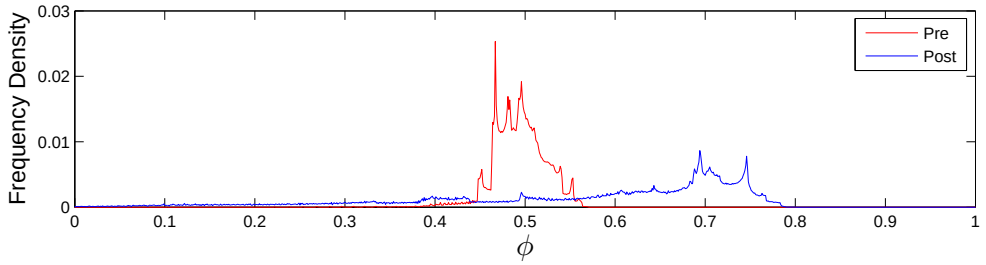

(c)

Figure 5.13: Density distribution $\phi(x, y)$ (interpolated) for $a = 0.72$. (a) Column. (b) Pile post collapse. (c) Density Signature.

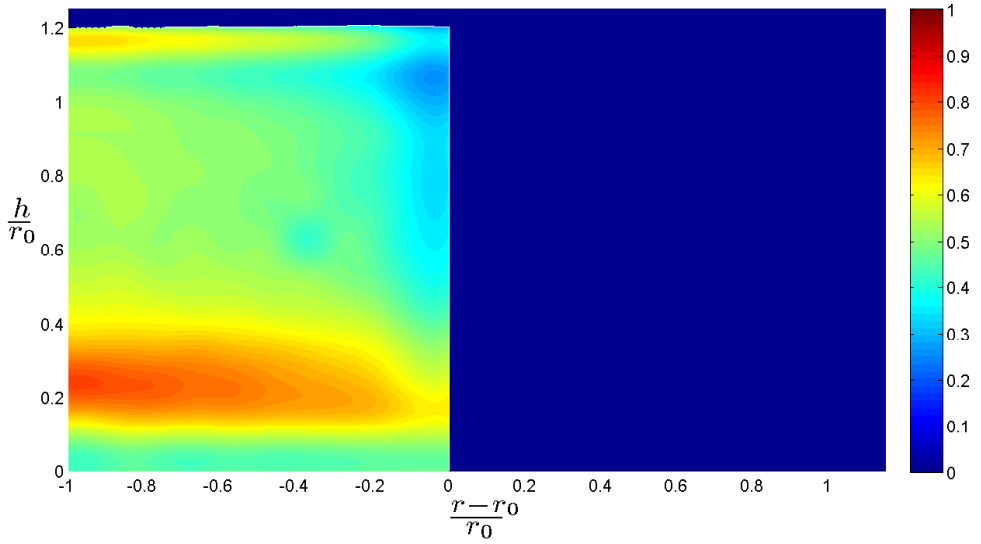

(a)

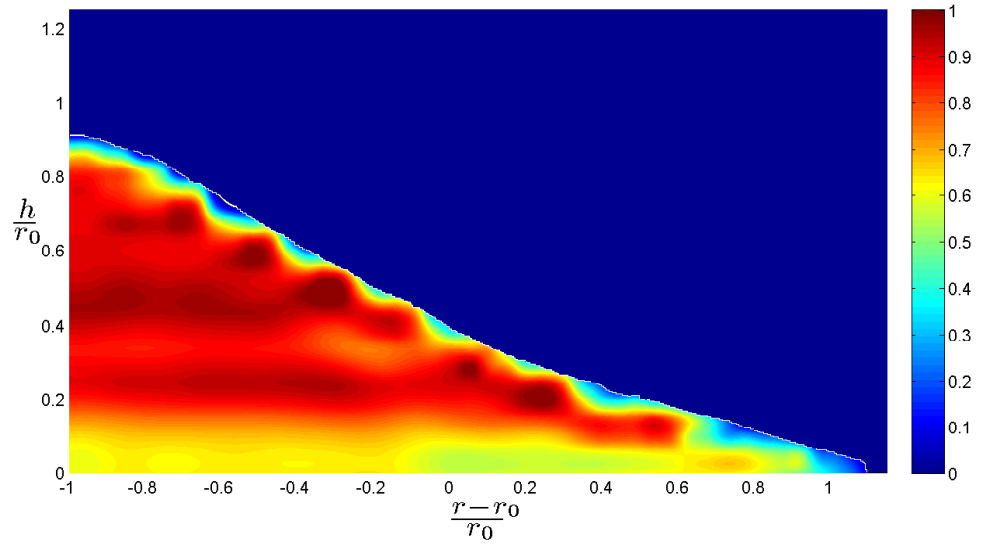

(b)

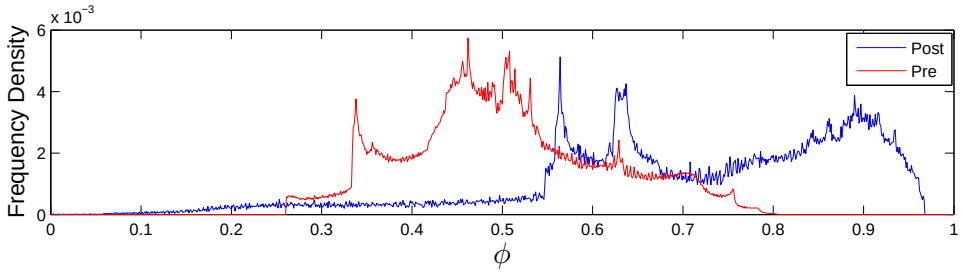

(c)

Figure 5.14: Density distribution $\phi(x, y)$ (interpolated) for $a = 1.20$. (a) Column. (b) Pile post collapse. (c) Density Signature.

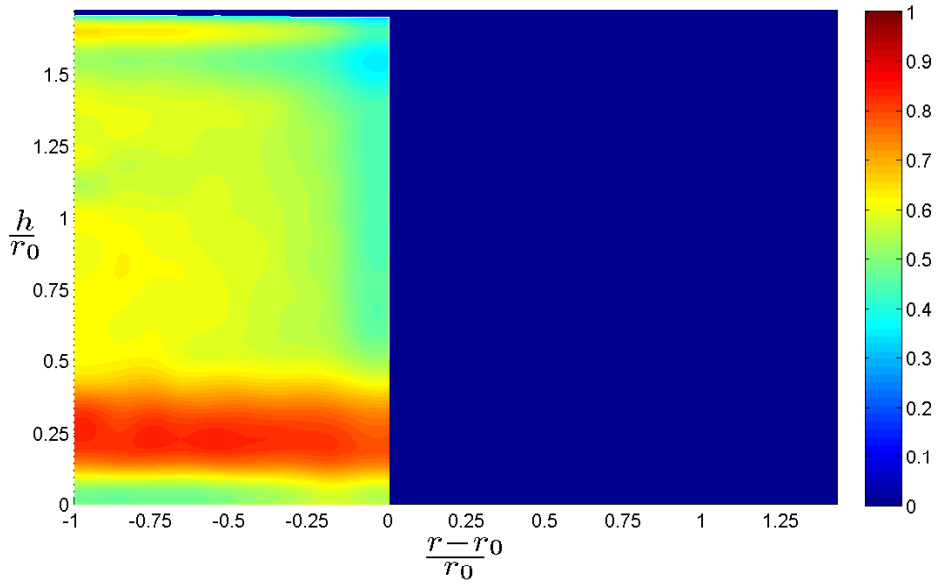

(a)

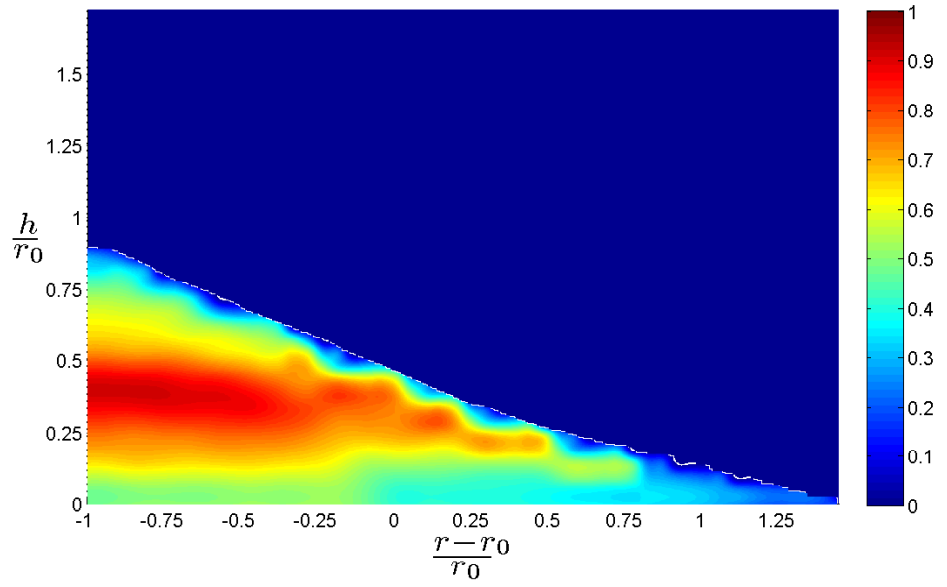

(b)

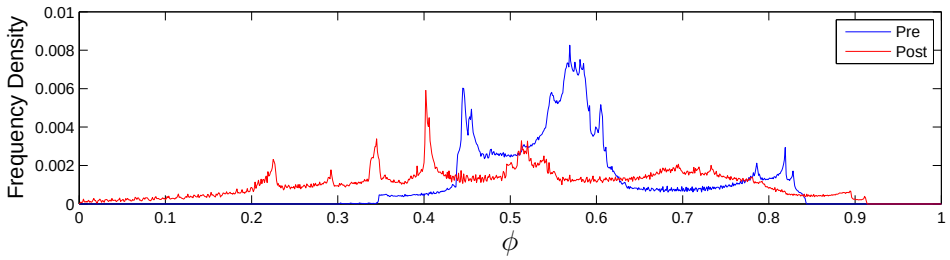

(c)

Figure 5.15: Density distribution $\phi(x, y)$ (interpolated) for $a = 1.70$. (a) Column. (b) Pile post collapse. (c) Density Signature.

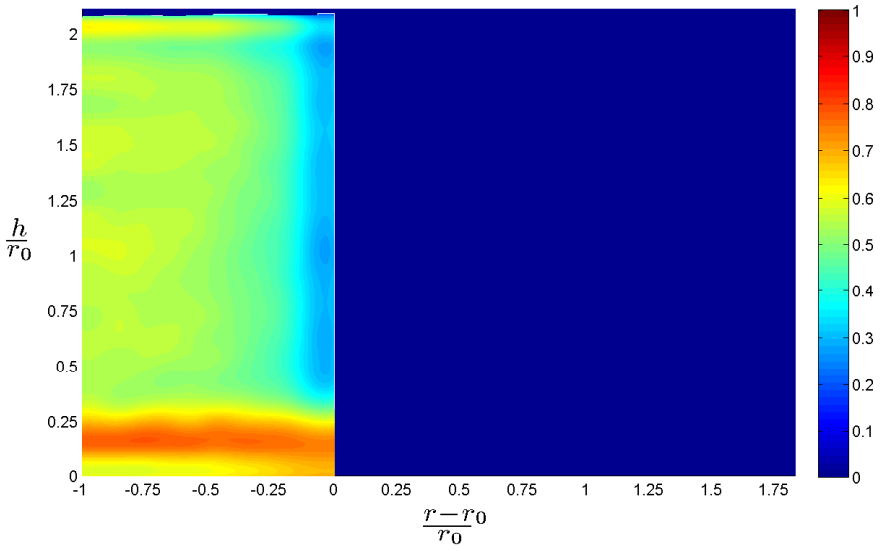

(a)

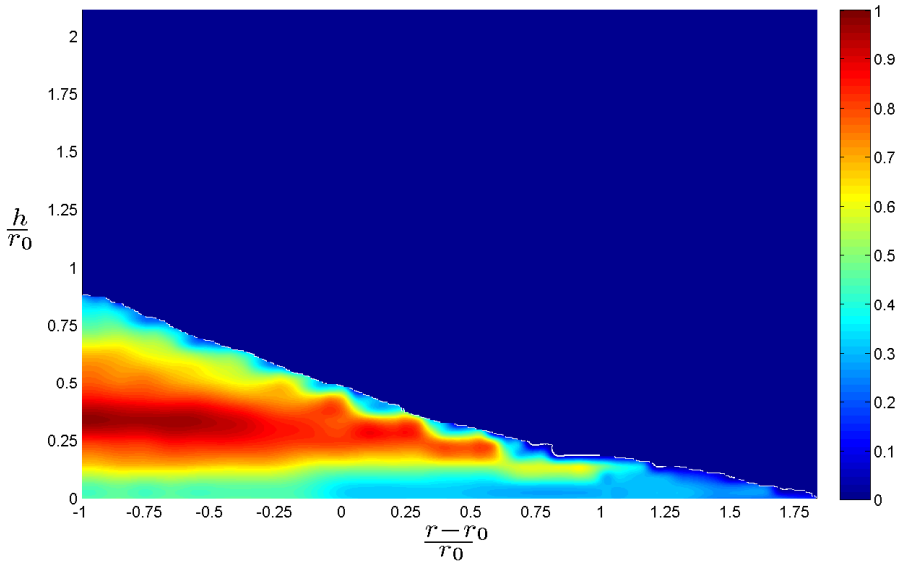

(b)

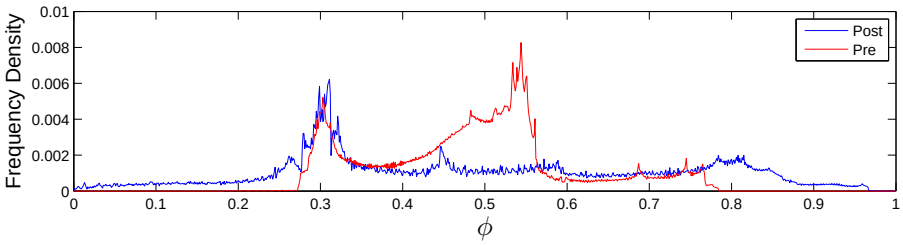

(c)

Figure 5.16: Density distribution $\phi(x, y)$ (interpolated) for $a = 2.04$. (a) Column. (b) Pile post collapse. (c) Density Signature.

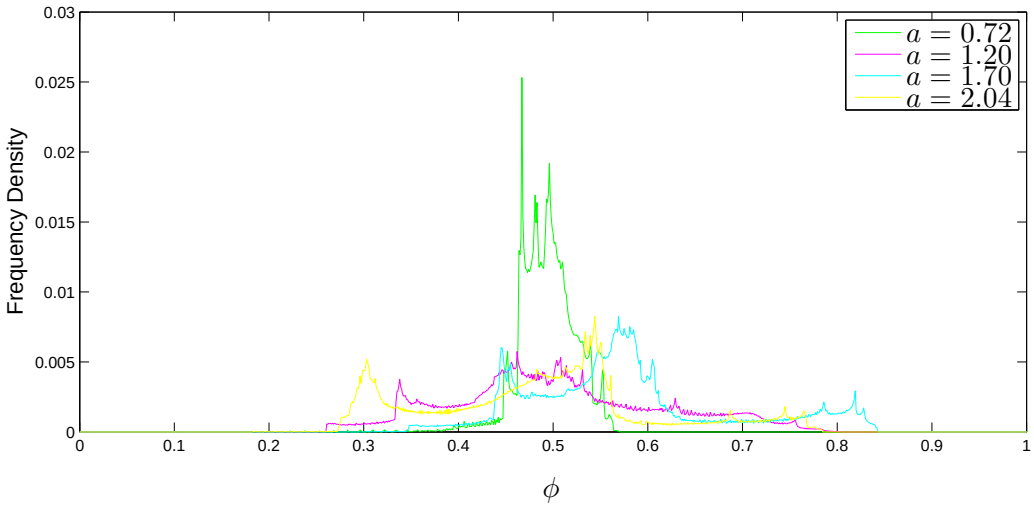

Figure 5.17: Density signatures of the initial columns.

Statistical evaluation of the density spread over the 3D volume is given in Table 5.5. Two averages of packing densities are considered; the mean μ which is arithmetic average of all values and the median which is the middle occuring value out of all packing data points. The lower quartile, LQ, is the packing value at which 25% of all packing data points are below and the upper quartile, UQ, is the packing value at which 75% of all packing data points are below. Similarly two measures of spread are considered; the variance which is a measure of the distance from the mean and the interquartile range which is the difference between the upper quartile and lower quartile. The interquartile range provides the width of range of the middle 50% of occuring packing data points.

5.8.3 Initial packing

A comparison of the density signatures of the initial columns are shown in Figure 5.17. Aspect ratio $a = 0.72$ demonstrates a significantly smaller spread of ϕ (calculated interquartile range is less than a third of other columns) and lower upper quartile compared to other columns. This is attributed to the relatively smaller height. The other columns are similar in spread and signature demonstrated by their quartiles and interquartile range. Despite $a = 0.72$ having presented these statistical differences, the mean and median is extremely similar across all columns. The similarity provides confidence to the repeatability of the packing method employed across all experiments in the thesis.

Across Figures 5.13, 5.14, 5.15 and 5.16 (a) it is observed that the columns can be split into four characteristic density regions; near wall, near base, summit and central (these areas can be found at (0,1), (-0.5,0.3), (-0.5,1.6) and (-0.75,1.0)

respectively in Figure 5.15 (a)). These are only marginally apparent in the case $a = 0.72$ due to the small spread.

Near the wall there is a less dense region approximately $0.15r_0 = 3.75\text{mm} \approx 5d$ thick which is well known to occur and simply referred to as the *'wall effect'*. Near the base a dense banding occurs that extends to the wall, interrupting the previously discussed effect. The band moves closer to the base with increasing aspect ratio, and while the thickness of this band is similar for $a = 1.20, 1.70$ it is thinner in the case of $a = 2.04$. At the summit there is a thin band of higher density resulting from the 'gentle' flattening of the top prior to removal of the column.

The central region, while largely transitional of the three previously described regions, displays some noticeable banding of higher density regions with the number of regions increasing as the height of the column increases; in the case of $a = 0.72, 1.20$ there is only one band, two where $a = 1.70$ and four where $a = 2.04$. This is likely to be due to a 'wave-like' effect of compacting media under the gentle flattening of the summit of the column.

While columns displaying similar features indicates a well repeated filling method the density variations within a single column are not as uniform one might have initially thought, with these divisions likely to affect the size of the resultant pile. If variations exist in the packing method between studies then it reasons why different proportional constants are often found when investigating axisymmetric collapse, for example between Lube et al. [2004] and Lajeunesse et al. [2004]. This difference could further increase difficulty in relating the constants arising from non-dimensional scalings to known granular coefficients. It is suspected that this is a meso-scale effect in the vertical direction; when the system size is large enough, variations in density signatures between small and large columns will become insignificant and appear more like the column with $a = 2.04$.

5.8.4 Final deposit

There is a distinct difference in the packings of the resultant deposits between $a = 0.72, 1.20$ and $a = 1.70, 2.04$ seen in Figures 5.13-5.16 (b), attributed to the change in collapse regime; for $a < 1.70$ the periphery of the column crumbles and propagates outwards while for $a > 1.70$ the entirety of the upper surface moves with the collapse. For $a = 0.72, 1.20$ it appears that the entirety of the region that resided within the original column becomes more compact with a tail of lower packing density. Furthermore the density appears relatively uniform within its core, ignoring the surface that would have contributed to the flow and the tail. This differs from $a = 1.70, 2.04$ which displays a compact central region in the pile with the density decreasing in an outwards direction.

Considering the differences between the mean and median for the final de-

posit it is observed that the density distribution evolves from being largely negatively skewed at $a = 0.72$ to negligible skew at $a = 1.70$ and then finally a positive skew at $a = 2.04$. This means that the total volume which displays larger density values than the mean is not only decreasing, but at the known transition stage of $a = 1.70$ the deposit starts to show a large proportion of the total volume containing density values less than the mean. In general this suggests that as aspect ratio increases the higher density region within the volume is becoming more compact. This is confirmed through observation of the ϕ plots in Figures 5.13- 5.16 (c).

The spread of density values increases with aspect ratio as demonstrated by the interquartile range, with the greatest increase occurring from $a = 1.70$ to $a = 2.04$. This is attributed to the greater amount of material contributing to the avalanching stage resulting in weaker packed periphery that grows in length with aspect ratio. Evidence of this effect is strongest for $a = 2.04$ as seen in Figure 5.16 (b) with a peak at $\phi = 0.3$ observed in Figure 5.16 (c).

An interesting characteristic observed in all final deposits is a region of lower packing compared to its surroundings at the tube edge i.e. $(r - r_0)/r_0 = 0$. Notice that directly above this area is an extension of the compact region within the pile, observable in all cases. The difference in packing in this region becomes more pronounced with higher aspect ratio. The reasoning for its occurrence is unknown and would require further investigation.

5.8.5 Initial and final state comparison

From the initial column to the resultant pile the spread of the density values increases as shown by the interquartile range and variance in Table 5.5 and respective density signatures in Figures 5.13 - 5.16 (c). The increase in the interquartile range from the initial column to the resultant pile becomes larger from $a = 1.20$ to 2.04. The largest increase is apparent in $a = 0.72$ but is caused by the suprisingly small spread of densities in the initial column. The upper quartile also increases in all cases, with the largest increases seen for $a = 0.72, 1.20$. The smallest increase in the upper quartile is seen for $a = 1.70$ but can be attributed to the higher median in the initial column compared to others.

Evaluation of the average density of the pile is provided by consideration of the mean and median. Both measures indicate that the average density increases from the initial column to the resultant pile for $a = 0.72, 1.20$, while it decreases for $a = 1.70$. There is little change observed in the mean for $a = 2.04$. The influence of skew of the data can be removed by considering the median which shows an increase for $a = 0.72, 1.20$ but this time a decrease in both $a = 1.70, 2.04$. This reasons when the different compaction of the piles are quantified and compared between the groups of aspect ratios.

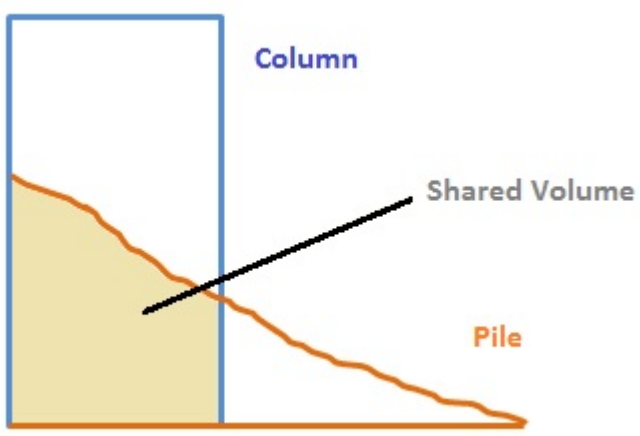

Figure 5.18: Illustration of the definition of the shared volume occupied by both the initial column and resultant pile

The shared volume between the initial column and resultant pile, as illustrated in Figure 5.18, provides a different route of comparison. The change in packing fraction between the column and pile in this region, calculated as $\Delta\phi = \phi_{pile} - -\phi_{column}$, is shown for all aspect ratios in Figure 5.19 and can physically be observed to be true by comparing relevant Figures 5.3– C.7. These graphs display the most exciting result of this study - that infact there is a non-negligible movement of grains within the failure envelope causing significant changes in density. What's more, the progression of the system is clear from one regime to the next, displaying different attributes.

In Figures 5.19 (a) and (b) there is a definite compaction of the granular media under the surface of the flowing region. With $\max(\Delta\phi) = 0.28$ and $\max(\Delta\phi) = 0.46$ in $a = 0.72$ and $a = 1.20$ respectively, the result is beyond any reasonable experimental error and can clearly be seen by comparison of the XCT images. This means that there is movement within the failure envelope assumed to be static by Lube et al. [2004]; Lajeunesse et al. [2004]. The degree of compaction through to the core is somewhat suprising in the case of $a = 0.72$ with the resultant shape being a truncated cone. This is an illustration of the impact of granular force chain networks and its complexity. This revelation does not discount the existence of the failure envelope, but insists that it must interact with the evidently fickle granular contacts and overall stability of the pile.

While the surface of the pile of the two aspect ratios present looser regions than in the column as one would expect, there is no decrease in packing density within the core of the pile. Beyond a truncated cone case to $a = 1.20$ shown in Figure 5.19 (b), we find that material avalanching over the entire surface as opposed to more of a 'fracture' situation results in far greater compaction towards the top

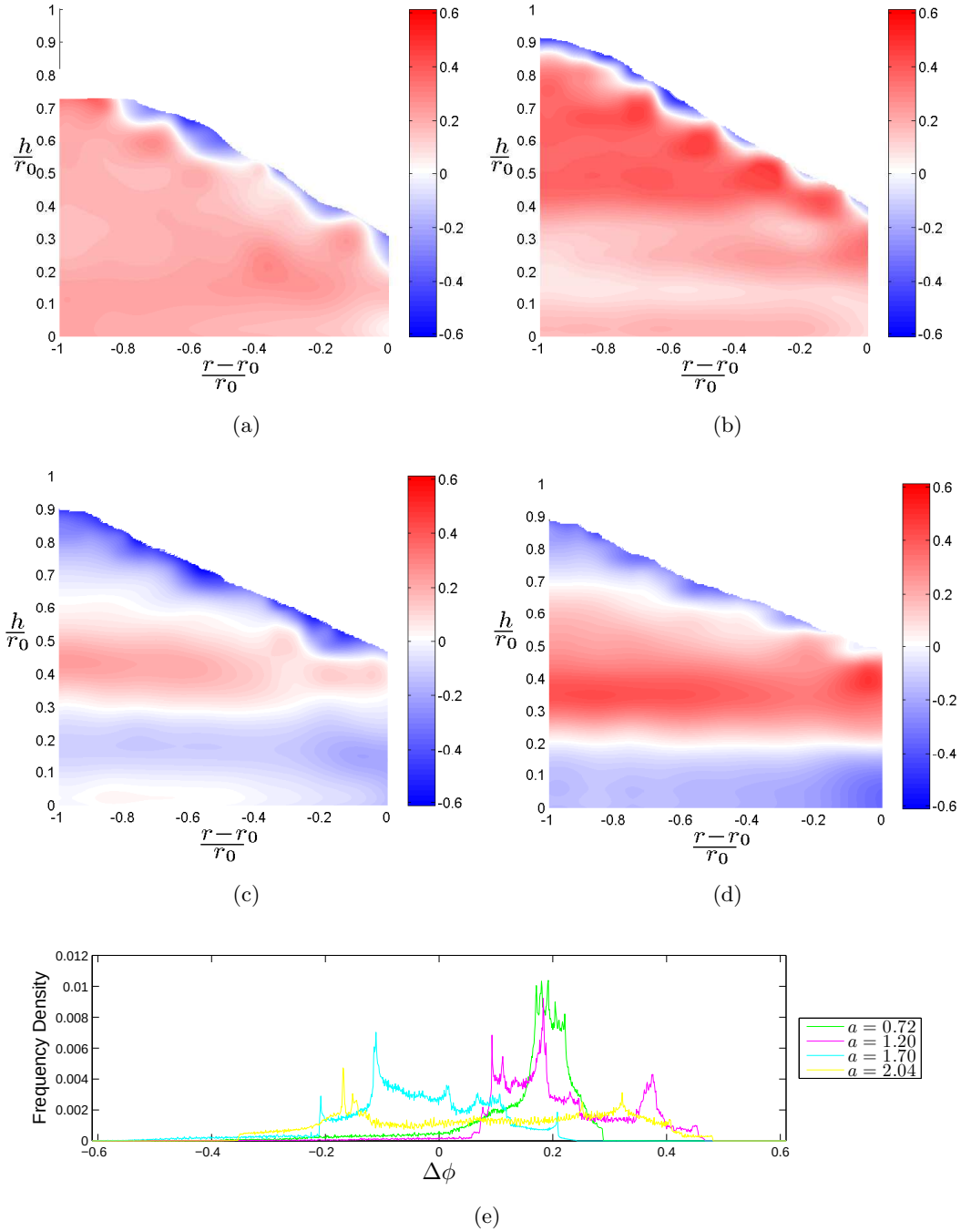

Figure 5.19: Change in packing between column and pile within shared volume. (a) $a = 0.72$ (b) $a = 1.20$ (c) $a = 1.70$ (d) $a = 2.04$ (e) Packing signatures.

of the resultant pile. Interestingly this has a limit, since in lower regions of the pile there is evidently little change in density with some areas as low as $\Delta\phi = 0.05$. This area coincides with the dense band in the lower region of the initially prepared column as can be seen in Figure 5.14 (a) which could be a contributing factor.

Moving to $a = 1.70, 2.04$ there is an entirely different distribution of $\Delta\phi$ resulting from the regime change. Recall that for $a > 1.70$ the entirety of the upper surface moves with the collapse as opposed to pure crumbling at the periphery, evidently having a significant impact. Instead of the entirety of the shared volume increasing in density, a thick band of increased density appears with a decrease in packing above and below it. Moreover this band becomes greater in size and displays a greater increase in density from $a = 1.70$ to $a = 2.04$. In the initial packings shown in Figures 5.15 and 5.16 (b) there is a denser region centred around $h/r_0 = 0.25, 0.15$ for $a = 1.70, 2.04$ respectively which is just below the band of increased density in the comparison. It appears that this comparably denser region provides a floor for material above to compact upon as the avalanching occurs, increasing in effect under taller columns which would impose a greater downwards force.

The fact that the shared volume can become less dense underneath this band seems counter-intuitive and has never previously been suggested or incorporated into a model. This area is not small being 7–12 particle diameters (3–4 ROIs) in height. With the greater packing above this region subject to collapsing material above it, this must force particles to spread in a radially outwards direction. It is assumed they do not move far from their original position, but far enough to significantly reduce the packing density while retaining support of the material above. Identification of individual particles from the column to the pile has not been possible with the tools available in this study, but digital volume correlation could potentially be used on the region for confirmation. This technique is reliant on the movement being small enough from column to pile to resolve between images, which may or may not be reasonable in this case.

The less dense packing above the compacted region implies movement of the material that was in its place prior to collapse. The decrease in ϕ in this region suggests the avalanching material interacts strongly with the particulate, entraining grains into the flow and depositing new material in its place. The significantly lower value of $\phi < 0.4$ in the area as can be seen in Figures 5.15,5.16 (b) supports this hypothesis.

5.9 Discussion

This study has employed a new technique to further understand the mechanics behind the collapse of an axisymmetric column. Previous understanding of the internal

characteristics have been limited to the reasonable assumption of an internally static region imposed by the angle of internal friction. Recall the angle of internal friction is the limiting angle of direct to shear stress at which failure occurs. Here a number of intricacies in the change in packing have been highlighted and discussed.

In general the existence of a *static* internal region over which the avalanche occurs has been proven false. This is not to say that the angle of internal friction does not define a failure envelope for the collapse. This is still believed to occur at least initially, but the downwards force and resultant compaction has a greater impact on the deposition of the particulate. This is a particularly dominating factor for higher aspect ratios.

A regime change is known to occur at $a \approx 1.7$ where the final runout stops increasing linearly with aspect ratio and adopts a power law. The reason for this is unknown in all previous works although Lube et al. [2004] reported observation of stationary bulges in the collapse of higher aspect ratios which dissipated as the avalanche ceased. This ties well with the observation of a compact core that reaches to the surface boundary in the resultant deposits of $a = 1.70, 2.04$ differing from the overall more uniform deposits of $a = 0.72, 1.20$.

Early theoretical models based on the approximation of Navier-Stokes equations have frequently struggled to capture the precise dynamics of column collapse for higher aspect ratios [Mangeney et al., 2000; Larrieu et al., 2006; Doyle et al., 2007] as discussed in Section 2.4 of the literature review. It was frequently found that beyond a threshold the pile over-relaxes and the runout of the pile is too large. As described above, there is a comparably compact core within the resultant pile beyond the regime transition and reasons why the model starts to diverge from the correct profile.

5.10 Acknowledgements

I would like to thank Dr John Thornby at Warwick Manufacturing Group for advice and training in the use of the CT scanner. The parameters for scanning were chosen by myself and checked by Dr John Thornby, but the reconstruction and data processing was performed entirely by myself. I would also like to thank Dan Norman at Warwick Manufacturing Group for training on relevant software.

Chapter 6

Rotating granular column collapse

6.1 Introduction

Dynamic granular flows with induced movement from a mechanical source can provide a useful method for the transport of granular material. An example of such a situation is the distribution of fertilisers and seeds achieved by a continuous injection of granular material via a hopper, which falls onto a centrifuging disk of a prescribed frequency to ensure the even spreading of the material. This has been a recent subject of investigation, both experimentally and computationally [Borovikov et al., 2002; Rioual et al., 2007; Shinbrot et al., 2007; Liedekerke et al., 2009].

Discussed in this section is an extension of the column collapse investigated in Chapter 4 by incorporating rotation of the plane upon which it falls, providing a variation of the setup described above. The aim is to find the effect that rotational frequency has on the scaling laws extracted from the stationary collapse in Chapter 4 (similarly recognised by Lube et al. [2004] and Lajeunesse et al. [2004]), and to find the onset and degree of granular spreading.

This is the first known study of such a setup, displaying similarities to experiments by Shinbrot et al. [2007] investigating the formation of sand piles achieved by a hopper dispensing onto a continuously rotating disk. The derived empirical relations could find future application in the testing of new granular rheologies in different flow regimes.

All raw data relating to experiments performed in this Chapter can be found in Appendix D. Results of this investigation have been published in *Powder Technology* per the reference Warnett et al. [2014b].

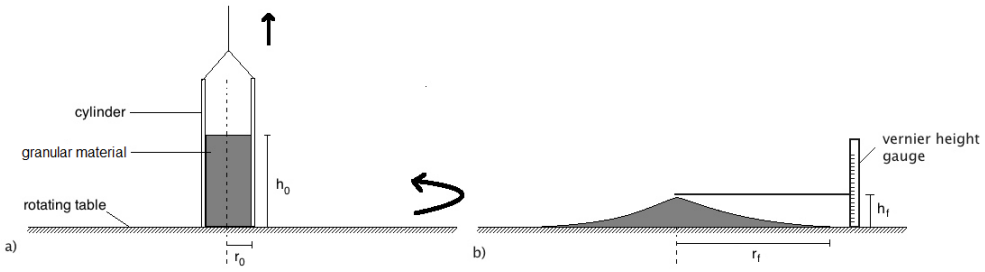

Figure 6.1: Experimental setup. a) Initial setup of granular column on rotating table. b) After collapse.

6.2 Experimental setup

6.2.1 Apparatus

The apparatus was setup as shown in Figure 6.1. The table from the previous experiments sat on a rotating turntable that was calibrated for concentricity as described in Section 3.2.4. This was placed inside the same housing described in Chapter 4 and outlined in Appendix A which consisted of a pulley system to remove the cylinder. A cylinder of radius r_0 was aligned centrally on a rotating turntable as described in Section 3.2.4 and filled with granular material to a specified height h_0. The table was then set into rotation at a frequency f, and the column of material allowed to enter solid body rotation. The cylinder was then quickly removed vertically and the granular material allowed to collapse. The rotational frequency of the turntable had been calibrated as described in Section 3.2.5

Cylinders of inner radius $r_0 = 20\,\text{mm}$, $25\,\text{mm}$, $30\,\text{mm}$, $36\,\text{mm}$ were used. For each cylinder radius, the initial height of the column of granular material, h_0, and frequency, f, were varied systematically. Recall the aspect ratio of the initial column is defined by $a = h_0/r_0$, determined by the initial mass of granular material m_0. The aspect ratio was varied in the range 0.28–1.75, and frequency in the range 0.0–1.7Hz.

The granular particulate remained the same as previous experiments as described in Section 3.4. The initial column was prepared by funnelling the granular material into the cylinder, and the top was flattened to ensure uniformity, accurate to $\pm 1\,\text{mm}$. The method of preparation was repeatable as seen in XCT studies in Chapter 5 with a mean packing density, $\phi = m_0/(\pi r_0^2 h_0 \rho)$, between 0.78 and 0.82 across all prepared columns.

6.2.2 Measurement and accuracy

Time evolution of the resultant flow was studied by recording the collapse within the rotating frame of reference using a high speed digital camera fixed to the spinning

table with a frame rate of 240 fps. This enabled data capture of the radial runout as a function of time, $r(t)$, and was also used to determine the collapse duration, t_f. Interpreting the video with image processing software *'ImageJ'* allowed a spatial resolution of 0.5mm when recording radial values. The resultant accuracy was of the order $\pm 3\,\text{mm}$ due to the uneven periphery observed, increasing to $\pm 5\,\text{mm}$ for the higher frequencies.

After the collapse occurs several quantities were measured from the resultant deposit. The final pile radius, r_f, was recorded using a calibration sheet fixed to the surface with radial markings of 10mm in conjunction with a horizontal vernier scale accurate to $\pm 0.2\,\text{mm}$. The final height, h_f, was recorded with similar accuracy using a vernier height gauge. In the case where granular material was lost from the main pile and thrown to the edge of the tank the final mass of the resultant pile, m_f, was recorded by sweeping up the granular material, but resulted in some particles being lost in transit. The method was trialled with known masses of granular material, and was found to be accurate to $\pm 1.5\,\text{g}$.

A known source of error in recording the final pile radius r_f is the uneven periphery. Experiments in Chapter 4 have shown that in the case of no rotation this is approximately 3–4 particle diameters for the range of aspect ratios trialled, with the effect becoming more pronounced for increased values of rotation observed to reach 6–7 particle diameters. This uncertainty was considered during repeatability testing performed across various aspect ratios and frequencies as can be found in Appendix D. If was found that r_f, h_f and m_f varied by $\pm 3.0\,\text{mm}$, $\pm 1.0\,\text{mm}$ and $\pm 2.0\,\text{g}$ respectively.

6.3 Collapse dynamics

6.3.1 Flow description

The collapse in the non-rotating case is well reported by previous authors Lube et al. [2004]; Lajeunesse et al. [2004] as discussed in Section 2.1.1. It begins with the periphery of the column starting to crumble and avalanche. This causes a frontal flow to develop at the foot of the column, which propagates radially outwards eventually defining the final pile radius. Simultaneously there is a discontinuity that separates the frontal flow and the cental static summittal region, which propagates inwards and is eventually consumed by the avalanche. The propogation of the discontunity may continue for a proportionally short phase after the column has ceased to spread, acting only to alter the profile of the deposit which can only sustain material at an angle less than the angle of repose. With the introduction of rotation a second set of dynamics envelopes as can be seen in Figure 6.2.

The avalanching begins in the same way as described above but the rotation

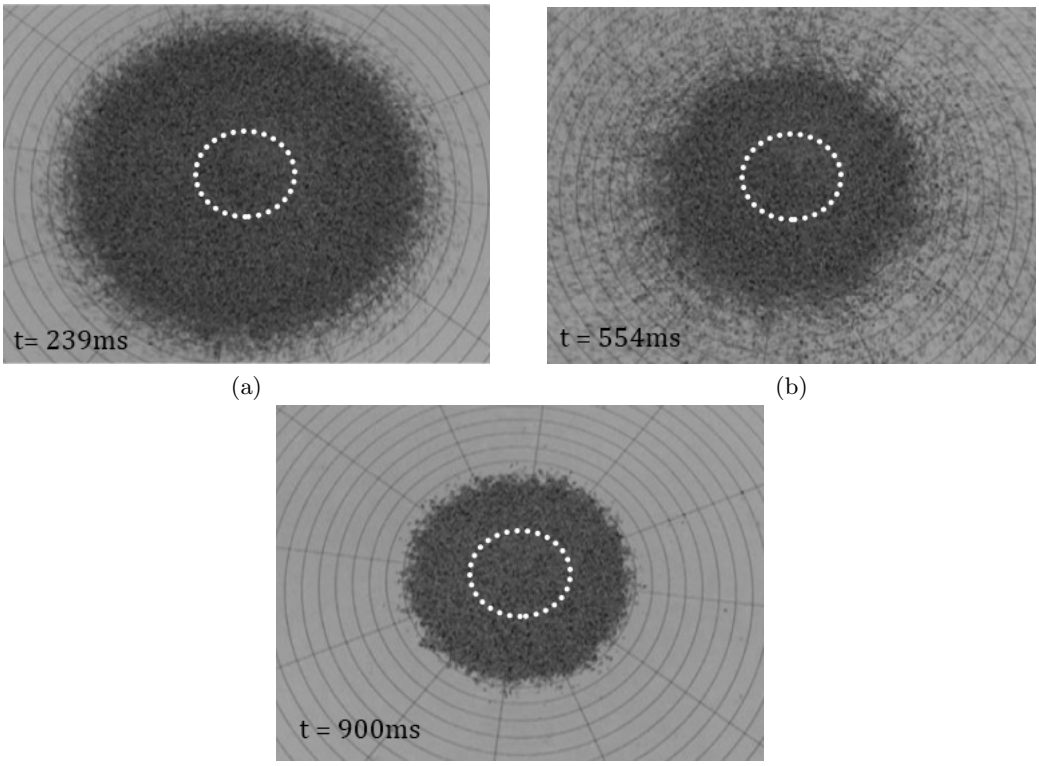

(a) (b)

(c)

Figure 6.2: Collapse of column with $r_0 = 3.6$cm, $a = 1.38$, $f = 1.41$Hz where material leaves the main pile. The white outline marks the initial position of the cylinder. a) Runout of the pile at its maximum. b) Material is leaving the main pile and being thrown to the edge of the tank. c) The final deposit left where no more material is drawn from the main pile.

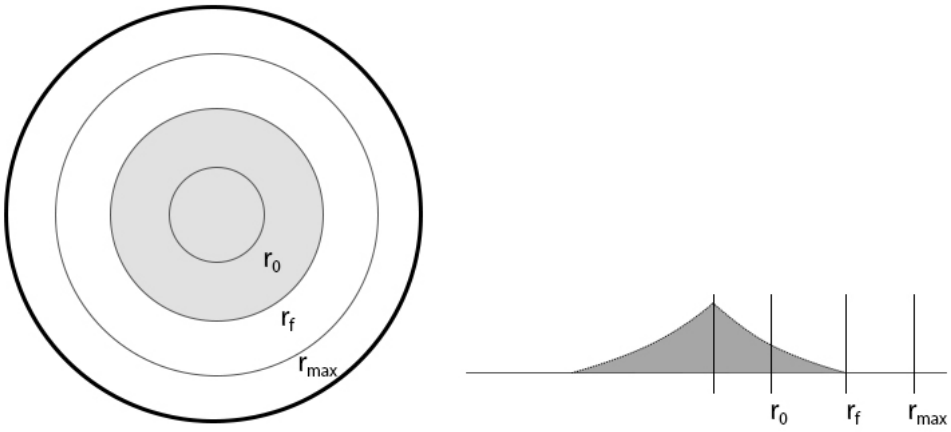

(a) (b)

Figure 6.3: Measured radial quantities of the rotational collapse showing the initial cylinder radius r_0, the maximal radius $r_{\max}$, and where a critical radius r_{crit} has been passed the final pile radius retracts to r_f. Grey marks the resting place of granular material when all movement has ceased. a) Top view. b) Side view.

of the table actuates a non-zero azimuthal component of the front flow at the foot of the pile as can be seen in Figure 6.2. The photos in Figure 6.2 are taken from the camera mounted on the tank rotating in an anticlockwise (azimuthal) direction. It is observed that the particulate moves in a positive azimuthal direction within the rotating frame of reference while flowing radially outwards, resulting in curvature of the runout. Rotation induces higher avalanche front speeds than in the non-rotating collapse, causing greater radial spread of granular material and results in a faster propagation rate of the discontinuity between central static and avalanching regions. The result is a greater final deposit radius, r_f, up to a given frequency f_{crit}. It appears that as the frequency increases, the discontinuity disappears before the spreading phase is over in contrast to the stationary collapse. It is difficult to pinpoint where this occurs given that this profile altering stage was extremely short, even in the stationary collapse, but it was observed that after the discontinuity disappears the avalanching flow continues to feed the front until the spreading ceases.

Where f_{crit} is passed for a particular cylinder size and aspect ratio there is a secondary rotation-induced spreading phase as described by Figure 6.3. The first stage of the collapse results in the pile spreading to a radius $r_{\max}$. If $f < f_{\text{crit}}$ then this radius is exactly r_f. If $f > f_{\text{crit}}$ then some material at the edge of the pile is lost and moves to the edge of the table. This rotation-induced spreading phase results in a retraction of the radius of the resultant pile to a value r_{crit} where the process of material ejection ceases and the radius stagnates. This is then the final pile radius r_f. The reason for this is that the centripetal force is great enough to overcome frictional effects felt by the particles at a specific radius, allowing the continued motion of granular material that overstretch the critical radius. Quantification of this dynamic is given in Section 6.6.1.

Where the secondary rotation-induced spreading phase causes mass ejection occurs the resultant boundary is significantly more uneven than in the stationary collapse, with the waviness shown in Figure 6.4. It could be argued that the patterning is somewhat respresentative of the channels and droplets observed by Shinbrot et al. [2007] but are less defined due to the short amount of time allowed to develop. It is certainly reminicent of the central patch that appears within the spiral patterns observed in centrifuging granular beds by Zoueshtiagh and Thomas [2000] as can be seen in Figure 2.26.

6.3.2 Deposit morphology

There are two distinct morphological deposits that result from the granular collapse dependent upon aspect ratio as discussed in Chapter 4 and shown in Figure 4.7; a truncated cone and a full conical shape. Recall the development of the full cone has been proposed to be dependent upon the internal friction angle θ_μ by Lajeunesse

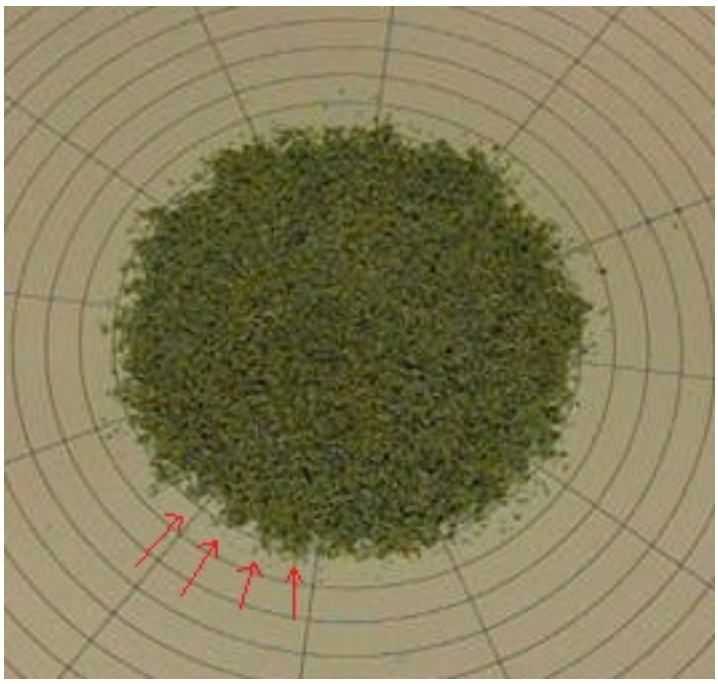

Figure 6.4: The secondary rotation-induced spreading phase results in a far greater uneven periphery of the resultant deposit. Red arrows indicate positions of example peaks seen in the periphery.

et al. [2004], where the avalanching occurs over an internal cone of radius r_0 and base angle θ_μ. In Chapter 5 it was shown that this may not entirely be true given the increase in packing within this internal region and final deposits indicating a jamming phase that would alter this envelope.

While the onset has been experimentally retrived for this particulate and setup in Chapter 4 with laser scanning, this has been repeated for the measurement method used throughout this chapter. In the case of no rotation a value of $a = 0.78$ is obtained which is in close agreement to the previous measurement of $a = 0.90$ obtained by laser scanning. With the introduction of rotation, the boundary between the frontal flow and the central static summital region propagates further inwards than in the case of no rotation. Overall this leads to the earlier appearance of the cone shape where the entirety of the summit is consumed. This is due to the effective direction of gravity being tilted by an angle

$$\tan\theta = \frac{F_r}{F_g} = \frac{(2\pi f)^2 r_0}{g} \tag{6.1}$$

arising from the ratio of centripetal force, F_r, and gravitational forces F_g. A natural non-dimensionalisation of frequency can be given

$$f_* = f\sqrt{\frac{r_0}{g}} \tag{6.2}$$

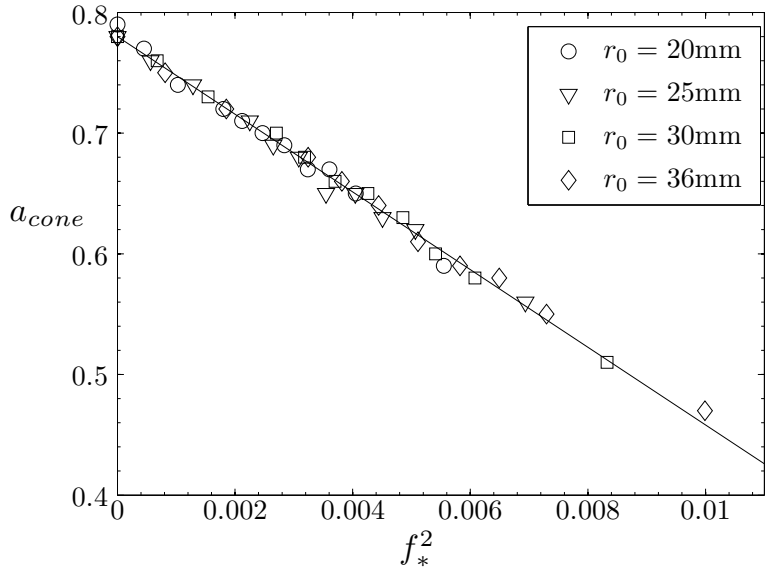

Figure 6.5: Dependence of frequency f_* on the onset of the full conical deposit shape at an aspect ratio a_{cone}. Line fit as given in equation (6.5).

hence

$$\tan\theta = (2\pi f_*)^2 \tag{6.3}$$

The onset of the cone shape is dependent on the internal angle of friction as suggested by Lube et al. [2004]; Lajeunesse et al. [2004] i.e. $a_{sec,f=0} = \tan\theta_\mu$. It is therefore expected that the onset of the full cone will approximately occur at an aspect ratio, a_{cone}:

$$a_{\text{cone}} = a_{sec,f=0} - (2\pi f_*)^2 \tag{6.4}$$

Experimentally achieved data for a_{cone} is plotted against normalised frequency f_* in Figure 6.5 revealing the relation

$$a_{\text{cone}} = 0.78 - 32.2 f_*^2 \tag{6.5}$$

in good agreement with the presented arguments.

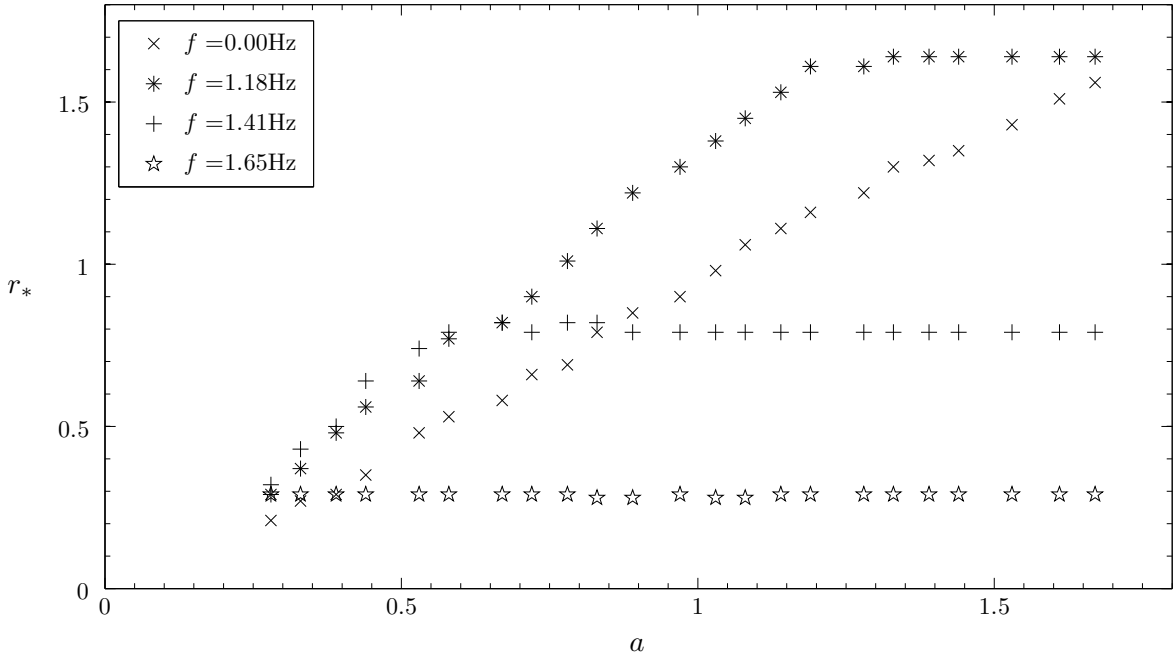

Figure 6.6: Normalised final pile radius, r_*, against aspect ratio where $r_0 = 36\,\text{mm}$ for various frequencies showing the eventual stagnation of the radius of the final deposit.

6.4 Quantitative results

6.4.1 Final radius scaling

Initially the final pile radius against aspect ratio was considered for each frequency individually. The final radius was normalised

$$r_* = \frac{r_f - r_0}{r_0} \tag{6.6}$$

as in equation 4.9. For all f the relationship between normalised final radius and aspect ratio was shown to be linear up to an aspect ratio a_{crit} as can be seen in Figure 6.6. Beyond this aspect ratio the final radius stagnates at a value r_{crit} due to the secondary rotation-induced spreading phase causing mass ejection from the main pile. This resulted in relations of the form

$$\begin{aligned} r_* &= \Lambda a & a < a_{\text{crit}} \\ r_* &= \tfrac{r_{\text{crit}} - r_0}{r_0} & a > a_{\text{crit}} \end{aligned} \tag{6.7}$$

where Λ is a frequency dependent constant. Grain size and type, inter-granular friction and surface roughness could also affect the value of Λ but has been discounted in this analysis.

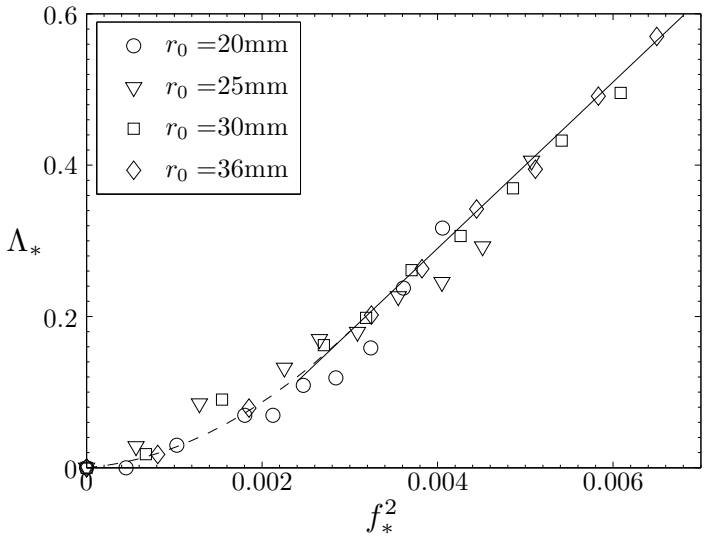

Figure 6.7: Increase in the value of Λ_* as f_*^2 varies for different cylinder sizes. Initially it follows a quadratic fit in f_*^2 shown by (- -), then when $f_*^2 > 0.0024$ the relation becomes linear in f_*^2 shown by (–) as described by Equation (6.9).

Λ is normalised as

$$\Lambda_* = \frac{\Lambda - \Lambda_0}{\Lambda_0} \tag{6.8}$$

where Λ_0 is the value of Λ for no rotation, and is compared with f_*^2 in Figure 6.7. While the gravitational forces dominate and the centrifugal force is weak, this follows a quadratic f_* order relation. Then as $f_*^2 > 0.0024$ the centrifugal forces begin to have a dominant role on the radial runout and a linear relationship develops, found to be where the centrifugal forces are approximately 10% of the gravitational force. These relations can be described

$$\begin{aligned} \Lambda_* &= 16700 f_*^4 + 10 f_*^2 \quad f_* < 0.049 \\ \Lambda_* &= 110 f_*^2 - 0.15 \qquad f_* > 0.049 \end{aligned} \tag{6.9}$$

The first of these relations for $f_* < 0.049$ is to summarize the data with no theoretical justification. The second relation is more expected due to the frequent balance of centripetal and frictional forces experienced that will give rise to an f_*^2 relation as seen in the derivation which follows.

A comparison of r_* with frequency for fixed a for $r_0 = 36\,\text{mm}$ is shown in Figure 6.8. The value of r_* steadily increases with rotation rate until the runout reaches a radius experiencing a centripetal acceleration strong enough to overcome frictional effects at a frequency f_{crit}. It is at this point where the secondary rotation-induced spreading phase starts and mass ejection begins to occur. Here it is found that r_* is inversely proportional to f^2, with all aspect ratios falling to the same line.

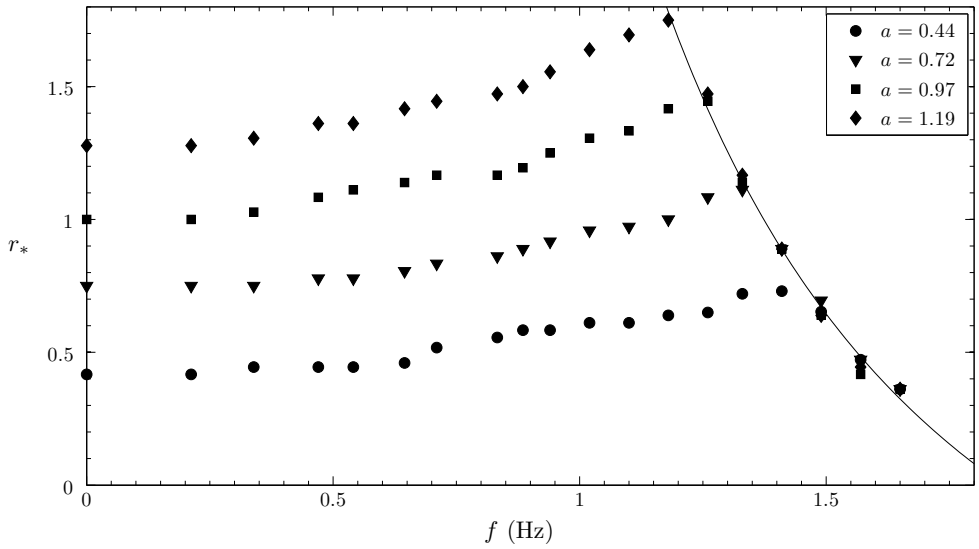

Figure 6.8: Normalised final pile radius, r_* against frequency for various aspect ratios where $r_0 = 36\,\text{mm}$. All cylinder radii followed the same dynamic, settling on the line fit shown given by equation (6.15).

By considering known values of f_{crit} for stagnating r_f and the centripetal acceleration at this radius it was found that

$$r_{\text{crit}}(2\pi f_{\text{crit}})^2 = 5.7\text{ms}^{-2} \tag{6.10}$$

as indicated by the solid line in Figure 6.8. It follows that the critical centripetal acceleration where material is lost from the main pile for this particulate and setup is $5.7\,\text{ms}^{-2}$. At this point the frictional force, $F_f = \mu mg$, and centripetal force, $F_r = mr(2\pi f)^2$, acting on a given particle are equal. By rearrangement of this equivalence the frictional coefficient between the table and granular material can be derived, giving

$$\mu = r_{\text{crit}}\frac{(2\pi f_{\text{crit}})^2}{g} \tag{6.11}$$

Using achieved values as per Figure 6.8 results in a frictional coefficient of 0.58. This was confirmed by calculating the value of friction using a slope made of Perspex as per the table and finding the angle at which the material begins to slide, and was found to be 0.57.

The aspect ratio of the secondary rotation-induced spreading onset, a_{crit}, occurs for

$$a_{\text{crit}} = \frac{r_{*,\text{crit}}}{\Lambda} \tag{6.12}$$

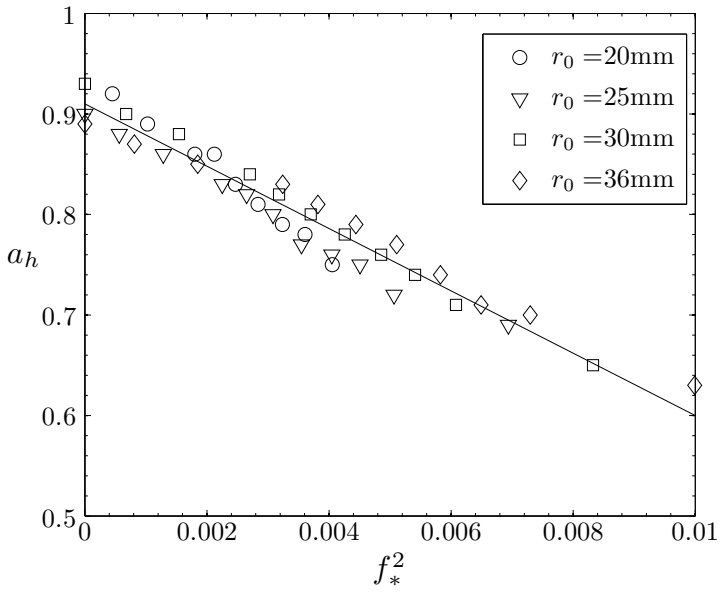

Figure 6.9: Onset of stagnating h_f at an aspect ratio a_h against normalised frequencyf_*. Line fit given by equation (6.18).

from equation (6.7) where $r_{*,\text{crit}}$ is the normalised critical radius that can be calculated from equation (6.10). Then by applying equations (6.8) and (6.9) we achieve

$$a_{\text{crit}} = \frac{r_{*,\text{crit}}}{\Lambda_0(110f_*^2 + 0.85)} \tag{6.13}$$

Equations (6.9) and (6.10) can be substituted into equation (6.7) to give a full description of the final pile radius for known a, Λ_0 and f_*. When $a < a_{\text{crit}}$ the normalised final pile radius r_* is given by

$$\begin{aligned} r_* &= a\Lambda_0(16700f_*^4 + 10f_*^2 + 1) \quad & f_* < 0.049 \\ r_* &= a\Lambda_0(110f_*^2 + 0.85) & f_* > 0.049 \end{aligned} \tag{6.14}$$

and from equations 7.7 and 7.10, when $a > a_{\text{crit}}$ the final pile radius is more simply defined

$$r_* = \frac{5.7\text{ms}^{-2}}{(2\pi f_*)^2 g} - 1 \tag{6.15}$$

6.4.2 Final Deposit Height

The evolution of the final height is similar to the non-rotating case as described in Section 4.4.2. Recall that without rotation the final height h_f is equal to the initial height h_0 while the deposit is a truncated cone. Where a full conical shape develops at an aspect ratio a_{cone}, the height almost stagnates for increasing aspect ratio, only marginally increasing in height from the first appearance of the full conical shape

as observed in Figure 4.11.

The same dynamic occurs in the rotating case, but increasing frequency causes an earlier onset of the full conical shape as shown in Figure 6.5. This then results in an earlier apparent stagnation of height at an aspect ratio a_h as shown in Figure 6.9. The height is likely to be increasing minutely as observed in laser scanning experiment performed in Chapter 4, but it is too small for the measurement accuracy of this experiment and aspect ratio range. The achieved values also appear to be independent of r_0. Following the same non-dimensionlisation as in Chapter 4, $h_* = h_f/r_0$, the result is a relation of the

$$h_* = a \quad a < a_h \tag{6.16}$$

$$h_* = a_h \quad a > a_h \tag{6.17}$$

where

$$a_h = 0.91 - 32.2 f_*^2 \tag{6.18}$$

obtained from a linear fit to data given in Figure 6.9. The earlier onset of stagnation of height with frequency is expected to follow this f_*^2 relation due to the tilt in the effective direction of gravity as discussed in Section 6.3.1.

In this case $a_{\text{cone}} \neq a_h$ as observed by Lube et al. [2004] with the height stagnation occuring slightly later, unlike in Chapter 4 where it was indicated that these coincide. This is due to the flat top becoming unobservable by eye as the limit is approached, but was significant to be captured by laser scanning. For this reason it is likely that infact $a_{\text{cone}} := a_h$.

6.4.3 Mass ejection from rotation-induced spreading

Integral to the application of the work presented is the movement of material from the main pile to the edge of the table. This occurs at the onset of the secondary rotation-induced spreading regime discussed in Section 6.3.1, shown in Section 6.4.1 to be directly related to the aspect ratio of an initial granular column exceeding a value a_{crit} for a specific frequency such that the runout exceeds a radius r_{crit}.

Fraction of mass loss, m_*, was calculated with $0 \leq m_* \leq 1$ and is plotted against a/a_{crit} in Figure 6.10. The value of r_0 does not affect the overall dynamic of the secondary rotation-induced spreading phase, but varies the onset as the runout will be different as defined by equation (6.14) in Section 6.4.1. It can be seen that this follows a logistic shaped curve with a period of acceleration, constant increase and then deceleration.

Mass ejection starts to occur minutely before the final pile radius reaches

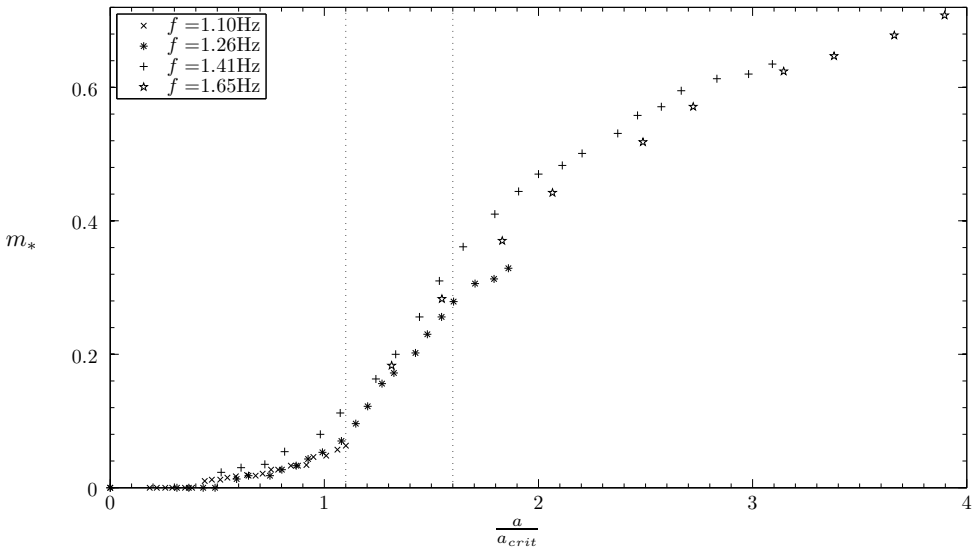

Figure 6.10: Mass loss percentage m_* against $\frac{a}{a_{\text{crit}}}$ for various frequencies where $r_0 = 36\,\text{mm}$. Dotted vertical lines indicate a change in the rate of increase of m_*, where it is constant inbetween them.

r_{crit} up to a value of $\approx 10\%$. This is seen in Figure 6.10 while $\frac{a}{a_{\text{crit}}} < 1$ where there is a period of acceleration. The mass loss can be attributed to the collapse itself causing some of the granular matter to saltate and jump from the main frontal flow and exceed the critical radius. While $1.1 < \frac{a}{a_{\text{crit}}} < 1.6$ there is a short phase of constant increase in mass loss at approximately the same rate across all frequencies. In this period the mass of the remaining pile continues to increase with height of the granular column, having not reached a saturating value where the pile is stable. Finally a deceleration stage begins where $\frac{a}{a_{\text{crit}}} > 1.6$ as the shape of the pile stagnates with any increase in aspect ratio. The additional material at the top of the granular column falls with the frontal flow that exceeds the critical radius and so is ejected from the resultant pile.

Theoretically there is no frequency at which the entirety of the mass spreads as the critcal radius can never be zero since equation (6.10) implies $f_{\text{crit}} = \infty$ for $r_{\text{crit}} = 0$. If you account that the average grain diameter is 700 microns and never sits centrally then every grain will be ejected from the centre at a frequency of approximately 13.5 Hz. It is expected that this would infact be lower, but was unable to be investigated due to the maximum rotation rate of the equipment.

6.4.4 Time evolution

Examples of the evolution of the runout of the pile recorded with the 240fps camera are given in Figure 6.11 where $a = 0.61, 1.03$ for $r_0 = 36\,\text{mm}$. Measurements were

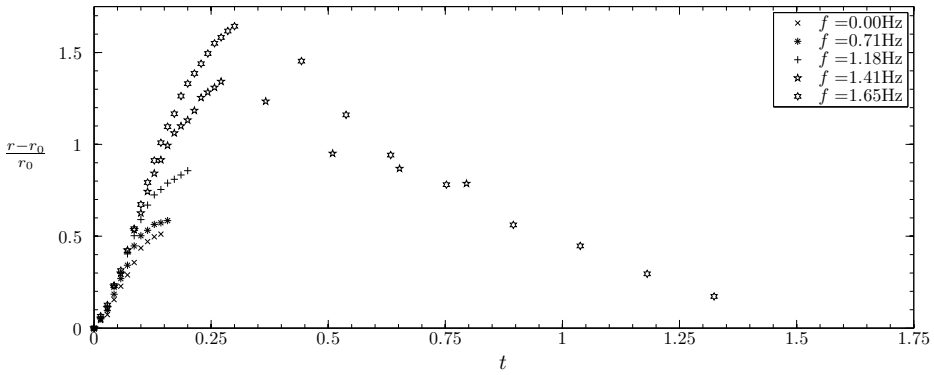

(a)

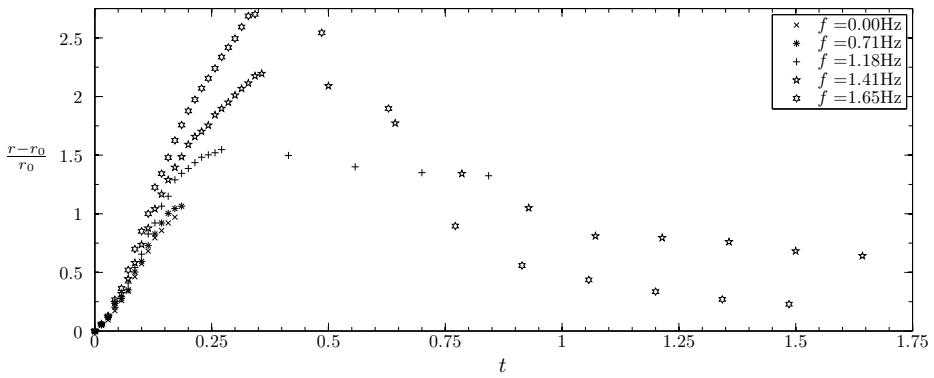

(b)

Figure 6.11: Evolution of the runout of granular matter for $r_0 = 36\,\mathrm{mm}$ a) a =0.61. b) a =1.03.

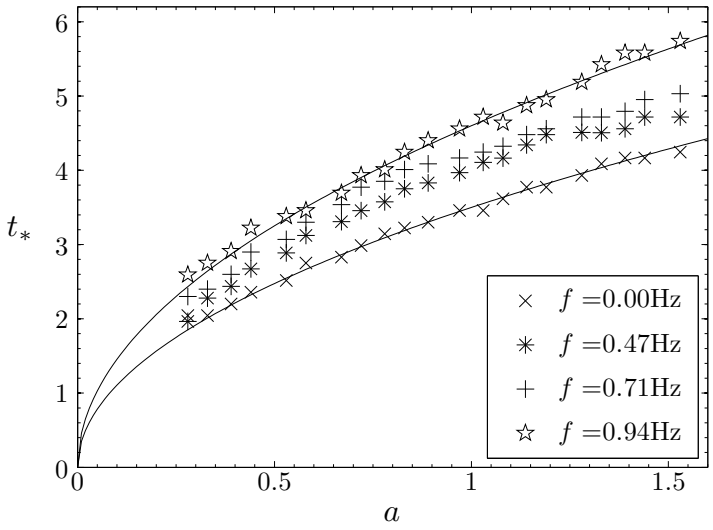

Figure 6.12: Normalised total time for collapse against aspect ratio for $r_0 = 36\,\text{mm}$. Each series follows a $\sqrt{a}$ relation as given in equation (6.20).

made using an alignment grid on the table marked every 10mm, and a pixel ruler in a photo editing package. Where the rotation is large enough such that the spreading of the granular pile exceed a radial value r_{crit}, as defined by equation (6.10), the pile achieves a maximal radius $r_{\max}$ at a time $t_{\max}$. After this time a period of volume loss occurs where the radius contracts, settling at a final value $r_f = r_{\text{crit}}$. Where material loss occurs the radius of the runout must be properly defined. This was determined to be the greatest radius where the density of particles still attached to the pile is approximately 1. There was some difficulty in determining this exact radius at times where large amounts of material are being transported from the pile to the edge of the tank, as observed in Figure 6.2, with the inaccuracy determined to be ± 3 mm.

In the case of no rotation, both aspect ratios exhibit an initial period of acceleration in radial runout then a period of linear growth, followed by a deceleration before settling at a value r_f. Comparing across Figures 6.11 (a) and (b), the length of these individual phases increase with aspect ratio. Considering the increase in frequency of rotation for each aspect ratio, the individual phases, speeds of growth and overall collapse time increases. When $f > 1.30\,\text{Hz}$ and $f > 1.18\,\text{Hz}$ for $a = 0.61$ and $a = 1.03$ respectively, after reaching a runout $r_{\max}$ at time $t_{\max}$ there are additional phases of radial decrease of the main pile when mass is lost from the periphery. The onset frequency values correspond to f_{crit} as discussed in Section 6.4.1 given in equation (6.10). Where this occurs there is a rapid acceleration in the decrease of the radius of the pile before decelerating and settling at a value r_f at time t_f. It is problematic to determine the end of this phase exactly; nearing the

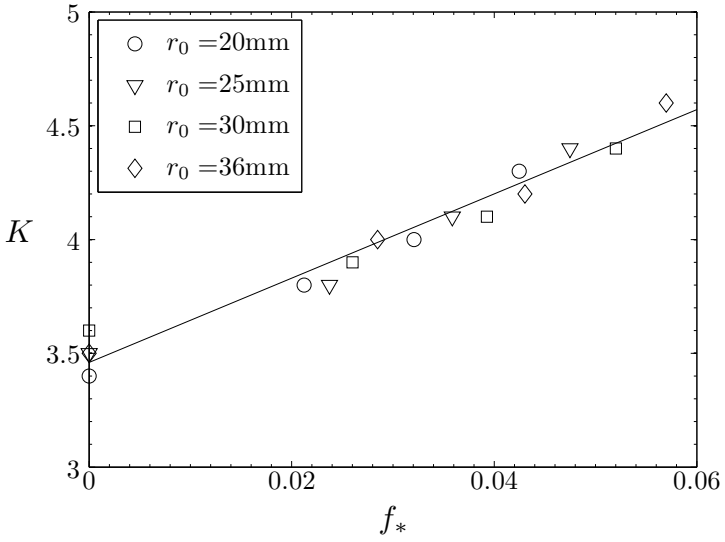

Figure 6.13: Dependence of proportional coefficient K given in equation (6.20) on f_*.

end of the period, the radius of the pile may remain essentially static while some material at the periphery of the pile may still eject itself. The error could be as much as $\pm 0.2\,\mathrm{s}$ at the highest frequencies, but a smaller error is incurred where the ejection phase is shorter. Determining the total time for collapse where ejection occurs is therefore difficult. In general, for a fixed aspect ratio the acceleration in radial decrease and duration of the phase is greater for increasing frequency. As expected for fixed frequency, the duration of this phase is longer for higher aspect ratios.

The non dimensionlisation of t_f is given by

$$t_* = \frac{t_f}{\sqrt{r_0/g}} \tag{6.19}$$

Non-dimensional time was evaluated against aspect ratio for varying frequencies across all cylinder sizes, with an example for $r_0 = 36\,\mathrm{mm}$ given in Figure 6.12, revealing

$$t_* = K\sqrt{a} \tag{6.20}$$

where K is a constant. This was considered for $f < 0.94\,\mathrm{Hz}$ where no volume loss from the main pile occurred. Considering the proportional constant K against non dimensional frequency f_* for all cylinder radii as in Figure 6.13, a linear relationship is evident with

$$K = 18.5 f_* + 3.5 \tag{6.21}$$

Substituting this into equation (6.20) gives

$$t_* = (18.5 f_* + 3.5)\sqrt{a} \tag{6.22}$$

The linearity in f is consistent with the effective direction of gravity being tilted due to the introduction of centripetal force and t_* being proportional to $\sqrt{a}$.

For $f > 0.94\,\text{Hz}$ a relation is no longer obvious between non-dimensionalised time and aspect ratio due to effect of volume loss increasing the collapse duration. This is compounded with the associated difficulty of realising t_f where even greater volume loss has occurred.

6.5 Discussion

This new experimental setup has revealed some new interesting dynamics, particularly relating to the secondary rotation-induced spreading phase, and extends non-dimensionalisations found for the stationary column collapse observed in the Chapter 4. Shinbrot et al. [2007] often observed features with the pile surface with a similar experimental setup consisting of a rotating disk and a continuous hopper injection as shown in Figure 2.21 in Section 2.3.1, but the fixed mass and short evolution time in this particular setup has prevented it.

Scalings for the final pile radius followed a similar linear rule to the stationary column collapse up to a rotation rate that causes a secondary spreading phase to occur, where a stagnation of the final pile radius emerges. This has been found to coincide with the point where the centripetal forces are able to overcome frictional forces. Reversal of this analysis to compare the final pile radius with frequency for fixed aspect ratios revealed the critical radius at which the stagnation occurred for a fixed frequency. Where there was a maximal runout radius, calculation of the coefficient of friction between the granular material and the tank surface was possible. While this is an empirical result it may find application later in the evaluation of different granular rheologies.

The final height of the deposit was less complicated than the radial relation given its stagnating nature and relationship with the effective tilt in gravity caused by the rotation. Together with the radial description, expressions for the two key scalings of the resulting deposit have been found.

The frequency required to initiate mass ejection from the main pile and the total mass loss was investigated. Mass loss experiences an initial constant increase where the aspect ratio is large enough that the radial runout exceeds the stagnating value of the final pile radius. This period is short, and the rate of increase begins to decelerate when the aspect ratio is 1.6 times the critical onset.

Differences in runout, height and critical values will exist with different ma-

terials and so direct numerical application of scalings found in this study must be used with some care, although the overall dynamics will remain the same. An interesting extension to this work would investigate the spreading of slurries under the same conditions and experimental setup as this would introduce a dependence on shear stresses and shear history.

Chapter 7

DEM simulations of rotating granular column collapse

7.1 Introduction

Discrete Element Method (DEM) numerics can simulate granular interaction through the generation of individual particles or 'elements', imposing forces and modelling the resultant interaction between these particles discussed in Section 2.5. It has proved to be a successful means to imitate a granular setup, with the ability to gather a greater amount of information about the micro-scale interaction not possible by experiments. Presented in this chapter is an initial investigation applying DEM to the axisymmetric collapse of a granular column under rotation described in Chapter 6. This study is incomplete, but displays some interesting initial results achieved that warrant further investigation and greater verification.

The collapse of a granular column using DEM has been performed in 2D by previous authors [Zenit, 2005; Staron and Hinch, 2005] but there exists only one published works by Cleary and Frank [2006] observing the collapse in 3D. Here the authors used spherical particles with one aspect ratio, $a = 1.91$, to assess the impact of parameters such as coefficient of restitution and friction. They note that the results largely overestimate the final runout and height of the resultant pile compared to experimental studies [Lube et al., 2004; Lajeunesse et al., 2004; Warnett et al., 2014a], likely due to the combination of low system size ($s = 28$) and spherical particles in the simulations. Conclusions of the study have influenced the selected parameters in the presented works.

The simulations were prepared with the *'LIGGGHTS'* DEM code that exists as a scripting language calling on modules to handle force interaction and time integration. Due to the available computing power the system size remained small as in Cleary and Frank [2006], which is known to exaggerate measured quantities

of the resultant pile in comparison to real grain geometry. The spherical particles under rotation were expected to travel further, but did so in an organised manner forming spiral arms remnicent of that observed by Zoueshtiagh and Thomas [2000]. The propagation of the arms is investigated and the distribution of velocity under varying parameter conditions. This has previously not been observed and steps have been taken towards its verification.

7.2 Computer Setup

7.2.1 Simulation software

DEM was performed using *'LIGGGHTS'* (Kloss and Goniva [2010], http://www.liggghts.com), an open source code developed by a group at Johannes Keppler University (Linz, Austria) based on a molecular dynamics codes *'LAMMPS'* (Sandia Labs, USA). The code is widely distributed, and its open source availability means that the code can be added to by any user with new features and frequently tested on benchmarks available for viewing at the website. This assurance has proved popular among researchers looking for a relatively painless implementation of DEM, with over 500 journal publications between 2000–2009 testament to their confidence.

Implementation of the code is simplified by the use of a scripting language as a front end, similar to MATLAB. A typical input script consists of the following parts:

System setup Define the physical boundaries of the system known as the *'simulation region'*.

Materials setup Define materials with properties for interaction between them such as friction and restitution. In this manner a material can be assigned to a boundary such as a wall or to particles themselves.

Interaction Define the contact models, integration scheme and timestep.

Particle setup Define the number of particles, material, size and initial position.

Environment setup If necessary define any movement within the system. This could include that of a imported meshes for particles to interact with.

Output setup Define the output required. Typically the parameters of every particles are written to a text file every fixed number of timesteps. Examples of potential outputs include particle ID, position, velocity and rotational velocity.

The text files can then be read for interpretation and evaluation.

This code is a pure DEM implementation as if the particles are within a vacuum and considers no fluid to exist around the particles. Users can implement

a fluid by coupling with a CFD code, but this has not been done in the simulations performed as the particles are large enough that this effect should be negligible.

7.2.2 Hardware

The simulations were performed on a dual processor computer with two 8-core Intel Xeon CPU's and 64Gb of memory. At the time of performing the simulations LIGGGHTS was capable of multi-core processing meaning that the calculations required for each timestep could be assigned to numerous cores to speed up the computation. With this setup and input script implemented (described below), the code took approximately one week to complete a simulation and is the reason for the low number of parameter investigations. The software has since moved to a GPU implementation that harnesses the power of graphics cards which can increase the simulation speed by up to 20 times with a single graphics card.

7.3 Simulation setup

7.3.1 Geometry generation

To fully recreate the experimental setup outlined in Chapter 6, this would require implementation of a cylinder to initially contain the collapse and a tank that would provide a rotating surface for the collapse. These were created in *'MeshLab'* (http://meshlab.sourceforge.net) which provided a simplified CAD style environment and exported as meshes in the standard STL format. Two cylinder sizes were created - 20 mm and 60 mm in diameter, both 200 mm in height. The tank was a hollow cylinder 800 mm in diameter and 200 mm in height. The generated meshes are shown in Figure 7.1.

7.3.2 Model implementation

The script applies the following general steps, ignoring simulation region setup. An example of the full script used can be found in Appendix E.

- Use Hertz (non-linear springs) model
- Define two materials - one for the meshes and one for the particles: Youngs modulus, Poisson ratio, coefficient restitution, coefficient of friction
- Define timestep of 0.0000001 s with NVE integration scheme (conserves volume and energy)
- Apply gravity
- Import meshes with material assigned and align centrally

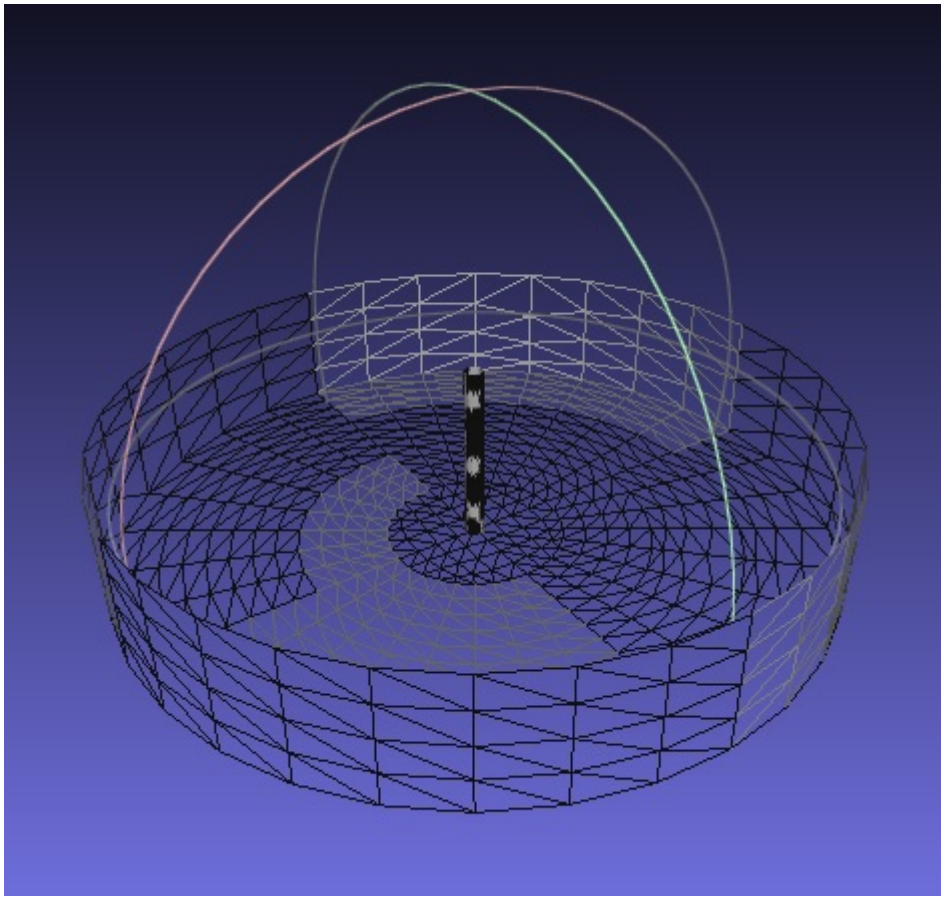

Figure 7.1: Meshes of 20mm cylinder and tank to be used in DEM simulations in LIGGGHTS.

- Assign particle material and deposit particles within the cylinder
- Simultaneously rotate cylinder and tank
- Dump particle positions
- Raise cylinder at 4 m/s
- Dump particle positions every 40 000 time steps = 0.004 seconds
- Run for 35 000 000 timesteps - 3.5 seconds total

This particular simulation uses a non-linear springs model, selected over linear due to rotation inducing more complex interaction. The linear springs model was described in Section 2.5.1 and the hertz differs only by the spring constants and particles overlap. The equations governing force are given

$$\boldsymbol{F_n} = -k_n(\Delta \boldsymbol{x_p})^{1.5} + c_n \Delta \boldsymbol{u_{p,n}} \tag{7.1}$$

$$\boldsymbol{F_t} = min \left\{ \left| k_t \int_{t_{c,0}}^{t} (\Delta \boldsymbol{u_{p,t}}\, dt + c_t \Delta \boldsymbol{u_{p,t}} \right|, \mu_c \boldsymbol{F_n} \right\} \tag{7.2}$$

where k_n, k_t are spring constants, c_n, c_t are damper constants. $\Delta \boldsymbol{x_p}$ is the overlap distance and $\Delta \boldsymbol{u_{p,n}}$ is the relative tangential velocity [Goniva et al., 2012]. The spring constants are given

$$k_n = k_t = \frac{4}{3} R'^{0.5} E' \tag{7.3}$$

with

$$\frac{1}{R'} = \frac{1}{R_i} + \frac{1}{R_j} \tag{7.4}$$

$$\frac{1}{E'} = \frac{1-\gamma_i^2}{E_i} + \frac{1-\gamma_j^2}{E_j} \tag{7.5}$$

where E_i, E_j is the Young's modulus, R_i, R_j is the particle radius of particles i and j respectively. The damping coefficient is defined by

$$c_n = 2\gamma \sqrt{\frac{k_n m_0 m_j}{m_0 + m_j}} \tag{7.6}$$

where

$$\gamma = -\frac{\ln e}{\sqrt{\pi^2 + \ln^2 e}} \tag{7.7}$$

r_0 (mm)	μ_{p-s}	f (Hz)
10	0.50	1.0
10	0.50	2.0
30	0.00	2.0
30	0.25	2.0
30	0.50	2.0

Table 7.1: Varying conditions in simulations where initial cylinder size r_0, particle-surface friction μ_{p-s}, frequency f

is set to give the coefficient of restitution e.

With this calculated for each particle, Newtons second law is used to calculate the particles' accelerations and calculate their subsequent states after the determined timestep.

7.3.3 Simulation parameters

A total of five different simulations were performed. Kept constant across all simulations were:

- Number of particles (N): 10 000
- Particle diameter (d): 1 mm
- Particle density (ρ): 8000 kg/m^3
- Youngs modulus (E): 3x10^7
- Poisson ratio (γ): 0.3
- Particle-particle friction (μ_{p-p}): 0.5
- Coefficient of restitiution (e): 0.6
- Timestep: 10^{-7} s

The cylinder size, particle-surface friction and rotation rate was varied between each of the five simulations as detailed in Table 7.1. The number of particles results in an aspect ratio $a = 0.31$ and $a = 2.80$ for cylinder $r_0 = 30$ mm and $r_0 = 10$ mm respectively. The system size in this case is particularly small with $s = 10$ and $s = 30$ for $r_0 = 10$ mm and $r_0 = 30$ mm respectively. Ideally the same system would have been repeated with smaller particles, and hence a greater number of them, but with the simulation times already in the order of a week this was unfeasible.

The combination of Youngs modulus and Poisson ratio contributes to the 'stiffness' of the particles and have been chosen mimic the properties of steel. The nature of DEM allows particles to overlap between timesteps which should be kept

below 1% for an accurate simulation, achieved by ensuring the timestep is small enough to integrate the collision. It is suggested the scheme should employ 15–25 integration steps per collision, which given the small time scales involved in this fast flowing system should be a minimum of 10^{-6} s [Cleary and Frank, 2006]. To give confidence to the results the timestep selected was of an order smaller.

7.4 Results

Here initial results are discussed from this preliminary investigation. First the flow is observed in 3D using *'Paraview'* (http://www.paraview.org). Noticing the suprising development of spiral arms, particles and sections are then traced to find their evolution to further understand the flow. Finally the distribution of velocity within the evolving shape is evaluated and discussed.

In all figures, the table rotates in an anticlockwise direction and the camera view remains stationary as opposed to within the rotating frame of reference.

7.4.1 Flow observation

The flow can be observed in $x - z$ plane in Figure 7.2, where in this particular example $r_0 = 10\,\text{mm}$, $\mu_{p-s} = 0.5$ and $f = 2.0\,\text{Hz}$. The collapse initiates in the way previously observed; a front flow propogates from the foot of the column and due to the high aspect ratio ($a = 2.80$) the summit falls horizontally with the column. Due to the small system size ($s = 10$) and sphericity of the particles, it continues to collapse to a monolayer in this view. The excessive collapse and runout of spherical particles is expected as in DEM simulations by Cleary and Frank [2006], but the rotation induces this further to eradicate the appearance of a pile. Further an interesting dynamic is observable in the $x - y$ plane seen in Figures 7.3–7.6.

Unexpectedly there is the development of 8 spiral arms, with their existence first noticeable at $t = 0.16\,\text{s}$ where the pile falls to a mono-layer as seen in Figure 7.4 (a). With time the arms continue to grow in length and curvature, while they become increasingly thinner. Eventually the arms start to touch one another at the extremity where the curvature in the arm is the greatest. As this patterning develops the centre of the structure becomes vacant of particles, increasing in size with time, evidently feeding the spiral arms. Eventually all particles move to the edge of the tank.

The structure is reminiscent of experiments performed by Zoueshtiagh and Thomas [2000] whom observed spiral arms with a central patch in a centrifuging granular bed immersed in water as discussed in Section 2.3.2, although they are able to achieve a number of arms between 5–120 and the onset mechanism in those experiments are shear induced.

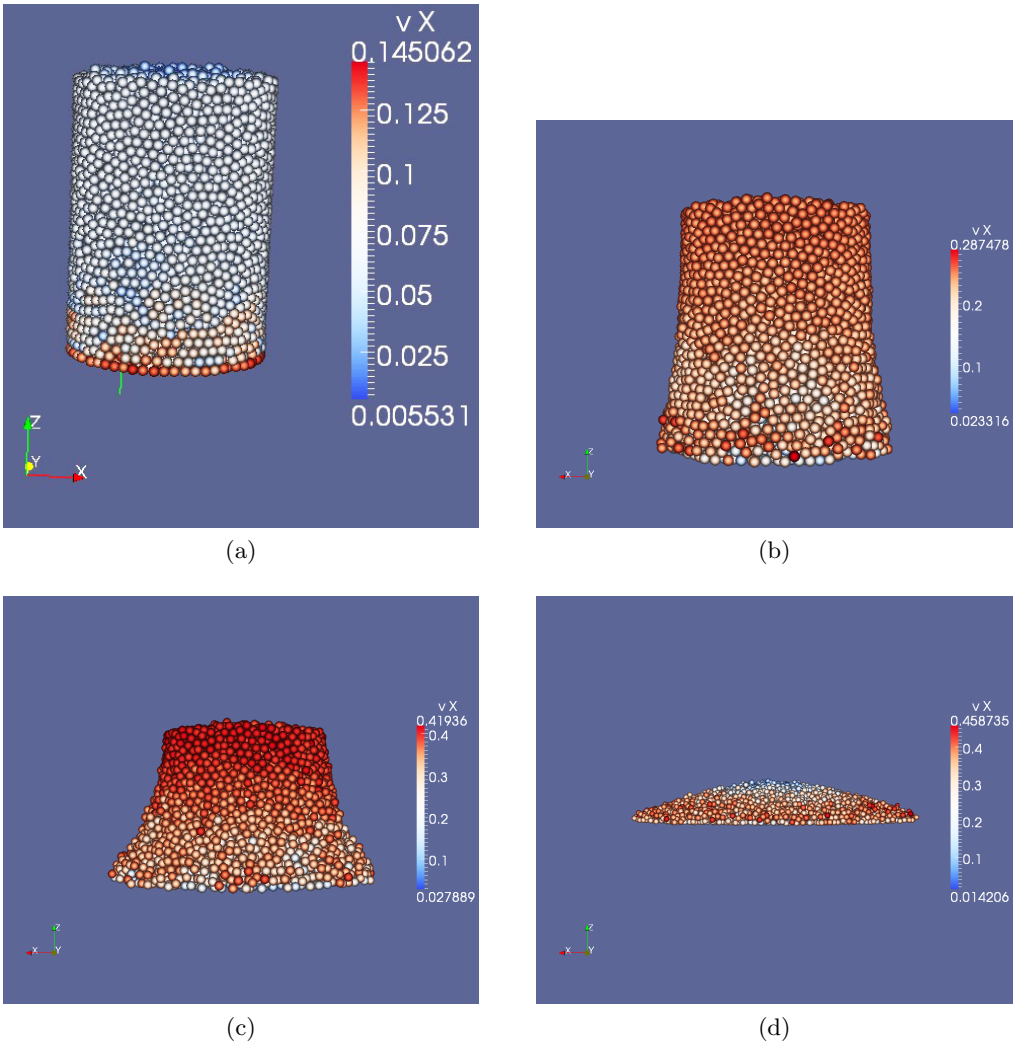

(a) (b)

(c) (d)

Figure 7.2: Start of collapse of cylinder $r_0 = 10\,\text{mm}$ rotating at a frequency $f = 2.0\,\text{Hz}$ coloured by velocity viewed in the $x - z$ plane. (a) $t = 0.00\,\text{s}$. (b) $t = 0.02\,\text{s}$. (c) $t = 0.04\,\text{s}$. (d) $t = 0.08\,\text{s}$.

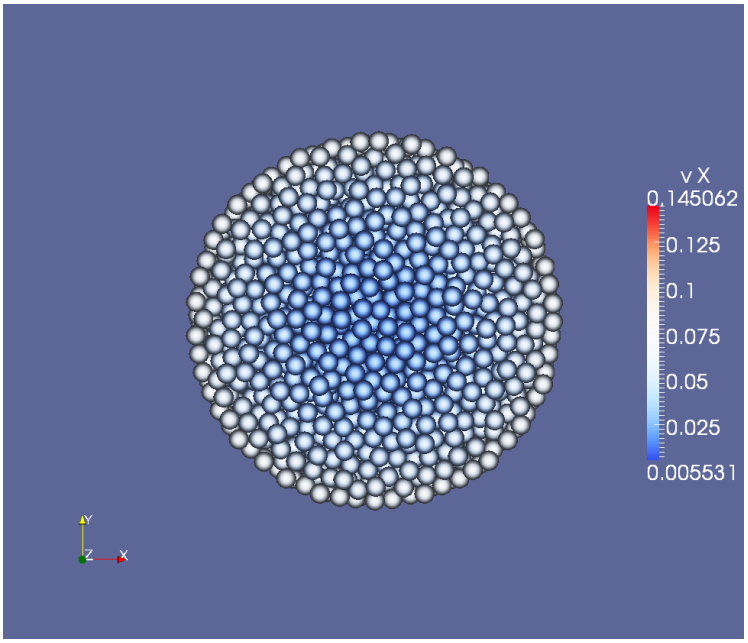

(a)

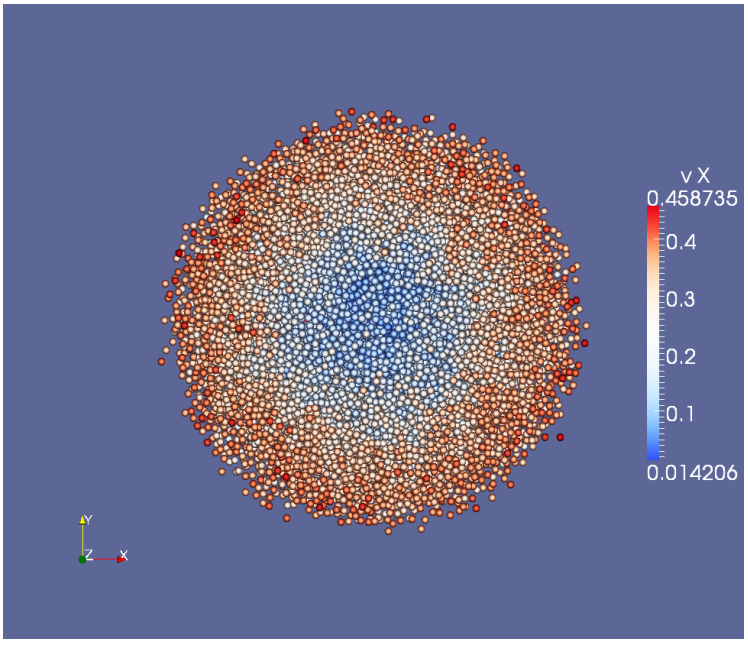

(b)

Figure 7.3: Start of collapse of cylinder $r_0 = 10\,\text{mm}$ rotating at a frequency $f = 2.0\,\text{Hz}$ (anticlockwise) coloured by velocity viewed in the $x-y$ plane. This is viewed in a stationary lab frame. (a) $t = 0.00\,\text{s}$. (b) $t = 0.08\,\text{s}$.

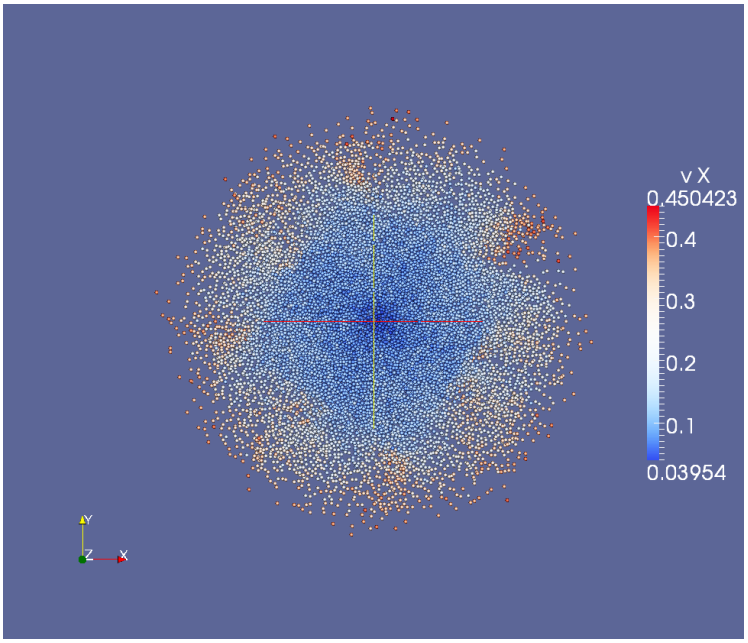

(a)

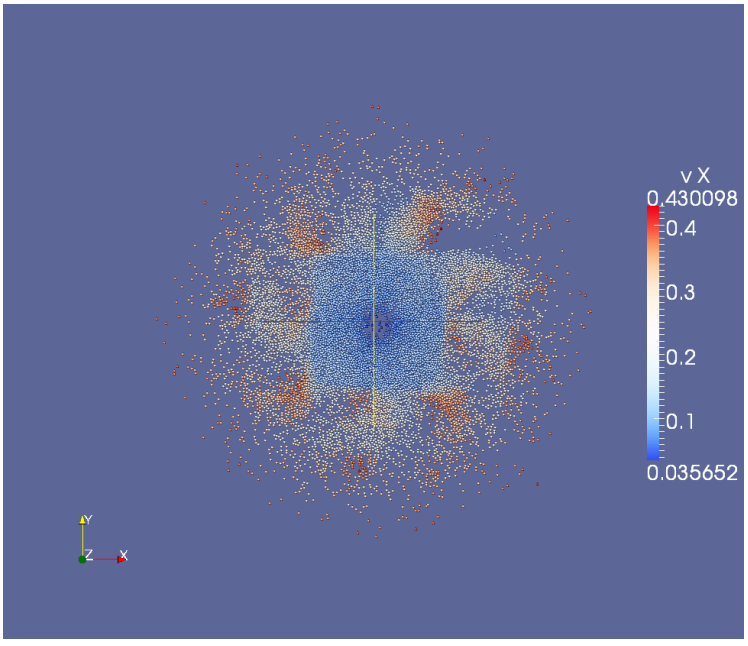

(b)

Figure 7.4: Collapse of cylinder $r_0 = 10\,\text{mm}$ rotating at a frequency $f = 2.0\,\text{Hz}$ (anticlockwise) coloured by velocity viewed in the $x - y$ plane. This is viewed in a stationary lab frame. (a) $t = 0.16\,\text{s}$. (b) $t = 0.24\,\text{s}$.

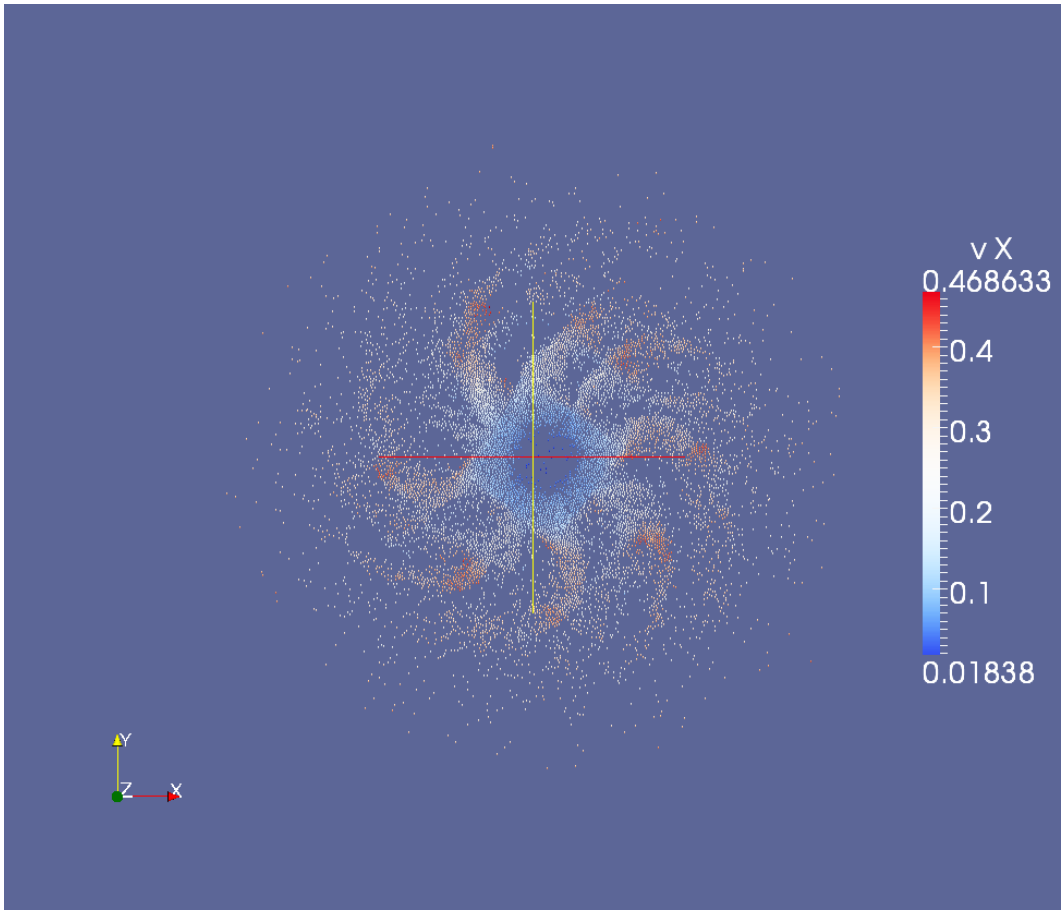

Figure 7.5: Collapse of cylinder $r_0 = 10\,\text{mm}$ rotating at a frequency $f = 2.0\,\text{Hz}$ (anticlockwise) coloured by velocity viewed in the $x - y$ plane at time $t = 0.40\,\text{s}$. This is viewed in a stationary lab frame.

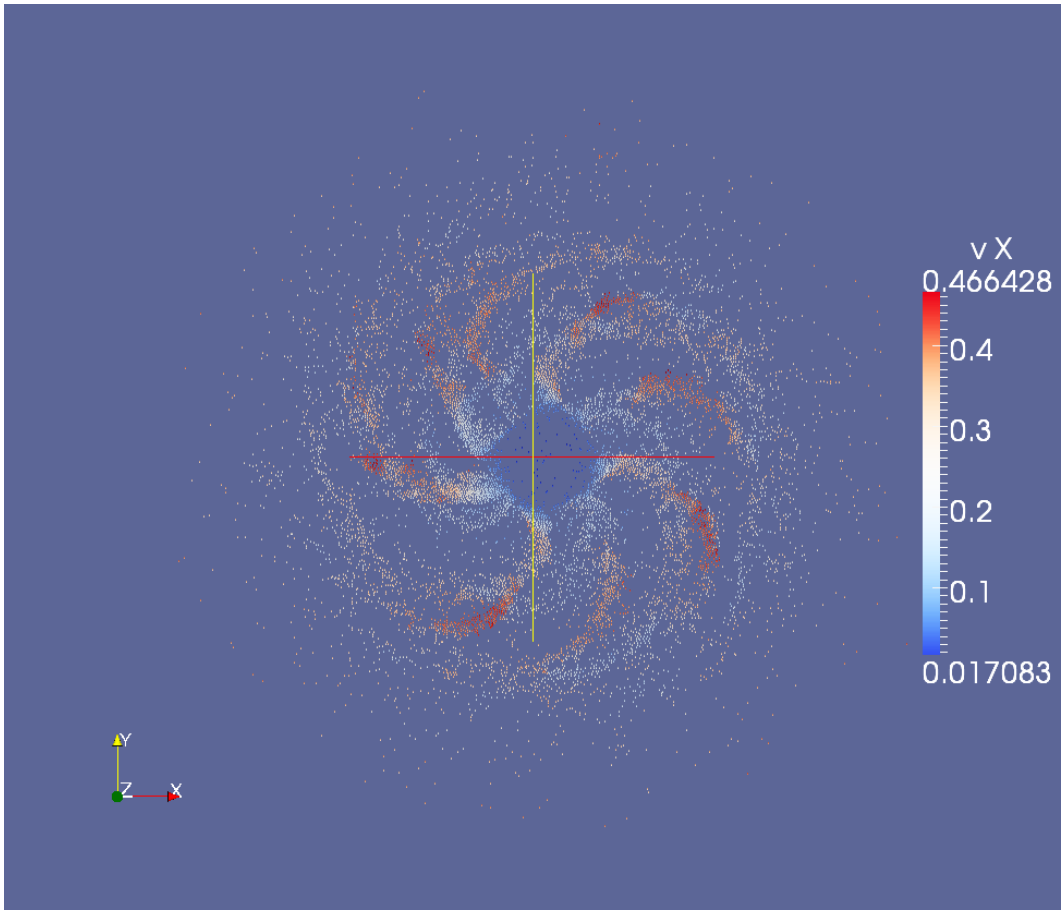

Figure 7.6: Collapse of cylinder $r_0 = 10\,\text{mm}$ rotating at a frequency $f = 2.0\,\text{Hz}$ (anticlockwise) coloured by velocity viewed in the $x - y$ plane at time $t = 0.60\,\text{s}$. This is viewed in a stationary lab frame.

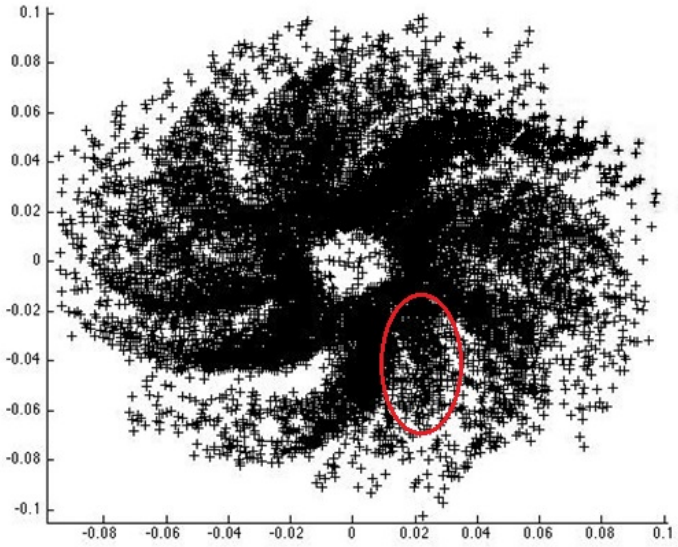

Figure 7.7: A larger initial cylinder size $r_0 = 30\,\text{mm}$ results in the addition of another spiral arm although it is weak and ill formed as shown by the red circle.

7.4.2 Pattern breaking

The same simulation was run but with a smaller frequency, $f = 1.0\,\text{Hz}$, and the same structure evolved with the same number of arms - only slower in development. In attempts to break the symmetry or vary the number of spiral arms, a wider cylinder $r_0 = 30\,\text{mm}$ was used with the same frequency $f = 2.0\,\text{Hz}$ and μ_{p-s} =0.5. With the same number of particles, this results in a much smaller aspect ratio $a = 0.31$ and larger system size $s = 30$. This resulted in the initial formation of 9 spiral arms, but one of the arms was weak and ill formed as seen in Figure 7.7. The development of the flow was the same, but arms were found to split at latter stages of collapse as seen in Figure 7.8. It is postulated that this is enabled by thicker arms than in the smaller cylinder case.

If the development of spiral arms always occurs at the periphery of the column then it reasons that an increase in cylinder size can lead to an increase in the number of arms; the circumference can be occupied by a greater number of particles and so can accomodate a greater number of arms. A variation in the rotation rate does not alter the number arms and if this setup can be assumed to conform to the same relationships as experiments by Zoueshtiagh and Thomas [2000] this is to be expected - the mobility parameter discussed in Section 2.3.2 given in Equation 2.20 is based on the instantaneous spin-up of the tank which doesn't occur here as the column is allowed to enter solid body rotation.

The onset of the patterning occured at a similar time to the smaller cylinder size, but due to the increased centripetal force experienced by the outermost particles

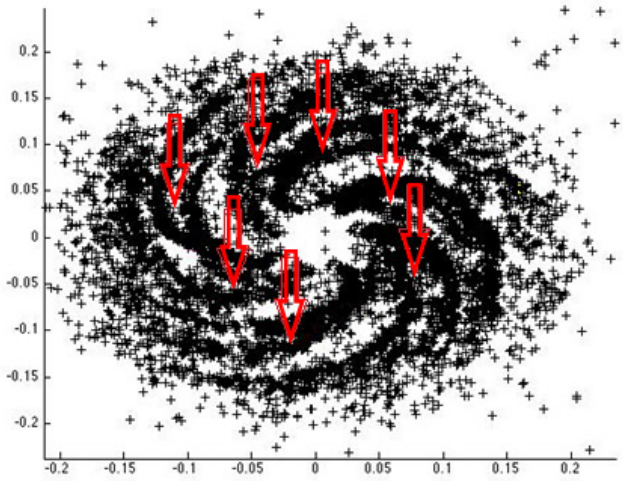

Figure 7.8: For $r_0 = 30\,\text{mm}$ splitting occurs within the spiral arms. This is observed in the timestep 0.62 s above marked with red arrows.

at the onset of collapse for this larger cylinder, the arms wound around one another in a more severe fashion. Observation of the increased winding can be made in Figures displayed in the Section 7.6.3 where $r_0 = 30\,\text{mm}$ results are used for evaluation of particle tracing.

The next step to try and alter the patterning was to vary particle-surface friction, where the thought was that a smaller value of friction allowing the particles to runout faster might affect the development of spiral arms. This was not found to be the case, where a higher particle-surface friction led only to the tighter winding of the arms. Again this observation can be made in figures in Section 7.6.3.

7.4.3 Arm development

It was an interesting consideration to find where particles within a spiral arm originated and where they then travelled to in time. Observation of clearly defined arms with minimal curvature could be made at 0.24 s. From this, particles were selected that lied within a single arm and coloured for tracing. The same particles were then selected within other timeframes with a selection shown for $r_0 = 30\,\text{mm}$, $f = 2.0\,\text{Hz}$, μ_{p-s}=0.25 in Figure 7.9.

The arm originates from a section of the column which is of opposite curvature to its eventual form. As the spiral evolves nearly all particles remain within the spiral arms themselves, with only a few near the centre moving to a different arm. This can be attributed to the method of selection of the particles of interest rather than particles actually moving arms. Where the arms start to wind into one another some particles at the extremity of one arm can be found to merge into another. With this knowledge, the next question is to find how particles move within

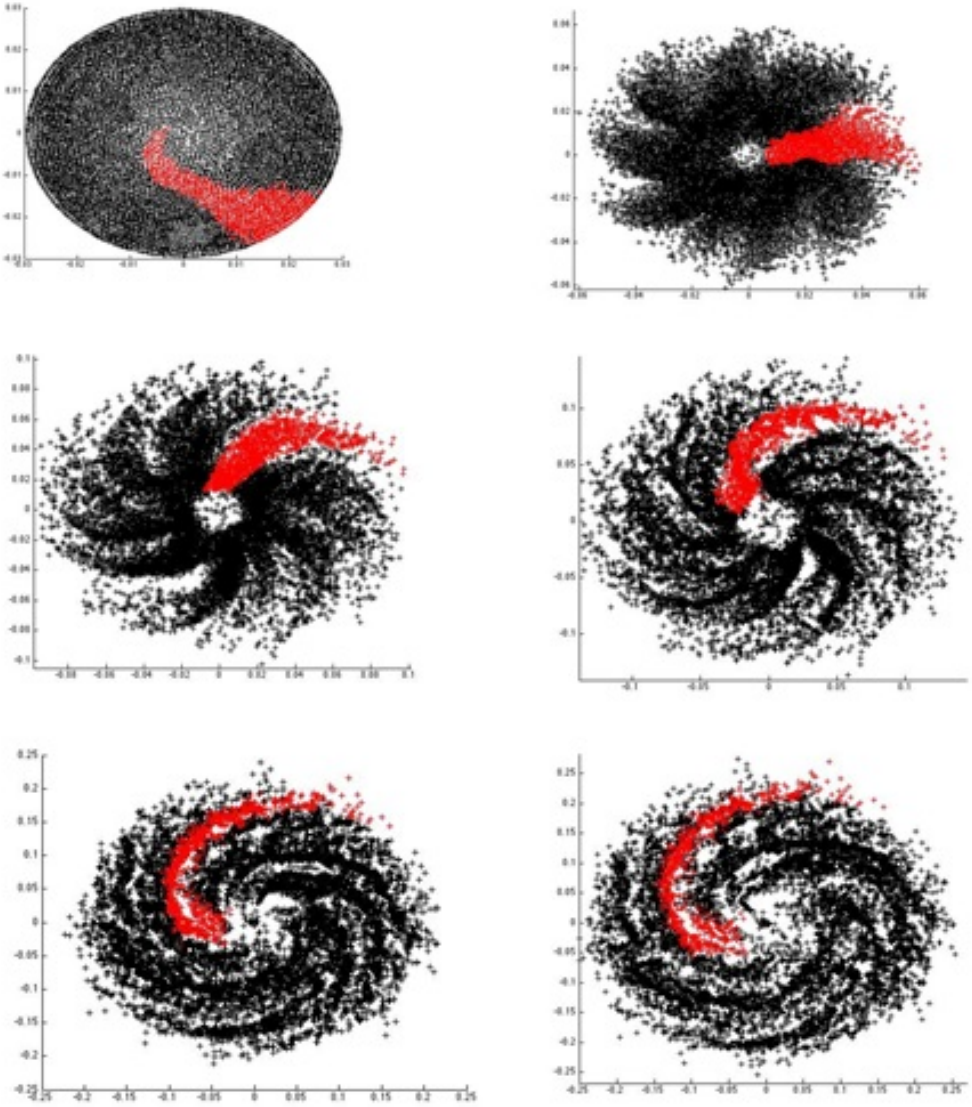

Figure 7.9: $r_0 = 30$mm, $f = 2.0$Hz, μ_{p-s}=0.25. A single spiral arm is highlighted at 0.24 s as shown top right and followed for all other time frames. Shown are views in $x - y$ plane for times $t = 0.00, 0.24, 0.48, 0.72, 0.96, 1.20$ s from left to right.

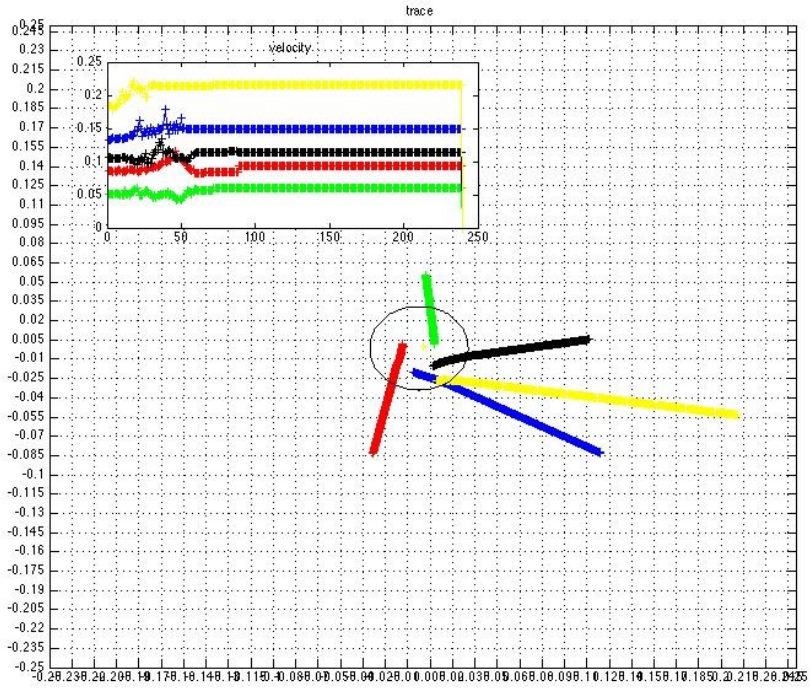

Figure 7.10: $r_0 = 30\,\text{mm}$, $f = 2.0\,\text{Hz}$, μ_{p-s}=0.0. Five random particles are selected within the column and their path followed for 0.96s and their velocity recorded. Plane dimensions given in metres. Trace is in the stationary lab frame.

an arm itself.

7.4.4 Particle tracking

To investigate the movement of specific particles, five particles were randomly selected and followed for the duration of the collapse for $r_0 = 30\text{mm}$ set of simulations where the μ_{p-s} was varied.

$\mu_{p-s} = 0$

The trace in Figure 7.10 shows that particles moved in a straight line, although not radially outwards from centre. Particles towards the edge of the cylinder moved with a greater velocity and travelled further. This is due to a greater initial velocity induced by the avalanching and there being a greater flow behind the particles. In general, the velocity of the particle settled quicker the closer to edge of the cylinder the particle began. This is of course an unrealistic situation, but used for a base case.

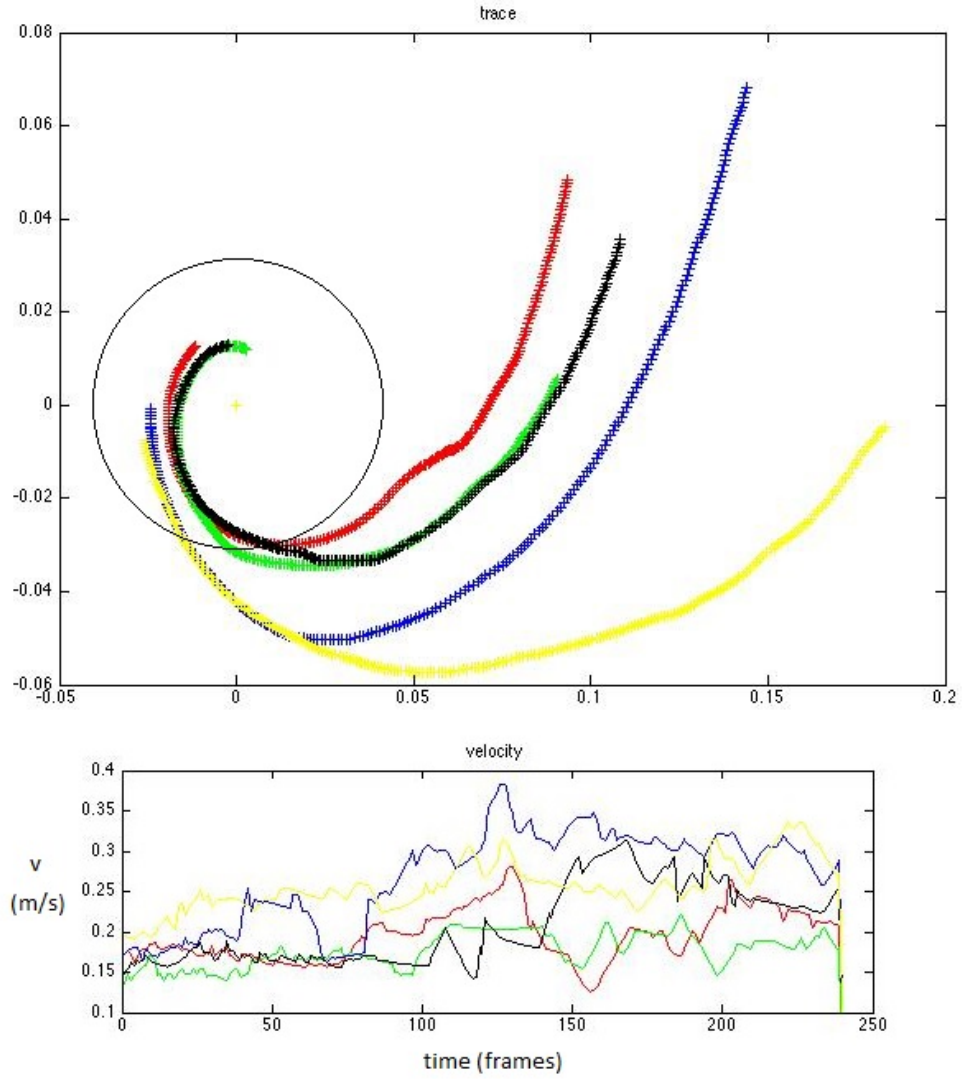

Figure 7.11: $r_0 = 30\,\text{mm}$, $f = 2.0\,\text{Hz}$, μ_{p-s}=0.25. Five random particles are selected within the column and their path followed for 0.96s and their velocity recorded. Plane dimensions given in metres. Trace is in the stationary lab frame. Their specific position at fixed timesteps can be seen in the next figure.

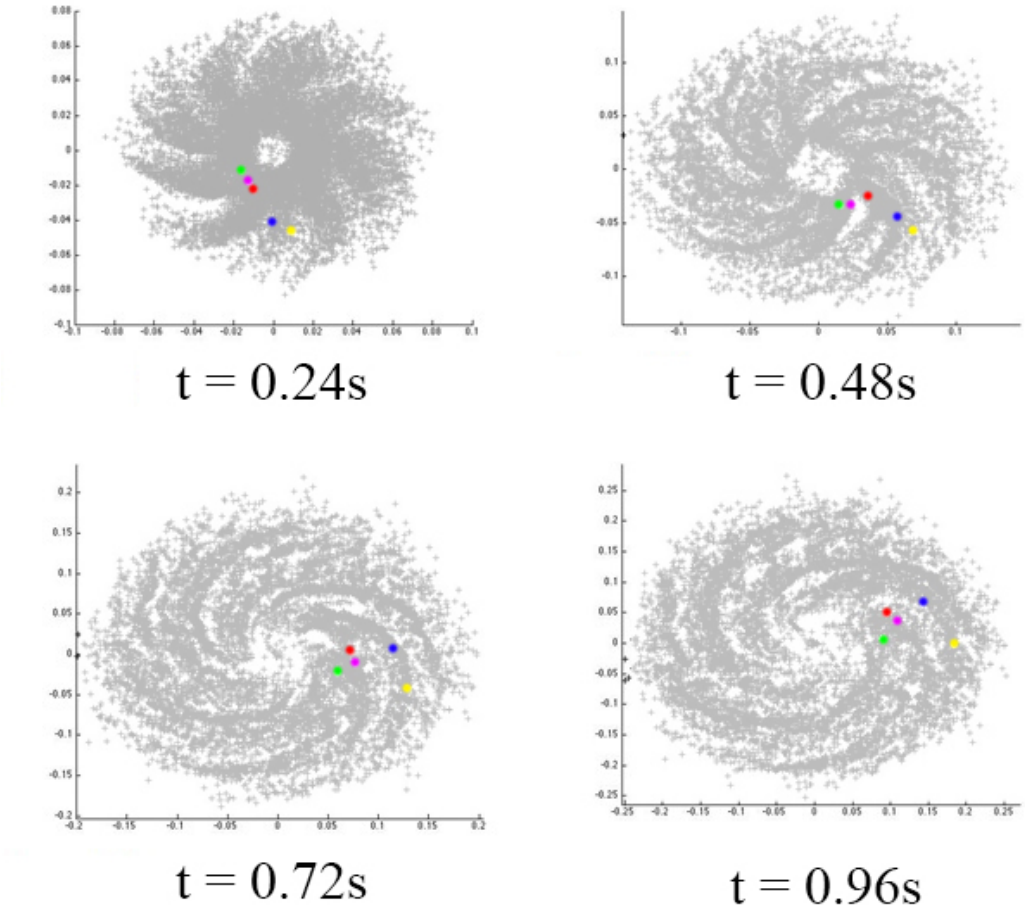

Figure 7.12: $r_0 = 30\,\text{mm}$, $f = 2.0\,\text{Hz}$, μ_{p-s}=0.25. Position of five random particles at increasing timesteps. Plane dimensions given in metres. Viewed in the stationary lab frame.

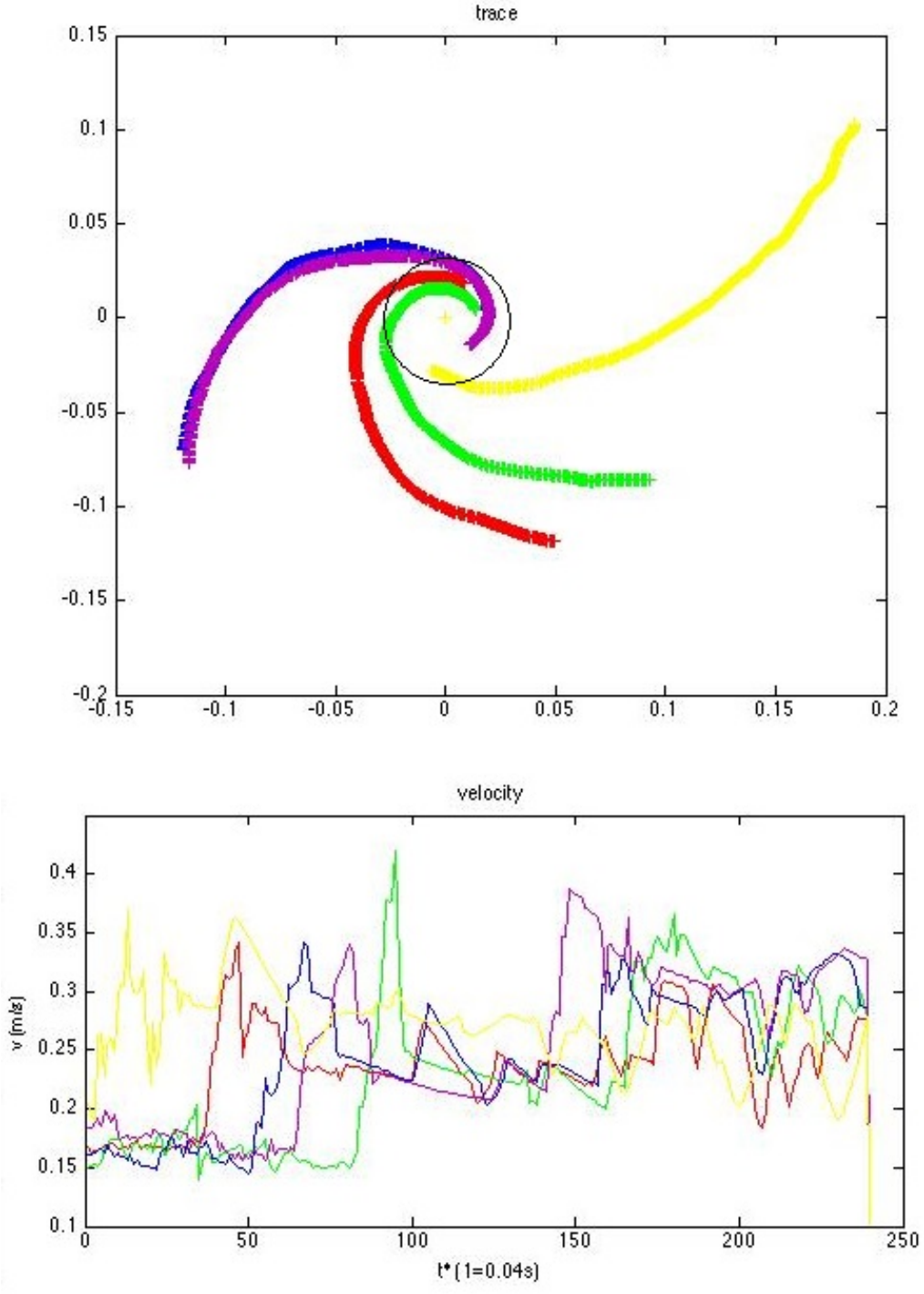

Figure 7.13: $r_0 = 30\,\text{mm}$, $f = 2.0\,\text{Hz}$, μ_{p-s}=0.5. Five random particles are selected within the column and their path followed for 0.96s and their velocity recorded. Plane dimensions given in metres. Trace is in the stationary lab frame. Their specific position at fixed timesteps can be seen in the next figure.

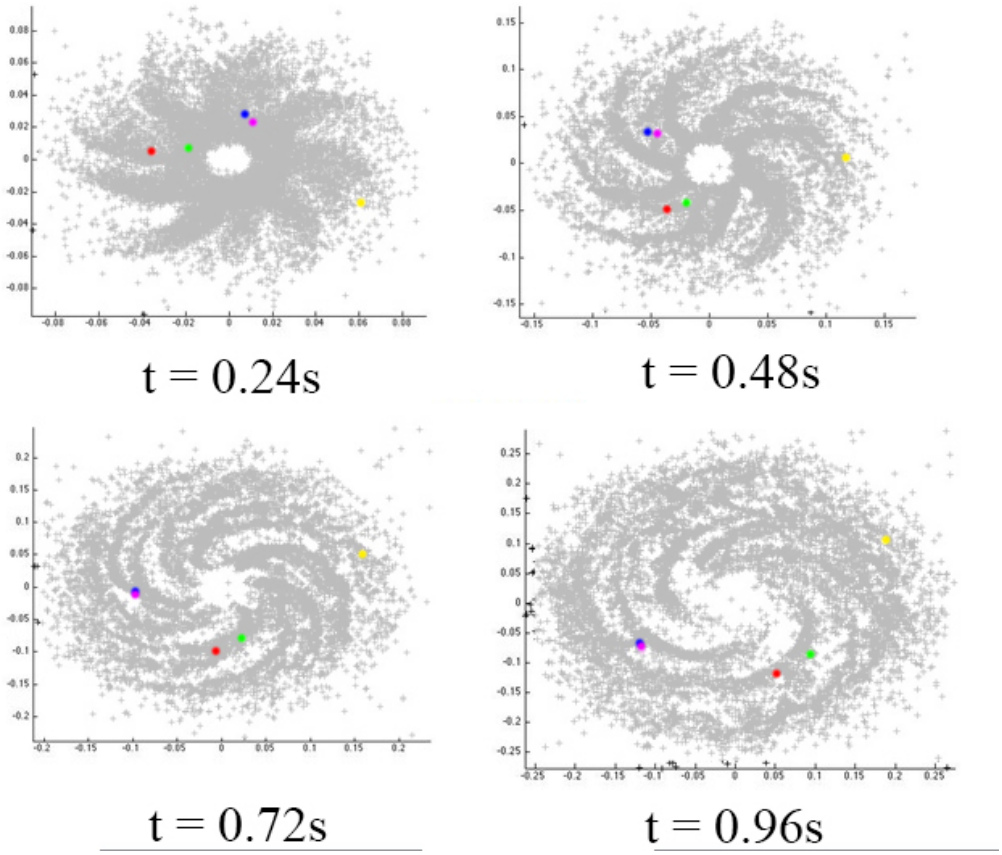

Figure 7.14: $r_0 = 30\,\text{mm}$, $f = 2.0\,\text{Hz}$, μ_{p-s}=0.5. Position of five random particles at increasing timesteps. Plane dimensions given in metres. Viewed in the stationary lab frame.

$\mu_{p-s} = 0.25$

The path of the particles can be observed in Figure 7.11 and its position within the spiral at discrete timesteps in Figure 7.12.

The blue and yellow particle are interesting to follow as in frame 60 the yellow particle is at the front of an arm, and the blue particle is at the back of the same arm. The yellow particle follows the rotation of the arm, but slides towards the radial extremity while falling to a more central position between the front and the back of the arm. The blue particle works its way to the centre of the same arm. There confirms there is certainly a lot of movement within the arm itself as it develops, although particles do not appear to leave the arm itself.

The red particle at frame 120 is towards the back of a spiral arm at a time where a split is starting to appear in the arm. As a result it appears at the front of the secondary spiral arm formed. During this period the velocity of the particle slows. While the red particle is slowing, the velocity of the magenta particle is increasing and allows time for this particle to catch up with the red particle. At this point the splitting phase of the arm occurs and it move out of its initial arm and into the secondary arm that the red particle eventually resides in.

The green particle starts centrally within an arm, and although appears to slip backwards with the arm, retains a relatively steady velocity throughout the motion.

The general movement within an arm (without the effect of the arm splitting) appears to be that particles initially at the front of the arm slip backwards while moving along the radius of the arm, and particles at the back of the arm push forwards with less translation along the arm radius. This particular trace indicates that particles only exchange arms during the splitting phase.

$\mu_{p-s} = 0.5$

Magenta and blue particles follow practically the same path and share similar velocity profiles. In frame 180 it is seen that these particles are at the front of a spiral arm and in frame 240 they move into the space between this arm and another arm infront.

The yellow particle is at radial extremity of a spiral arm, starting centrally between the front and back of the arm. Due to it being at the extremity it appears to fall backwards within the same arm. This trace has the least curvature and overall has a higher velocity at the start. So in this case the runout has dominated its path

The red particle jumps arms between frames 120 and 180 and at frame 180 sits at a splitting point of the arm it has joined. After the splitting, it remains at the front of the secondary arm as shown in frame 240.

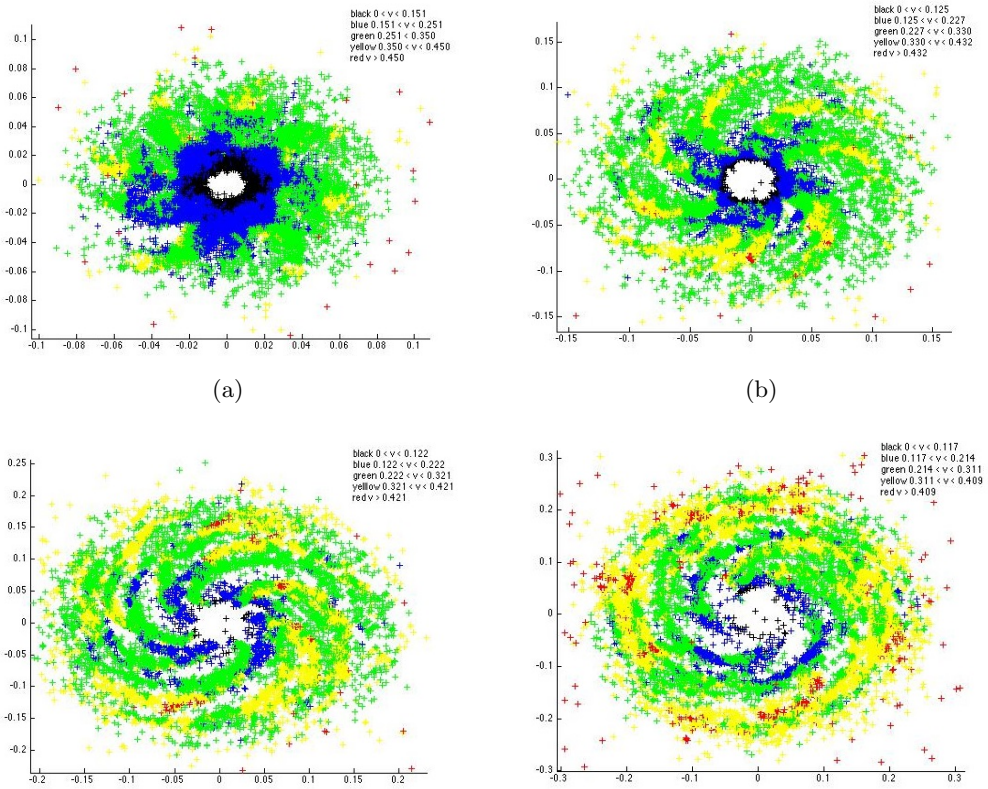

(a) (b)

(c) (d)

Figure 7.15: Velocity (m/s) distributions within collapse for $r_0 = 30\,\text{mm}$ rotating at a frequency $f = 2.0\,\text{Hz}$ (anticlockwise) and $\mu_{p-s} = 0.5$. This is shown in the stationary lab frame. (a) $t = 0.24\,\text{s}$. (b) $t = 0.48\,\text{s}$. (c) $t = 0.72\,\text{s}$. (d) $t = 0.96\,\text{s}$.

The green particle takes until frame 120 to settle into an arm, sitting close to the centre radially. It skips into the next arm at frame 180 where it then remains at the front of this arm

7.4.5 Velocity distributions

The distribution of velocity within the flow is investigated for $r_0 = 30\,\text{mm}$, $f = 2.0\,\text{Hz}$ and $\mu_{p-s} = 0.5$. Initially while the runout is dominating the flow in the first $0.24\,\text{s}$ as shown in Figure 7.15 (a), the greater velocities are at the extremities and not really at arm fronts. Beyond this phase the velocity still increases radially outwards, but with greater velocities prevalent at the front of the arms evident at $t = 0.48\,\text{s}$ as seen in Figure 7.15 (b). As this develops, velocity bands wind into layers within the arm as seen in Figures 7.15 (c), (d). Where the spiral arms split from Figure 7.15 (b) to (c) the arms appear to split at regions of higher velocity within the arm, with the higher velocity particles forming the front of the arm after the split.

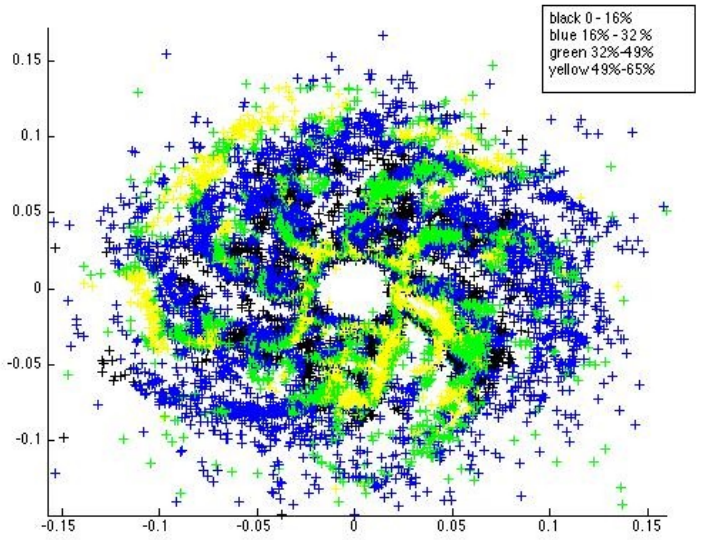

(a)

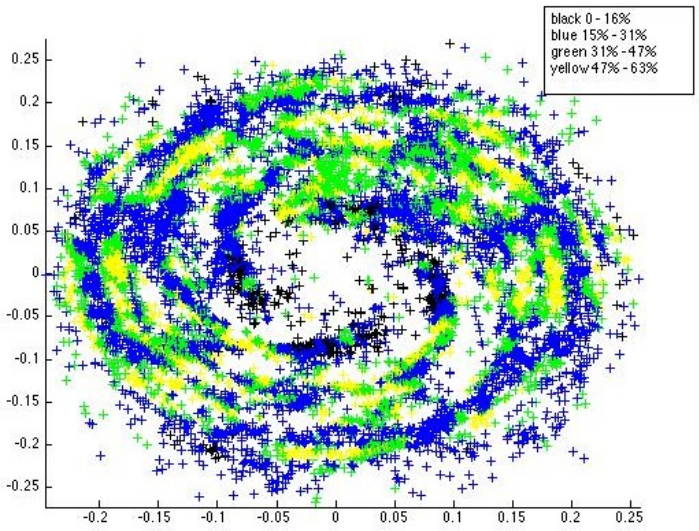

(b)

Figure 7.16: Particle slipping as a percentage of the difference between the particle velocity and the velocity of the take. Distributions shown are within the collapse for $r_0 = 30\,\text{mm}$ rotating at a frequency $f = 2.0\,\text{Hz}$ and $\mu_{p-s} = 0.5$ viewed in the stationary lab frame (a) $t = 0.48\,\text{s}$. (b) $t = 0.96\,\text{s}$.

Consideration was given to the degree of particle slipping as shown in figure 7.16. This was calculated as a percentage:

$$v_{slip} = \frac{v_p - v_s}{v_s} \times 100\% \tag{7.8}$$

where v_p and v_s are the velocities of the particle and surface respectively. There is evidently some patterning due to the relative symmetry of the collapse but the only clear relation is that the greatest amount of slipping occurs in the densest regions, assumed to be due to the restriction in movement.

7.5 Steps to verification

To attempt to verify that the simulations represent real artefacts, some experiments were run to try and recreate it. It is important that the particles were spherical as this was likely a contributing factor, and the system size s was kept small. The same experimental setup was used as in Chapter 6 with the rotational turntable within the Bosch housing to mount the pulley system for cylinder removal. The collapse was recorded with a camera mounted within the rotating frame of reference recording at 30 fps. The high speed camera was not available at this time as used in the rotational collapse investigation.

Initially spherical metallic particles with $d = 0.5\,\text{mm}$ were used but a pile remained in the middle after the collapse as in Chapter 6. This was a suprise as the system size is still small for the smallest cylinder size of $r_0 = 20\,\text{mm}$ ($s = 40$) but could have been potentially due to some residual magnetism in the particles hindering movement. A second attempt was made using plastic BB pellets (spheres) with $d = 5\text{mm}$. The collapse is shown in Figures 7.17–7.19 where $r_0 = 25\,\text{mm}$ $a = 1.30$ ($s = 5$) with a rotational frequency $f = 0.98\text{Hz}$. The manufacturer was unable to provide sphericity estimates, but given their application (bearings, and passing through the shaft of a cylindrical gun) its eccentricity is assumed to be low and on the whole spherical.

In this case the entire pile collapses into a monolayer as in the simulations. The appearance of the arms would be expected to occur at approximately $0.20\,\text{s}$ if the simulations are believed, shown for the collapse in Figure 7.18 (a). Curvature in the runout is observed while there is little relative movement towards the centre. As the collapse continues the particles continue to spread out radially with curavature but no banding or spiral arms are evident. It is possible in this case that the system size is infact too small for the spiral arms to form.

Further verification attempts are yet to be made, in particular to trial a variety of spherical particulates. It is thought that the patterning is extremely sensitive to experimental conditions, and so any small peturbation from concentricity

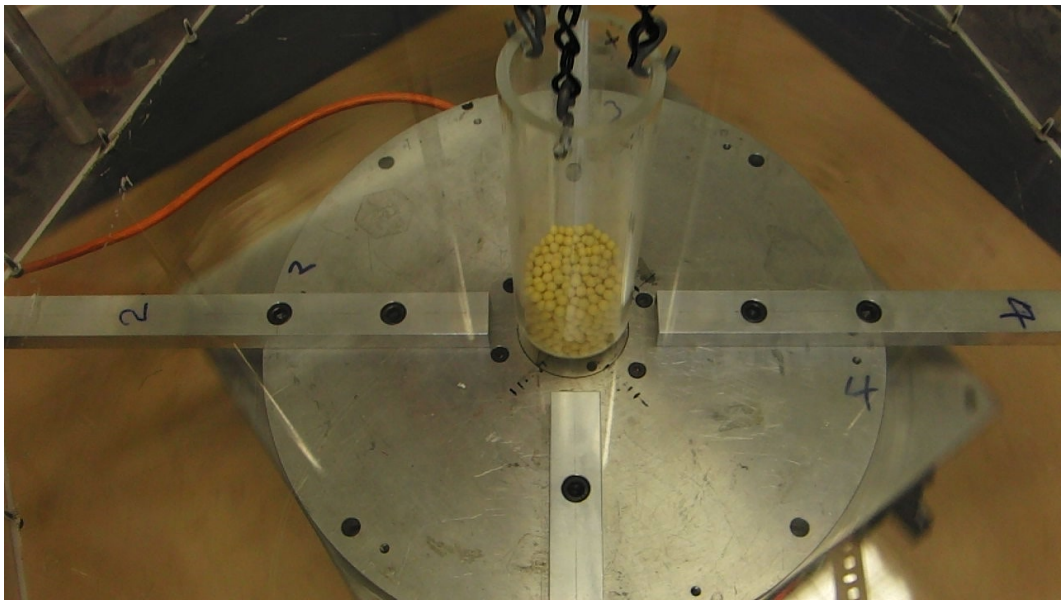

(a)

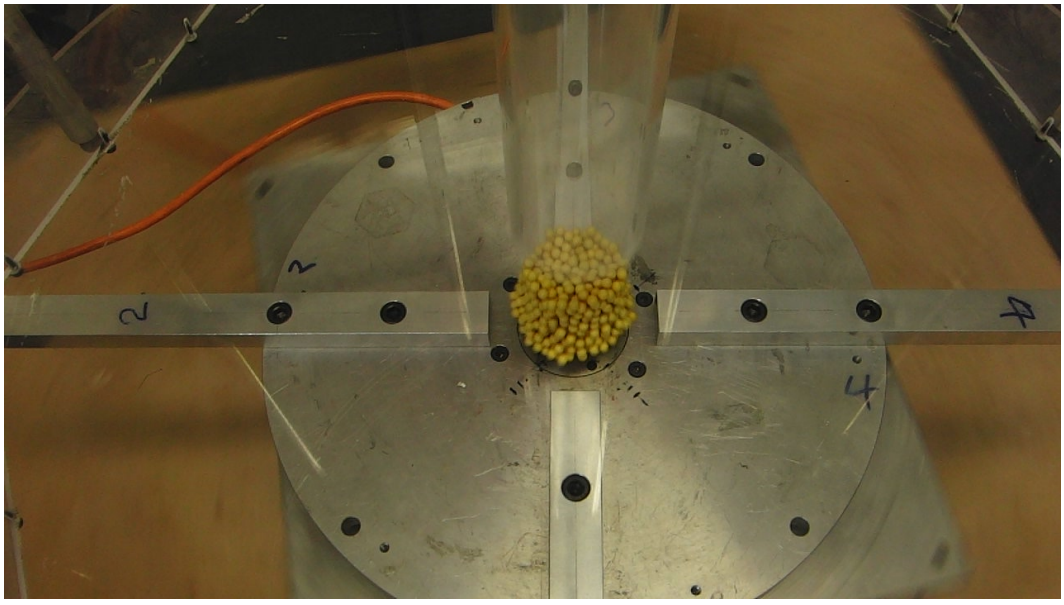

(b)

Figure 7.17: Column collapse of $r_0 = 25\,\mathrm{mm}$ $a = 1.30$ consisting of BB pellets with $d = 5\,\mathrm{mm}$ ($s = 5$) with a rotational frequency $f = 0.98\,\mathrm{Hz}$ (anticlockwise). The camera is mounted within the rotating frame of reference. (a) 0.00 s. (b) 0.07 s.

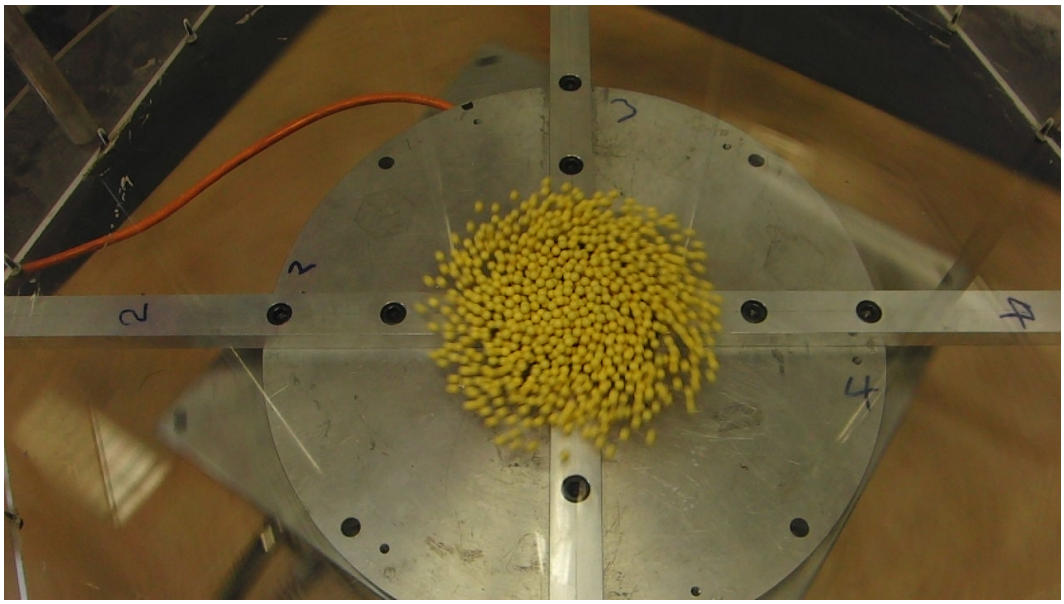

(a)

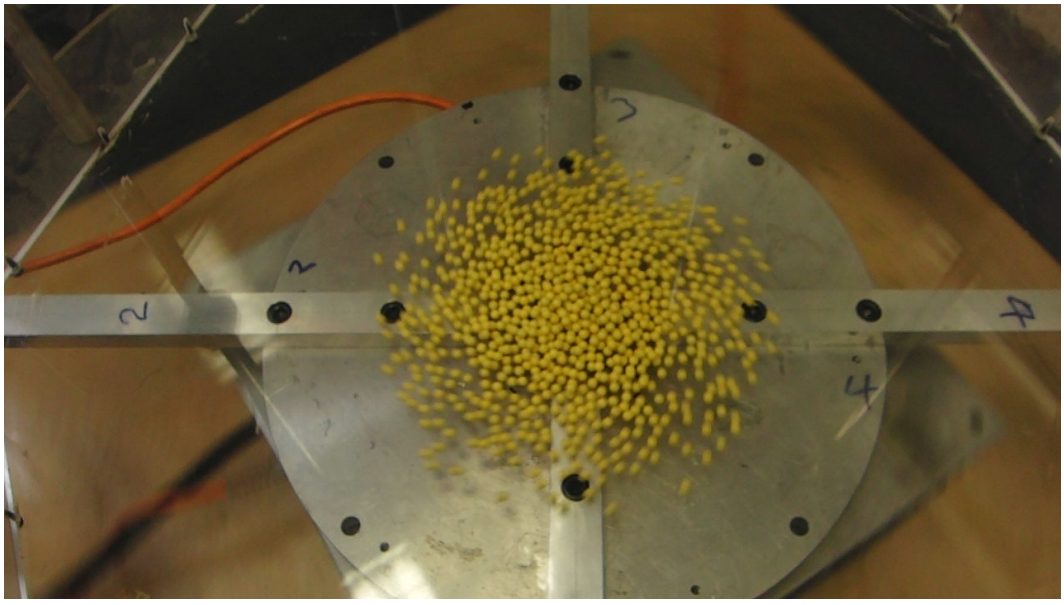

(b)

Figure 7.18: Column collapse of $r_0 = 25\,\mathrm{mm}$ $a = 1.30$ consisting of BB pellets with $d = 5\,\mathrm{mm}$ ($s = 5$) with a rotational frequency $f = 0.98\,\mathrm{Hz}$ (anticlockwise). The camera is mounted within the rotating frame of reference. (a) 0.20 s. (b) 0.27 s.

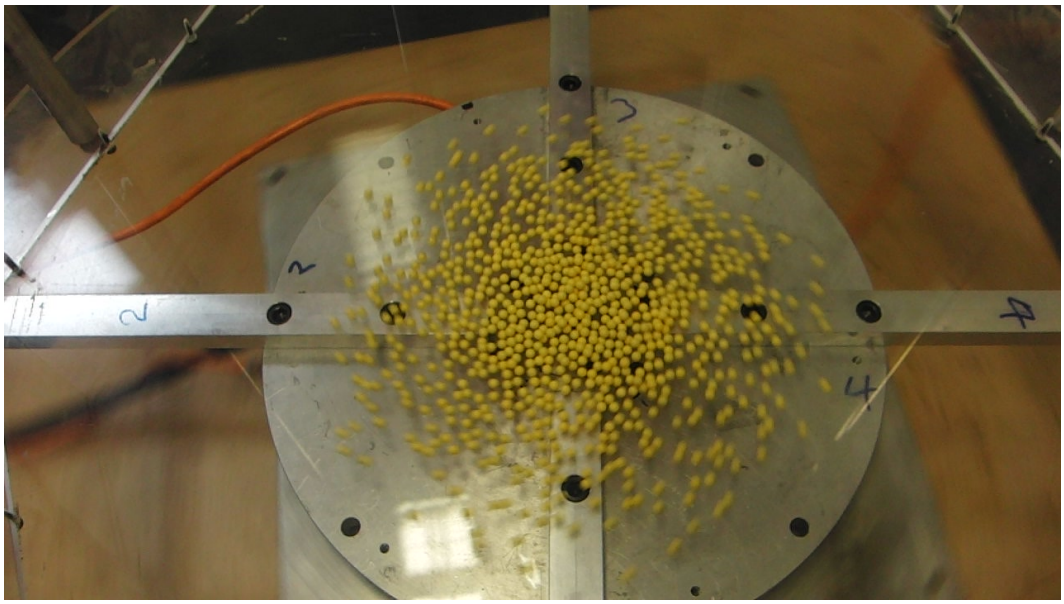

(a)

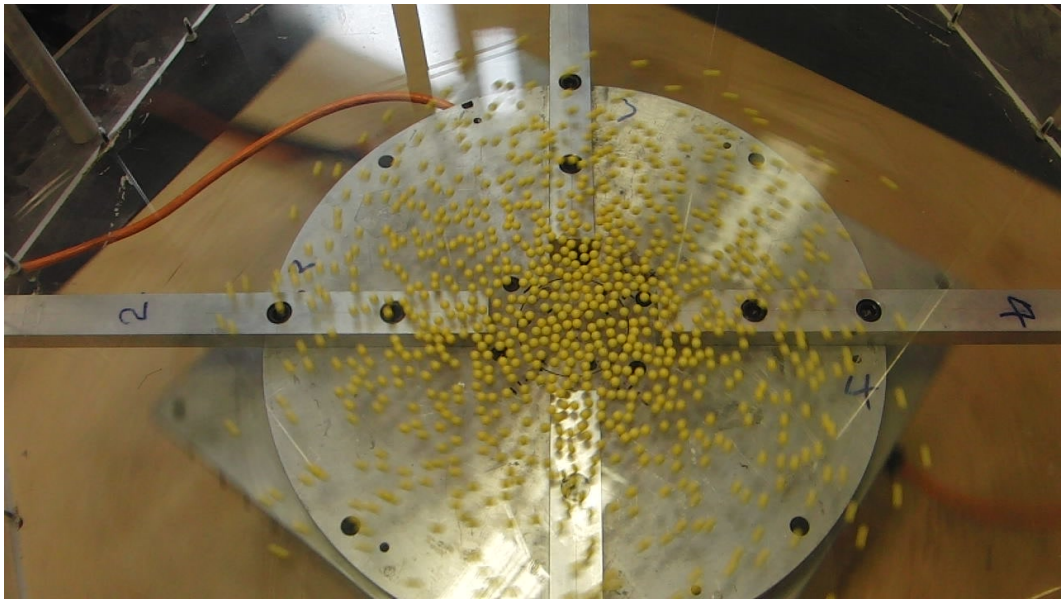

(b)

Figure 7.19: Column collapse of $r_0 = 25\,\mathrm{mm}$ $a = 1.30$ consisting of BB pellets with $d = 5\,\mathrm{mm}$ ($s = 5$) with a rotational frequency $f = 0.98\,\mathrm{Hz}$ (anticlockwise). The camera is mounted within the rotating frame of reference. (a) 0.33 s. (b) 0.47 s.

or removing the cylinder vertically could severly affect spiral arm development.

7.6 Discussion

This prelimary investigation using DEM has produced some intriguing dynamics and pattern formation processes, which if proven with greater verification display a previously unobserved flow regime. Its existence evidently stems from the sphericity of the particles that allow rolling and ease of reorganisation, and the small system size preventing stability of granular force chains also due to the small contact area arising from sphericity. Non-spherical particles are more likely to slide than roll and so will not travel further - this reasons why this was not observed in experiments in Chapter 6 although an uneven periphery seen in the resultant pile in Figure 6.4 could be the result of attempts to form such structures. DEM simulations with spherical particles of stationary 2D column collapse severely overestimate the runout in comparison to the physical experiments using irregular shaped grit and sand as discussed in Section 2.5.3. Observing an even greater exaggerated runout (to the extent of a monolayer) when including rotation in 3D DEM simulations of spherical particles is then not that much of a suprise when making the comparison to experiments in Chapter 6 which use irregular shaped limestone particles.

The simulation setup resulted in the formation of several spiral arms which appear insensitive to large changes in frequency, with particle-surface friction only affecting the curvature of resultant arms. An increase in the initial cylinder size, and hence system size, caused an additional arm to form although it was weak in appearance. This suggests that the system size is largely responsible for the exact pattern formation, although it is possible that this in combination with initial cylinder size for a fixed frequency given that a particles at the periphery of a larger cylinder will experience a greater initial velocity. The morphology of the arms is reminicent of experiments performed by Zoueshtiagh and Thomas [2000] where spiral arms formed with a central patch in a rotated granular bed immersed in water.

The simulations took a long time to run (approximately a week) as the code relied on CPU processing which has a limited amount of processing cores. LIGGGHTS has recently been ported to run on GPUs (graphics cards) which can have in excess of 20 times the processing power, allowing a greater number of simulations to be run. It is intended in the future to complete futher simulations to further probe the effect of parameters on the formation of the spiral structures.

Chapter 8

Conclusions

8.1 Objectives evaluation

Throughout this thesis several experimental and numerical studies have been discussed that have lead to a greater understanding of the stationary granular column collapse, and its response to induced rotation. A large part of this thesis has resulted in several submitted/accepted publications as listed in the declaration.

The stationary collapse of a granular column has been the subject of numerous studies of the last decade as discussed in the literature review in Chapter 2, but investigations have found further intracacies that were not previously observed. The use of a laser scanning arm has significantly increased measurement accuracy in the evaluation of the measurements of a resultant deposit. With measurements being sub-grain size (0.12 mm accuracy against a $0.60 - -0.80$ mm particle size) the inaccuracies arising are purely due to experimental method. The key result from this investigation is that column collapse is not an exception to meso scale effects - something not uncovered in the two key studies by Lube et al. [2004]; Lajeunesse et al. [2004]. This effect appears to saturate at system sizes in excess of $s = 100$ but the onset is evidently dependent on the quantity investigated.

The use of XCT to investigate the internal structure of the column pre and post collapse is an experimental first, and further one of the first applications to an evolving granular system. For this reason, all results displayed are previously physically unexplored. This unique study concentrates on the packing fraction within the column and pile, revealing a different distribution of particle density within the pile for different flow regimes. Furthermore this indicates the onset of a jamming phase for aspect ratios $a > 1.7$ which as stated by Staron and Hinch [2005] becomes problematic to hydrodynamic approximations to theoretically model the flow. The best approximation is given by the $\mu(I)$ rheology as proposed by Lagrée et al. [2011] discussed in Section 2.4.4. This knowledge reasons why the modelled runout of the pile starts to diverge from the reality, which could be used to further improve the

model, likely to lead to local rheology considerations.

Consideration given to the collapse under rotation is the first such study exploring this adaptation. Many of the scaling laws previously found by Lube et al. [2004]; Lajeunesse et al. [2004] for the stationary collapse have been reworked to include this effect, often saturating following mass ejection resulting from a secondary rotation-induced spreading phase where a different scaling takes over. This work consisted of three independent variables, a, r_0 and f, leading to a great number of experiments and evaluation to find appropriate relationships. The setup is a simplification of a spreader system to distribute grains and seeds, with the analysis providing information on how such a system system evolves. With hydrodynamic approximations being sensitive to jamming phases, a data set would be required to verify a model of this particular setup which has been provided by this investigation.

Further, preliminary results from a numerical DEM study are given for the simulated rotating column collapse with spherical particles. This endeavour resulted in the unexpected development of spiral arms with some analysis of the new flow regime and particle movement presented. Their existence results from the sphericity of the pile and the small system size enabling weak granular chains preventing the formation of a resultant pile, but instead spread to a monolayer. The difficulty lies with proper verification that this is infact real; some initial attempts have been made and while progress towards a resulting monolayer has been made, the particles have yet to form dense bands. The experimental verification has been slowed by difficulty in obtaining appropriate particulates, but is something for future investigation. There is also the strong possiblity of the structures formation being sensitive to small peturbations in concentricity of the equipment and raising of the cylinder which could be playing equal part in their production.

8.2 Suggestions for further work

The flow and scalings of stationary axisymmetric column collapse are well known, with the precision increased in the presented study. Further information could yet be gleaned from XCT investigations pre and post collapse. It is now known that there is movement within the proposed conical failure envelope of the column collapse, but it is expected that the movement is small. If the movement is small enough then digital volume correlation (DVC) could be applied to find how particles within this region have redistributed themselves.

Another potential work could find grain contacts resulting in realisation of force chain networks within the column and resultant pile. This is not a small task working with hundreds/ a few thousand 2D slices requiring significant image processing through a method known as *'watershedding'*, noted as a future challenge

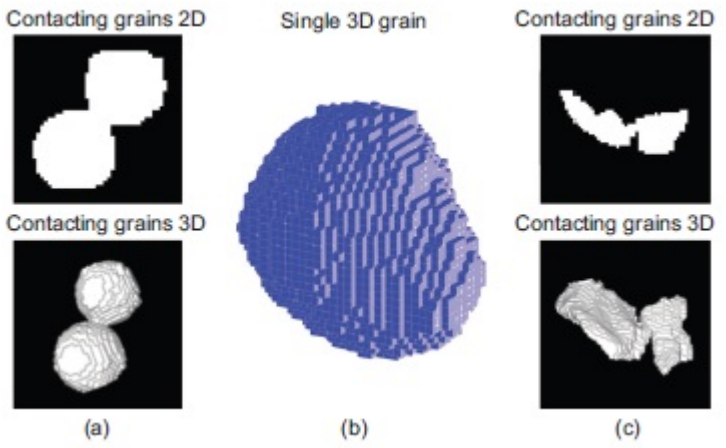

Figure 8.1: The method of watershedding must be applied to grains to find their contacts. XCT scans of two spherical ballotini particles in (a) 2D. (b) 3D. (c) 'Voxelised' grain from segmentation. XCT scans of two 'real' particles in (d) 2D. (e) 3D [**?**]

to be overcome by researchers Andò et al. [2013]. This is where a volume is grown within a single grain until there is contact with another grain's growing volume. At this point the contact could be marked, and the grain volume reduced by a pixel to prevent two grains being realised as one. Examples of two grains in contact can be seen in Figure 8.1, where the difficulty in separation can be seen as XCT frequently realises the grains as one volume.

Of course in an ideal world, XCT could be applied fast enough such that the entire internal variations of the pile can be seen at discrete timesteps within the collapse. Quick scans can be performed with particular setups, but induce rotation on the sample which changes the experiment. An appropriate arrangement of the technology is yet to be designed to keep the object stationary and acquire images in all views of a rotational plane fast enough.

As suggested at the end of Chapter 6, a further adaptation of the collapse of column under rotation would be to use slurries. The non-newtonian nature of the material is sure to produce interesting shearing results and likely to result in the formation of surface structures. Unsure of the precise dynamic of how the flow would evolve, it is certainly sparks curiosity.

It is obvious that preliminary results in Chapter 7 need to be brought to a satisfying conclusion. Initial satisfaction could be gained by better verification that the effect is indeed real. A range of spherical particulates and cylinder sizes need to be trialled while keeping the system size small. If the experimental setup is extremely sensitive to initial conditions, it could be that the sprial arms are only observable on a handful of occasions and will suffer from repeatability issues. If this

could be overcome then further steps towards symmetry breaking could be made.

8.3 Closing remarks

Two of the studies presented used investigative technology that is sparsely used within the granular community; a laser scanning arm and an XCT scanner. The obvious limitation is that there is no temporal scale - it requires the object being investigated to be static. But it is my belief that technologies such as this, in particular XCT, and their development will prove to be invaluable within granular research in years to come - just as PIV was revolutionary to the study of fluid flows.

While XCT requires items to be static for the duration of the scan, this can be overcome in certain experiments where the condition applied to the setup can be stepped in time. In this manner a pseudo temporal scale can be utilised for micro structure characterisation of granular materials. There is a large amount of development in XCT at the moment where setups exist that can perform a scan in 30 pico-seconds which is ideal for a granular flow, but suffers as the object must complete a full rotation in this time which could alter the experiment. In addition for 'quick' scanning the field of view is often significantly smaller so the beam can be concentrated and brighter to overcome additional technicalities. To overcome this a more complex system consisting of a rotating gantry with multiple sources and detectors could be used, currently being considered by a group at University of Manchester.

In its generality, I believe the advancement of these technologies will be integral to garnering a deeper understanding of granular structures and flows and certainly an area to watch - further it is an avenue I will continue to explore after the completion of my PhD.

Appendix A

Equipment technical drawings

Contained within this appendix is a series of technical drawings that were used by technicians for the manufacture of the equipment outlined in Chapter 3. Each part is divided into a series of modules as detailed in page 2 of the full assembly technical drawings. Part A refers to a mirror housing to be placed above the inner rig. This was never used in experiments so not been included in this appendix, although it is clearly shown in the full assembly technical drawing.

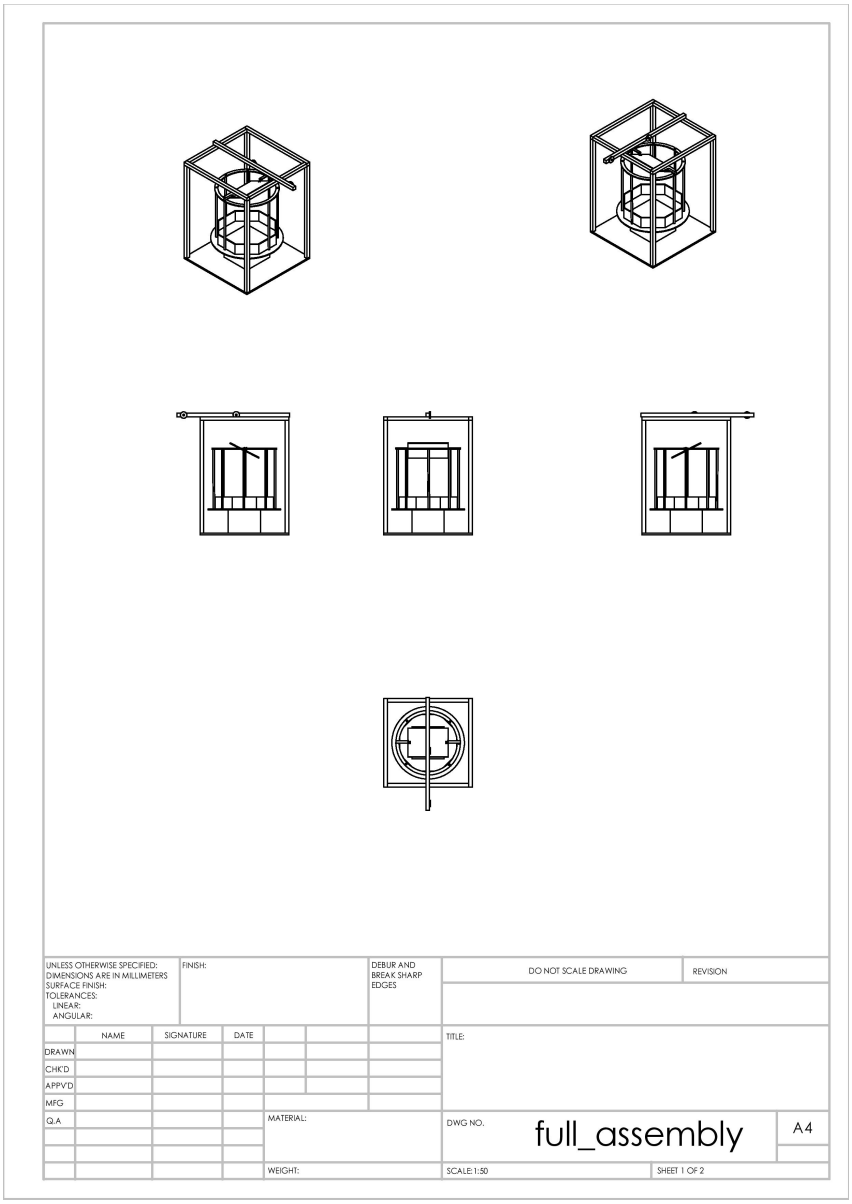

Figure A.1: Full assembly page 1.

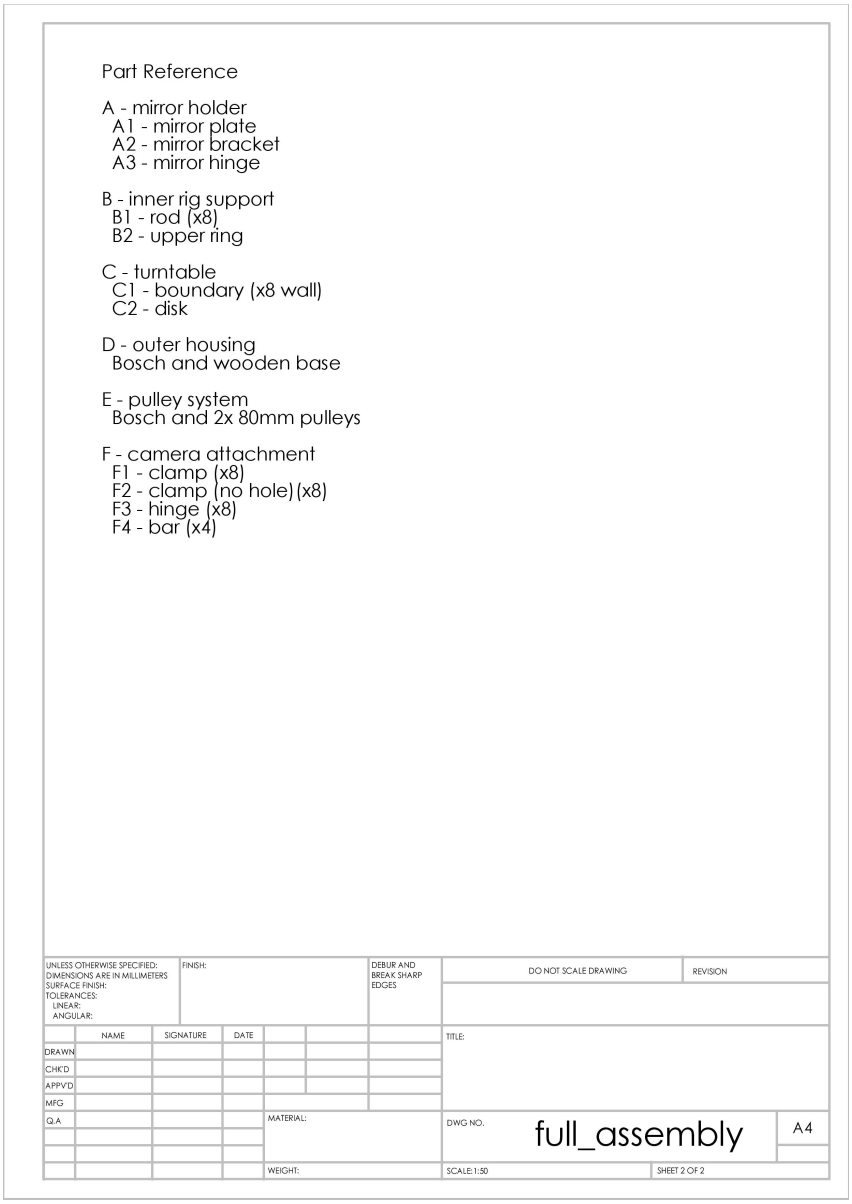

Figure A.2: Full assembly page 2.

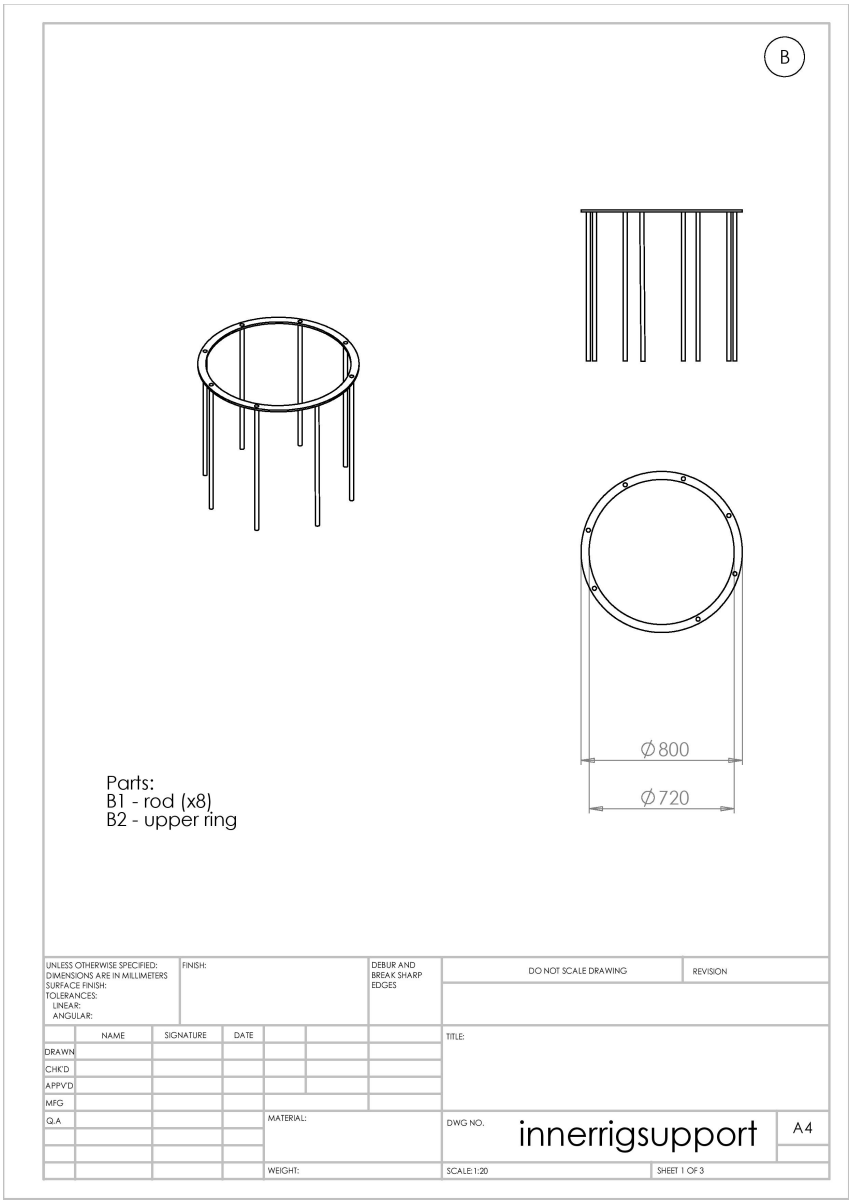

Figure A.3: Inner rig support page 1.

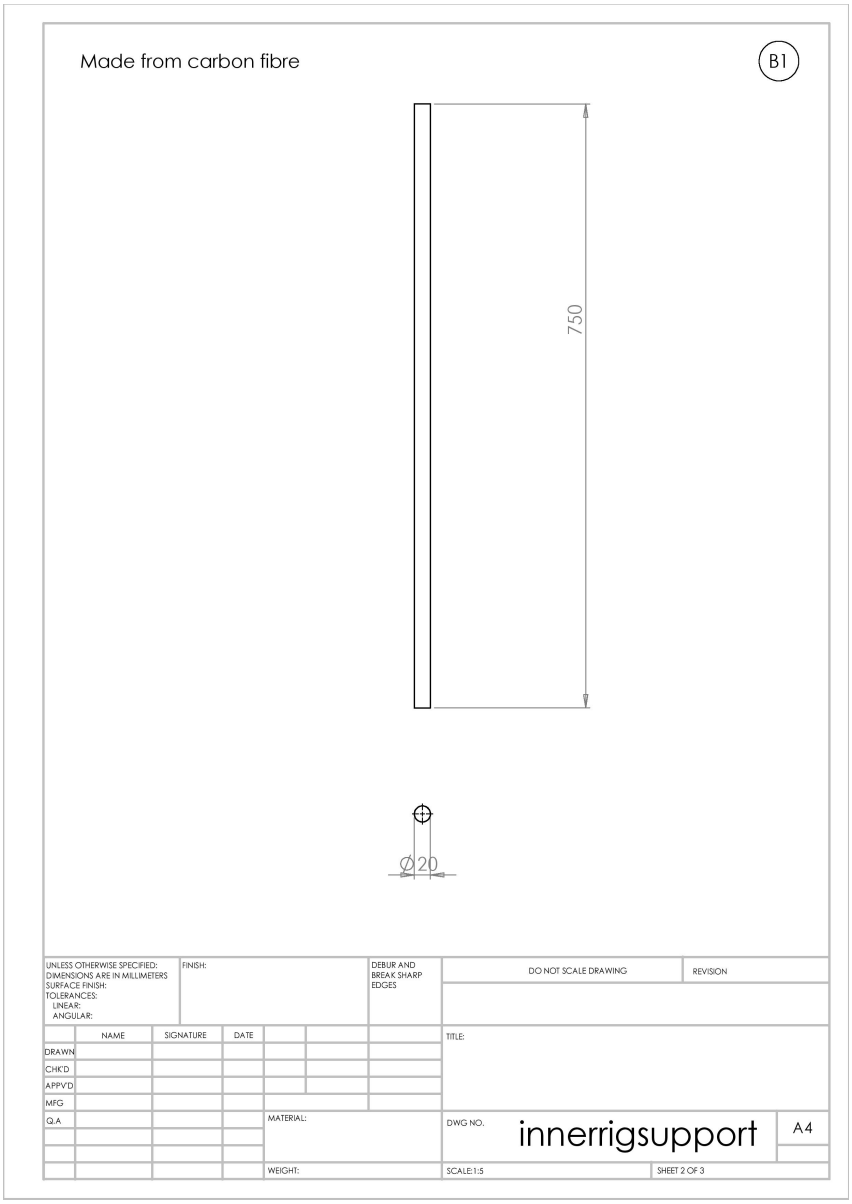

Figure A.4: Inner rig support page 2.

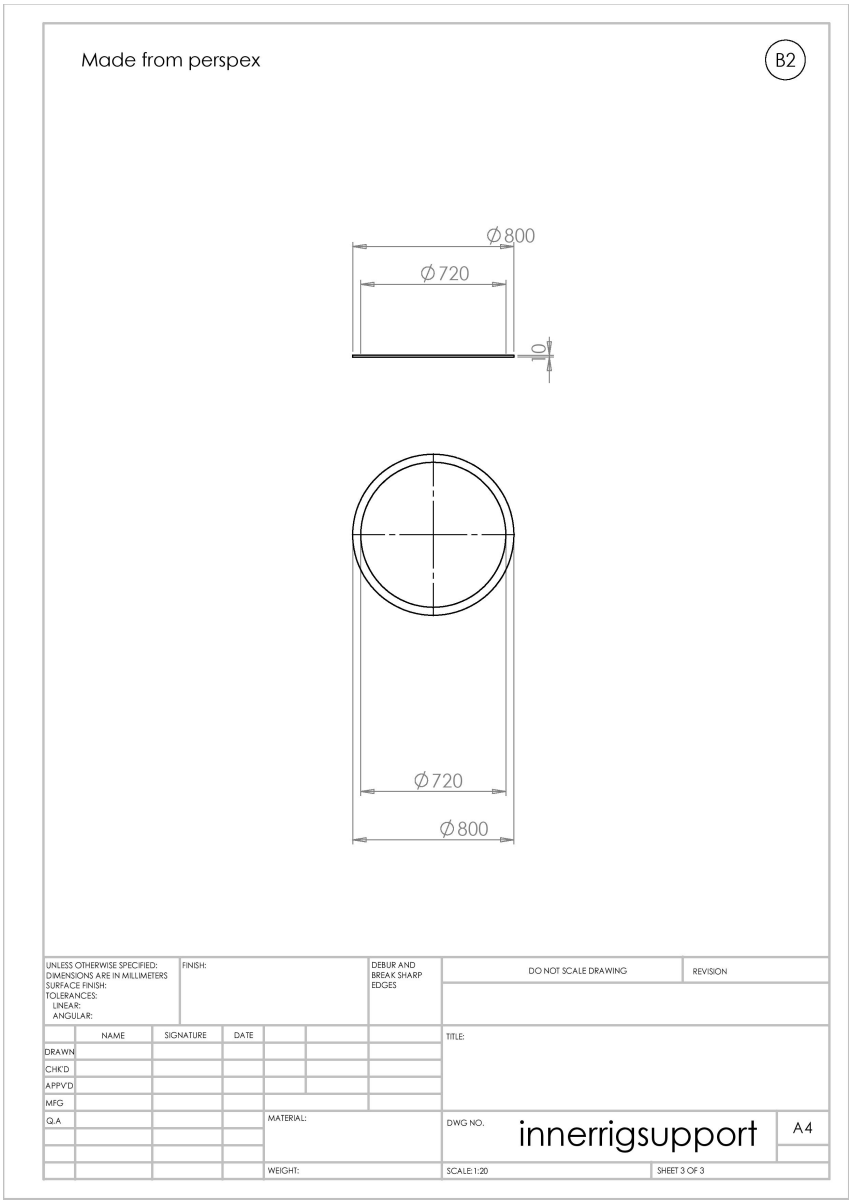

Figure A.5: Inner rig support page 3.

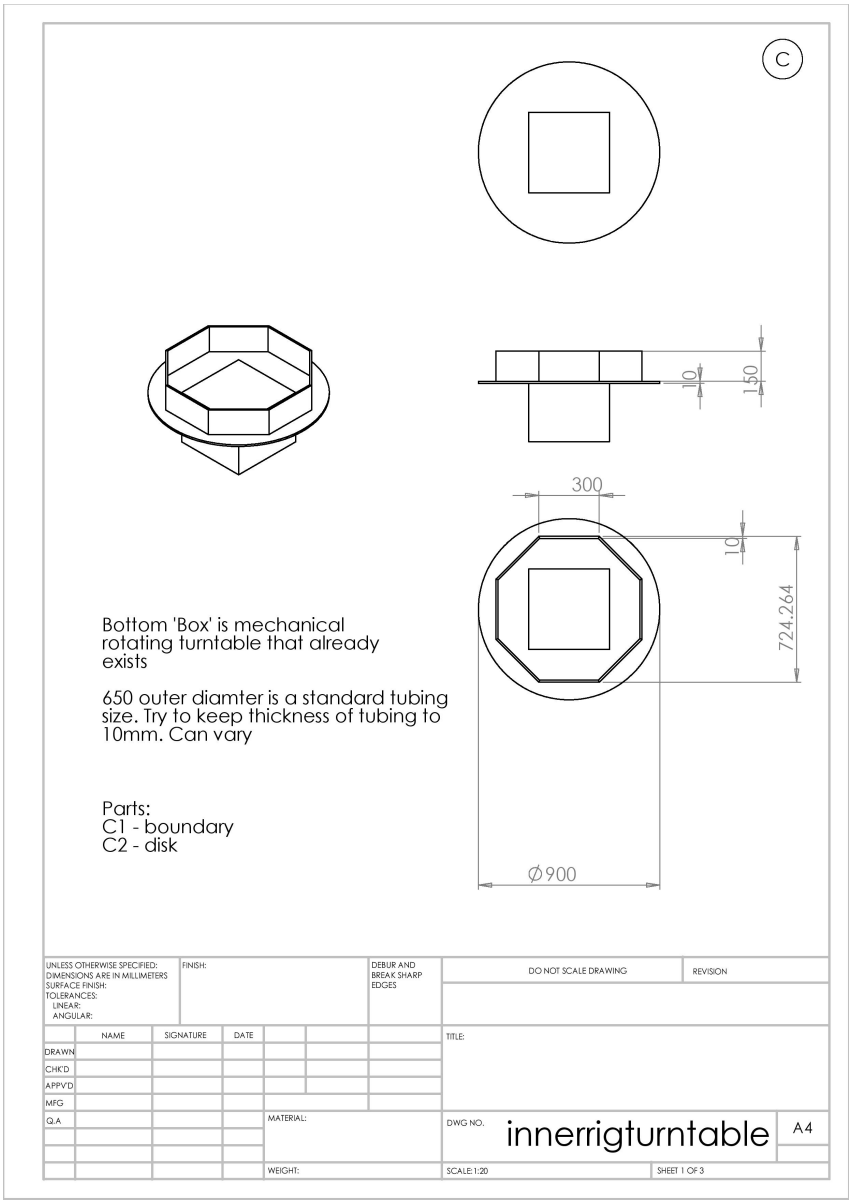

Figure A.6: Inner rig turntable page 1.

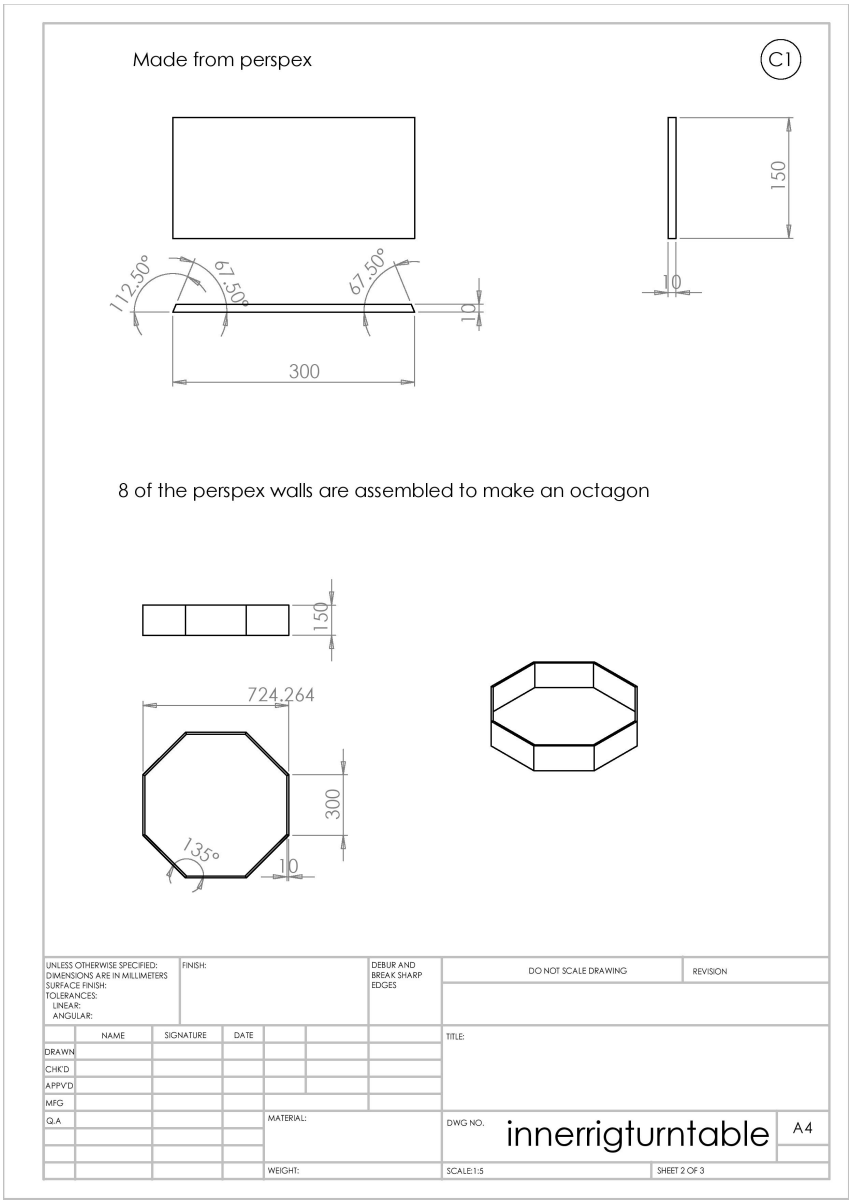

Figure A.7: Inner rig turntable page 2.

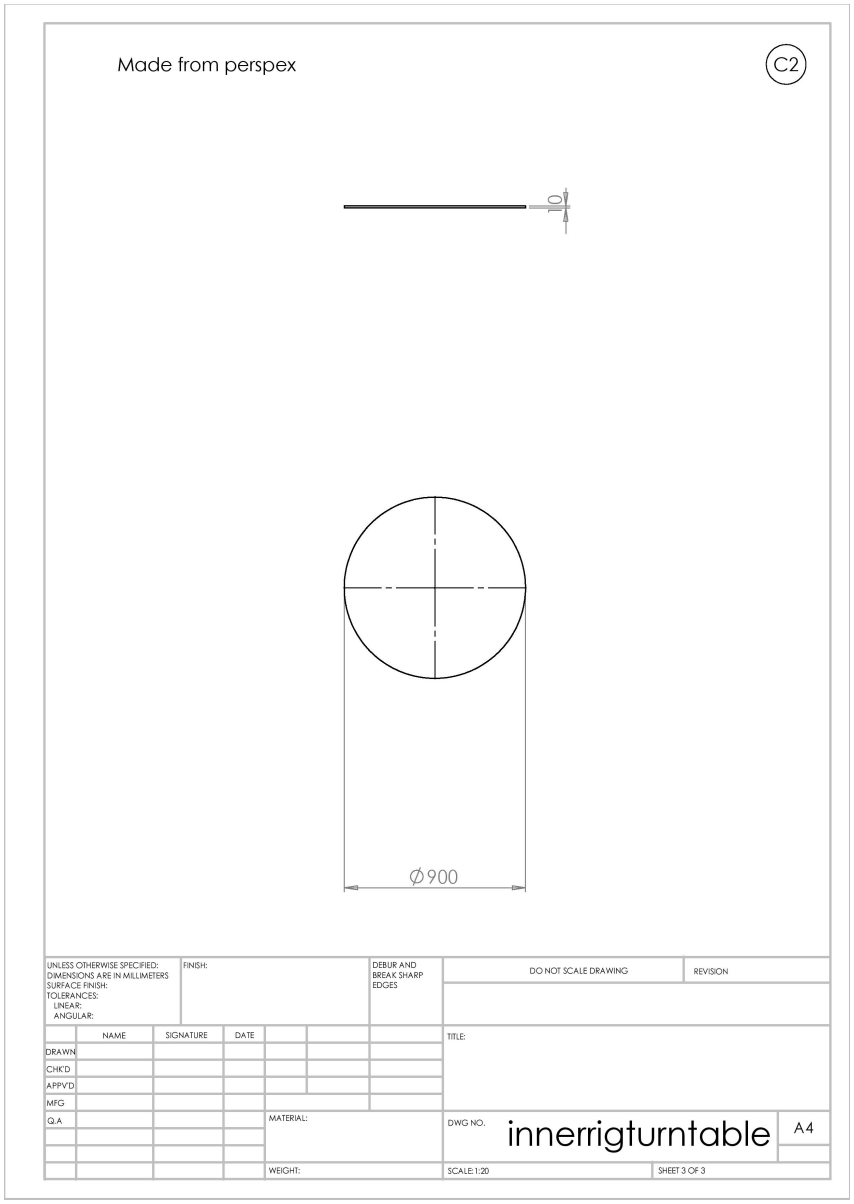

Figure A.8: Inner rig turntable page 3.

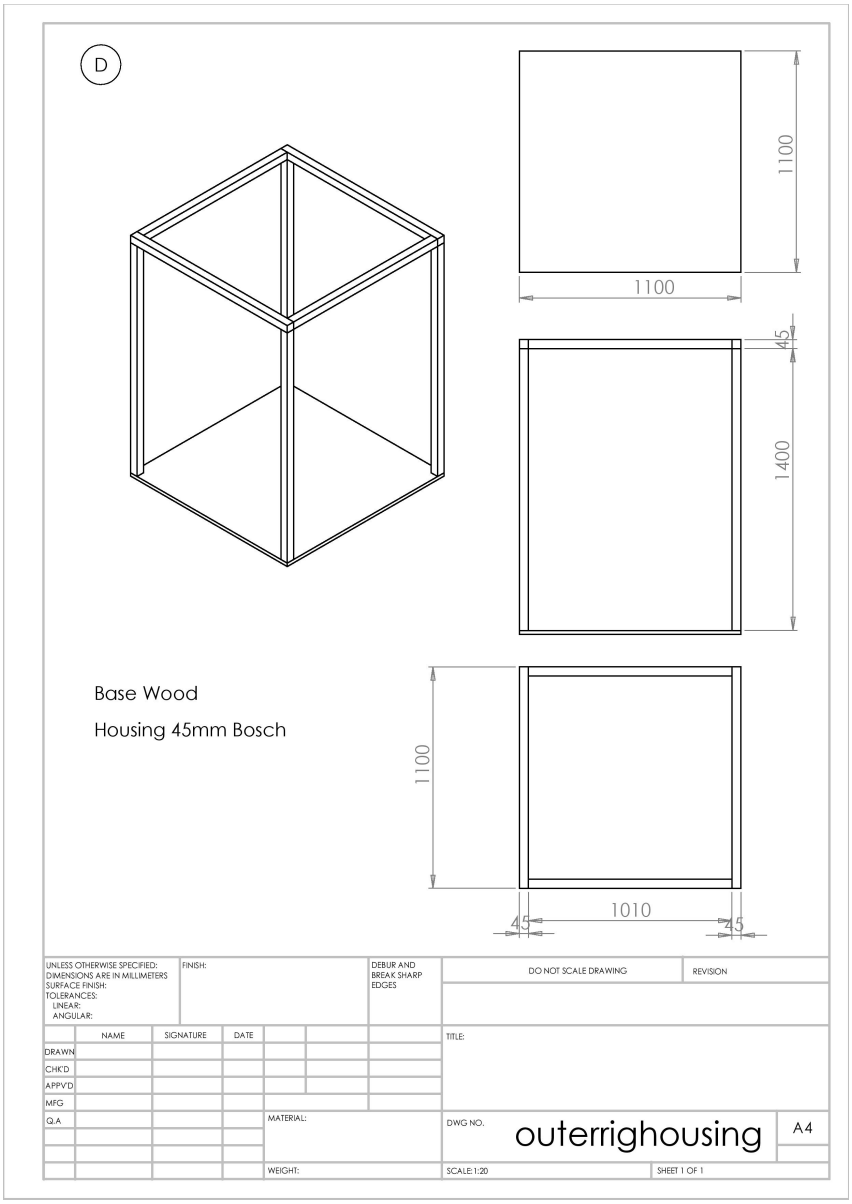

Figure A.9: Outer rig housing page 1.

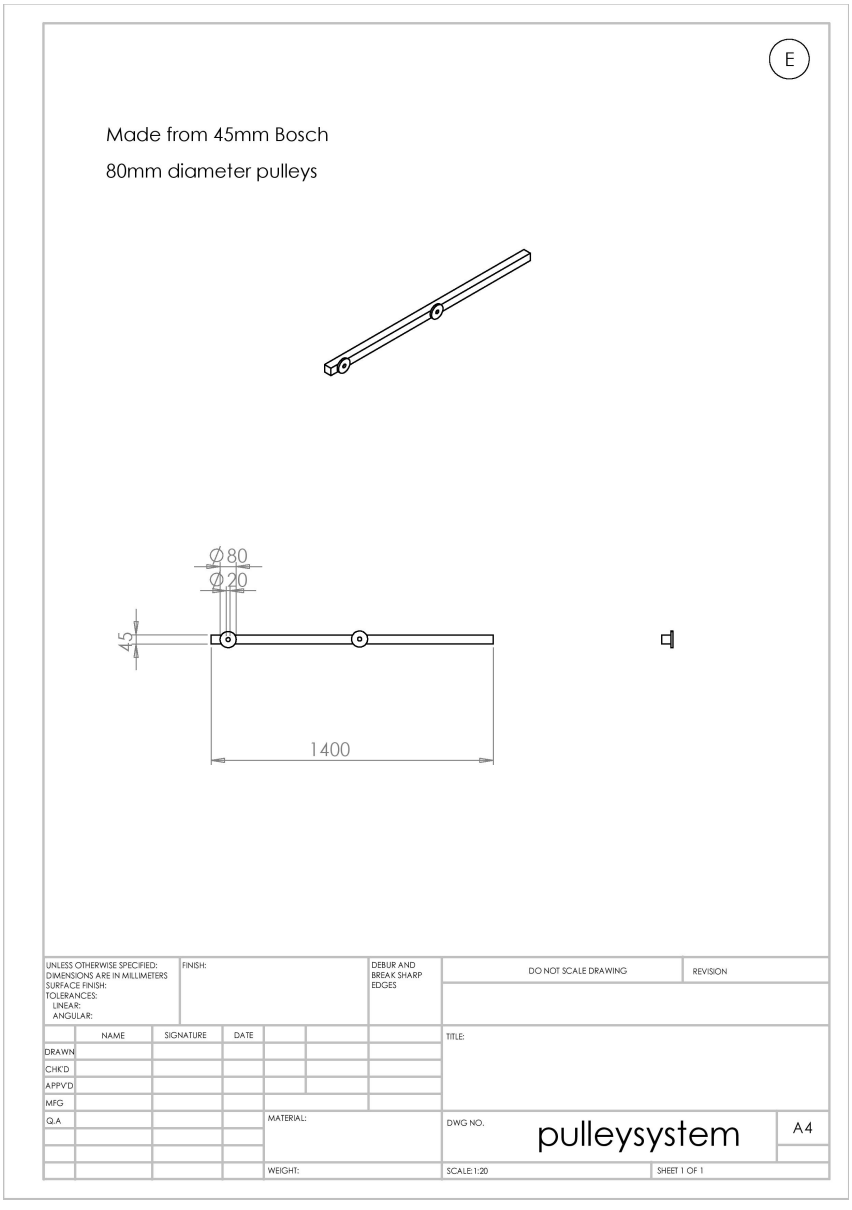

Figure A.10: Pulley system with plinth. Note that the plinth material states 'Bosch' where infact it was decided that wood was appropriate.

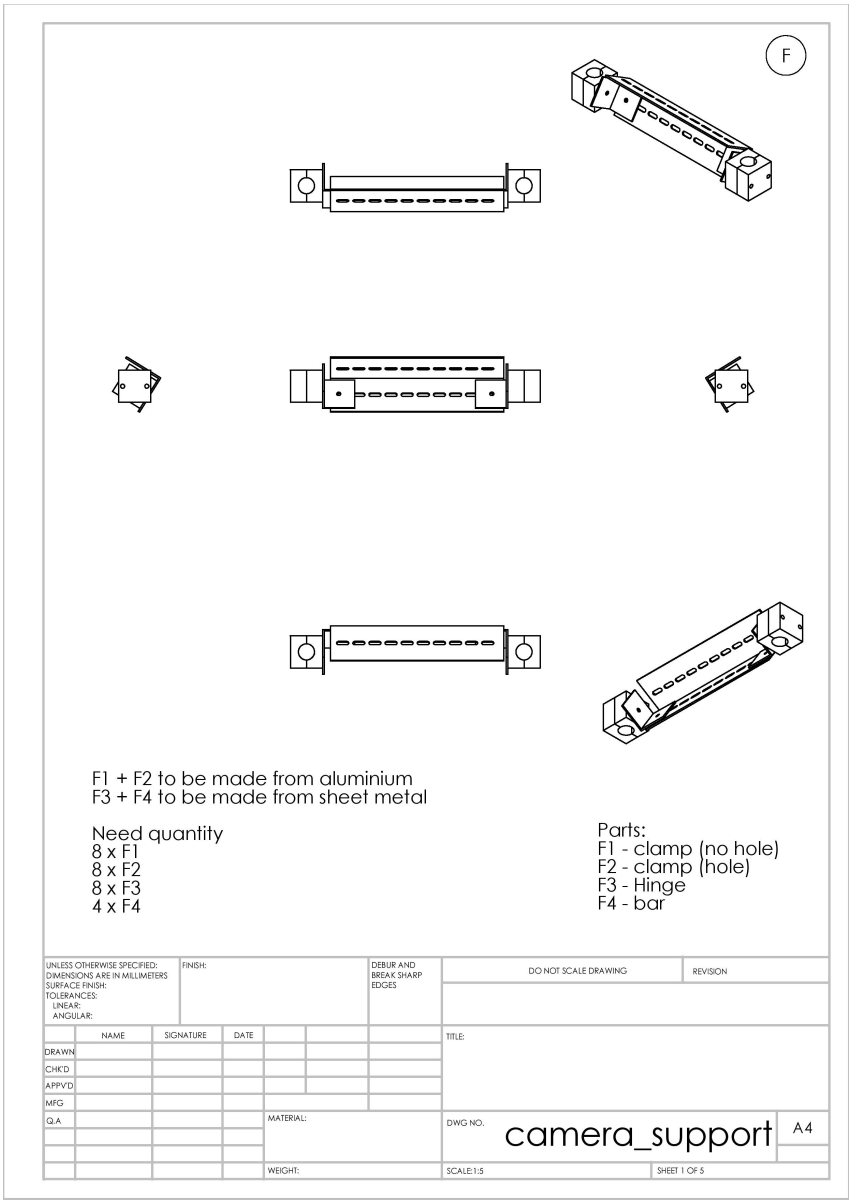

Figure A.11: Camera support page 1.

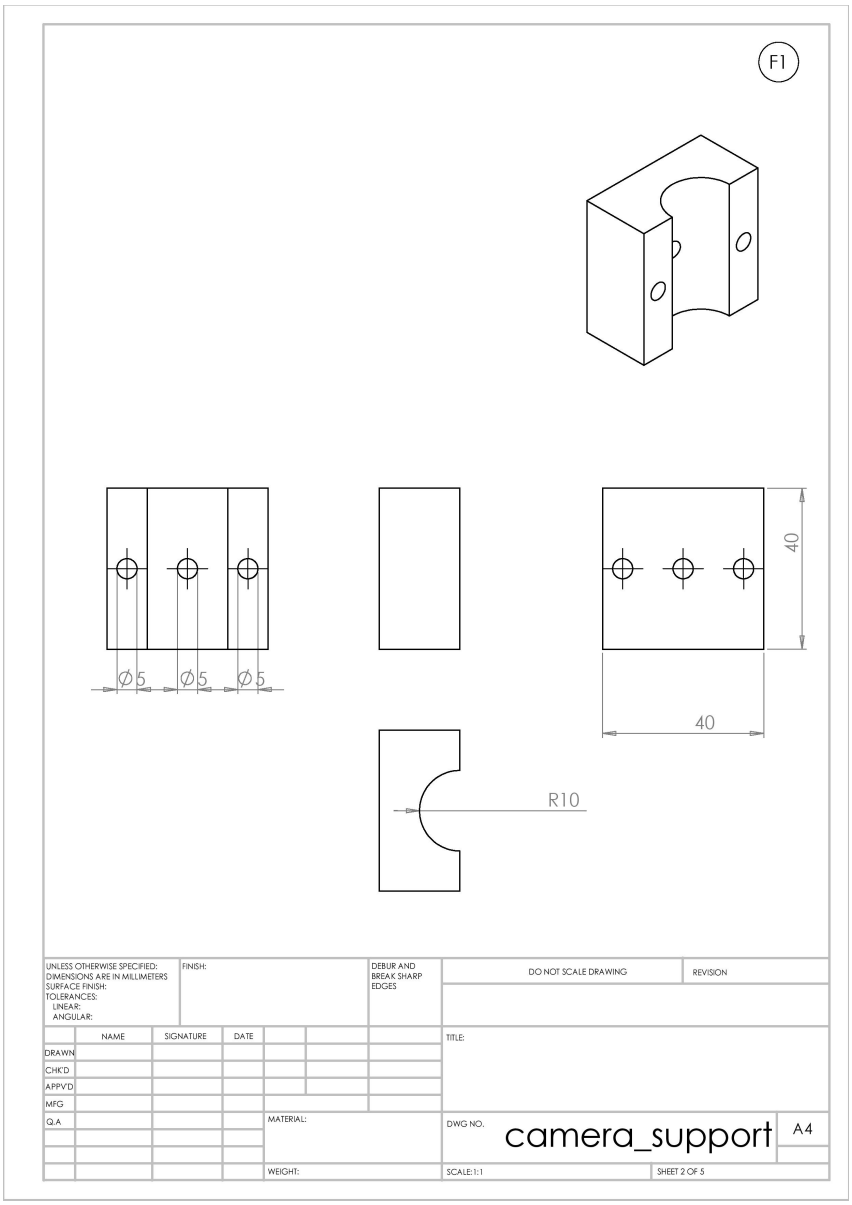

Figure A.12: Camera support page 2.

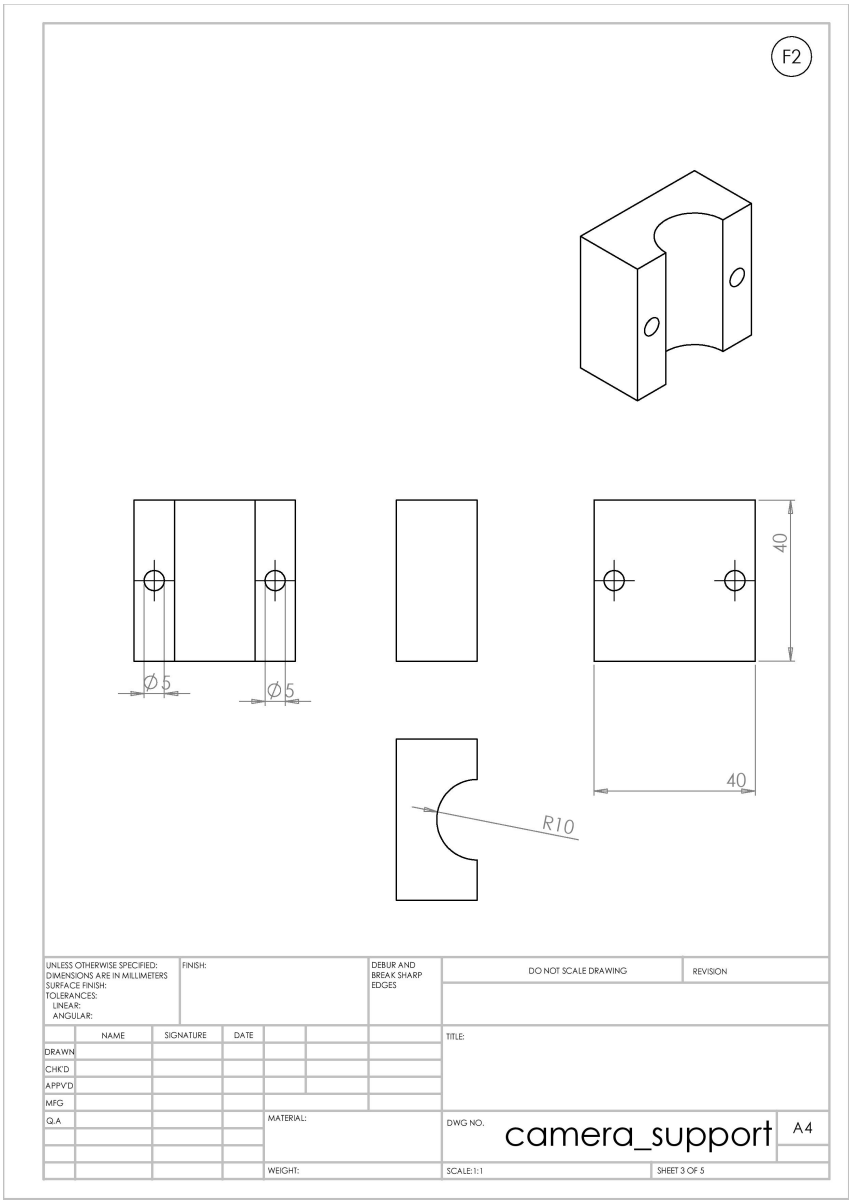

Figure A.13: Camera support page 3.

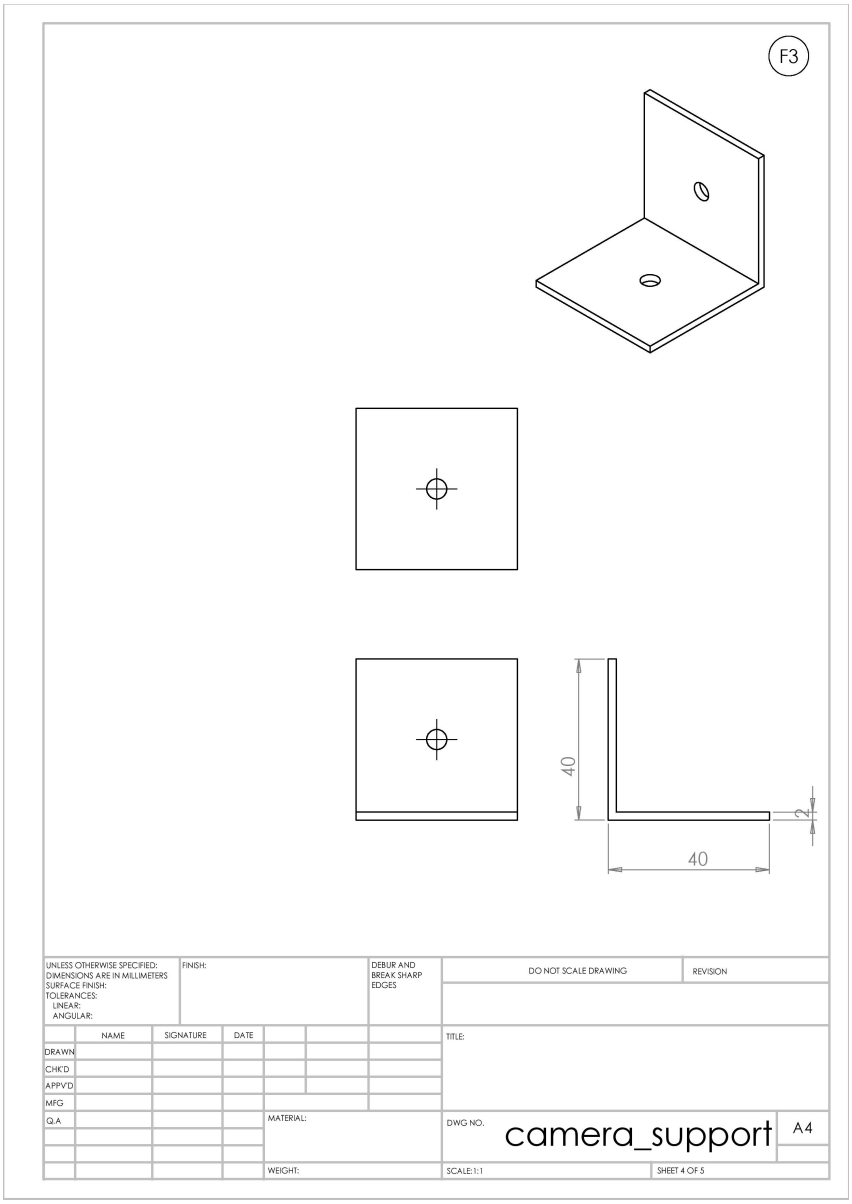

Figure A.14: Camera support page 4.

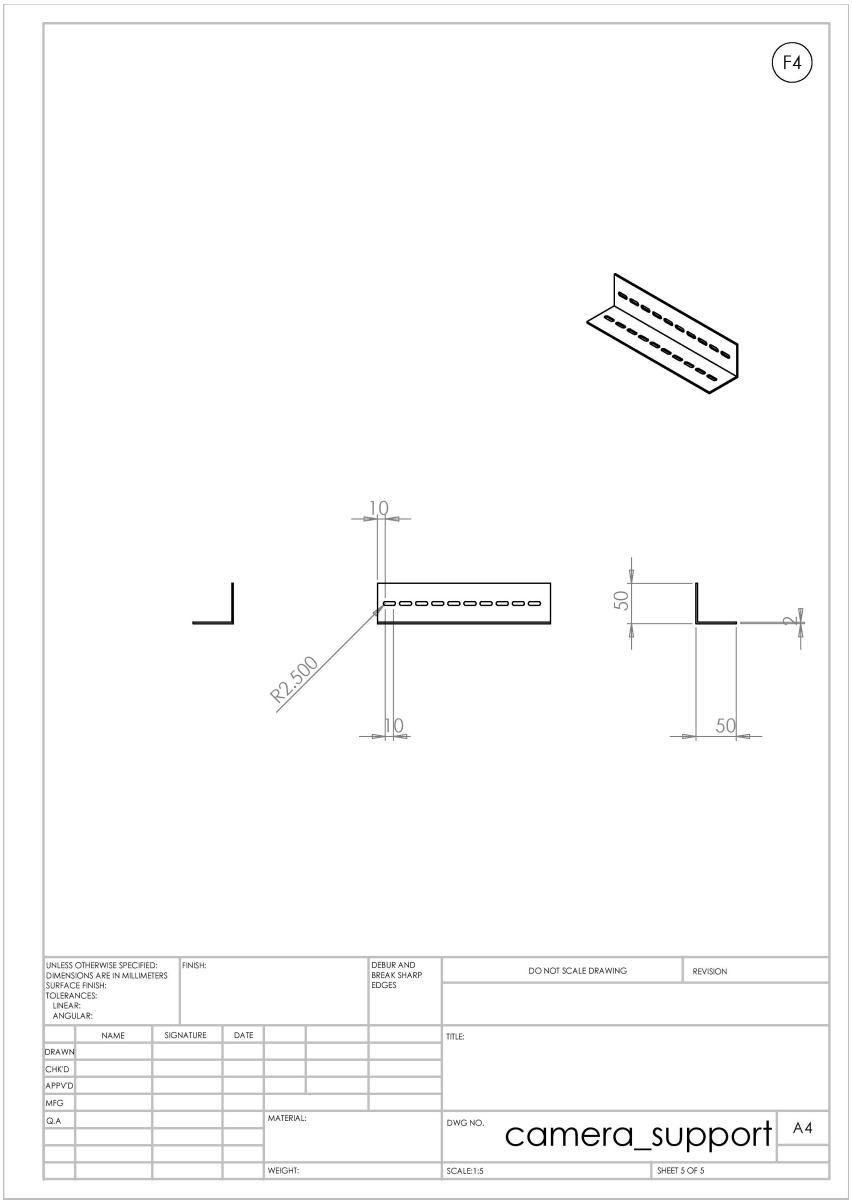

Figure A.15: Camera support page 5.

Appendix B

Experimental data: Stationary Collapse

This appendix contains the data evaluated in the static collapse of a granular column outlined in Chapter 4

Nonclamenture:

$\#$	run number
r_0	(mm) initial column radius
$r_{f,i}$	(mm) final pile radius where $i = 1, 2, 3, 4, av$ (av=average)
r_*	normalised final pile radius
r_s	(mm) pile summit radius
r_s^*	normalised pile summit radius
h_0	(mm) initial column height
h_f	(mm) final pile height
h_*	normalised final pile height
a	initial column aspect ratio
d	(mm) particle diameter
ϕ	mean packing fraction
$\alpha_{b,i}$	($^\circ$) angle at base of pile where $i = 1, ..., 8, av$ (av=average)
$\alpha_{s,i}$	($^\circ$) angle at summit of pile where $i = 1, ..., 8, av$ (av=average)

Repeatability study:

all r_0	Tables B.1 and B.2

Main results:

$r_0 = 20$mm	Tables B.3–B.6
$r_0 = 25$mm	Tables B.7–B.10
$r_0 = 30$mm	Tables B.11–B.14
$r_0 = 35$mm	Tables B.15–B.18
$r_0 = 40$mm	Tables B.19–B.22
$r_0 = 45$mm	Tables B.23–B.26
$r_0 = 150$mm	Tables B.27–B.30

r_0	h_0	a	min r_f	max r_f	(max - min)/d	Δr	h_f
20	10.0	0.50	29.87	31.42	2.2	2.71	10.0
20	10.0	0.50	29.12	30.59	2.1		10.0
20	10.0	0.50	28.71	30.08	2.0		10.0
20	25.0	1.25	40.00	42.80	4.0	3.63	18.0
20	25.0	1.25	40.95	43.55	3.7		18.3
20	25.0	1.25	39.92	42.17	3.2		18.3
20	50.0	2.50	54.88	58.02	4.5	5.65	18.4
20	50.0	2.50	55.31	58.10	4.0		19.0
20	50.0	2.50	52.45	55.97	5.0		18.0
25	10.0	0.40	36.21	36.89	1.0	2.04	10.0
25	10.0	0.40	35.36	36.71	1.9		10.0
25	10.0	0.40	34.93	36.97	2.9		10.0
25	30.0	1.20	53.48	54.91	2.0	2.88	23.8
25	30.0	1.20	52.35	54.81	3.5		22.5
25	30.0	1.20	52.03	53.95	2.7		22.6
25	90.0	3.60	94.58	97.82	4.6	5.59	24.7
25	90.0	3.60	92.90	96.36	4.9		23.0
25	90.0	3.60	94.89	98.49	5.1		24.9
30	20.0	0.67	50.43	51.99	2.2	3.21	20.0
30	20.0	0.67	50.67	52.35	2.4		20.0
30	20.0	0.67	49.14	51.30	3.1		20.0
30	55.0	1.83	86.24	89.70	4.9	3.94	27.4
30	55.0	1.83	86.32	89.15	4.0		28.9
30	55.0	1.83	85.76	89.28	5.0		28.4
30	100.0	3.33	111.61	114.92	4.7	4.47	29.8
30	100.0	3.33	112.39	115.82	4.9		29.1
30	100.0	3.33	112.60	116.08	5.0		31.0
35	30.0	0.86	66.47	68.61	3.1	3.98	30.0
35	30.0	0.86	65.17	67.72	3.6		30.0
35	30.0	0.86	66.98	69.15	3.1		30.0
35	75.0	2.14	111.32	114.76	4.9	5.16	33.5
35	75.0	2.14	110.57	114.38	5.4		33.1
35	75.0	2.14	109.06	112.41	4.8		34.6
35	180.0	5.14	171.51	174.37	4.1	5.14	35.4
35	180.0	5.14	169.73	173.18	4.9		36.2
35	180.0	5.14	169.23	172.61	4.8		37.1

Table B.1: Results from repeatability testing to find the minimal and maximal radius, the difference between them on a single run and the height. The difference between the smallest minimum and the largest maximum is given by Δr.All measurements are given in millimeters with the exception of (max - min)/d which is a number of particle diameters.

r_0	h_0	a	min r_f	max r_f	(max - min)/d	Δr	h_f
40	70.0	1.75	115.86	119.32	4.9	4.23	38.5
40	70.0	1.75	116.47	119.73	4.7		37.9
40	70.0	1.75	115.50	118.79	4.7		37.5
40	120.0	3.00	148.00	151.41	4.9	3.49	38.8
40	120.0	3.00	147.80	151.29	5.0		39.9
40	120.0	3.00	149.12	152.05	4.2		39.5
40	155.0	3.88	167.61	171.15	5.1	5.97	39.1
40	155.0	3.88	170.24	173.58	4.8		41.8
40	155.0	3.88	169.80	172.95	4.5		41.0
45	45.0	1.00	97.24	99.57	3.3	3.08	39.6
45	45.0	1.00	96.53	99.16	3.8		40.8
45	45.0	1.00	97.09	99.61	3.6		40.6
45	65.0	1.44	122.71	125.38	3.8	3.14	41.2
45	65.0	1.44	123.29	125.85	3.6		40.8
45	65.0	1.44	123.17	125.83	3.8		41.9
45	180.0	4.00	193.66	197.16	5.0	4.30	44.9
45	180.0	4.00	194.12	197.74	5.2		45.3
45	180.0	4.00	193.44	196.78	4.8		45.6
75	30.0	0.40	102.81	104.68	2.7	2.82	30.0
75	30.0	0.40	102.10	104.16	2.9		30.0
75	30.0	0.40	103.00	104.92	2.7		30.0
75	90.0	1.20	180.42	183.18	3.9	3.53	67.7
75	90.0	1.20	179.94	182.65	3.9		68.4
75	90.0	1.20	179.65	182.48	4.0		69.1
75	120.0	1.60	218.73	221.49	3.9	4.65	69.2
75	120.0	1.60	218.86	222.13	4.7		70.9
75	120.0	1.60	217.48	220.94	4.9		70.4

Table B.2: Results from repeatability testing to find the minimal and maximal radius, the difference between them on a single run and the height. The difference between the smallest minimum and the largest maximum is given by Δr. All measurements are given in millimeters with the exception of (max - min)/d which is a number of particle diameters.

#	h_0	a	m_0	ϕ	$2r_{f,1}$	$2r_{f,2}$	$2r_{f,3}$	$2r_{f,4}$	$2r_{f,av}$	$r_{*,av}$	h_f	h_*
8	4.8	0.24	10	0.810	48.4	47.8	50.2	50.4	49.2	0.23	4.8	0.24
116	7.8	0.39	15	0.824	53.2	55.1	55.3	53.2	54.2	0.36	7.8	0.39
143	9.8	0.49	20	0.806	59.8	58.2	60.6	60.0	59.7	0.49	9.8	0.49
7	12.2	0.61	25	0.807	63.9	63.3	62.1	63.5	63.2	0.58	12.2	0.61
109	15.6	0.78	30	0.824	66.5	66.8	67.8	68.5	67.4	0.69	15.6	0.78
172	17.9	0.90	35	0.799	71.6	73.7	72.7	71.8	72.4	0.81	17.9	0.90
130	21.2	1.06	40	0.812	77.0	78.5	78.7	78.2	78.1	0.95	18.1	0.91
60	24.8	1.24	45	0.781	83.0	82.9	81.4	80.7	82.0	1.05	18.0	0.90
177	27.1	1.36	50	0.794	87.4	87.9	86.9	88.2	87.6	1.19	18.2	0.91
14	29.1	1.46	55	0.813	90.3	90.6	91.8	91.7	91.1	1.28	18.4	0.92
3	32.4	1.62	60	0.797	93.1	95.2	94.3	94.2	94.2	1.36	18.5	0.93
66	35.1	1.76	65	0.797	97.4	96.5	97.6	96.5	97.0	1.43	18.3	0.92
164	37.4	1.87	70	0.805	100.8	103.1	102.1	101.2	101.8	1.54	18.7	0.93
34	40.2	2.01	75	0.803	105.9	107.1	106.4	105.0	106.1	1.65	19.0	0.95
25	45.0	2.25	88	0.811	108.4	107.9	109.8	107.9	108.5	1.71	18.8	0.94
67	54.0	2.70	100	0.797	117.5	115.6	116.2	116.3	116.4	1.91	19.1	0.96
159	60.2	3.01	112	0.800	121.8	124.5	124.4	124.1	123.7	2.09	19.6	0.98
81	66.0	3.30	124	0.808	129.0	128.4	127.4	128.0	128.2	2.20	20.0	1.00
171	73.2	3.66	136	0.799	132.5	133.7	133.7	134.9	133.7	2.34	20.1	1.01
5	79.5	3.98	148	0.801	136.9	138.1	137.9	139.1	138.0	2.45	20.1	1.01
31	86.3	4.31	160	0.797	144.5	145.4	143.1	143.8	144.2	2.60	20.6	1.03
4	93.1	4.65	172	0.795	147.8	150.2	149.3	149.1	149.1	2.73	20.4	1.02
41	98.7	4.94	184	0.802	153.9	152.4	154.6	151.5	153.1	2.83	20.7	1.03
69	105.1	5.25	196	0.802	156.1	157.4	158.4	158.5	157.6	2.94	20.4	1.02
92	114.2	5.71	208	0.783	164.2	164.9	166.1	164.4	164.9	3.12	20.5	1.02
85	120.1	6.00	220	0.788	169.5	170.9	169.2	173.2	170.7	3.27	20.8	1.04
33	127.9	6.40	238	0.800	177.5	175.4	176.2	174.9	176.0	3.40	20.5	1.02
11	133.2	6.66	252	0.814	180.0	177.6	178.1	177.1	178.2	3.45	20.3	1.02
123	142.6	7.13	266	0.802	181.8	184.0	183.1	183.9	183.2	3.58	20.0	1.00
73	150.3	7.52	280	0.801	186.4	187.2	187.1	186.9	186.9	3.67	20.8	1.04
110	159.6	7.98	294	0.792	195.5	193.9	194.2	195.2	194.7	3.87	19.6	0.98
6	166.4	8.32	308	0.796	198.7	197.0	197.4	197.3	197.6	3.94	20.7	1.03
165	173.8	8.69	322	0.797	200.2	201.9	202.4	199.5	201.0	4.03	20.3	1.02

Table B.3: $r_0 = 20\,\mathrm{mm}$.

#	a	α_b	α_s	$2r_s$	r_s^*
8	0.24	27.8	40.7	32.0	0.2
116	0.39	23.8	35.2	28.2	0.3
143	0.49	18.6	33.2	23.3	0.4
7	0.61	15.8	29.1	16.7	0.6
109	0.78	13.4	27.4	12.7	0.7
172	0.90	12.6	26.5	5.8	0.9
130	1.06	12.0	24.9		
60	1.24	11.7	23.4		
177	1.36	11.1	22.3		
14	1.46	10.7	21.3		
3	1.62	10.3	22.0		
66	1.76	10.1	21.2		
164	1.87	9.3	20.8		
34	2.01	9.5	20.6		
25	2.25	7.5	19.6		
67	2.70	6.6	18.6		
159	3.01	8.4	18.4		
81	3.30	6.7	18.5		
171	3.66	6.9	18.0		
5	3.98	6.9	18.3		
31	4.31	7.9	18.0		
4	4.65	6.3	17.5		
41	4.94	8.2	17.8		
69	5.25	7.6	18.0		
92	5.71	7.4	17.7		
85	6.00	8.0	17.9		
33	6.40	8.1	17.6		
11	6.66	6.8	17.3		
123	7.13	7.2	17.5		
73	7.52	7.8	17.4		
110	7.98	7.6	17.2		
6	8.32	8.6	16.9		
165	8.69	7.7	16.8		

Table B.4: $r_0 = 20\,\mathrm{mm}$.

a	$\alpha_{b,1}$	$\alpha_{b,2}$	$\alpha_{b,3}$	$\alpha_{b,4}$	$\alpha_{b,5}$	$\alpha_{b,6}$	$\alpha_{b,7}$	$\alpha_{b,8}$	$\alpha_{b,av}$
0.24	28.3	27.8	28.3	27.5	27.0	27.9	28.2	27.7	27.8
0.39	23.7	23.9	23.4	24.0	23.6	24.2	24.0	23.4	23.8
0.49	18.3	19.0	18.2	18.6	18.3	19.0	18.5	18.9	18.6
0.61	15.6	16.2	16.0	16.0	16.2	16.1	14.6	15.8	15.8
0.78	13.3	14.5	13.7	13.2	13.1	13.2	13.2	13.1	13.4
0.90	12.9	12.9	12.8	11.6	12.7	12.3	12.8	12.8	12.6
1.06	12.0	11.6	11.7	11.9	12.3	12.5	12.4	11.6	12.0
1.24	11.8	11.7	11.5	11.3	12.9	11.5	11.5	11.4	11.7
1.36	11.8	11.1	11.1	10.9	11.4	10.9	10.8	10.7	11.1
1.46	10.8	11.0	10.9	11.0	10.5	10.0	10.8	10.5	10.7
1.62	10.6	10.5	9.9	10.1	10.3	10.2	10.6	10.1	10.3
1.76	10.4	10.3	9.2	10.3	10.3	10.3	10.1	9.9	10.1
1.87	9.0	10.3	9.2	9.3	9.4	9.0	9.0	9.3	9.3
2.01	9.2	9.3	9.8	9.5	9.3	9.7	9.7	9.5	9.5
2.25	7.5	6.6	7.8	7.8	7.5	7.4	7.7	7.7	7.5
2.70	6.2	6.5	6.6	6.6	6.8	6.8	6.9	6.4	6.6
3.01	8.1	9.6	8.2	8.3	8.2	8.4	8.1	8.1	8.4
3.30	7.0	6.5	6.6	6.5	6.4	7.0	6.6	6.9	6.7
3.66	7.1	7.0	6.6	7.0	7.0	6.8	7.0	6.7	6.9
3.98	6.8	7.0	7.0	7.0	6.7	6.8	6.7	7.1	6.9
4.31	7.9	7.9	8.0	7.7	8.2	7.8	7.8	8.0	7.9
4.65	6.2	6.8	6.3	6.2	6.3	6.4	6.2	6.2	6.3
4.94	8.3	8.2	8.3	7.9	7.9	8.5	8.2	8.2	8.2
5.25	7.7	7.8	7.5	7.0	7.9	7.4	7.9	7.7	7.6
5.71	7.2	7.2	7.2	7.6	7.6	7.4	7.6	7.3	7.4
6.00	8.0	8.6	7.7	8.1	7.7	8.0	7.9	8.0	8.0
6.40	8.0	9.1	8.0	8.0	7.9	8.1	8.0	7.8	8.1
6.66	6.5	6.8	7.6	6.6	6.5	6.9	6.7	6.8	6.8
7.13	7.2	7.2	6.9	7.1	7.1	7.2	6.9	7.9	7.2
7.52	7.8	7.8	7.9	7.9	7.5	7.9	8.0	7.5	7.8
7.98	7.6	7.7	7.7	7.9	7.5	7.4	7.5	7.4	7.6
8.32	8.4	8.9	8.5	8.9	8.3	8.4	8.7	8.6	8.6
8.69	7.5	7.6	7.6	8.3	8.0	7.4	7.7	7.5	7.7

Table B.5: $r_0 = 20\,\mathrm{mm}$.

a	$\alpha_{s,1}$	$\alpha_{s,2}$	$\alpha_{s,3}$	$\alpha_{s,4}$	$\alpha_{s,5}$	$\alpha_{s,6}$	$\alpha_{s,7}$	$\alpha_{s,8}$	$\alpha_{s,av}$
0.24	40.1	42.2	40.6	41.0	40.5	40.8	40.1	40.2	40.7
0.39	35.5	35.1	34.7	35.3	35.3	34.9	35.2	35.6	35.2
0.49	34.5	33.6	32.9	32.8	33.0	32.8	33.1	32.9	33.2
0.61	29.1	30.0	29.2	29.1	28.8	29.1	28.8	28.7	29.1
0.78	27.8	27.0	27.1	28.3	27.4	27.2	27.1	27.4	27.4
0.90	26.5	26.6	26.2	26.0	26.9	26.2	26.9	26.6	26.5
1.06	25.1	25.0	25.2	24.6	24.6	24.6	24.7	25.5	24.9
1.24	23.4	23.9	23.8	23.6	23.4	22.8	22.9	23.4	23.4
1.36	22.6	22.6	22.2	22.6	22.1	22.2	21.6	22.7	22.3
1.46	21.6	21.2	21.0	22.1	21.6	21.0	21.2	21.0	21.3
1.62	22.5	22.1	22.3	22.4	21.7	22.4	21.8	20.8	22.0
1.76	21.1	20.9	21.5	20.8	21.0	21.6	21.2	21.3	21.2
1.87	20.9	20.3	21.2	21.0	19.5	21.2	21.3	20.9	20.8
2.01	20.4	20.1	20.3	21.0	20.9	21.1	20.2	20.9	20.6
2.25	19.5	19.5	20.0	19.7	19.4	19.5	19.4	19.8	19.6
2.70	18.3	18.9	18.4	18.7	18.7	18.9	18.5	18.4	18.6
3.01	18.2	18.1	19.5	18.0	18.7	18.5	18.1	18.2	18.4
3.30	18.5	18.7	18.9	18.5	18.2	18.6	18.1	18.6	18.5
3.66	18.5	17.7	17.9	18.0	17.7	17.8	18.1	18.2	18.0
3.98	18.6	18.6	18.4	17.9	18.3	17.9	18.6	18.1	18.3
4.31	17.7	18.4	17.9	18.3	18.1	17.9	17.8	18.0	18.0
4.65	16.8	17.7	17.9	17.6	17.6	17.5	17.8	17.1	17.5
4.94	18.0	17.4	17.4	17.4	18.2	17.8	17.9	18.2	17.8
5.25	18.3	17.6	17.8	18.2	17.7	18.2	18.1	18.1	18.0
5.71	17.6	17.9	17.8	17.8	17.2	17.8	17.8	17.8	17.7
6.00	18.2	17.5	17.5	18.1	18.0	17.9	17.6	18.3	17.9
6.40	17.6	17.5	17.5	17.4	17.3	18.0	17.7	17.7	17.6
6.66	17.5	17.3	17.1	17.0	17.9	17.5	17.1	17.0	17.3
7.13	17.2	18.4	17.4	17.4	17.3	17.4	17.2	17.8	17.5
7.52	17.4	17.3	17.3	17.5	17.6	16.7	17.8	17.6	17.4
7.98	16.9	18.2	17.3	16.8	17.2	17.1	17.3	16.9	17.2
8.32	17.0	17.3	16.9	16.4	17.1	16.9	16.6	17.0	16.9
8.69	16.8	16.7	16.4	16.6	17.7	16.4	16.6	17.2	16.8

Table B.6: $r_0 = 20\,\mathrm{mm}$.

#	h_0	a	m_0	ϕ	$2r_{f,1}$	$2r_{f,2}$	$2r_{f,3}$	$2r_{f,4}$	$2r_{f,av}$	$r_{*,av}$	h_f	h_*
169	7.5	0.30	20	0.816	69.8	67.9	68.6	69.7	69.0	0.38	7.5	0.30
72	10.4	0.42	30	0.830	70.5	69.2	70.8	70.9	70.4	0.41	10.4	0.42
133	14.6	0.59	40	0.836	79.1	79.9	80.4	79.8	79.8	0.60	14.6	0.59
77	18.1	0.72	50	0.844	84.4	83.5	84.0	84.9	84.2	0.68	18.1	0.72
83	21.6	0.87	60	0.848	93.6	91.9	92.0	92.1	92.4	0.85	21.6	0.87
46	26.0	1.04	70	0.824	102.1	101.6	102.7	102.8	102.3	1.05	22.2	0.89
152	30.0	1.20	80	0.816	108.8	108.2	107.6	107.8	108.1	1.16	22.5	0.90
115	34.5	1.38	90	0.798	117.9	118.1	119.3	119.5	118.7	1.37	21.8	0.87
43	38.8	1.55	100	0.788	121.3	120.2	122.4	121.3	121.3	1.43	21.9	0.88
139	42.5	1.70	110	0.792	127.9	129.7	130.3	129.3	129.3	1.59	21.8	0.87
87	46.5	1.86	120	0.789	138.0	137.7	140.1	138.2	138.5	1.77	22.0	0.88
13	50.0	2.00	130	0.795	143.1	142.9	141.7	141.1	142.2	1.84	22.1	0.88
37	53.8	2.15	140	0.796	149.5	148.3	150.2	149.6	149.4	1.99	22.1	0.88
157	57.5	2.30	150	0.798	152.4	153.9	154.7	154.2	153.8	2.08	21.6	0.86
104	62.5	2.50	160	0.783	157.8	156.8	157.5	157.9	157.5	2.15	21.9	0.88
156	65.3	2.61	170	0.796	160.9	163.0	163.1	161.0	162.0	2.24	22.3	0.89
36	71.9	2.88	190	0.807	172.0	171.6	171.4	169.4	171.1	2.42	23.6	0.94
64	80.3	3.20	211	0.807	188.6	191.1	190.2	189.7	189.9	2.80	23.6	0.94
122	89.2	3.56	230	0.790	193.7	196.2	195.5	194.6	195.0	2.90	23.4	0.94
55	95.5	3.80	250	0.805	203.3	204.1	206.2	206.0	204.9	3.10	24.1	0.96
79	102.8	4.12	270	0.802	209.5	210.8	211.6	212.1	211.0	3.22	24.3	0.97
102	111.5	4.46	290	0.796	218.1	215.4	215.0	217.9	216.6	3.33	24.8	0.99
135	120.4	4.80	310	0.790	226.2	227.9	227.3	228.2	227.4	3.55	24.6	0.98
47	128.6	5.12	330	0.789	225.9	229.8	228.5	228.6	228.2	3.56	24.8	0.99
68	135.7	5.44	350	0.787	241.6	240.4	239.7	241.9	240.9	3.82	24.9	1.00
61	145.2	5.80	370	0.781	242.5	244.1	244.8	241.4	243.2	3.86	24.9	1.00
42	151.1	6.06	390	0.787	249.7	246.3	248.5	247.9	248.1	3.96	24.6	0.98
19	166.5	6.66	430	0.790	264.2	265.7	266.8	266.1	265.7	4.31	24.9	1.00
98	175.4	7.00	450	0.787	272.4	271.0	274.1	270.9	272.1	4.44	25.0	1.00

Table B.7: $r_0 = 25\,\mathrm{mm}$.

#	a	α_b	α_s	$2r_s$	r_s^*
169	0.30	21.7	37.4	36.7	0.27
72	0.42	16.3	35.7	31.1	0.38
133	0.59	14.0	33.0	22.5	0.55
77	0.72	12.7	30.2	15.9	0.68
83	0.87	12.9	27.9	8.9	0.82
46	1.04	12.6	26.4		
152	1.20	12.0	24.2		
115	1.38	11.7	23.1		
43	1.55	11.0	21.9		
139	1.70	10.6	21.0		
87	1.86	10.2	20.6		
13	2.00	9.9	20.2		
37	2.15	9.3	19.9		
157	2.30	9.0	19.8		
104	2.50	9.0	19.5		
156	2.61	8.8	19.7		
36	2.88	7.9	19.1		
64	3.20	8.2	18.7		
122	3.56	6.8	19.0		
55	3.80	6.9	18.4		
79	4.12	7.7	18.0		
102	4.46	6.9	17.6		
135	4.80	8.0	17.9		
47	5.12	8.2	17.9		
68	5.44	6.5	17.6		
61	5.80	7.6	17.4		
42	6.06	6.3	17.8		
19	6.66	7.1	17.3		
98	7.00	7.1	17.4		

Table B.8: $r_0 = 25\,\mathrm{mm}$.

a	$\alpha_{b,1}$	$\alpha_{b,2}$	$\alpha_{b,3}$	$\alpha_{b,4}$	$\alpha_{b,5}$	$\alpha_{b,6}$	$\alpha_{b,7}$	$\alpha_{b,8}$	$\alpha_{b,av}$
0.30	21.9	21.4	21.3	21.6	21.3	21.7	21.3	23.2	21.7
0.42	16.2	16.3	16.6	16.1	15.9	15.9	16.7	16.6	16.3
0.59	13.9	14.1	13.9	14.2	13.8	13.6	14.6	14.0	14.0
0.72	12.9	13.0	11.8	12.8	12.9	12.4	12.9	12.6	12.7
0.87	12.6	13.0	12.7	13.0	13.6	12.9	12.9	12.5	12.9
1.04	12.5	12.6	12.5	12.3	13.2	12.3	12.4	13.0	12.6
1.20	12.2	12.2	11.9	11.9	12.1	11.7	12.3	11.8	12.0
1.38	11.4	12.0	12.1	11.8	11.6	11.8	11.5	11.5	11.7
1.55	11.4	11.1	10.7	11.3	10.9	10.7	11.3	10.6	11.0
1.70	10.9	10.9	10.9	10.6	10.5	10.4	9.7	10.9	10.6
1.86	9.9	10.2	10.3	10.4	10.2	10.3	10.0	10.4	10.2
2.00	9.8	10.1	10.3	9.7	9.6	9.7	9.8	10.1	9.9
2.15	9.4	9.2	9.0	9.4	9.5	9.2	9.3	9.3	9.3
2.30	9.1	8.9	8.7	9.4	9.0	8.9	8.7	9.2	9.0
2.50	8.7	9.0	9.0	9.1	9.5	8.9	9.0	8.8	9.0
2.61	8.8	8.7	8.8	9.0	8.7	8.7	8.8	9.0	8.8
2.88	8.0	7.9	7.9	7.8	7.7	8.1	7.7	8.1	7.9
3.20	8.4	8.3	7.9	8.1	8.2	8.0	8.4	8.4	8.2
3.56	7.1	7.0	7.1	6.7	6.5	6.8	6.7	6.6	6.8
3.80	6.6	7.0	7.0	6.8	6.6	6.7	7.2	7.2	6.9
4.12	7.9	7.9	8.0	7.7	7.4	7.5	7.7	7.6	7.7
4.46	6.8	6.8	6.9	7.0	7.0	6.8	6.8	7.2	6.9
4.80	8.3	8.0	7.7	8.0	8.0	8.1	7.7	8.1	8
5.12	8.1	8.0	8.3	8.5	8.3	8.5	7.5	8.4	8.2
5.44	6.4	6.6	6.4	6.7	6.2	6.6	6.9	6.3	6.5
5.80	7.8	7.7	7.5	7.4	7.7	7.3	7.6	7.8	7.6
6.06	6.1	6.5	6.4	6.0	6.3	6.7	6.2	6.2	6.3
6.66	7.1	7.2	7.1	7.1	6.9	7.3	6.9	7.3	7.1
7.00	6.9	7.2	7.2	7.2	7.1	7.2	6.9	7.1	7.1

Table B.9: $r_0 = 25\,\mathrm{mm}$.

a	$\alpha_{s,1}$	$\alpha_{s,2}$	$\alpha_{s,3}$	$\alpha_{s,4}$	$\alpha_{s,5}$	$\alpha_{s,6}$	$\alpha_{s,7}$	$\alpha_{s,8}$	$\alpha_{s,av}$
0.30	36.9	37.4	37.0	37.2	37.3	37.8	38.0	37.6	37.4
0.42	35.7	35.4	35.7	35.8	35.6	35.9	35.2	36.3	35.7
0.59	33.5	33.6	32.8	33.6	32.4	33.3	32.4	32.5	33.0
0.72	30.2	30.8	30.1	30.2	30.6	29.2	30.0	30.5	30.2
0.87	27.8	27.5	28.2	28.0	27.8	27.9	28.4	27.6	27.9
1.04	26.7	26.2	25.9	26.7	26.3	26.5	26.0	26.7	26.4
1.20	24.7	22.4	24.2	24.4	24.3	24.6	24.6	24.3	24.2
1.38	22.8	22.7	22.8	22.9	22.8	22.7	25.5	22.6	23.1
1.55	21.9	23.1	21.4	21.8	22.2	21.6	21.5	21.8	21.9
1.70	21.4	21.3	20.7	21.1	21.3	20.5	20.6	21.2	21.0
1.86	20.7	20.7	21.0	20.3	20.3	20.3	20.7	20.7	20.6
2.00	20.1	19.8	19.8	22.3	19.9	19.9	19.8	20.1	20.2
2.15	20.2	20.1	19.7	20.2	20.0	19.7	19.9	19.4	19.9
2.30	19.6	20.2	19.7	19.8	20.0	20.0	19.9	19.1	19.8
2.50	19.6	19.5	19.9	19.9	18.8	19.2	19.3	19.9	19.5
2.61	19.9	18.9	19.9	20.0	19.7	19.7	19.7	19.7	19.7
2.88	19.4	18.9	19.2	19.1	18.5	18.9	19.5	19.1	19.1
3.20	18.9	18.4	19.1	18.4	18.4	19.0	18.9	18.6	18.7
3.56	18.9	18.6	18.9	18.6	18.9	19.0	20.0	18.9	19.0
3.80	18.2	18.7	18.7	18.0	18.6	18.6	18.1	18.3	18.4
4.12	18.0	17.7	18.2	18.3	18.0	17.7	17.6	18.6	18.0
4.46	17.5	17.4	17.4	17.5	17.8	17.8	18.0	17.5	17.6
4.80	17.7	18.1	17.0	18.0	17.9	18.2	18.3	17.9	17.9
5.12	17.8	17.7	18.1	18.3	17.8	18.2	17.7	17.7	17.9
5.44	17.2	18.0	17.8	17.6	17.4	17.6	17.5	17.8	17.6
5.80	17.8	17.5	17.5	16.2	17.2	17.5	17.8	17.6	17.4
6.06	17.8	17.4	17.7	17.6	17.9	18.1	18.2	17.7	17.8
6.66	17.2	17.6	16.9	17.0	17.6	17.4	17.3	17.4	17.3
7.00	16.5	17.7	17.8	17.8	17.1	17.3	17.7	17.5	17.4

Table B.10: $r_0 = 25\,\mathrm{mm}$.

#	h_0	a	m_0	ϕ	$2r_{f,1}$	$2r_{f,2}$	$2r_{f,3}$	$2r_{f,4}$	$2r_{f,av}$	$r_{*,av}$	h_f	h_*
71	6.0	0.20	30	0.829	69.9	70.2	70.6	71.4	70.5	0.18	6.0	0.20
153	9.4	0.33	45	0.823	83.2	81.7	81.8	82.9	82.4	0.37	9.8	0.33
10	13.8	0.46	60	0.822	88.0	88.6	88.5	87.2	88.1	0.47	13.8	0.46
15	17.5	0.58	75	0.820	99.1	100.3	99.5	100.3	99.8	0.66	17.3	0.58
74	21.7	0.72	90	0.819	102.7	102.9	101.9	102.3	102.5	0.71	21.7	0.72
138	24.5	0.82	105	0.819	113.3	113.4	114.4	114.3	113.8	0.90	24.6	0.82
29	29.6	0.99	120	0.819	119.4	120.8	120.3	119.9	120.1	1.00	26.1	0.87
49	32.3	1.09	135	0.834	128.5	128.1	127.7	129.1	128.4	1.14	26.6	0.89
91	37.2	1.25	150	0.808	134.4	136.0	135.4	136.2	135.5	1.26	26.4	0.88
117	41.1	1.37	165	0.813	144.6	146.1	145.8	144.9	145.3	1.42	26.3	0.88
142	44.8	1.48	180	0.817	155.2	156.5	156.0	156.7	156.1	1.60	26.7	0.89
32	49.0	1.65	195	0.796	163.0	162.7	161.4	161.9	162.2	1.70	26.4	0.88
128	52.5	1.76	210	0.802	167.4	168.6	167.7	167.6	167.8	1.80	26.8	0.89
146	56.1	1.87	225	0.812	171.1	173.9	172.2	172.7	172.5	1.87	27.2	0.91
170	60.6	2.02	240	0.802	177.8	178.6	179.8	179.4	178.9	1.98	26.9	0.90
161	67.7	2.27	270	0.802	190.0	190.5	190.6	189.3	190.1	2.17	27.6	0.92
176	77.3	2.57	305	0.801	198.6	200.4	200.1	200.1	199.8	2.33	28.2	0.94
89	84.2	2.80	335	0.806	209.8	209.5	208.8	208.7	209.2	2.49	28.7	0.96
40	93.9	3.13	370	0.796	218.7	218.1	219.4	220.6	219.2	2.65	29.0	0.97
24	103.8	3.47	405	0.787	228.3	230.0	229.8	228.3	229.1	2.82	29.8	0.99
97	113.4	3.77	440	0.787	239.6	239.8	240.7	241.5	240.4	3.01	29.8	0.99
52	122.5	4.08	475	0.784	247.4	246.5	246.1	246.0	246.5	3.11	30.1	1.00
20	131.2	4.37	510	0.787	254.1	253.6	254.1	254.6	254.1	3.23	29.8	0.99
90	139.7	4.67	545	0.787	259.1	258.9	259.7	259.9	259.4	3.32	30.8	1.03
132	151.6	5.03	585	0.783	274.9	273.9	237.6	310.0	274.1	3.57	31.3	1.04
108	161.5	5.38	625	0.782	286.5	284.7	285.1	285.7	285.5	3.76	30.8	1.03
23	171.8	5.73	665	0.782	293.2	294.3	293.5	294.6	293.9	3.90	30.8	1.03
54	181.5	6.05	705	0.785	298.0	299.0	299.4	300.4	299.2	3.99	31.0	1.03

Table B.11: $r_0 = 30\,\mathrm{mm}$.

#	a	α_b	α_s	$2r_s$	r_s^*
71	0.20	20.1	41.7	50.9	0.15
153	0.33	17.0	36.1	42.8	0.29
10	0.46	13.9	34.1	34.4	0.43
15	0.58	13.4	33.0	27.1	0.55
74	0.72	12.9	31.3	19.1	0.68
138	0.82	12.4	29.4	10.1	0.83
29	0.99	12.2	27.1		
49	1.09	11.9	25.2		
91	1.25	11.2	24.1		
117	1.37	10.6	23.5		
142	1.48	9.6	22.6		
32	1.65	10.1	21.3		
128	1.76	9.7	21.1		
146	1.87	9.8	20.3		
170	2.02	8.3	20.5		
161	2.27	7.8	19.7		
176	2.57	7.0	19.0		
89	2.80	6.7	18.7		
40	3.13	6.8	18.4		
24	3.47	6.4	18.7		
97	3.77	5.8	18.3		
52	4.08	5.1	18.0		
20	4.37	7.1	18.1		
90	4.67	6.6	18.1		
132	5.03	7.2	17.8		
108	5.38	6.3	17.9		
23	5.73	5.6	17.6		
54	6.05	6.2	17.4		

Table B.12: $r_0 = 30\,\mathrm{mm}$.

a	$\alpha_{b,1}$	$\alpha_{b,2}$	$\alpha_{b,3}$	$\alpha_{b,4}$	$\alpha_{b,5}$	$\alpha_{b,6}$	$\alpha_{b,7}$	$\alpha_{b,8}$	$\alpha_{b,av}$
0.20	20.3	19.8	19.5	20.2	20.3	20.6	20.0	20.2	20.1
0.33	16.9	16.9	16.8	16.7	17.1	17.3	16.8	17.5	17.0
0.46	14.3	13.7	13.9	13.5	14.2	13.7	14.2	13.7	13.9
0.58	13.2	13.5	13.8	13.4	12.6	13.7	13.3	13.5	13.4
0.72	12.5	13.1	13.1	12.9	12.9	13.0	13.0	12.7	12.9
0.82	12.8	12.3	12.2	12.1	12.4	12.1	12.4	12.9	12.4
0.99	12.4	12.4	11.8	11.9	12.5	12.6	12.0	12.0	12.2
1.09	12.2	11.5	11.9	11.3	12.2	11.9	12.1	12.1	11.9
1.25	11.4	11.6	10.8	10.9	11.0	11.1	12.1	10.9	11.2
1.37	10.6	10.7	10.4	10.6	10.9	10.4	10.8	10.3	10.6
1.48	9.7	9.5	9.8	9.5	9.9	9.4	9.6	9.6	9.6
1.65	9.8	9.7	10.1	10.5	10.3	9.8	9.9	10.6	10.1
1.76	9.5	9.9	9.5	9.8	9.9	9.8	9.6	9.6	9.7
1.87	9.9	9.9	9.8	10.0	9.6	9.7	9.6	9.7	9.8
2.02	8.3	8.0	8.9	8.2	8.2	8.2	8.4	8.2	8.3
2.27	8.0	8.0	7.7	7.3	7.8	7.9	7.7	8.0	7.8
2.57	6.4	7.2	7.2	7.3	7.3	7.1	6.7	6.8	7.0
2.80	6.5	6.6	7.0	7.0	6.9	6.4	7.0	6.2	6.7
3.13	6.8	6.5	6.7	6.8	7.0	7.4	6.6	6.5	6.8
3.47	6.2	6.4	6.6	6.2	6.4	6.5	6.6	6.2	6.4
3.77	5.8	6.1	4.9	5.9	6.0	5.9	6.0	5.7	5.8
4.08	4.9	4.8	5.6	5.1	4.9	5.2	5.0	5.3	5.1
4.37	6.9	6.9	7.0	7.5	7.2	7.1	6.9	7.3	7.1
4.67	6.4	6.5	6.6	6.5	6.7	6.7	6.6	6.8	6.6
5.03	7.5	7.2	7.2	7.3	6.8	7.1	7.2	7.5	7.2
5.38	6.6	6.4	6.1	6.6	6.1	6.3	6.0	6.3	6.3
5.73	6.1	5.8	5.4	5.8	5.4	5.3	5.5	5.4	5.6
6.05	6.2	6.3	5.9	6.2	6.1	5.9	6.8	6.1	6.2

Table B.13: $r_0 = 30\,\mathrm{mm}$.

a	$\alpha_{s,1}$	$\alpha_{s,2}$	$\alpha_{s,3}$	$\alpha_{s,4}$	$\alpha_{s,5}$	$\alpha_{s,6}$	$\alpha_{s,7}$	$\alpha_{s,8}$	$\alpha_{s,av}$
0.20	41.9	41.3	41.1	42.7	41.5	41.2	41.7	42.1	41.7
0.33	36.4	36.6	36.6	36.0	34.6	36.6	36.1	35.8	36.1
0.46	33.8	34.7	33.9	34.0	34.2	34.0	33.8	34.4	34.1
0.58	33.4	33.4	33.4	30.7	33.5	32.9	33.6	33.0	33.0
0.72	31.7	31.5	31.3	31.1	31.1	30.5	31.3	31.8	31.3
0.82	29.8	29.8	29.6	29.9	29.4	29.4	29.2	28.2	29.4
0.99	27.5	26.6	27.1	27.4	26.7	27.5	26.7	27.4	27.1
1.09	25.0	24.9	25.7	25.2	24.9	25.6	24.7	25.6	25.2
1.25	24.1	24.3	24.2	24.3	23.9	24.4	23.7	23.8	24.1
1.37	23.2	23.1	23.2	23.9	23.1	23.6	23.8	24.2	23.5
1.48	23.0	21.9	22.5	22.6	22.6	22.8	22.3	23.1	22.6
1.65	21.8	21.3	21.4	20.3	20.9	21.3	21.5	21.8	21.3
1.76	21.2	21.4	21.4	21.6	21.0	19.3	21.5	21.4	21.1
1.87	20.6	20.6	20.6	19.9	20.2	20.2	20.0	20.3	20.3
2.02	20.8	20.8	20.1	20.7	19.6	20.7	20.4	20.8	20.5
2.27	20.3	19.6	19.9	19.6	19.5	19.6	19.5	19.8	19.7
2.57	18.9	19.1	18.7	18.7	19.7	18.7	19.3	19.0	19.0
2.80	18.3	18.6	18.6	18.6	18.7	19.0	19.4	18.5	18.7
3.13	18.4	18.7	18.3	18.5	18.5	17.5	18.8	18.4	18.4
3.47	18.8	18.7	18.3	18.6	18.6	18.4	19.6	18.6	18.7
3.77	18.6	18.2	18.6	18.2	18.0	18.0	18.6	18.2	18.3
4.08	18.1	18.3	18.3	17.9	17.1	18.4	17.9	18.1	18.0
4.37	18.4	17.7	17.8	18.4	17.9	18.1	18.4	18.1	18.1
4.67	18.4	18.0	18.4	17.6	18.0	18.3	18.4	17.8	18.1
5.03	17.5	17.9	17.4	18.0	18.1	17.3	18.0	18.2	17.8
5.38	17.6	18.1	17.9	17.7	17.9	18.1	17.8	18.1	17.9
5.73	17.7	17.6	17.3	17.4	17.7	18.0	17.4	17.8	17.6
6.05	17.0	17.5	17.7	17.6	17.3	17.2	17.8	17.1	17.4

Table B.14: $r_0 = 30\,\mathrm{mm}$.

#	h_0	a	m_0	ϕ	$2r_{f,1}$	$2r_{f,2}$	$2r_{f,3}$	$2r_{f,4}$	$2r_{f,av}$	$r_{*,av}$	h_f	h_*
16	8.3	0.24	50	0.809	89.4	88.7	88.9	89.4	89.1	0.27	8.3	0.24
121	11.7	0.34	75	0.810	97.4	97.0	97.8	98.2	97.6	0.39	11.7	0.34
84	16.9	0.48	100	0.798	102.9	103.7	103.2	104.6	103.6	0.48	16.9	0.48
28	20.9	0.60	125	0.794	115.7	114.6	115.4	114.3	115.0	0.64	20.9	0.60
103	25.1	0.72	150	0.784	125.5	125.9	124.7	125.5	125.4	0.79	29.1	0.83
96	29.8	0.85	175	0.825	132.1	133.8	132.9	132.8	132.9	0.90	29.8	0.85
144	34.6	0.99	200	0.812	145.6	146.5	146.1	146.2	146.1	1.09	31.2	0.89
119	39.2	1.12	225	0.806	156.3	156.4	155.3	155.2	155.8	1.23	30.8	0.88
158	43.8	1.25	250	0.802	162.8	164.1	164.1	163.4	163.6	1.34	30.6	0.87
141	48.2	1.38	275	0.801	173.2	173.0	173.6	172.6	173.1	1.47	30.6	0.88
101	52.4	1.50	300	0.804	184.0	185.9	185.6	184.9	185.1	1.64	31.6	0.90
129	57.3	1.64	325	0.797	194.2	195.3	194.0	195.9	194.8	1.78	30.8	0.88
137	62.2	1.78	350	0.790	205.8	205.2	206.5	206.5	206.0	1.94	31.4	0.90
112	66.3	1.89	375	0.794	210.3	211.6	210.7	210.2	210.7	2.01	32.1	0.92
120	74.2	2.11	415	0.788	228.1	226.7	227.4	226.6	227.2	2.25	32.5	0.93
151	84.6	2.43	475	0.785	230.4	231.8	232.1	229.7	231.0	2.30	33.2	0.95
168	96.5	2.74	535	0.783	263.5	262.0	261.8	261.9	262.3	2.75	34.1	0.97
162	103.9	3.03	595	0.788	253.2	254.4	253.0	254.6	253.8	2.63	34.4	0.98
174	116.7	3.34	655	0.786	275.9	274.3	273.9	274.3	274.6	2.92	34.4	0.98
175	128.2	3.66	715	0.785	287.9	289.9	290.0	289.8	289.4	3.13	35.8	1.02
155	140.4	4.00	775	0.778	306.5	306.2	305.3	305.2	305.8	3.37	36.6	1.05
39	150.1	4.29	835	0.782	319.7	319.1	320.6	320.6	320.0	3.57	36.2	1.03
12	162.8	4.66	895	0.790	327.6	328.7	329.1	328.6	328.5	3.69	36.5	1.04
26	173.0	4.94	954	0.783	342.2	341.9	341.0	340.5	341.4	3.88	36.5	1.04
93	184.5	5.29	1015	0.781	342.3	344.6	343.2	343.5	343.4	3.91	37.1	1.06

Table B.15: $r_0 = 35\,\mathrm{mm}$.

#	a	α_b	α_s	$2r_s$	r_s^*
16	0.24	16.3	41.1	56.9	0.19
121	0.34	13.9	36.3	48.9	0.30
84	0.48	13.8	33.0	39.4	0.44
28	0.60	13.2	31.3	32.9	0.53
103	0.72	13.1	29.4	22.4	0.68
96	0.85	12.7	26.8	11.2	0.84
144	0.99	11.6	25.1		
119	1.12	11.2	23.4		
158	1.25	10.8	24.6		
141	1.38	10.3	22.3		
101	1.50	10.1	21.6		
129	1.64	10.3	21.2		
137	1.78	9.6	20.3		
112	1.89	9.4	20.6		
120	2.11	8.4	19.7		
151	2.43	7.9	19.5		
168	2.74	7.3	18.6		
162	3.03	7.1	18.8		
174	3.34	7.1	18.2		
175	3.66	6.7	18.0		
155	4.00	7.1	18.1		
39	4.29	5.1	17.7		
12	4.66	6.9	18.1		
26	4.94	6.5	18.0		
93	5.29	7.8	17.8		
108	5.38	6.3	17.9		
23	5.73	5.6	17.6		
54	6.05	6.2	17.4		

Table B.16: $r_0 = 35\,\mathrm{mm}$.

a	$\alpha_{b,1}$	$\alpha_{b,2}$	$\alpha_{b,3}$	$\alpha_{b,4}$	$\alpha_{b,5}$	$\alpha_{b,6}$	$\alpha_{b,7}$	$\alpha_{b,8}$	$\alpha_{b,av}$
0.24	16.7	16.1	16.3	16.5	15.5	16.2	16.5	16.5	16.3
0.34	13.5	13.4	13.8	13.9	14.0	14.3	14.1	14.1	13.9
0.48	13.9	14.1	14.2	13.5	13.5	13.7	13.5	13.8	13.8
0.60	13.5	12.9	13.4	13.4	13.1	13.1	13.4	12.9	13.2
0.72	12.9	13.0	12.8	13.2	12.9	13.4	13.5	13.1	13.1
0.85	13.1	12.8	13.0	12.4	12.3	12.7	12.9	12.5	12.7
0.99	11.4	11.6	11.9	11.5	11.8	11.2	11.7	11.8	11.6
1.12	11.3	10.9	11.1	11.6	11.2	11.2	11.3	11.2	11.2
1.25	11.0	11.0	10.7	10.5	10.8	10.7	10.5	11.2	10.8
1.38	10.0	10.6	10.6	10.1	10.5	10.2	10.1	10.4	10.3
1.50	10.5	10.0	10.3	9.9	10.0	10.0	9.9	10.5	10.1
1.64	10.3	10.5	10.3	10.5	10.4	9.9	10.3	10.2	10.3
1.78	9.3	9.9	9.4	9.6	9.7	9.8	9.8	9.4	9.6
1.89	9.3	9.5	9.3	9.6	9.6	9.4	9.5	9.2	9.4
2.11	8.2	8.2	8.2	8.4	8.3	8.5	9.3	8.1	8.4
2.43	7.8	7.9	7.6	7.8	7.6	7.8	7.8	8.8	7.9
2.74	7.0	7.4	7.4	7.2	7.3	7.3	7.3	7.5	7.3
3.03	7.3	7.3	7.1	7.2	7.0	7.0	6.5	7.3	7.1
3.34	7.2	7.4	6.9	7.0	7.3	6.9	7.2	6.8	7.1
3.66	6.4	6.9	6.7	6.4	6.7	6.6	6.9	6.9	6.7
4.00	7.2	7.0	6.9	7.2	7.0	7.0	7.6	7.0	7.1
4.29	5.4	4.8	4.9	4.8	5.0	4.9	5.3	5.8	5.1
4.66	7.0	6.8	7.1	6.8	6.8	6.7	7.2	6.8	6.9
4.94	6.6	6.9	6.4	6.2	6.6	6.5	6.3	6.5	6.5
5.29	8.0	7.7	7.6	8.1	7.8	7.7	7.8	7.9	7.8

Table B.17: $r_0 = 35\,\mathrm{mm}$.

a	$\alpha_{s,1}$	$\alpha_{s,2}$	$\alpha_{s,3}$	$\alpha_{s,4}$	$\alpha_{s,5}$	$\alpha_{s,6}$	$\alpha_{s,7}$	$\alpha_{s,8}$	$\alpha_{s,av}$
0.24	41.4	41.3	40.8	41.7	40.9	41.4	40.1	41.2	41.1
0.34	35.7	36.7	36.5	36.1	36.7	36.3	35.8	36.5	36.3
0.48	33.0	33.5	32.8	32.9	33.0	33.6	31.6	33.6	33.0
0.60	30.4	31.6	30.8	31.9	31.2	31.0	31.7	31.8	31.3
0.72	29.1	28.9	29.1	29.3	29.6	29.5	29.4	30.3	29.4
0.85	26.2	27.0	26.8	26.9	26.9	27.1	26.3	27.1	26.8
0.99	25.2	24.9	25.3	24.8	25.6	25.0	24.6	25.5	25.1
1.12	23.7	23.3	23.2	23.0	23.8	23.8	23.0	23.4	23.4
1.25	25.1	25.0	25.1	24.9	23.0	24.5	24.5	24.7	24.6
1.38	22.7	22.4	21.8	22.3	22.2	21.8	22.7	22.2	22.3
1.50	21.6	21.7	21.7	21.9	21.2	21.1	22.0	21.5	21.6
1.64	21.6	20.8	21.5	20.9	21.2	20.9	20.6	21.6	21.2
1.78	20.2	20.7	20.0	21.0	19.9	20.3	19.9	20.5	20.3
1.89	21.1	20.7	20.5	20.4	20.2	20.5	20.5	21.1	20.6
2.11	19.9	19.6	20.1	19.5	19.8	19.7	19.6	19.4	19.7
2.43	19.6	19.7	19.2	19.1	19.4	19.2	19.5	20.3	19.5
2.74	18.4	18.9	19.0	18.3	17.9	18.9	18.7	18.8	18.6
3.03	19.0	18.4	19.0	18.6	19.1	19.0	18.9	18.5	18.8
3.34	18.6	17.9	18.3	18.3	18.1	18.1	18.2	18.1	18.2
3.66	18.1	17.8	17.7	17.8	17.8	17.7	18.3	18.8	18.0
4.00	18.4	17.7	17.7	17.9	19.4	18.1	17.9	17.7	18.1
4.29	17.6	17.4	17.8	18.1	17.8	17.6	17.7	17.6	17.7
4.66	18.3	16.9	18.2	17.9	18.3	18.5	18.5	18.2	18.1
4.94	18.7	17.7	17.6	17.8	17.8	18.3	17.7	18.4	18.0
5.29	17.7	18.1	17.4	17.9	17.8	17.9	17.6	17.9	17.8

Table B.18: $r_0 = 35\,\mathrm{mm}$.

#	h_0	a	m_0	ϕ	$2r_{f,1}$	$2r_{f,2}$	$2r_{f,3}$	$2r_{f,4}$	$2r_{f,av}$	$r_{*,av}$	h_f	h_*
57	10.0	0.25	70	0.788	98.8	98.2	98.0	99.2	98.6	0.23	10.0	0.25
127	14.1	0.35	100	0.800	106.7	106.9	107.5	108.0	107.3	0.34	14.1	0.35
100	17.3	0.43	130	0.823	118.1	118.7	118.5	118.5	118.4	0.48	17.3	0.43
131	22.4	0.56	160	0.801	122.3	123.4	122.6	121.9	122.6	0.53	22.4	0.56
167	27.0	0.67	190	0.792	136.6	137.4	137.7	137.4	137.3	0.72	27.0	0.67
86	30.9	0.77	220	0.800	143.4	142.6	142.3	142.8	142.8	0.78	30.9	0.77
118	35.5	0.89	250	0.791	159.5	159.3	160.4	160.8	160.0	1.00	35.5	0.89
136	38.9	0.97	280	0.809	171.7	170.1	170.1	171.3	170.8	1.14	36.3	0.91
99	43.3	1.08	310	0.805	179.4	180.5	180.7	181.0	180.4	1.26	35.9	0.90
62	48.5	1.21	340	0.788	191.2	191.9	192.2	191.5	191.7	1.40	35.9	0.90
2	51.8	1.29	370	0.803	197.2	198.8	197.8	197.8	197.9	1.47	36.1	0.90
1	54.4	1.36	400	0.826	205.1	206.6	206.5	205.8	206.0	1.58	36.0	0.90
70	60.0	1.50	430	0.806	213.8	212.5	212.6	213.1	213.0	1.66	36.3	0.91
22	64.9	1.62	460	0.797	223.9	224.3	225.0	224.0	224.3	1.80	36.6	0.92
166	69.6	1.74	490	0.791	229.6	231.7	229.8	231.3	230.6	1.88	36.4	0.91
126	73.2	1.83	520	0.798	238.7	238.7	237.9	237.7	238.3	1.98	36.8	0.92
148	79.6	1.99	550	0.777	247.9	248.1	249.2	249.2	248.6	2.11	37.2	0.93
80	88.3	2.21	625	0.796	265.5	264.0	264.3	265.8	264.9	2.31	37.0	0.93
78	99.9	2.50	700	0.788	283.6	282.4	282.1	282.7	282.7	2.53	38.3	0.96
51	111.5	2.79	775	0.781	289.4	290.2	290.9	290.3	290.2	2.63	39.4	0.98
111	121.2	3.03	850	0.788	309.2	310.5	309.5	310.4	309.9	2.87	39.0	0.97
35	133.0	3.33	925	0.782	314.7	316.3	316.4	314.6	315.5	2.94	40.3	1.01
45	142.0	3.55	1000	0.792	324.0	324.6	323.7	325.3	324.4	3.05	40.8	1.02
163	154.1	3.85	1075	0.784	337.5	335.9	337.0	334.4	336.2	3.20	41.2	1.03
173	166.6	4.17	1150	0.776	351.3	352.1	350.8	351.8	351.5	3.39	41.6	1.04
145	175.8	4.40	1225	0.783	359.2	358.4	357.6	358.0	358.3	3.48	41.9	1.05

Table B.19: $r_0 = 40\,\mathrm{mm}$.

#	a	α_b	α_s	$2r_s$	r_s^*
57	0.25	15.1	40.0	63.8	0.20
127	0.35	13.7	34.7	58.1	0.27
100	0.43	13.2	33.8	51.3	0.36
131	0.56	12.4	31.5	41.2	0.49
167	0.67	12.0	30.3	33.0	0.59
86	0.77	11.8	28.5	27.1	0.66
118	0.89	11.5	27.1	10.3	0.87
136	0.97	11.3	26.8		
99	1.08	11.1	25.6		
62	1.21	10.6	24.2		
2	1.29	10.2	23.0		
1	1.36	10.0	23.0		
70	1.50	9.9	22.6		
22	1.62	9.7	21.9		
166	1.74	9.6	21.0		
126	1.83	9.5	20.5		
148	1.99	9.5	20.0		
80	2.21	8.4	19.6		
78	2.50	8.0	19.0		
51	2.79	7.6	18.5		
111	3.03	7.2	18.3		
35	3.33	6.9	18.6		
45	3.55	7.0	18.3		
163	3.85	6.8	18.0		
173	4.17	6.3	17.5		
145	4.40	6.9	17.8		

Table B.20: $r_0 = 40\,\mathrm{mm}$.

a	$\alpha_{b,1}$	$\alpha_{b,2}$	$\alpha_{b,3}$	$\alpha_{b,4}$	$\alpha_{b,5}$	$\alpha_{b,6}$	$\alpha_{b,7}$	$\alpha_{b,8}$	$\alpha_{b,av}$
0.25	15.2	15.0	15.4	15.0	14.8	14.9	14.8	15.7	15.1
0.35	13.6	13.3	13.5	13.9	13.4	14.0	13.8	14.1	13.7
0.43	13.6	13.3	13.2	13.1	12.8	13.0	12.9	13.8	13.2
0.56	12.6	12.8	12.1	13.0	12.0	12.1	12.5	12.2	12.4
0.67	12.5	11.7	12.2	11.7	12.0	12.2	12.0	11.8	12.0
0.77	11.8	11.4	13.0	11.5	11.5	11.6	12.0	11.6	11.8
0.89	11.4	11.6	11.7	11.6	11.3	11.3	11.4	11.7	11.5
0.97	11.1	11.4	11.6	11.1	11.1	11.8	11.2	11.3	11.3
1.08	10.8	11.0	12.3	10.8	11.1	10.7	11.0	11.2	11.1
1.21	10.7	10.8	10.4	10.3	11.5	10.2	10.3	10.7	10.6
1.29	10.1	10.0	10.2	10.6	10.0	10.2	10.4	10.0	10.2
1.36	10.3	9.8	10.3	9.8	9.6	10.1	10.1	9.9	10.0
1.50	9.7	10.0	9.8	10.1	9.8	9.9	10.1	9.8	9.9
1.62	9.4	10.0	9.7	9.9	9.5	10.1	9.4	9.6	9.7
1.74	9.8	9.6	9.7	9.8	9.7	9.6	9.2	9.4	9.6
1.83	9.3	9.7	9.5	9.6	9.5	9.2	9.4	9.6	9.5
1.99	9.5	9.8	9.8	9.0	9.4	9.4	9.6	9.5	9.5
2.20	8.9	8.1	8.3	8.7	8.2	8.3	8.3	8.3	8.4
2.50	7.8	8.2	8.2	8.1	7.7	8.0	8.2	7.8	8.0
2.77	7.6	7.8	7.7	7.8	7.0	7.3	7.8	7.8	7.6
3.02	7.5	7.0	7.1	7.4	7.3	7.1	7.2	7.0	7.2
3.33	7.2	6.8	6.8	6.8	7.0	6.7	6.8	7.2	6.9
3.55	7.0	7.3	6.8	7.1	6.8	7.2	7.0	6.8	7.0
3.85	6.8	6.6	6.8	6.8	7.0	6.7	6.7	7.0	6.8
4.15	6.2	6.5	6.2	6.6	6.3	6.4	6.3	6.0	6.3
4.40	6.8	6.7	7.5	6.6	7.1	6.7	6.8	7.0	6.9

Table B.21: $r_0 = 40\,\mathrm{mm}$.

a	$\alpha_{s,1}$	$\alpha_{s,2}$	$\alpha_{s,3}$	$\alpha_{s,4}$	$\alpha_{s,5}$	$\alpha_{s,6}$	$\alpha_{s,7}$	$\alpha_{s,8}$	$\alpha_{s,av}$
0.25	39.7	39.7	40.0	40.6	39.9	40.6	39.7	39.9	40.0
0.35	34.9	34.7	35.0	35.2	33.0	35.2	34.6	35.0	34.7
0.43	33.3	34.4	33.8	33.3	33.5	34.8	34.0	33.4	33.8
0.56	31.4	31.4	31.7	31.4	31.6	30.9	31.6	32.0	31.5
0.67	30.3	29.9	30.1	30.1	30.7	30.6	30.5	30.3	30.3
0.77	28.1	28.4	28.6	29.5	28.1	28.3	28.2	28.7	28.5
0.89	27.0	27.6	27.5	27.5	27.3	26.9	25.5	27.5	27.1
0.97	26.6	26.3	27.0	26.8	27.3	27.0	26.7	26.7	26.8
1.08	25.4	25.5	25.8	25.8	25.9	25.7	25.9	24.7	25.6
1.21	24.1	24.6	24.2	24.6	24.3	23.9	23.8	24.1	24.2
1.29	22.8	23.4	23.0	23.0	22.6	23.3	22.9	23.0	23.0
1.36	22.6	22.6	25.0	22.5	22.7	22.8	22.8	23.0	23.0
1.50	22.7	22.2	23.1	23.0	23.0	22.4	22.1	22.2	22.6
1.62	21.9	21.6	21.6	21.6	21.9	22.1	22.2	22.4	21.9
1.74	20.5	21.4	20.8	21.3	21.0	21.2	21.3	20.5	21.0
1.83	21.0	20.3	20.1	20.7	20.3	20.3	20.4	20.9	20.5
1.99	20.4	19.2	20.2	20.0	20.1	20.3	20.1	19.7	20.0
2.20	19.4	19.9	19.5	19.4	19.9	19.7	19.1	19.9	19.6
2.50	18.8	18.7	19.0	18.7	19.9	18.8	19.1	19.2	19.0
2.77	18.4	18.8	18.5	18.3	18.3	18.6	18.5	18.6	18.5
3.02	17.6	18.6	18.4	18.3	18.1	18.3	18.4	18.6	18.3
3.33	19.0	18.8	18.7	18.7	17.7	18.7	18.9	18.3	18.6
3.55	18.6	18.0	18.4	18.0	18.4	18.5	18.2	18.4	18.3
3.85	18.2	18.0	18.3	17.8	17.7	17.9	17.7	18.4	18.0
4.15	17.2	17.2	17.7	17.8	17.2	17.6	17.7	17.5	17.5
4.40	17.2	18.1	18.0	17.9	18.1	17.6	17.7	17.7	17.8

Table B.22: $r_0 = 40\,\mathrm{mm}$.

#	h_0	a	m_0	ϕ	$2r_{f,1}$	$2r_{f,2}$	$2r_{f,3}$	$2r_{f,4}$	$2r_{f,av}$	$r_{*,av}$	h_f	h_*
63	10.8	0.24	100	0.804	111.9	111.4	112.0	111.0	111.6	0.24	10.8	0.24
106	15.1	0.34	140	0.805	117.7	118.5	118.3	118.5	118.3	0.31	15.1	0.34
154	19.0	0.42	180	0.821	124.6	125.4	125.3	125.1	125.1	0.39	19.0	0.42
44	24.4	0.54	220	0.784	142.3	141.6	141.7	142.5	142.0	0.58	24.4	0.54
134	29.0	0.65	260	0.778	146.5	145.8	146.6	146.3	146.3	0.63	29.0	0.65
147	32.8	0.73	300	0.794	152.2	153.1	153.4	153.0	152.9	0.70	32.8	0.73
50	37.1	0.83	340	0.795	168.0	167.9	168.5	168.5	168.2	0.87	37.1	0.83
124	41.1	0.91	380	0.803	179.8	179.5	178.9	178.7	179.2	0.99	41.1	0.91
150	45.7	1.02	420	0.798	194.4	193.7	193.5	195.2	194.2	1.16	41.4	0.92
95	50.0	1.11	460	0.799	204.6	204.3	203.4	203.7	204.0	1.27	41.3	0.92
160	54.5	1.21	500	0.797	212.9	213.2	213.9	214.0	213.5	1.37	41.7	0.93
94	59.2	1.32	540	0.792	228.9	227.6	229.0	228.1	228.4	1.54	41.7	0.93
17	64.4	1.43	580	0.782	242.1	242.5	243.2	243.4	242.8	1.70	41.9	0.93
140	68.4	1.52	620	0.787	252.4	253.8	254.1	253.0	253.3	1.81	41.6	0.92
18	71.9	1.60	660	0.797	257.5	258.9	258.6	259.0	258.5	1.87	42.2	0.94
75	76.5	1.70	705	0.800	266.6	266.1	267.7	266.8	266.8	1.96	42.0	0.93
114	84.4	1.88	785	0.808	279.8	279.7	280.8	280.1	280.1	2.11	42.4	0.94
48	94.1	2.09	865	0.798	299.3	300.5	299.9	299.1	299.7	2.33	42.3	0.94
105	106.7	2.37	990	0.806	310.5	312.3	310.9	311.5	311.3	2.46	42.7	0.95
107	125.3	2.78	1155	0.801	331.7	330.2	331.5	332.2	331.4	2.68	44.4	0.99
53	141.6	3.15	1300	0.797	354.6	353.9	353.4	354.1	354	2.93	45	1.00
59	155.4	3.45	1425	0.796	365.9	367.0	367.2	365.5	366.4	3.07	45.7	1.02
76	166.5	3.70	1526	0.796	385.8	387.4	388.3	388.1	387.4	3.30	47.9	1.06
113	180.9	4.02	1650	0.792	391.1	390.8	392.0	392.5	391.6	3.35	47.6	1.06

Table B.23: $r_0 = 45\,\mathrm{mm}$.

#	a	α_b	α_s	$2r_s$	r_s^*
63	0.25	15.1	40.0	63.8	0.27
106	0.35	13.7	34.7	58.1	0.36
154	0.43	13.2	33.8	51.3	0.49
44	0.56	12.4	31.5	41.2	0.59
134	0.67	12.0	30.3	33.0	0.66
147	0.77	11.8	28.5	27.1	0.87
50	0.89	11.5	27.1	10.3	1.00
124	0.97	11.3	26.8		
150	1.08	11.1	25.6		
95	1.21	10.6	24.2		
160	1.29	10.2	23.0		
94	1.36	10.0	23.0		
17	1.50	9.9	22.6		
140	1.62	9.7	21.9		
18	1.74	9.6	21.0		
75	1.83	9.5	20.5		
114	1.99	9.5	20.0		
48	2.21	8.4	19.6		
105	2.50	8.0	19.0		
107	2.79	7.6	18.5		
53	3.03	7.2	18.3		
59	3.33	6.9	18.6		
76	3.55	7.0	18.3		
113	3.85	6.8	18.0		
173	4.17	6.3	17.5		
145	4.40	6.9	17.8		

Table B.24: $r_0 = 45\,\mathrm{mm}$.

a	$\alpha_{b,1}$	$\alpha_{b,2}$	$\alpha_{b,3}$	$\alpha_{b,4}$	$\alpha_{b,5}$	$\alpha_{b,6}$	$\alpha_{b,7}$	$\alpha_{b,8}$	$\alpha_{b,av}$
0.24	13.6	12.8	13.3	13.3	13.6	13.4	13.6	13.5	13.4
0.34	12.5	12.6	12.8	12.9	12.9	12.2	12.1	12.7	12.6
0.42	12.4	11.1	12.0	12.3	12.0	12.5	12.2	12.4	12.1
0.54	11.7	12.1	12.1	11.8	11.9	11.3	11.5	11.3	11.7
0.65	11.4	11.4	10.8	11.4	11.0	10.9	11.5	11.3	11.2
0.73	10.7	11.0	10.6	10.8	11.2	10.7	11.3	11.7	11.0
0.83	10.8	11.3	10.8	11.1	11.2	11.4	11.5	10.8	11.1
0.91	10.7	11.2	10.7	11.0	10.6	10.8	10.6	10.9	10.8
1.02	10.5	10.7	10.8	11.0	10.6	10.4	10.3	10.5	10.6
1.11	10.7	10.7	10.7	10.3	9.2	10.4	10.7	10.5	10.4
1.21	10.7	10.3	9.9	10.1	10.0	10.4	10.4	10.7	10.3
1.32	9.9	10.0	10.2	10.2	9.8	9.7	10.3	9.9	10.0
1.43	10.0	9.5	10.0	9.5	9.7	9.2	9.9	9.8	9.7
1.52	9.8	9.8	10.0	9.4	9.8	9.8	9.8	10.0	9.8
1.60	9.7	8.9	9.7	9.5	9.6	9.4	9.6	9.6	9.5
1.70	9.0	8.9	9.6	9.3	9.4	9.2	9.3	8.9	9.2
1.87	8.9	8.9	8.6	9.0	8.9	8.6	9.0	8.5	8.8
2.09	8.8	8.3	8.0	8.0	8.1	7.9	8.4	8.0	8.2
2.38	7.7	7.6	7.5	8.0	8.1	7.9	8.1	7.5	7.8
2.78	7.6	7.6	7.9	7.9	7.9	7.6	7.9	8.0	7.8
3.16	7.2	7.5	7.7	7.1	7.4	7.8	7.3	7.2	7.4
3.44	7.0	7.0	7.0	8.2	6.9	7.2	7.1	7.2	7.2
3.71	7.4	6.9	7.0	7.4	6.9	6.9	7.9	7.2	7.2
4.02	7.4	6.8	6.9	7.2	7.1	7.2	6.9	7.3	7.1

Table B.25: $r_0 = 45\,\mathrm{mm}$.

a	$\alpha_{s,1}$	$\alpha_{s,2}$	$\alpha_{s,3}$	$\alpha_{s,4}$	$\alpha_{s,5}$	$\alpha_{s,6}$	$\alpha_{s,7}$	$\alpha_{s,8}$	$\alpha_{s,av}$
0.24	40.2	41.2	40.2	41.2	40.7	40.6	41.1	40.3	40.7
0.34	36.8	37.4	36.8	37.2	36.7	36.8	36.4	37.1	36.9
0.42	33.3	33.2	33.6	32.9	34.0	34.0	32.3	34.0	33.4
0.54	31.1	30.8	31.1	30.5	30.4	30.6	30.5	31.4	30.8
0.65	29.2	29.6	29.6	29.8	28.5	29.7	29.8	29.8	29.5
0.73	28.4	28.0	28.4	28.8	27.9	28.4	28.3	29.0	28.4
0.83	27.4	27.3	27.6	25.7	27.4	27.3	27.3	26.8	27.1
0.91	26.6	26.7	26.6	25.7	26.7	26.0	26.3	25.9	26.3
1.02	25.1	25.5	25.2	24.5	24.8	24.9	24.8	24.5	24.9
1.11	24.6	25.0	24.8	23.2	25.1	25.0	24.6	24.5	24.6
1.21	23.7	24.4	23.2	23.3	23.4	24.1	23.4	23.3	23.6
1.32	23.7	23.9	23.4	23.2	23.0	23.2	23.5	23.4	23.4
1.43	22.2	23.1	22.9	23.1	22.9	22.7	23.0	21.6	22.7
1.52	22.8	22.0	21.9	22.4	22.4	22.5	21.8	22.6	22.3
1.60	22.2	21.0	21.8	21.8	21.8	21.7	21.4	21.9	21.7
1.70	20.5	21.9	21.7	21.6	21.9	21.7	21.1	21.0	21.4
1.87	19.9	20.6	21.3	21.2	21.0	21.4	20.5	21.4	20.9
2.09	19.0	19.5	19.6	20.1	20.1	20.0	19.6	19.7	19.7
2.38	19.0	18.7	19.7	19.6	19.2	19.6	19.1	19.6	19.3
2.78	18.6	18.6	18.6	18.4	18.8	18.4	18.2	18.3	18.5
3.16	19.0	19.0	19.0	18.9	18.5	18.4	18.7	19.0	18.8
3.44	18.1	17.7	18.9	18.0	17.8	17.7	18.4	18.3	18.1
3.71	18.5	18.3	18.5	18.1	18.3	18.4	18.5	18.6	18.4
4.02	19.0	17.9	17.8	17.5	17.7	17.8	17.7	17.7	17.9

Table B.26: $r_0 = 45\,\mathrm{mm}$.

#	h_0	a	m_0	ϕ	$2r_{f,1}$	$2r_{f,2}$	$2r_{f,3}$	$2r_{f,4}$	$2r_{f,av}$	$r_{*,av}$	h_f	h_*
82	20.9	0.28	560	0.829	185.8	186.3	186.4	185.9	186.1	0.24	20.9	0.28
58	29.7	0.40	810	0.795	206.5	205.9	206.7	205.7	206.2	0.37	29.7	0.40
27	36.7	0.49	1030	0.812	223.4	224.4	224.3	223.5	223.9	0.49	36.7	0.49
149	46.6	0.62	1250	0.829	251.6	251.1	249.6	251.7	251.0	0.67	46.6	0.62
88	56.2	0.75	1470	0.809	275.7	275.6	276.4	276.7	276.1	0.84	56.2	0.75
65	64.3	0.86	1705	0.820	295.9	295.5	295.2	296.6	295.8	0.97	64.3	0.86
30	74.8	1.00	1950	0.806	323.3	324.2	323.9	323.4	323.7	1.16	64.4	0.86
38	85.6	1.14	2200	0.795	353.5	353.0	352.6	353.3	353.1	1.35	63.2	0.84
21	94.8	1.26	2450	0.799	374.7	373.8	373.2	373.9	373.9	1.49	64.1	0.85
125	106.0	1.41	2700	0.788	404.6	405.4	404.8	404.8	404.9	1.70	64.3	0.86
56	115.9	1.55	2950	0.787	431.0	432.1	431.5	431.8	431.6	1.88	64.2	0.86
9	126.8	1.69	3200	0.780	457.5	456.1	455.9	456.9	456.6	2.04	64.4	0.86

Table B.27: $r_0 = 75\,\mathrm{mm}$.

#	a	α_b	α_s	$2r_s$	r_s^*
82	0.28	12.0	36.8	117.1	0.33
58	0.40	11.0	33.7	100.2	0.40
27	0.49	10.8	31.0	90.2	0.59
149	0.62	10.6	29.5	61.6	0.70
88	0.75	10.2	28.1	45.1	0.85
65	0.86	10.4	26.9	22.5	1.00
30	1.00	9.8	26.4		
38	1.14	10.0	23.6		
21	1.26	9.6	23.0		
125	1.41	9.0	22.1		
56	1.55	8.8	21.7		
9	1.69	8.8	21.4		

Table B.28: $r_0 = 75\,\mathrm{mm}$.

a	$\alpha_{b,1}$	$\alpha_{b,2}$	$\alpha_{b,3}$	$\alpha_{b,4}$	$\alpha_{b,5}$	$\alpha_{b,6}$	$\alpha_{b,7}$	$\alpha_{b,8}$	$\alpha_{b,av}$
0.28	11.9	11.9	12.2	11.9	12.2	12.3	12.0	11.6	12.0
0.40	10.9	11.1	10.8	11.0	11.2	11.4	10.9	10.7	11.0
0.49	10.5	10.9	10.6	10.7	10.9	11.0	10.7	10.9	10.8
0.62	11.0	10.8	10.3	10.8	10.5	10.7	10.1	10.6	10.6
0.75	10.2	9.8	10.3	10.4	10.3	10.1	10.1	10.3	10.2
0.86	10.4	10.7	10.7	10.0	10.4	10.1	10.7	10.2	10.4
1.00	9.9	9.6	9.9	9.7	10.1	9.6	9.6	10.0	9.8
1.14	10.1	10.1	10.0	9.6	10.1	10.4	9.7	10.0	10.0
1.26	9.8	9.7	9.8	9.8	9.7	8.5	9.8	9.6	9.6
1.41	9.1	8.8	8.4	9.3	9.0	9.0	9.1	9.3	9.0
1.55	8.9	8.6	9.0	8.6	8.6	8.6	8.8	9.3	8.8
1.69	8.8	8.7	9.0	9.1	8.5	8.9	8.8	8.7	8.8

Table B.29: $r_0 = 75\,\mathrm{mm}$.

a	$\alpha_{s,1}$	$\alpha_{s,2}$	$\alpha_{s,3}$	$\alpha_{s,4}$	$\alpha_{s,5}$	$\alpha_{s,6}$	$\alpha_{s,7}$	$\alpha_{s,8}$	$\alpha_{s,av}$
0.28	37.1	37.0	36.9	37.2	36.5	36.5	36.6	36.6	36.8
0.40	33.7	33.6	33.2	33.6	33.4	33.7	34.6	33.9	33.7
0.49	31.2	31.2	31.4	30.6	31.2	29.7	31.3	31.4	31.0
0.62	29.5	29.8	29.0	29.2	30.0	29.7	29.4	29.4	29.5
0.75	28.3	28.2	27.8	27.9	28.3	28.0	28.2	28.0	28.1
0.86	26.8	27.0	27.4	27.1	25.9	27.3	26.7	26.9	26.9
1.00	27.0	26.1	26.4	26.7	26.9	26.0	26.2	26.0	26.4
1.14	23.7	23.9	23.5	22.7	23.5	23.8	23.8	24.0	23.6
1.26	22.7	22.8	23.8	23.5	23.4	22.6	22.6	22.6	23.0
1.41	21.7	22.1	22.6	21.6	22.2	21.7	23.2	21.7	22.1
1.55	21.3	21.3	22.0	21.6	21.6	22.2	22.1	21.5	21.7
1.69	21.6	21.5	21.0	21.0	21.3	21.8	21.4	21.7	21.4

Table B.30: $r_0 = 75\,\mathrm{mm}$.

Appendix C

Experimental data: Density values from CT

This appendix contains additional cross-sectional XCT images of the column pre and post collapse for aspect ratios $a = 1.20, 1.70, 2.04$ as discussed in Section 5.3, and the raw data related to packing fraction of ROI's of the column and pile from XCT investigations outlined in Chapter 5.

The XCT images can be found in the follwing figures:

$a = 1.20$ column Figure C.1

$a = 1.20$ pile Figure C.2

$a = 1.70$ column Figure C.3

$a = 1.70$ pile Figure C.4

$a = 2.04$ column Figure C.5

$a = 2.04$ pile Figure C.6

Recall that the column/pile was regularly divided into annular ROI's with $\Delta r = 2.4\,\text{mm}$ and $\Delta h = 2.4\,\text{mm}$. In the tables that follow the rings are labelled in the r direction by a number increasing from the centre, and in the h direction by a letter (starting from A) upwards from the base. For example the ring C5 would be on the third row from the bottom (C) and the fifth ring radially (5). This is further illustrated in Figure C.1. The volume of material (in mm^3) within each ring was evaluated in *'VG Studio Max'* using the methodology described as in Section 6.6. This was then divided by the volume of the ring itself to calculate the packing fraction of that ring ϕ. In this appendix both the volume of material (mm^3) and ϕ is given for each ring and can be found in the tables detailed below.

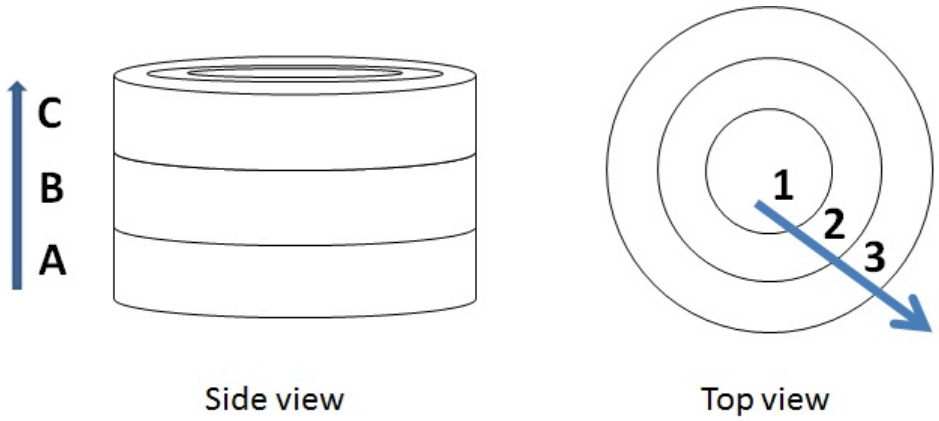

Figure C.1: How each ring is numbered from the collection of annular ROIs generated.

$a = 0.72$ column Figure C.8

$a = 0.72$ pile Figure C.9

$a = 1.20$ column Figure C.10

$a = 1.20$ pile Figure C.11

$a = 1.70$ column Figure C.12

$a = 1.70$ pile Figure C.13

$a = 2.04$ column Figure C.14

$a = 2.04$ pile Figure C.15

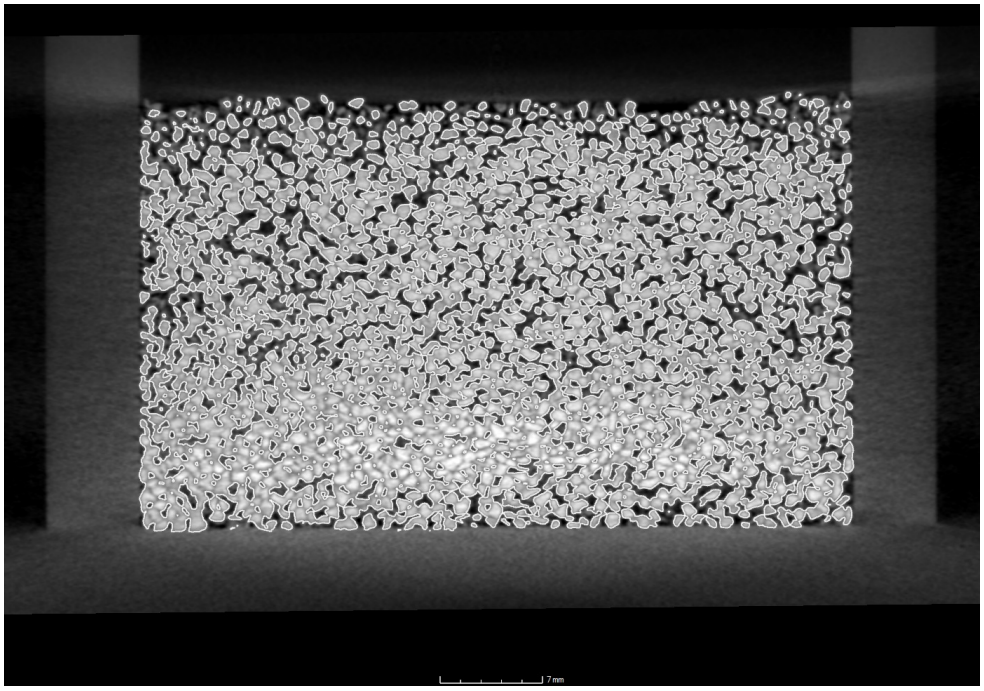

Figure C.2: 2D slice through $a = 1.20$ pre collapse to depict grain position.

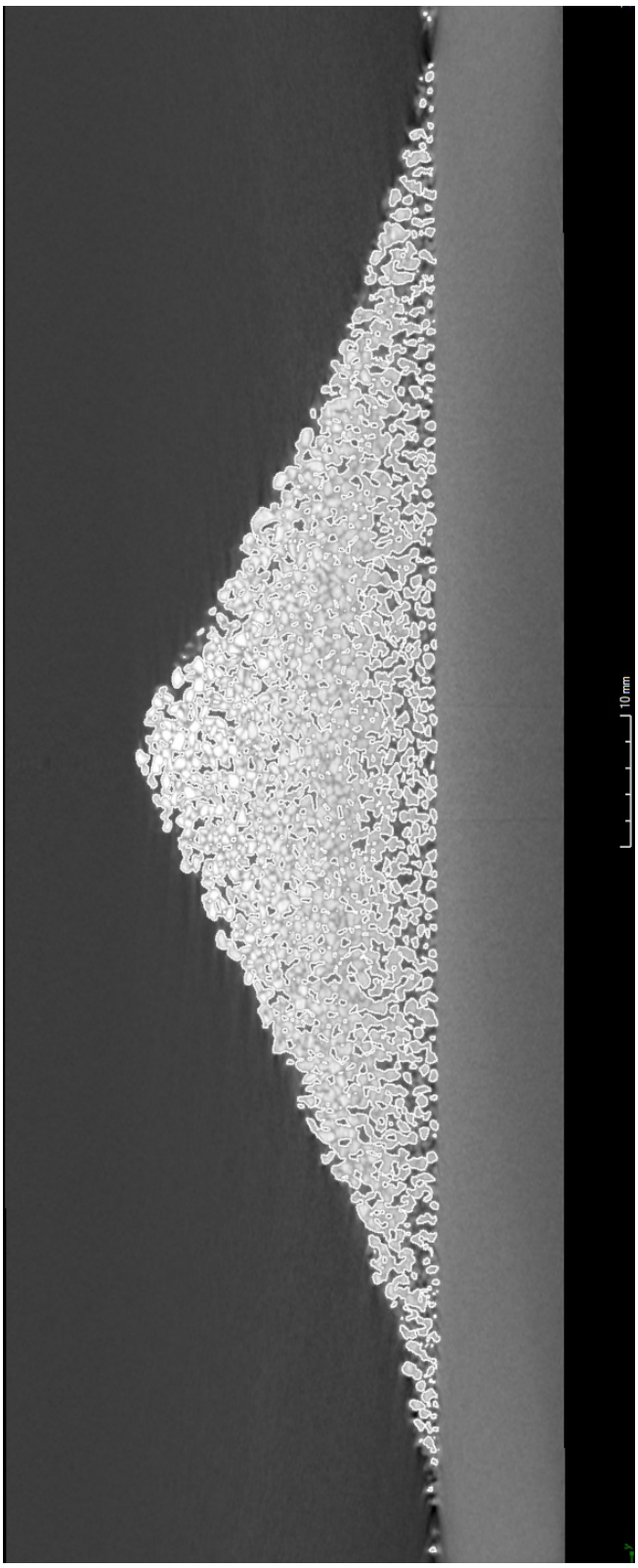

Figure C.3: 2D slice through $a = 1.20$ post collapse to depict grain position.

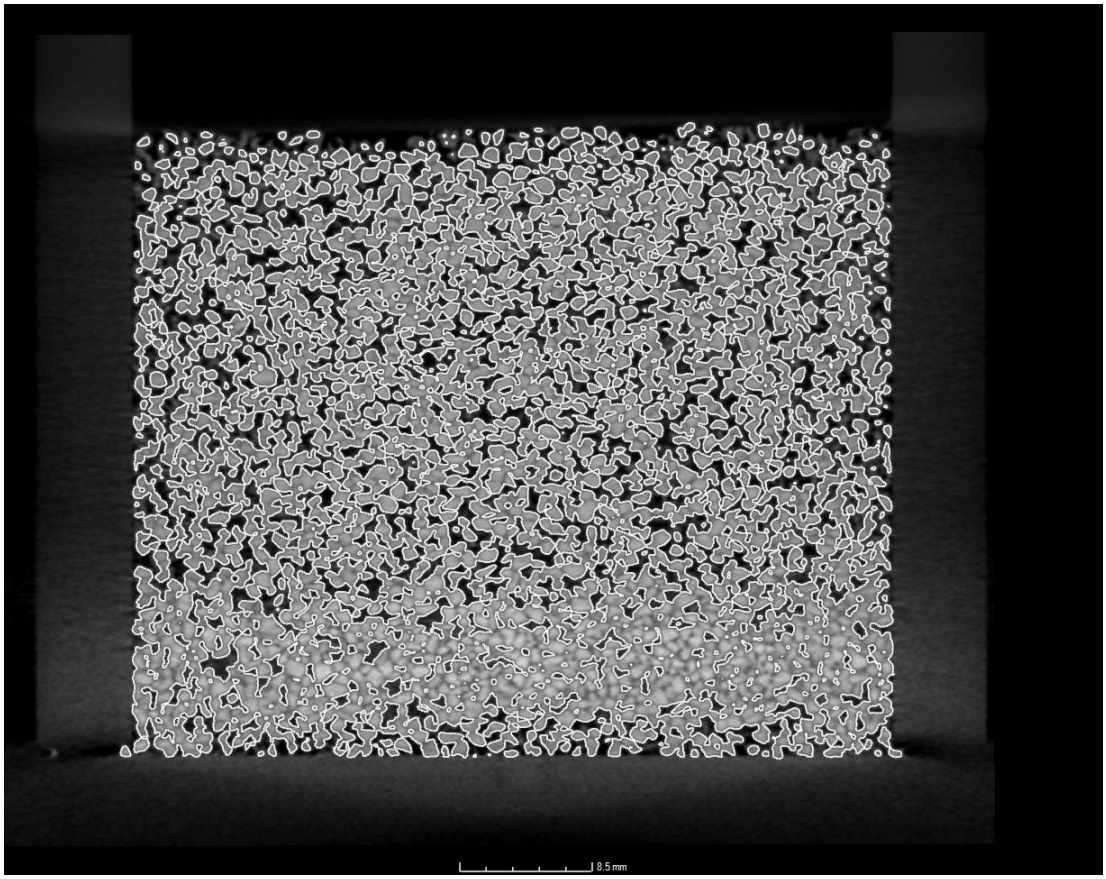

Figure C.4: 2D slice through $a = 1.70$ pre collapse to depict grain position.

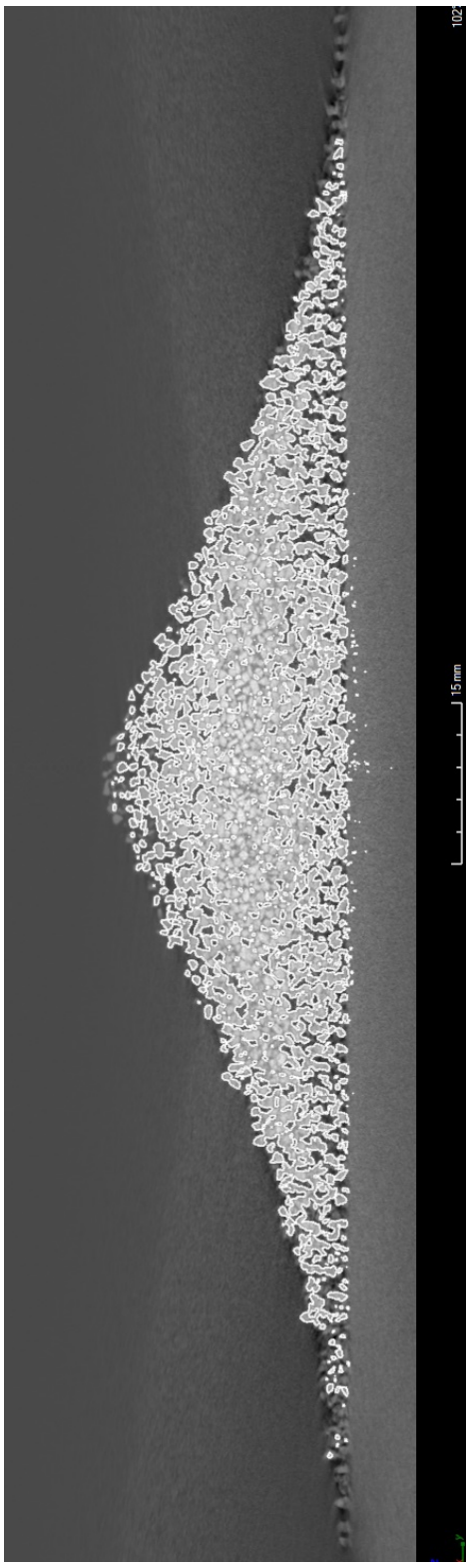

Figure C.5: 2D slice through $a = 1.70$ post collapse to depict grain position.

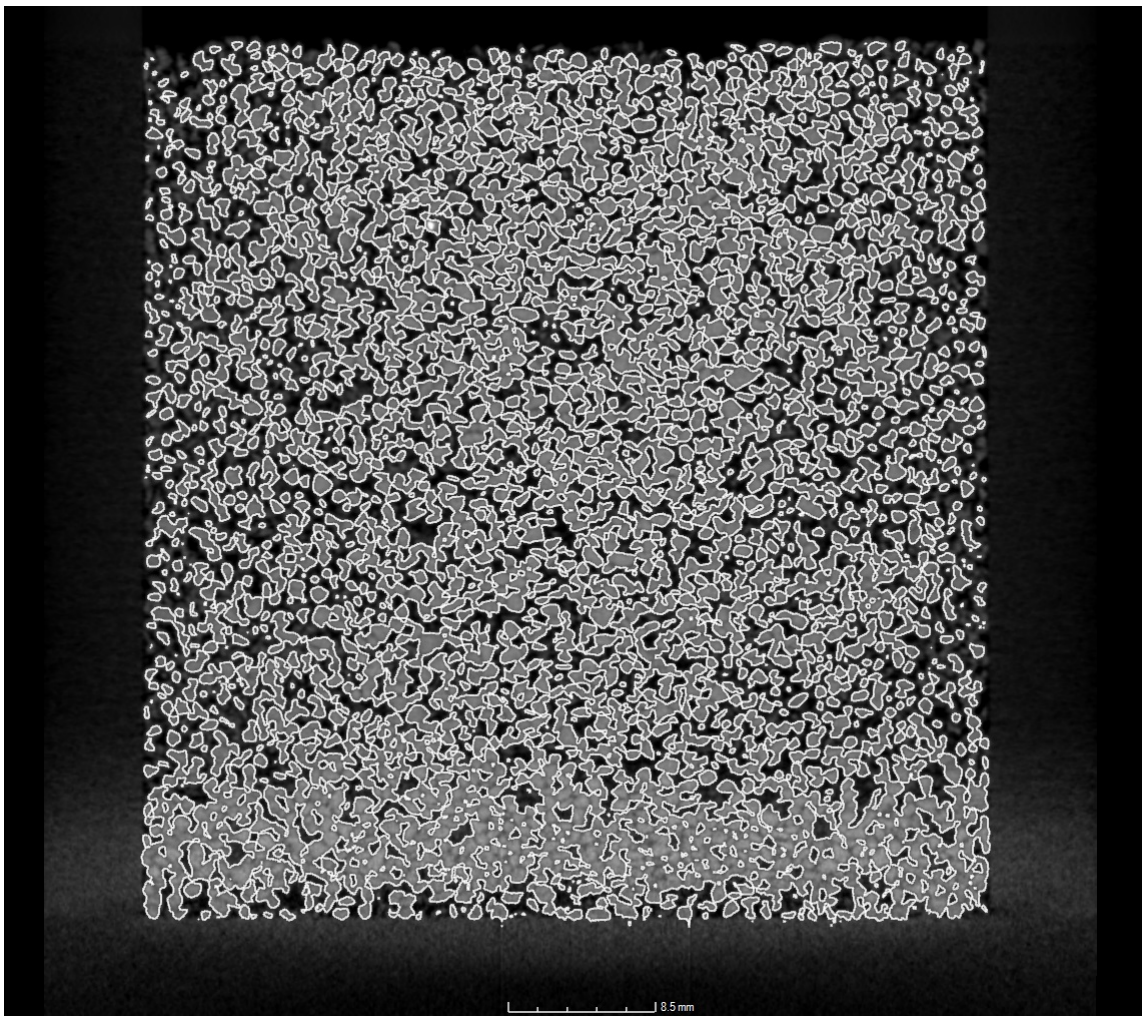

Figure C.6: 2D slice through $a = 2.04$ pre collapse to depict grain position.

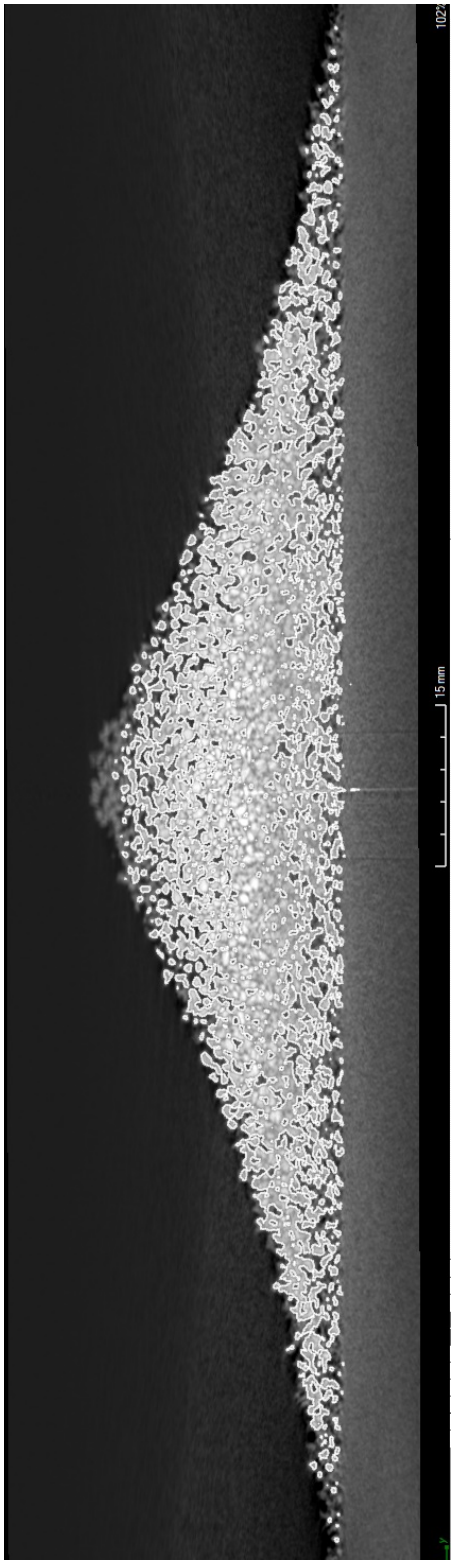

Figure C.7: 2D slice through $a = 2.04$ post collapse to depict grain position.

Volume of material

	1	2	3	4	5	6	7	8	9	10
G	20.55	62.49	101.80	143.25	182.25	216.36	256.96	290.86	314.95	341.11
F	21.54	65.95	108.24	152.69	195.64	234.74	277.70	309.88	337.01	366.42
E	21.72	64.82	107.27	152.39	194.40	229.85	271.37	306.41	336.25	360.08
D	20.24	64.11	103.58	145.50	184.67	226.55	265.35	300.80	325.61	354.93
C	20.02	60.98	103.25	142.35	181.14	218.07	262.64	296.43	324.69	353.07
B	20.96	62.68	104.30	147.88	189.18	224.61	268.17	302.39	331.96	359.54
A	22.57	68.15	113.10	157.96	202.00	243.56	285.31	320.43	348.70	368.84

Φ

	1	2	3	4	5	6	7	8	9	10
G	0.473182	0.466666	0.453684	0.45496	0.449622	0.436369	0.438276	0.429774	0.410491	0.397689
F	0.495978	0.492505	0.482385	0.484941	0.482656	0.473439	0.473651	0.457878	0.439243	0.427197
E	0.500122	0.484066	0.478062	0.483988	0.479596	0.463577	0.462854	0.452751	0.438252	0.419806
D	0.466044	0.478764	0.461617	0.462106	0.455592	0.456921	0.452587	0.444461	0.424385	0.413801
C	0.460978	0.45539	0.460146	0.452101	0.446883	0.439818	0.447964	0.438004	0.423185	0.411633
B	0.482623	0.468085	0.464826	0.469665	0.466718	0.453008	0.457396	0.446811	0.432661	0.419176
A	0.519694	0.508934	0.504044	0.501679	0.498346	0.491228	0.486631	0.473466	0.454479	0.430019

Figure C.8: Volume of material (mm^3) and packing fraction for each ring of column with $a = 0.72$.

Volume of material

	1	2	3	4	5	6	7	8	9	10	11	12	13
G	28.73	86.19	138.71	173.70	0.00	0.00	0	0	0	0	0	0	0
F	29.17	86.89	145.91	203.87	238.29	233.73	0	0	0	0	0	0	0
E	28.74	87.05	142.76	204.50	258.23	285.80	308.47	284.87	0	0	0	0	0
D	26.87	85.05	140.53	200.18	254.43	306.30	349.80	371.94	392.74	0	0	0	0
C	26.90	84.11	139.87	197.53	258.08	311.78	411.40	431.03	467.02	478.38	0	0	0
B	29.87	89.24	148.63	211.25	272.38	330.58	399.91	457.27	494.34	499.39	559.04	584.25	0
A	31.35	93.43	154.86	214.29	272.25	322.97	377.33	422.25	454.65	450.47	453.85	487.05	486.58

ϕ

	1	2	3	4	5	6	7	8	9	10	11	12	13
G	0.661534	0.643654	0.618178	0.551669	0	0	0	0	0	0	0	0	0
F	0.671665	0.648882	0.650266	0.647488	0.587876	0.471402	0	0	0	0	0	0	0
E	0.661764	0.650077	0.636228	0.649489	0.637069	0.57642	0.526133	0.420923	0	0	0	0	0
D	0.618706	0.635141	0.626289	0.635769	0.627694	0.617766	0.596626	0.549577	0.511879	0	0	0	0
C	0.619396	0.628121	0.623348	0.627352	0.636699	0.628819	0.701693	0.636889	0.608692	0.557728	0	0	0
B	0.687783	0.666431	0.662388	0.670927	0.671978	0.666736	0.682095	0.675661	0.644299	0.582223	0.589575	0.56249	0
A	0.721862	0.697722	0.690153	0.680582	0.671657	0.651387	0.643582	0.623915	0.592569	0.525188	0.47864	0.46891	0.430921

Figure C.9: Volume of material (mm^3) and packing fraction for each ring of pile with $a = 0.72$.

Volume of material

K	20.82	63.01	99.79	138.85	171.48	201.62	232.07	252.50	252.76	227.87
J	21.19	65.09	106.31	144.12	186.18	218.33	253.07	276.61	289.18	267.23
I	21.52	65.54	105.69	147.96	185.40	221.30	252.97	271.93	283.41	266.80
H	20.74	66.52	105.33	145.75	185.18	213.74	254.27	274.54	290.65	270.31
G	20.97	64.82	103.84	149.51	185.67	221.82	221.82	288.18	298.06	279.18
F	22.20	69.00	109.45	155.66	197.98	234.43	273.06	301.36	315.20	298.86
E	24.05	74.15	120.95	168.17	215.98	254.58	299.76	339.27	356.92	341.39
D	27.66	85.10	139.12	197.86	249.00	295.07	343.18	383.92	410.47	403.63
C	32.05	96.50	157.33	216.54	275.92	322.40	375.41	422.93	453.09	455.88
B	26.31	83.84	138.51	194.06	251.05	299.32	356.70	410.18	451.79	477.29
A	17.58	57.65	93.51	128.90	170.59	202.63	243.11	284.64	324.43	362.01
	1	2	3	4	5	6	7	8	9	10

ϕ

K	0.479399	0.47055	0.444726	0.440985	0.423051	0.406641	0.395824	0.373093	0.329435	0.265666
J	0.487919	0.486083	0.473784	0.457723	0.459317	0.440342	0.431642	0.408718	0.376903	0.311555
I	0.495517	0.489443	0.471021	0.469919	0.457393	0.446332	0.431471	0.401803	0.369383	0.311054
H	0.477557	0.496762	0.469416	0.4629	0.45685	0.431085	0.433688	0.40566	0.378819	0.315146
G	0.482853	0.484066	0.462776	0.474841	0.458059	0.447381	0.378341	0.425814	0.388477	0.325487
F	0.511175	0.515282	0.487777	0.494374	0.488428	0.472814	0.465737	0.445289	0.410817	0.348431
E	0.553773	0.553742	0.539029	0.534105	0.532836	0.513454	0.511277	0.501304	0.465192	0.398016
D	0.636896	0.635515	0.620005	0.6284	0.614298	0.595117	0.585335	0.567279	0.534987	0.470579
C	0.73798	0.720648	0.701161	0.687728	0.680711	0.650238	0.640307	0.62492	0.590536	0.531496
B	0.605811	0.626105	0.617287	0.616332	0.619355	0.603688	0.608395	0.606081	0.588841	0.556457
A	0.404795	0.430522	0.416739	0.409384	0.420856	0.408678	0.414654	0.420583	0.422847	0.422056
	1	2	3	4	5	6	7	8	9	10

Figure C.10: Volume of material (mm^3) and packing fraction for each ring of column with $a = 1.20$.

Volume of material

	1	2	3	4	5	6	7	8	9	10	11	12	13
I	32.58	0	0	0	0	0	0	0	0	0	0	0	0
H	35.00	105.29	167.70	0	0	0	0	0	0	0	0	0	0
G	35.76	109.90	179.77	251.12	305.48	0	0	0	0	0	0	0	0
F	36.38	114.56	184.97	262.76	335.47	393.72	453.13	0	0	0	0	0	0
E	37.98	116.29	189.98	272.62	350.94	419.67	486.19	559.22	604.48	530.83	0	0	0
D	34.09	103.45	170.93	245.49	316.14	379.08	437.06	466.57	516.82	589.96	646.21	0	0
C	35.56	111.75	184.96	265.80	343.21	414.89	500.16	573.04	611.85	678.92	791.41	849.09	920.62
B	29.01	91.00	152.62	216.08	277.79	336.04	408.37	480.21	529.25	561.94	665.27	730.30	824.93
A	24.04	77.77	125.90	179.59	234.91	280.09	333.90	389.52	438.73	456.84	488.04	524.58	587.10
	14	**15**	**16**	**17**	**18**	**19**	**20**						
C	831.50	0	0	0	0	0	0						
B	887.83	1005.85	1004.58	0	0	0	0						
A	615.09	705.31	745.16	834.12	888.28	930.30	824.70						

Φ

	1	2	3	4	5	6	7	8	9	10	11	12	13
I	0.75018	0	0	0	0	0	0	0	0	0	0	0	0
H	0.80591	0.78629	0.74738	0	0	0	0	0	0	0	0	0	0
G	0.82341	0.82072	0.80117	0.79755	0.75364	0	0	0	0	0	0	0	0
F	0.83768	0.85552	0.82434	0.83452	0.82762	0.79408	0.77287	0	0	0	0	0	0
E	0.87452	0.86844	0.84667	0.86584	0.86579	0.84642	0.82926	0.8263	0.78785	0.61888	0	0	0
D	0.78495	0.77255	0.76177	0.77967	0.77994	0.76455	0.74546	0.6894	0.6736	0.68782	0.68151	0	0
C	0.8188	0.83453	0.8243	0.84418	0.84672	0.83678	0.85308	0.84672	0.79746	0.79153	0.83464	0.81747	0.81531
B	0.66798	0.67957	0.68017	0.68627	0.68532	0.67775	0.69652	0.70956	0.6898	0.65515	0.70161	0.7031	0.73057
A	0.55354	0.58078	0.56109	0.57038	0.57954	0.5649	0.56951	0.57555	0.57182	0.53262	0.5147	0.50504	0.51994
	14	**15**	**16**	**17**	**18**	**19**	**20**						
C	0.68176	0	0	0	0	0	0						
B	0.72794	0.76775	0.71725	0	0	0	0						
A	0.50432	0.53836	0.53203	0.55941	0.56165	0.55639	0.46791						

Figure C.11: Volume of material (mm^3) and packing fraction for each ring of pile with $a = 1.20$.

Volume of material

	1	2	3	4	5	6	7	8	9	10
P	22.07	66.46	109.80	153.88	192.34	225.64	262.65	290.08	303.20	292.09
O	23.87	72.56	118.81	166.43	214.22	253.31	297.64	320.87	332.92	341.61
N	23.30	73.77	119.48	168.74	211.29	255.22	295.80	328.00	350.79	344.77
M	23.69	69.33	115.13	164.84	209.95	251.40	296.03	330.34	349.05	347.07
L	21.81	70.38	115.48	163.10	214.61	253.14	297.88	335.75	357.49	348.91
K	24.58	73.86	120.82	169.72	214.71	255.87	300.64	337.73	356.36	349.66
J	23.95	76.10	122.37	170.48	216.77	259.74	305.06	335.85	366.23	349.34
I	24.18	76.85	124.07	174.37	219.13	259.99	304.32	336.89	361.00	355.44
H	24.63	75.59	121.33	172.11	222.41	259.06	300.55	343.05	365.66	356.87
G	24.65	74.04	122.98	172.59	219.46	257.61	300.60	336.21	366.88	359.97
F	24.77	75.56	125.14	170.41	214.44	259.34	303.82	349.93	383.54	390.94
E	26.18	81.65	136.55	185.67	240.18	289.48	340.97	395.34	437.10	459.94
D	31.83	94.38	157.94	218.25	279.71	339.98	400.31	463.56	513.43	550.61
C	33.21	100.01	169.78	236.12	308.74	367.55	437.70	499.68	556.88	597.32
B	29.60	92.84	152.79	213.86	278.22	337.92	398.70	463.99	527.96	572.15
A	19.74	60.08	100.85	142.00	185.69	232.13	287.40	345.46	405.45	432.11

Φ

	1	2	3	4	5	6	7	8	9	10
P	0.50818	0.49631	0.48934	0.48872	0.47451	0.45509	0.44798	0.42862	0.39518	0.34054
O	0.54963	0.54187	0.52949	0.52858	0.52849	0.51089	0.50766	0.47412	0.43391	0.39827
N	0.5365	0.5509	0.53248	0.53592	0.52127	0.51474	0.50452	0.48465	0.4572	0.40196
M	0.54548	0.51775	0.51309	0.52353	0.51796	0.50704	0.50492	0.48811	0.45494	0.40464
L	0.50219	0.52559	0.51465	0.518	0.52946	0.51055	0.50807	0.4961	0.46594	0.40678
K	0.56598	0.55158	0.53845	0.53903	0.5297	0.51606	0.51278	0.49903	0.46446	0.40766
J	0.55147	0.5683	0.54536	0.54144	0.53478	0.52386	0.52032	0.49625	0.47733	0.40728
I	0.55677	0.5739	0.55293	0.5538	0.54061	0.52437	0.51905	0.49779	0.47051	0.4144
H	0.56713	0.5645	0.54072	0.54662	0.5487	0.52249	0.51262	0.50689	0.47658	0.41606
G	0.56759	0.55292	0.54808	0.54814	0.54142	0.51956	0.51271	0.49678	0.47817	0.41968
F	0.57035	0.56427	0.5577	0.54122	0.52904	0.52305	0.5182	0.51706	0.49989	0.45578
E	0.60282	0.60975	0.60855	0.58969	0.59254	0.58384	0.58157	0.58415	0.5697	0.53623
D	0.73291	0.70482	0.70388	0.69316	0.69006	0.68569	0.68278	0.68495	0.66918	0.64194
C	0.76469	0.74686	0.75665	0.74991	0.76168	0.7413	0.74655	0.73833	0.72581	0.6964
B	0.68157	0.69332	0.68093	0.67922	0.68639	0.68154	0.68003	0.68559	0.68812	0.66705
A	0.45453	0.44867	0.44945	0.45099	0.45811	0.46818	0.4902	0.51045	0.52844	0.50378

Figure C.12: Volume of material (mm^3) and packing fraction for each ring of column with $a = 1.70$.

Volume of material

I	13.73	0	0	0	0	0	0	0	0	0	0	0	0	0	0	0	0	0	0	0
H	21.19	62.35	91.91	101.50	0	0	0	0	0	0	0	0	0	0	0	0	0	0	0	0
G	24.94	75.55	120.85	156.92	184.82	197.98	0	0	0	0	0	0	0	0	0	0	0	0	0	0
F	28.84	86.45	142.35	193.97	234.41	272.19	313.63	337.58	0	0	0	0	0	0	0	0	0	0	0	0
E	35.78	109.25	178.77	244.87	310.80	353.74	395.95	437.14	481.22	491.88	0	0	0	0	0	0	0	0	0	0
D	34.81	107.08	178.57	251.41	322.60	389.87	445.03	489.41	532.42	579.09	635.45	636.73	594.82							
C	30.13	91.05	151.70	215.09	282.26	339.53	403.63	449.29	476.99	524.25	610.52	659.61	710.18							
B	25.72	81.15	132.80	185.57	241.08	292.61	343.07	388.74	412.55	412.65	471.78	495.88	540.34							
A	19.32	61.65	102.63	143.82	187.05	230.96	273.06	318.53	356.38	358.11	357.34	381.31	416.95							
	1	2	3	4	5	6	7	8	9	10	11	12	13							
C	732.94	766.76	0	0	0	0	0	0	0	0	0									
B	570.26	634.92	662.62	716.37	735.55	667.88	0	0	0	0										
A	433.26	477.10	476.30	500.99	516.04	526.15	532.90	533.17	496.80	418.10										
	1	2	3	4	5	6	7	21	22	23										

Φ

I	0.31615	0	0	0	0	0	0	0	0	0	0	0	0	0	0	0	0	0	0	0
H	0.48792	0.46562	0.40961	0.32236	0	0	0	0	0	0	0	0	0	0	0	0	0	0	0	0
G	0.57427	0.5642	0.53858	0.49838	0.45596	0.3993	0	0	0	0	0	0	0	0	0	0	0	0	0	0
F	0.66407	0.6456	0.6344	0.61605	0.5783	0.54897	0.53493	0.49881	0	0	0	0	0	0	0	0	0	0	0	0
E	0.82387	0.81586	0.79671	0.7777	0.76676	0.71345	0.67534	0.64592	0.6272	0.57347	0	0	0							
D	0.80153	0.79966	0.79582	0.79847	0.79587	0.78632	0.75905	0.72315	0.69393	0.67514	0.67016	0.61301	0.52678							
C	0.69377	0.67995	0.67607	0.68312	0.69635	0.68479	0.68844	0.66387	0.62169	0.61121	0.64387	0.63504	0.62894							
B	0.59223	0.60602	0.59184	0.58937	0.59476	0.59016	0.58515	0.5744	0.5377	0.4811	0.49755	0.47741	0.47853							
A	0.44486	0.46039	0.45738	0.45677	0.46146	0.46582	0.46574	0.47066	0.46449	0.41751	0.37686	0.36711	0.36926							
	1	2	3	4	5	6	7	8	9	10	11	12	13							
C	0.60095	0.58526	0	0	0	0	0	0	0	0	0									
B	0.46756	0.48463	0.4731	0.48044	0.46508	0.39944	0	0	0	0										
A	0.35524	0.36417	0.34007	0.33599	0.32629	0.31468	0.30235	0.28774	0.25563	0.20556										
	14	15	16	17	18	19	20	21	22	23										

Figure C.13: Volume of material (mm^3) and packing fraction for each ring of pile with $a = 1.70$.

Volume of material

	1	2	3	4	5	6	7	8	9	10
T	21.36	65.04	105.65	145.47	186.59	222.13	249.60	265.60	272.91	235.96
S	22.37	68.78	111.29	155.53	199.06	237.13	269.57	290.93	292.86	250.19
R	20.77	65.02	110.43	154.34	200.21	238.64	274.05	295.31	298.89	248.46
Q	22.44	68.76	111.18	158.77	203.05	240.12	280.92	301.07	301.50	256.19
P	23.00	69.73	113.34	160.17	202.83	242.18	275.02	297.63	299.31	252.51
O	22.59	67.24	112.01	157.09	198.89	232.80	272.68	290.68	291.48	245.79
N	20.74	66.65	107.71	152.44	195.90	234.88	265.32	294.17	290.61	247.51
M	22.30	66.91	111.22	156.73	200.53	230.57	263.01	288.58	288.32	245.83
L	22.96	69.75	114.75	157.18	200.72	229.84	261.73	279.89	283.19	236.23
K	23.02	71.34	114.56	158.76	195.60	226.78	256.34	277.97	281.19	230.38
J	21.96	69.02	112.75	153.94	193.41	226.27	257.77	282.05	278.55	236.58
I	22.27	67.21	110.32	153.79	194.86	227.13	260.64	286.12	286.90	243.33
H	21.48	68.77	109.87	154.53	198.91	231.38	261.40	288.63	288.45	242.30
G	22.14	68.45	111.61	158.77	196.40	227.30	262.12	282.42	283.88	236.70
F	21.78	65.44	110.04	153.05	193.73	230.70	258.78	278.14	276.22	238.10
E	21.45	65.39	105.81	145.57	188.54	221.97	256.00	281.46	288.42	250.26
D	22.56	66.21	111.82	160.64	206.84	248.49	292.26	322.03	341.50	326.70
C	27.51	83.41	142.20	201.00	251.54	314.14	368.15	418.09	459.60	480.10
B	30.77	94.73	156.81	220.14	282.32	334.76	404.02	466.16	519.06	567.40
A	24.04	73.69	121.48	175.21	225.87	276.56	339.23	400.60	462.71	525.19

Φ

	1	2	3	4	5	6	7	8	9	10
T	0.49183	0.48571	0.47084	0.46201	0.46033	0.44801	0.42572	0.39245	0.3557	0.2751
S	0.51509	0.51364	0.49598	0.49396	0.49109	0.47826	0.45978	0.42988	0.3817	0.29169
R	0.47825	0.48556	0.49214	0.49018	0.49393	0.4813	0.46743	0.43635	0.38956	0.28967
Q	0.5167	0.51349	0.49549	0.50425	0.50094	0.48429	0.47914	0.44486	0.39296	0.29868
P	0.5296	0.52073	0.50511	0.5087	0.50039	0.48844	0.46908	0.43978	0.39011	0.29439
O	0.52015	0.50214	0.49919	0.49892	0.49067	0.46953	0.46509	0.42951	0.3799	0.28656
N	0.47756	0.49773	0.48002	0.48415	0.4833	0.47372	0.45254	0.43466	0.37877	0.28856
M	0.51348	0.49967	0.49567	0.49777	0.49472	0.46503	0.4486	0.4264	0.37578	0.28661
L	0.52867	0.52088	0.5114	0.4992	0.49519	0.46356	0.44641	0.41356	0.3691	0.27541
K	0.53006	0.53276	0.51055	0.50422	0.48256	0.45738	0.43722	0.41073	0.36649	0.26859
J	0.50565	0.51543	0.50248	0.48891	0.47715	0.45636	0.43966	0.41676	0.36305	0.27582
I	0.51279	0.50191	0.49165	0.48843	0.48073	0.45809	0.44455	0.42277	0.37393	0.28369
H	0.4946	0.51356	0.48965	0.49078	0.49072	0.46666	0.44585	0.42648	0.37595	0.28249
G	0.50979	0.51117	0.4974	0.50425	0.48453	0.45843	0.44708	0.4173	0.37	0.27596
F	0.5015	0.4887	0.49041	0.48608	0.47794	0.46529	0.44138	0.41098	0.36001	0.27759
E	0.49391	0.48832	0.47156	0.46233	0.46514	0.44768	0.43664	0.41588	0.37591	0.29177
D	0.51946	0.49445	0.49834	0.51019	0.51029	0.50117	0.49848	0.47583	0.44509	0.38089
C	0.63344	0.62289	0.63373	0.63837	0.62056	0.63358	0.62792	0.61777	0.59902	0.55973
B	0.70851	0.70743	0.69884	0.69916	0.6965	0.67517	0.68911	0.6888	0.67652	0.66151
A	0.55354	0.55031	0.54139	0.55646	0.55723	0.55778	0.5786	0.59193	0.60307	0.6123

Figure C.14: Volume of material (mm^3) and packing fraction for each ring of column with $a = 2.04$.

Volume of material

I	14.16	36.53	0	0	0	0	0	0	0	0	0	0	0	0
H	19.49	62.38	89.22	106.26	0	0	0	0	0	0	0	0	0	0
G	27.06	81.59	122.93	164.67	188.15	202.59	201.86	0	0	0	0	0	0	0
F	30.37	83.46	148.88	197.34	239.68	268.6	298.56	326.37	329.02	0	0	0	0	0
E	34.12	102.37	166.88	231.34	296.33	341.56	384.97	434.58	468.91	508.5	551	0	0	0
D	39.02	117.99	194.06	275.46	352.65	413.26	479.67	520.74	567.11	611.05	674.52	702.26	730.26	
C	32.41	101.11	165.9	243.81	311.69	378.18	447.82	507.71	555.91	615.92	702.84	747.38	813.48	
B	26.34	84.23	138.82	197.24	250.62	295.25	352.71	406.42	426.62	434.79	432.1	514.15	575.41	
A	17.88	58.01	90.09	133.46	164.33	201.54	242.79	279.07	305.01	299.59	295.36	302.5	333.91	
	1	2	3	4	5	6	7	8	9	10	11	12	13	
D	712.63	0	0	0	0	0	0	0	0	0	0	0	0	0
C	837.23	921.98	923.36	905.32	0	0	0	0	0	0	0	0	0	0
B	593.26	667.57	686.02	749.72	803.21	871.77	894.25	856.09	0	0	0	0	0	0
A	352.83	395.3	391.96	407.99	433.41	456.06	478.46	508.73	519.28	555.15	584.17	571.36	503.14	
	14	15	16	17	18	19	20	21	22	23	24	25	26	

ϕ

I	0.326	0.2728	0	0	0	0	0	0	0	0	0	0	0	0
H	0.4488	0.4658	0.3976	0.3375	0	0	0	0	0	0	0	0	0	0
G	0.6231	0.6093	0.5479	0.523	0.4642	0.4086	0.3443	0	0	0	0	0	0	0
F	0.6993	0.6681	0.6635	0.6267	0.5913	0.5417	0.5092	0.4822	0.4288	0	0	0	0	0
E	0.7856	0.7645	0.7437	0.7347	0.7311	0.6889	0.6566	0.6421	0.6112	0.5928	0.5811	0	0	0
D	0.8985	0.8811	0.8649	0.8749	0.87	0.8335	0.8181	0.7694	0.7391	0.7124	0.7114	0.6761	0.6467	
C	0.7463	0.7551	0.7394	0.7743	0.769	0.7627	0.7638	0.7502	0.7245	0.7181	0.7412	0.7195	0.7204	
B	0.6065	0.629	0.6187	0.6264	0.6183	0.5955	0.6016	0.6005	0.556	0.5069	0.519	0.495	0.5096	
A	0.4117	0.4332	0.4015	0.4239	0.4054	0.4065	0.4141	0.4124	0.3975	0.3493	0.3115	0.2912	0.2957	
	1	2	3	4	5	6	7	8	9	10	11	12	13	
D	0.5843	0	0	0	0	0	0	0	0	0	0	0	0	0
C	0.6865	0.7037	0.6593	0.6072	0	0	0	0	0	0	0	0	0	0
B	0.4864	0.5095	0.4898	0.5028	0.5079	0.5214	0.5074	0.462	0	0	0	0	0	0
A	0.2893	0.3017	0.2799	0.2736	0.274	0.2728	0.2715	0.2745	0.2672	0.2729	0.275	0.258	0.2182	
	14	15	16	17	18	19	20	21	22	23	24	25	26	

Figure C.15: Volume of material (mm^3) and packing fraction for each ring of pile with $a = 2.04$.

Appendix D

Experimental data: Rotational Collapse

This appendix contains all the data obtained in experiments outline in Chapter 7.

Nonclamenture:

r_0	(mm) initial column radius
r_i	(mm) runout radius where $i = 1, 2, 3, av$ (av=average)
r_*	normalised final pile radius
h_0	(mm) initial column height
h_f	(mm) final pile height
h_*	normalised final pile height
a	initial column aspect ratio
a_{cone}	aspect ratio for onset of full conical shape
a_h	aspect ratio for the apparent stagnation of final height
f	(Hz) frequency
f_*	normalised frequency
m_0	(g) initial mass of particulate
m_f	(g) final mass of particulate
m_*	fraction mass loss
t	(s) time

t_f	(s) total collapse time
t_*	normalised total collapse time
Λ	proportional constant in relation $r_* = \Lambda a + \epsilon$
Λ_*	$\Lambda_* = \frac{\Lambda - \Lambda_0}{\Lambda_0}$ where Λ_0 is Λ for no rotation

The tables are organised in the following manner:

D.1	Results from repeatability testing
D.2	Results $r_0 = 20\,\text{mm}$, fixed f, increasing a
D.3	Results $r_0 = 20\,\text{mm}$, fixed f, increasing a
D.4	Results $r_0 = 20\,\text{mm}$, fixed f, increasing a
D.5	Results $r_0 = 25\,\text{mm}$, fixed f, increasing a
D.6	Results $r_0 = 25\,\text{mm}$, fixed f, increasing a
D.7	Results $r_0 = 25\,\text{mm}$, fixed f, increasing a
D.8	Results $r_0 = 30\,\text{mm}$, fixed f, increasing a
D.9	Results $r_0 = 30\,\text{mm}$, fixed f, increasing a
D.10	Results $r_0 = 30\,\text{mm}$, fixed f, increasing a
D.11	Results $r_0 = 36\,\text{mm}$, fixed f, increasing a
D.12	Results $r_0 = 36\,\text{mm}$, fixed f, increasing a
D.13	Results $r_0 = 36\,\text{mm}$, fixed f, increasing a
D.14	Results $r_0 = 36\,\text{mm}$, fixed f, increasing a
D.15	Results $r_0 = 36\,\text{mm}$, fixed f, increasing a
D.16	Results $r_0 = 36\,\text{mm}$, fixed f, increasing a
D.17	Results $r_0 = 36\,\text{mm}$, fixed a, increasing f
D.18	Results $r_0 = 36\,\text{mm}$, fixed a, increasing f
D.19	Onset of full conical shape, a_{cone}
D.20	Evaluation of Λ
D.21	Onset of stagnating height, a_h

r_0	h_0	a	m_0	f	f_*	r_f	h_f	m_f	t_f	r_*	h_*	m_*	t_*
20	11	0.55	20.0	0.47	0.02	32	11	20.0	0.113	0.60	1.00	0.00	2.50
20	11	0.55	20.0	0.47	0.02	33	11	20.0	0.121	0.63	1.00	0.00	2.68
20	11	0.55	20.1	0.47	0.02	32	11	20.1	0.121	0.60	1.00	0.00	2.68
20	22	1.10	40.0	1.02	0.05	46	18	40.0		1.32	0.83	0.00	
20	22	1.10	40.1	1.02	0.05	46	18	40.1		1.29	0.84	0.00	
20	22	1.10	40.0	1.02	0.05	45	18	40.0		1.29	0.83	0.00	
20	33	1.65	60.0	1.33	0.06	64	16	57.6		2.18	0.49	0.04	
20	33	1.65	60.0	1.33	0.06	63	16	58.8		2.15	0.50	0.02	
20	33	1.65	60.0	1.33	0.06	62	16	57.9		2.14	0.49	0.04	
25	15	0.60	40.0	0.94	0.05	43	15	40.0	0.141	0.74	1.00	0.00	2.79
25	15	0.60	40.0	0.94	0.05	43	15	40.0	0.141	0.72	1.00	0.00	2.79
25	15	0.60	40.0	0.94	0.05	42	15	40.0	0.137	0.71	1.00	0.00	2.71
25	26	1.04	70.0	1.26	0.06	62	18	68.7		1.49	0.72	0.02	
25	26	1.04	70.0	1.26	0.06	63	19	68.9		1.51	0.74	0.02	
25	26	1.04	70.0	1.26	0.06	63	19	68.2		1.52	0.74	0.03	
25	38	1.52	100.0	1.65	0.08	51	16	44.6		1.07	0.44	0.55	
25	38	1.52	100.0	1.65	0.08	52	17	45.3		1.08	0.46	0.55	
25	38	1.52	100.0	1.65	0.08	52	17	43.9		1.09	0.45	0.56	
30	16	0.53	60.1	0.71	0.04	48	16	60.1	0.137	0.63	1.00	0.00	2.48
30	16	0.53	60.0	0.71	0.04	49	16	60.0	0.145	0.65	1.00	0.00	2.62
30	16	0.53	60.0	0.71	0.04	49	16	60.0	0.145	0.64	1.00	0.00	2.62
30	30	1.00	120.0	1.10	0.06	72	24	117.2		1.40	0.79	0.02	
30	30	1.00	120.0	1.10	0.06	73	23	118.3		1.44	0.79	0.01	
30	30	1.00	120.0	1.10	0.06	73	24	118.0		1.45	0.79	0.02	
30	46	1.53	180.0	1.41	0.08	73	20	105.7		1.45	0.45	0.41	
30	46	1.53	180.0	1.41	0.08	74	21	107.2		1.46	0.47	0.40	
30	46	1.53	180.0	1.41	0.08	73	21	104.0		1.44	0.46	0.42	
36	19	0.53	100.4	0.47	0.03	59	19	100.4	0.177	0.65	1.00	0.00	2.92
36	19	0.53	100.5	0.47	0.03	59	19	100.5	0.181	0.64	1.00	0.00	2.99
36	19	0.53	100.5	0.47	0.03	60	19	100.5	0.177	0.66	1.00	0.00	2.92
36	37	1.03	200.1	1.18	0.07	96	29	189.2	0.363	1.66	0.78	0.05	5.99
36	37	1.03	200.0	1.18	0.07	94	28	192.1	0.359	1.62	0.76	0.04	5.93
36	37	1.03	200.1	1.18	0.07	95	28	191.3	0.363	1.63	0.77	0.04	5.99
36	55	1.53	300.6	1.33	0.08	82	26	157.9		1.27	0.48	0.47	
36	55	1.53	300.6	1.33	0.08	82	26	161.2		1.27	0.48	0.46	
36	55	1.53	300.5	1.33	0.08	82	27	164.6		1.28	0.48	0.45	

Table D.1: Repeatability testing.

f	f_*	h_0	a	m_0	r_f	h_f	m_f	t_f	r_*	h_*	m_*	t_*
0.00	0.00	5	0.25	10.0	26	5	10.0	0.079	0.30	0.25	0.00	1.75
		8	0.40	15.0	28	8	15.0	0.100	0.40	0.40	0.00	2.21
		11	0.55	20.1	31	11	20.1	0.117	0.55	0.55	0.00	2.60
		14	0.70	25.1	34	14	25.1	0.132	0.70	0.70	0.00	2.93
		17	0.85	30.1	38	16	30.1	0.146	0.90	0.80	0.00	3.23
		20	1.00	35.0	41	18	35.0	0.158	1.05	0.90	0.00	3.50
		22	1.10	40.1	42	20	40.1	0.166	1.10	1.00	0.00	3.67
		25	1.25	45.1	44	20	45.1	0.177	1.20	1.00	0.00	3.91
		28	1.40	50.1	48	20	50.1	0.187	1.40	1.00	0.00	4.14
		30	1.50	55.1	51	20	55.1	0.194	1.55	1.00	0.00	4.29
		33	1.65	60.1	53	20	60.1	0.203	1.65	1.00	0.00	4.50
0.47	0.02	5	0.25	10.1	26	5	10.1	0.079	0.32	0.25	0.00	1.76
		8	0.40	15.0	29	8	15.0	0.100	0.47	0.40	0.00	2.21
		11	0.55	20.1	32	11	20.1	0.117	0.58	0.55	0.00	2.60
		14	0.70	25.0	34	14	25.0	0.132	0.68	0.70	0.00	2.93
		17	0.85	30.1	38	17	30.1	0.146	0.89	0.82	0.00	3.23
		20	1.00	35.1	41	18	35.1	0.158	1.05	0.90	0.00	3.50
		22	1.10	40.1	43	19	40.1	0.166	1.16	0.93	0.00	3.67
		25	1.25	45.1	46	19	45.1	0.177	1.32	0.93	0.00	3.91
		28	1.40	50.0	49	19	50.0	0.187	1.47	0.93	0.00	4.14
		30	1.50	55.0	52	19	55.0	0.194	1.58	0.93	0.00	4.29
		33	1.65	60.1	54	19	60.1	0.203	1.68	0.93	0.00	4.50
0.71	0.03	5	0.25	10.1	26	5	10.1	0.080	0.32	0.25	0.00	1.76
		8	0.40	15.0	29	8	15.0	0.100	0.47	0.40	0.00	2.21
		11	0.55	20.1	32	11	20.1	0.117	0.58	0.55	0.00	2.60
		14	0.70	25.0	35	14	25.0	0.132	0.74	0.70	0.00	2.93
		17	0.85	30.0	39	17	30.0	0.146	0.95	0.82	0.00	3.23
		20	1.00	35.0	41	18	35.0	0.158	1.05	0.90	0.00	3.50
		22	1.10	40.0	44	18	40.0	0.166	1.21	0.90	0.00	3.67
		25	1.25	45.1	47	18	45.1	0.177	1.37	0.90	0.00	3.91
		28	1.40	50.0	51	18	50.0	0.187	1.53	0.90	0.00	4.14
		30	1.50	55.0	53	18	55.0	0.194	1.63	0.90	0.00	4.29
		33	1.65	60.1	54	18	60.1	0.203	1.68	0.90	0.00	4.50
0.94	0.04	5	0.25	10.0	27	5	10.0	0.080	0.37	0.25	0.00	1.77
		8	0.40	15.0	31	8	15.0	0.100	0.53	0.40	0.00	2.21
		11	0.55	20.0	33	11	20.0	0.117	0.63	0.55	0.00	2.60
		14	0.70	25.0	35	14	25.0	0.132	0.74	0.70	0.00	2.93
		17	0.85	30.0	40	17	30.0	0.146	1.00	0.85	0.00	3.23
		20	1.00	35.0	42	18	35.0	0.158	1.11	0.88	0.00	3.50
		22	1.10	4004.0	45	18	4004.0	0.166	1.26	0.88	0.00	3.67
		25	1.25	45.0	49	18	45.0	0.177	1.47	0.90	0.00	3.91
		28	1.40	50.0	52	18	50.0	0.187	1.58	0.88	0.00	4.14
		30	1.50	55.1	54	18	55.1	0.194	1.68	0.88	0.00	4.29
		33	1.65	60.1	57	18	60.1	0.203	1.84	0.88	0.00	4.50

Table D.2: Main results from rotational experiments with $r_0 = 20\,\text{mm}$.

f	f_*	h_0	a	m_0	r_f	h_f	m_f	r_*	h_*	m_*
1.02	0.05	5	0.25	10.1	27	5	10.1	0.37	0.25	0.00
		8	0.40	15.1	31	8	15.1	0.53	0.40	0.00
		11	0.55	20.1	33	11	20.1	0.63	0.55	0.00
		14	0.70	25.0	37	14	25.0	0.84	0.70	0.00
		17	0.85	30.0	41	16	30.0	1.05	0.80	0.00
		20	1.00	35.1	43	17	35.1	1.16	0.86	0.00
		22	1.10	40.0	46	18	40.0	1.32	0.88	0.00
		25	1.25	45.0	51	18	45.0	1.53	0.88	0.00
		28	1.40	50.0	52	18	50.0	1.58	0.88	0.00
		30	1.50	55.1	54	18	55.1	1.68	0.88	0.00
		33	1.65	60.0	57	18	60.0	1.84	0.88	0.00
1.10	0.05	5	0.25	10.1	27	5	10.1	0.37	0.25	0.00
		8	0.40	15.1	32	8	15.1	0.58	0.40	0.00
		11	0.55	20.0	34	11	20.0	0.68	0.55	0.00
		14	0.70	25.0	38	14	25.0	0.89	0.70	0.00
		17	0.85	30.1	41	16	30.1	1.05	0.80	0.00
		20	1.00	35.0	44	17	35.0	1.21	0.85	0.00
		22	1.10	40.0	47	17	40.0	1.37	0.85	0.00
		25	1.25	45.1	51	18	45.1	1.53	0.88	0.00
		28	1.40	50.0	53	17	50.0	1.63	0.85	0.00
		30	1.50	55.0	54	17	55.0	1.68	0.85	0.00
		33	1.65	60.0	56	17	60.0	1.79	0.85	0.00
1.18	0.05	5	0.25	10.0	28	5	10.0	0.42	0.25	0.00
		8	0.40	15.0	32	8	15.0	0.58	0.40	0.00
		11	0.55	20.1	35	11	20.1	0.74	0.55	0.00
		14	0.70	25.0	39	14	25.0	0.95	0.70	0.00
		17	0.85	30.0	41	16	30.0	1.05	0.78	0.00
		20	1.00	35.0	44	17	35.0	1.21	0.82	0.00
		22	1.10	40.1	47	17	40.1	1.37	0.85	0.00
		25	1.25	45.0	52	17	45.0	1.58	0.85	0.00
		28	1.40	50.0	54	17	50.0	1.68	0.82	0.00
		30	1.50	55.0	57	17	55.0	1.84	0.82	0.00
		33	1.65	60.1	60	17	60.1	2.00	0.82	0.00
1.26	0.06	5	0.25	10.0	28	5	10.0	0.42	0.25	0.00
		8	0.40	15.0	32	8	15.0	0.58	0.40	0.00
		11	0.55	20.0	34	11	20.0	0.68	0.55	0.00
		14	0.70	25.1	39	14	25.1	0.95	0.70	0.00
		17	0.85	30.0	42	15	30.0	1.11	0.75	0.00
		20	1.00	35.0	44	17	34.6	1.21	0.82	0.01
		22	1.10	40.1	48	17	39.6	1.42	0.82	0.01
		25	1.25	45.1	52	17	44.4	1.58	0.82	0.02
		28	1.40	50.0	54	17	49.2	1.68	0.82	0.02
		30	1.50	55.0	58	17	53.9	1.89	0.82	0.02
		33	1.65	60.0	61	17	58.8	2.05	0.82	0.02

Table D.3: Result for $r_0 = 20\,\mathrm{mm}$ with fixed frequency, increasing aspect ratio.

f	f_*	h_0	a	m_0	r_f	h_f	m_f	r_*	h_*	m_*
1.33	0.06	5	0.25	10.1	28	5	10.1	0.42	0.25	0.00
		8	0.40	15.0	32	8	15.0	0.58	0.40	0.00
		11	0.55	20.0	35	11	20.0	0.74	0.55	0.00
		14	0.70	25.0	39	14	25.0	0.95	0.70	0.00
		17	0.85	30.1	42	16	30.1	1.11	0.81	0.00
		20	1.00	35.0	45	16	35.0	1.26	0.81	0.00
		22	1.10	40.0	49	16	40.0	1.47	0.81	0.00
		25	1.25	45.0	52	17	44.0	1.58	0.82	0.02
		28	1.40	50.1	56	17	48.9	1.79	0.82	0.02
		30	1.50	55.1	60	17	53.6	2.00	0.82	0.03
		33	1.65	60.0	63	16	58.1	2.16	0.81	0.03
1.41	0.06	5	0.25	10.1	29	5	10.1	0.47	0.25	0.00
		8	0.40	15.0	32	8	14.9	0.58	0.40	0.01
		11	0.55	20.0	36	11	19.9	0.79	0.55	0.01
		14	0.70	25.0	40	14	24.8	1.00	0.70	0.01
		17	0.85	30.1	42	16	29.6	1.11	0.80	0.02
		20	1.00	35.0	46	16	34.4	1.32	0.80	0.02
		22	1.10	40.0	51	16	39.1	1.53	0.80	0.02
		25	1.25	45.0	53	16	43.9	1.63	0.80	0.02
		28	1.40	50.0	56	16	48.6	1.79	0.80	0.03
		30	1.50	55.0	60	16	53.1	2.00	0.80	0.03
		33	1.65	60.0	63	16	57.5	2.16	0.80	0.04

Table D.4: Result for $r_0 = 20\,\mathrm{mm}$ with fixed frequency, increasing aspect ratio.

f	f_*	h_0	a	m_0	r_f	h_f	m_f	t_f	r_*	h_*	m_*	t_*
0.00	0.00	8	0.32	20.1	33	8	20.1	0.100	0.31	0.32	0.00	1.98
		12	0.48	30.0	38	12	30.0	0.122	0.52	0.48	0.00	2.42
		15	0.60	40.0	41	15	40.0	0.137	0.64	0.60	0.00	2.71
		19	0.76	50.0	44	19	50.0	0.154	0.77	0.76	0.00	3.05
		22	0.88	60.0	49	22	60.0	0.166	0.98	0.88	0.00	3.28
		26	1.04	70.1	53	23	70.1	0.180	1.11	0.92	0.00	3.57
		30	1.20	80.0	58	23	80.0	0.194	1.32	0.90	0.00	3.83
		35	1.38	90.0	61	23	90.0	0.208	1.44	0.90	0.00	4.11
		38	1.52	100.0	64	23	100.0	0.218	1.57	0.90	0.00	4.32
		41	1.64	110.0	69	23	110.0	0.226	1.78	0.90	0.00	4.48
0.47	0.02	8	0.32	20.1	33	8	20.1	0.101	0.31	0.32	0.00	1.99
		12	0.48	30.1	39	12	30.1	0.122	0.56	0.48	0.00	2.42
		15	0.60	40.1	41	15	40.1	0.137	0.64	0.60	0.00	2.71
		19	0.76	50.0	46	19	50.0	0.154	0.85	0.76	0.00	3.05
		22	0.88	60.0	51	22	60.0	0.166	1.02	0.86	0.00	3.28
		26	1.04	70.1	54	22	70.1	0.180	1.15	0.88	0.00	3.57
		30	1.20	80.1	59	22	80.1	0.194	1.36	0.88	0.00	3.83
		35	1.38	90.1	62	22	90.1	0.208	1.48	0.88	0.00	4.11
		38	1.52	100.1	65	22	100.1	0.218	1.61	0.88	0.00	4.32
		41	1.64	110.0	71	22	110.0	0.226	1.82	0.88	0.00	4.48
0.71	0.04	8	0.32	20.1	33	8	20.1	0.101	0.31	0.32	0.00	2.00
		12	0.48	30.0	39	12	30.0	0.122	0.56	0.48	0.00	2.42
		15	0.60	40.0	42	15	40.0	0.137	0.68	0.60	0.00	2.71
		19	0.76	50.0	46	19	50.0	0.154	0.85	0.76	0.00	3.05
		22	0.88	60.0	52	22	60.0	0.166	1.06	0.88	0.00	3.28
		26	1.04	70.0	55	22	70.0	0.180	1.19	0.88	0.00	3.57
		30	1.20	80.0	61	22	80.0	0.194	1.44	0.86	0.00	3.83
		35	1.38	90.0	63	22	90.0	0.208	1.53	0.86	0.00	4.11
		38	1.52	100.0	68	22	100.0	0.218	1.74	0.86	0.00	4.32
		41	1.64	110.0	72	22	110.0	0.226	1.86	0.86	0.00	4.48
0.94	0.05	8	0.32	20.0	33	8	20.0	0.101	0.31	0.32	0.00	2.00
		12	0.48	30.1	40	12	30.1	0.122	0.60	0.48	0.00	2.42
		15	0.60	40.0	43	15	40.0	0.137	0.73	0.60	0.00	2.71
		19	0.76	50.0	48	19	50.0	0.154	0.94	0.76	0.00	3.05
		22	0.88	60.0	53	22	60.0	0.166	1.11	0.86	0.00	3.28
		26	1.04	70.1	58	21	70.1	0.180	1.32	0.84	0.00	3.57
		30	1.20	80.0	62	21	80.0	0.194	1.48	0.82	0.00	3.83
		35	1.38	90.0	65	21	90.0	0.208	1.61	0.82	0.00	4.11
		38	1.52	100.1	71	21	100.1	0.218	1.82	0.84	0.00	4.32
		41	1.64	110.1	74	21	110.1	0.226	1.95	0.82	0.00	4.48

Table D.5: Result for $r_0 = 25\,\mathrm{mm}$ with fixed frequency, increasing aspect ratio.

f	f_*	h_0	a	m_0	r_f	h_f	m_f	r_*	h_*	m_*
1.02	0.05	8	0.32	20.0	33	8	20.0	0.31	0.32	0.00
		12	0.48	30.1	40	12	30.1	0.60	0.48	0.00
		15	0.60	40.0	43	15	40.0	0.73	0.60	0.00
		19	0.76	50.0	49	19	50.0	0.98	0.76	0.00
		22	0.88	60.0	53	21	60.0	1.11	0.84	0.00
		26	1.04	70.0	59	21	70.0	1.36	0.84	0.00
		30	1.20	80.0	62	20	80.0	1.48	0.80	0.00
		35	1.38	90.0	66	20	89.5	1.65	0.80	0.01
		38	1.52	100.1	72	20	99.2	1.86	0.80	0.01
		41	1.64	110.0	75	20	108.6	1.99	0.80	0.01
1.10	0.06	8	0.32	20.1	34	8	20.1	0.35	0.32	0.00
		12	0.48	30.0	41	12	30.0	0.64	0.48	0.00
		15	0.60	40.1	44	15	40.1	0.77	0.60	0.00
		19	0.76	50.0	51	19	50.0	1.02	0.76	0.00
		22	0.88	60.0	54	21	59.7	1.15	0.82	0.00
		26	1.04	70.0	60	20	69.6	1.40	0.80	0.01
		30	1.20	80.0	63	20	79.5	1.53	0.80	0.01
		35	1.38	90.1	68	20	89.4	1.74	0.80	0.01
		38	1.52	100.1	73	20	99.3	1.91	0.80	0.01
		41	1.64	110.0	76	20	109.0	2.03	0.80	0.01
1.18	0.06	8	0.32	20.1	35	8	20.1	0.39	0.32	0.00
		12	0.48	30.0	41	12	30.0	0.64	0.48	0.00
		15	0.60	40.0	44	15	40.0	0.77	0.60	0.00
		19	0.76	50.0	51	19	49.8	1.02	0.76	0.00
		22	0.88	60.0	55	20	59.7	1.19	0.78	0.01
		26	1.04	70.1	61	19	69.5	1.44	0.76	0.01
		30	1.20	80.0	64	19	79.2	1.57	0.76	0.01
		35	1.38	90.0	71	19	88.8	1.82	0.76	0.01
		38	1.52	100.0	74	19	98.5	1.95	0.76	0.02
		41	1.64	110.0	78	19	107.9	2.12	0.76	0.02
1.26	0.06	8	0.32	20.0	35	8	20.0	0.39	0.32	0.00
		12	0.48	30.0	41	12	30.0	0.64	0.48	0.00
		15	0.60	40.0	44	15	40.0	0.77	0.60	0.00
		19	0.76	50.0	52	19	50.0	1.06	0.76	0.00
		22	0.88	60.1	56	19	59.3	1.23	0.74	0.01
		26	1.04	70.0	62	19	69.0	1.48	0.76	0.01
		30	1.20	80.0	66	19	78.7	1.65	0.76	0.02
		35	1.38	90.0	71	19	88.1	1.82	0.76	0.02
		38	1.52	100.0	74	19	97.6	1.95	0.76	0.02
		41	1.64	110.0	79	19	106.3	2.16	0.76	0.03

Table D.6: Result for $r_0 = 25\,\mathrm{mm}$ with fixed frequency, increasing aspect ratio.

f	f_*	h_0	a	m_0	r_f	h_f	m_f	r_*	h_*	m_*
1.33	0.07	8	0.32	20.0	36	8	20.0	0.43	0.32	0.00
		12	0.48	30.0	41	12	30.0	0.64	0.48	0.00
		15	0.60	40.1	45	15	39.8	0.81	0.60	0.01
		19	0.76	50.0	52	19	49.4	1.06	0.76	0.01
		22	0.88	60.0	58	19	59.1	1.32	0.76	0.02
		26	1.04	70.0	63	19	68.3	1.53	0.76	0.02
		30	1.20	80.0	68	19	77.6	1.74	0.74	0.03
		35	1.38	90.0	73	19	86.1	1.91	0.74	0.04
		38	1.52	100.0	75	19	94.5	1.99	0.74	0.06
		41	1.64	110.1	79	19	101.1	2.16	0.74	0.08
		45	1.80	120.0	82	19	106.6	2.28	0.74	0.11
		49	1.96	130.0	82	19	109.9	2.28	0.74	0.15
1.41	0.07	8	0.32	20.0	37	8	20.0	0.47	0.32	0.00
		12	0.48	30.0	42	12	30.0	0.68	0.48	0.00
		15	0.60	40.0	47	15	39.5	0.89	0.60	0.01
		19	0.76	50.1	53	18	49.2	1.11	0.72	0.02
		22	0.88	60.0	59	19	58.5	1.36	0.74	0.03
		26	1.04	70.0	64	19	67.4	1.57	0.74	0.04
		30	1.20	80.0	68	19	75.1	1.74	0.74	0.06
		35	1.38	90.0	72	19	81.1	1.86	0.74	0.10
		38	1.52	100.1	72	19	85.5	1.86	0.74	0.15
		41	1.64	110.0	72	19	89.9	1.86	0.74	0.18
1.65	0.08	8	0.32	20.0	38	8	19.6	0.52	0.32	0.02
		12	0.48	30.0	43	12	28.9	0.73	0.48	0.04
		15	0.60	40.0	48	15	36.3	0.94	0.60	0.09
		19	0.76	50.0	52	18	41.3	1.06	0.70	0.17
		22	0.88	60.0	52	17	43.8	1.06	0.69	0.27
		26	1.04	70.1	52	17	41.8	1.06	0.69	0.40
		30	1.20	80.0	52	17	43.5	1.06	0.68	0.46
		35	1.38	90.0	51	17	45.0	1.04	0.68	0.50
		38	1.52	100.0	52	17	43.5	1.06	0.69	0.57
		41	1.64	110.0	51	17	45.2	1.04	0.68	0.59

Table D.7: Result for $r_0 = 25\,\mathrm{mm}$ with fixed frequency, increasing aspect ratio.

f	f_*	h_0	a	m_0	r_f	h_f	m_f	t_f	r_*	h_*	m_*	t_*
0.00	0.00	8	0.25	30.1	40	8	30.1	0.097	0.33	0.25	0.00	1.75
		12	0.40	45.0	42	12	45.0	0.122	0.40	0.40	0.00	2.21
		16	0.53	60.0	46	16	60.0	0.141	0.54	0.53	0.00	2.56
		19	0.63	75.0	52	19	75.0	0.154	0.72	0.63	0.00	2.79
		23	0.77	90.0	56	23	90.0	0.169	0.86	0.77	0.00	3.06
		27	0.90	105.1	61	27	105.1	0.184	1.04	0.90	0.00	3.32
		30	1.00	120.0	63	29	120.0	0.194	1.11	0.95	0.00	3.50
		34	1.13	135.0	68	28	135.0	0.206	1.28	0.93	0.00	3.73
		37	1.23	150.0	73	28	150.0	0.215	1.42	0.93	0.00	3.89
		41	1.37	165.0	76	28	165.0	0.226	1.53	0.93	0.00	4.09
		46	1.53	180.0	81	28	180.0	0.240	1.70	0.93	0.00	4.33
		49	1.63	195.0	83	28	195.0	0.247	1.77	0.93	0.00	4.47
0.47	0.03	8	0.25	30.0	39	8	30.0	0.098	0.30	0.25	0.00	1.76
		12	0.40	45.1	43	12	45.1	0.122	0.44	0.40	0.00	2.21
		16	0.53	60.0	48	16	60.0	0.141	0.61	0.53	0.00	2.56
		19	0.63	75.0	53	19	75.0	0.154	0.75	0.63	0.00	2.79
		23	0.77	90.0	56	23	90.0	0.169	0.86	0.77	0.00	3.06
		27	0.90	105.1	62	27	105.1	0.184	1.07	0.90	0.00	3.32
		30	1.00	120.0	64	27	120.0	0.194	1.14	0.90	0.00	3.50
		34	1.13	135.0	71	27	135.0	0.206	1.35	0.90	0.00	3.73
		37	1.23	150.1	74	27	150.1	0.215	1.46	0.90	0.00	3.89
		41	1.37	165.1	77	27	165.1	0.226	1.56	0.90	0.00	4.09
		46	1.53	180.0	82	27	180.0	0.240	1.74	0.90	0.00	4.33
		49	1.63	195.0	84	27	195.0	0.247	1.81	0.90	0.00	4.47
0.71	0.04	8	0.27	30.1	40	8	30.1	0.101	0.33	0.27	0.00	1.83
		12	0.40	45.0	43	12	45.0	0.122	0.44	0.40	0.00	2.21
		16	0.53	60.1	49	16	60.1	0.141	0.65	0.53	0.00	2.56
		19	0.63	75.0	53	19	75.0	0.154	0.75	0.63	0.00	2.79
		23	0.77	90.0	58	23	90.0	0.169	0.93	0.77	0.00	3.06
		27	0.90	105.1	62	27	105.1	0.184	1.07	0.88	0.00	3.32
		30	1.00	120.1	66	26	120.1	0.194	1.21	0.87	0.00	3.50
		34	1.13	135.0	73	26	135.0	0.206	1.42	0.87	0.00	3.73
		37	1.23	150.0	75	26	150.0	0.215	1.49	0.87	0.00	3.89
		41	1.37	165.0	81	26	165.0	0.226	1.70	0.87	0.00	4.09
		46	1.53	180.0	84	26	180.0	0.240	1.81	0.87	0.00	4.33
		49	1.63	195.0	88	26	195.0	0.247	1.95	0.87	0.00	4.47

Table D.8: Result for $r_0 = 30\,\mathrm{mm}$ with fixed frequency, increasing aspect ratio.

f	f_*	h_0	a	m_0	r_f	h_f	m_f	t_f	r_*	h_*	m_*	t_*
0.94	0.05	8	0.25	30.0	40	8	30.0	0.098	0.33	0.27	0.00	1.78
		12	0.40	45.0	44	12	45.0	0.122	0.47	0.40	0.00	2.21
		16	0.53	60.1	51	16	60.1	0.141	0.68	0.53	0.00	2.56
		19	0.63	75.0	54	19	75.0	0.154	0.79	0.63	0.00	2.79
		23	0.77	90.1	61	23	90.1	0.169	1.04	0.77	0.00	3.06
		27	0.90	105.0	64	26	105.0	0.184	1.14	0.85	0.00	3.32
		30	1.00	120.0	71	25	120.0	0.194	1.35	0.83	0.00	3.50
		34	1.13	135.0	74	26	135.0	0.206	1.46	0.85	0.00	3.73
		37	1.23	150.1	80	25	149.4	0.215	1.67	0.83	0.00	3.89
		41	1.37	165.0	83	25	164.0	0.226	1.77	0.83	0.01	4.09
		46	1.53	180.0	87	25	178.5	0.240	1.91	0.83	0.01	4.33
		49	1.63	195.0	93	25	193.5	0.247	2.09	0.83	0.01	4.47
1.02	0.06	8	0.27	30.0	40	8	30.0		0.33	0.27	0.00	
		12	0.40	45.1	44	12	45.1		0.47	0.40	0.00	
		16	0.53	60.0	52	16	60.0		0.72	0.53	0.00	
		19	0.63	75.1	55	19	75.1		0.82	0.63	0.00	
		23	0.77	90.0	62	23	90.0		1.07	0.77	0.00	
		27	0.90	105.1	65	25	105.1		1.18	0.82	0.00	
		30	1.00	120.0	72	25	119.2		1.39	0.82	0.01	
		34	1.13	135.0	75	25	134.0		1.49	0.82	0.01	
		37	1.23	150.0	81	25	148.7		1.70	0.82	0.01	
		41	1.37	165.0	84	25	163.4		1.81	0.82	0.01	
		46	1.53	180.1	91	25	178.0		2.02	0.82	0.01	
		49	1.63	195.0	94	25	192.6		2.12	0.82	0.01	
1.10	0.06	8	0.25	30.0	41	8	30.0		0.37	0.27	0.00	
		12	0.40	45.1	45	12	45.1		0.51	0.40	0.00	
		16	0.53	60.0	52	16	60.0		0.72	0.53	0.00	
		19	0.63	75.0	56	19	75.0		0.86	0.63	0.00	
		23	0.77	90.0	62	23	89.4		1.07	0.77	0.01	
		27	0.90	105.0	67	24	104.2		1.25	0.80	0.01	
		30	1.00	120.0	73	24	118.8		1.42	0.80	0.01	
		34	1.13	135.1	79	24	133.5		1.63	0.78	0.01	
		37	1.23	150.1	83	24	148.0		1.77	0.78	0.01	
		41	1.37	165.0	87	24	162.2		1.91	0.80	0.02	
		46	1.53	180.0	94	24	176.3		2.12	0.78	0.02	
		49	1.63	195.1	97	24	190.7		2.23	0.80	0.02	
1.18	0.07	8	0.27	30.0	41	8	30.0		0.37	0.27	0.00	
		12	0.40	45.1	45	12	45.1		0.51	0.40	0.00	
		16	0.53	60.0	53	16	60.0		0.75	0.53	0.00	
		19	0.63	75.0	58	19	75.0		0.93	0.63	0.00	
		23	0.77	90.0	63	23	89.3		1.11	0.77	0.01	

Table D.9: Result for $r_0 = 30\,\text{mm}$ with fixed frequency, increasing aspect ratio.

f	f_*	h_0	a	m_0	r_f	h_f	m_f	r_*	h_*	m_*
1.18	0.07	27	0.90	105.0	69	23	103.8	1.32	0.77	0.01
		30	1.00	120.0	74	23	118.4	1.46	0.77	0.01
		34	1.13	135.0	81	23	132.8	1.70	0.77	0.02
		37	1.23	150.0	84	23	146.9	1.81	0.77	0.02
		41	1.37	165.1	91	23	160.6	2.02	0.77	0.03
		46	1.53	180.1	95	23	173.7	2.16	0.77	0.04
		49	1.63	195.0	99	23	185.6	2.30	0.77	0.05
1.26	0.07	8	0.25	30.1	42	8	30.1	0.40	0.27	0.00
		12	0.40	45.0	46	12	44.7	0.54	0.40	0.01
		16	0.53	60.1	53	16	59.6	0.75	0.53	0.01
		19	0.63	75.0	60	19	74.3	1.00	0.63	0.01
		23	0.77	90.1	64	23	88.8	1.14	0.75	0.01
		27	0.90	105.1	72	23	103.1	1.39	0.75	0.02
		30	1.00	120.1	75	23	117.2	1.49	0.75	0.02
		34	1.13	135.0	82	23	130.5	1.74	0.75	0.03
		37	1.23	150.0	85	23	142.6	1.84	0.75	0.05
		41	1.37	165.0	92	23	153.9	2.05	0.75	0.07
		46	1.53	180.0	93	23	159.9	2.09	0.75	0.11
		49	1.63	195.0	93	23	156.9	2.09	0.75	0.20
1.33	0.07	8	0.25	30.1	42	8	30.0	0.40	0.27	0.00
		12	0.40	45.0	47	12	45.0	0.58	0.40	0.00
		16	0.53	60.1	54	16	59.4	0.79	0.53	0.01
		19	0.63	75.1	61	19	74.0	1.04	0.63	0.01
		23	0.77	90.1	67	22	87.8	1.25	0.73	0.03
		27	0.90	105.0	72	22	101.1	1.39	0.73	0.04
		30	1.00	120.0	77	22	112.1	1.56	0.73	0.07
		34	1.13	135.0	80	22	119.8	1.67	0.73	0.11
		37	1.23	150.1	81	22	125.5	1.70	0.73	0.16
		41	1.37	165.1	81	22	129.3	1.70	0.73	0.22
		46	1.53	180.0	81	22	131.5	1.70	0.73	0.27
		49	1.63	195.0	82	22	134.2	1.74	0.73	0.31
1.41	0.08	8	0.25	30.1	42	8	30.1	0.40	0.27	0.00
		12	0.40	45.1	48	12	45.0	0.61	0.40	0.00
		16	0.53	60.0	55	16	58.7	0.82	0.53	0.02
		19	0.63	75.0	61	19	72.5	1.04	0.63	0.03
		23	0.77	90.1	67	21	84.9	1.25	0.70	0.06
		27	0.90	105.0	72	21	103.8	1.39	0.70	0.01
		30	1.00	120.1	72	21	98.9	1.39	0.70	0.18
		34	1.13	135.0	72	21	100.8	1.39	0.70	0.25
		37	1.23	150.0	72	21	102.4	1.39	0.70	0.32
		41	1.37	165.0	73	21	106.2	1.42	0.70	0.36
		46	1.53	180.0	73	21	108.9	1.42	0.70	0.40
		49	1.63	195.0	72	21	110.1	1.39	0.70	0.44

Table D.10: Result for $r_0 = 30\,\text{mm}$ with fixed frequency, increasing aspect ratio.

f	f_*	h_0	a	m_0	r_f	h_f	m_f	t_f	r_*	h_*	m_*	t_*
0.00	0.00	10	0.28	50.2	48	10	50.2	0.124	0.35	0.28	0.00	2.04
		12	0.33	62.5	51	12	62.5	0.124	0.40	0.33	0.00	2.04
		14	0.39	75.4	52	14	75.4	0.133	0.43	0.39	0.00	2.20
		16	0.44	87.4	54	16	87.4	0.143	0.49	0.44	0.00	2.36
		19	0.53	100.6	59	19	100.6	0.152	0.64	0.53	0.00	2.52
		21	0.58	112.7	61	21	112.7	0.167	0.70	0.58	0.00	2.75
		24	0.67	124.7	63	24	124.7	0.171	0.75	0.67	0.00	2.83
		26	0.72	137.5	66	26	137.5	0.181	0.84	0.72	0.00	2.99
		28	0.78	149.9	67	28	149.9	0.190	0.87	0.78	0.00	3.14
		30	0.83	162.2	72	29	162.2	0.195	0.99	0.81	0.00	3.22
		32	0.89	176.4	74	31	176.4	0.200	1.05	0.86	0.00	3.30
		35	0.97	187.6	76	31	187.6	0.210	1.11	0.86	0.00	3.46
		37	1.03	200.2	79	33	200.2	0.210	1.19	0.92	0.00	3.46
		39	1.08	212.7	82	32	212.7	0.219	1.28	0.89	0.00	3.62
		41	1.14	226.3	84	32	226.3	0.229	1.34	0.89	0.00	3.77
		43	1.19	237.0	86	32	237.0	0.229	1.40	0.89	0.00	3.77
		46	1.28	250.5	88	31	250.5	0.238	1.46	0.86	0.00	3.93
		48	1.33	262.8	92	31	262.8	0.248	1.54	0.86	0.00	4.09
		50	1.39	275.6	93	31	275.6	0.252	1.57	0.86	0.00	4.17
		52	1.44	287.5	94	32	287.5	0.252	1.60	0.89	0.00	4.17
		55	1.53	300.8	97	32	300.8	0.257	1.69	0.89	0.00	4.24
		58	1.61	312.1	100	33	312.1	0.257	1.78	0.92	0.00	4.24
		60	1.67	325.0	102	33	325.0	0.262	1.84	0.92	0.00	4.32
0.47	0.03	10	0.28	50.0	49	10	50.0	0.119	0.37	0.28	0.00	1.97
		12	0.33	62.5	52	12	62.5	0.138	0.43	0.33	0.00	2.28
		14	0.39	75.0	53	14	75.0	0.148	0.46	0.39	0.00	2.44
		16	0.44	87.5	56	16	87.5	0.162	0.55	0.44	0.00	2.67
		19	0.53	100.1	60	19	100.1	0.181	0.67	0.53	0.00	2.99
		21	0.58	112.1	62	21	112.1	0.195	0.73	0.58	0.00	3.22
		24	0.67	125.1	63	24	125.1	0.210	0.75	0.67	0.00	3.46
		26	0.72	137.6	67	26	137.6	0.219	0.87	0.72	0.00	3.62
		28	0.78	150.5	69	28	150.5	0.224	0.93	0.76	0.00	3.69
		30	0.83	162.6	73	28	162.6	0.233	1.02	0.78	0.00	3.85
		32	0.89	175.4	76	30	175.4	0.238	1.11	0.83	0.00	3.93
		35	0.97	187.6	80	30	187.6	0.243	1.22	0.83	0.00	4.01
		37	1.03	200.1	83	32	200.1	0.252	1.31	0.88	0.00	4.17
		39	1.08	212.6	85	31	212.6	0.257	1.37	0.85	0.00	4.24
		41	1.14	225.1	87	30	225.1	0.267	1.43	0.82	0.00	4.40
		43	1.19	237.6	89	30	237.6	0.271	1.49	0.83	0.00	4.48
		46	1.28	250.1	92	31	250.1	0.276	1.54	0.86	0.00	4.56
		48	1.33	262.5	94	31	262.5	0.271	1.60	0.85	0.00	4.48
		50	1.39	275.1	96	30	275.1	0.276	1.66	0.83	0.00	4.56
		52	1.44	287.8	98	30	287.8	0.286	1.72	0.83	0.00	4.72
		55	1.53	300.0	100	31	300.0	0.286	1.78	0.85	0.00	4.72
		58	1.61	312.7	103	31	312.7	0.286	1.87	0.85	0.00	4.72
		60	1.67	325.4	106	31	325.4	0.295	1.95	0.85	0.00	4.87

Table D.11: Result for $r_0 = 36\,\text{mm}$ with fixed frequency, increasing aspect ratio.

f	f_*	h_0	a	m_0	r_f	h_f	m_f	t_f	r_*	h_*	m_*	t_*
0.71	0.04	10	0.28	50.0	51	10	50.0		0.40	0.28	0.00	
		12	0.33	62.7	53	12	62.7		0.46	0.33	0.00	
		14	0.39	75.0	55	14	75.0		0.52	0.39	0.00	
		16	0.44	87.5	58	16	87.5		0.61	0.44	0.00	
		19	0.53	100.1	61	19	100.1		0.70	0.53	0.00	
		21	0.58	112.6	63	21	112.6		0.75	0.58	0.00	
		24	0.67	125.1	66	24	125.1	0.214	0.84	0.67	0.00	3.54
		26	0.72	137.8	69	26	137.8	0.229	0.93	0.72	0.00	3.77
		28	0.78	150.1	73	28	150.1	0.233	1.02	0.76	0.00	3.85
		30	0.83	162.7	76	28	162.7	0.243	1.11	0.78	0.00	4.01
		32	0.89	175.1	79	29	175.1	0.248	1.19	0.81	0.00	4.09
		35	0.97	187.7	82	30	187.7	0.252	1.28	0.82	0.00	4.17
		37	1.03	200.0	85	30	200.0	0.257	1.37	0.82	0.00	4.24
		39	1.08	212.5	87	30	212.5	0.262	1.43	0.82	0.00	4.32
		41	1.14	225.1	91	30	225.1	0.271	1.51	0.82	0.00	4.48
		43	1.19	237.6	93	30	237.6	0.276	1.57	0.82	0.00	4.56
		46	1.28	250.1	95	30	250.1	0.286	1.63	0.82	0.00	4.72
		48	1.33	262.5	98	30	262.5	0.286	1.72	0.82	0.00	4.72
		50	1.39	275.2	101	30	275.2	0.290	1.81	0.82	0.00	4.80
		52	1.44	287.8	103	29	287.8	0.300	1.87	0.81	0.00	4.95
		55	1.53	300.1	105	29	300.1	0.305	1.92	0.81	0.00	5.03
		58	1.61	312.8	106	29	312.8	0.305	1.95	0.81	0.00	5.03
		60	1.67	325.2	111	29	325.2	0.310	2.07	0.81	0.00	5.11
0.94	0.06	10	0.28	50.1	51	10	50.1	0.157	0.40	0.28	0.00	2.59
		12	0.33	62.7	54	12	62.7	0.167	0.49	0.33	0.00	2.75
		14	0.39	75.0	56	14	75.0	0.176	0.55	0.39	0.00	2.91
		16	0.44	87.7	60	16	87.7	0.195	0.67	0.44	0.00	3.22
		19	0.53	100.0	63	19	100.0	0.205	0.75	0.53	0.00	3.38
		21	0.58	112.5	66	21	112.5	0.210	0.84	0.58	0.00	3.46
		24	0.67	125.1	69	24	125.1	0.224	0.93	0.67	0.00	3.69
		26	0.72	137.8	73	26	137.8	0.238	1.02	0.71	0.00	3.93
		28	0.78	150.0	77	27	150.0	0.243	1.13	0.75	0.00	4.01
		30	0.83	162.7	80	29	162.7	0.257	1.22	0.81	0.00	4.24
		32	0.89	175.1	82	30	175.1	0.267	1.28	0.83	0.00	4.40
		35	0.97	187.5	85	30	185.8	0.276	1.37	0.83	0.01	4.56
		37	1.03	200.0	89	30	197.7	0.286	1.49	0.83	0.01	4.72
		39	1.08	212.5	92	29	209.2	0.281	1.54	0.81	0.02	4.64
		41	1.14	225.2	94	29	222.0	0.295	1.60	0.81	0.01	4.87
		43	1.19	237.5	97	29	234.1	0.300	1.69	0.81	0.01	4.95
		46	1.28	250.4	100	29	246.7	0.314	1.78	0.81	0.01	5.19
		48	1.33	262.5	103	29	258.9	0.329	1.87	0.81	0.01	5.42
		50	1.39	275.2	106	30	271.1	0.338	1.95	0.82	0.02	5.58
		52	1.44	287.5	109	28	283.0	0.338	2.04	0.78	0.02	5.58
		55	1.53	300.1	113	29	295.0	0.348	2.13	0.79	0.02	5.74
		58	1.61	312.5	116	29	307.1	0.352	2.22	0.81	0.02	5.82
		60	1.67	325.2	118	29	319.2	0.367	2.27	0.81	0.02	6.05

Table D.12: Result for $r_0 = 36\,\mathrm{mm}$ with fixed frequency, increasing aspect ratio.

f	f_*	h_0	a	m_0	r_f	h_f	m_f	t_f	r_*	h_*	m_*	t_*
1.02	0.06	10	0.28	50.0	51	10	50.0		0.40	0.28	0.00	
		12	0.33	62.6	53	12	62.6		0.46	0.33	0.00	
		14	0.39	75.1	57	14	75.1		0.58	0.39	0.00	
		16	0.44	87.6	61	16	87.6		0.70	0.44	0.00	
		19	0.53	100.1	64	19	100.1		0.78	0.53	0.00	
		21	0.58	112.5	68	21	112.5		0.90	0.58	0.00	
		24	0.67	125.0	71	24	125.0		0.97	0.67	0.00	
		26	0.72	137.6	74	25	137.6		1.06	0.69	0.00	
		28	0.78	150.2	79	27	148.5		1.19	0.74	0.01	
		30	0.83	162.5	82	28	160.7		1.27	0.76	0.01	
		32	0.89	175.2	85	29	172.8		1.37	0.81	0.01	
		35	0.97	187.7	87	29	184.9		1.43	0.79	0.01	
		37	1.03	200.1	93	29	197.1		1.57	0.79	0.01	
		39	1.08	212.7	95	29	209.4		1.63	0.79	0.02	
		41	1.14	225.0	97	29	221.2		1.69	0.79	0.02	
		43	1.19	237.6	100	29	233.4		1.78	0.79	0.02	
		46	1.28	249.9	104	29	244.9		1.89	0.79	0.02	
		48	1.33	262.7	107	29	256.9		1.98	0.79	0.02	
		50	1.39	275.1	109	29	268.7		2.04	0.79	0.02	
		52	1.44	287.6	113	29	281.0		2.13	0.79	0.02	
		55	1.53	300.1	116	29	293.0		2.22	0.79	0.02	
		58	1.61	312.5	119	29	304.0		2.30	0.79	0.03	
		60	1.67	325.0	122	29	315.7		2.39	0.79	0.03	
1.10	0.07	10	0.28	50.0	52	10	50.0		0.43	0.28	0.00	
		12	0.33	62.5	54	12	62.5		0.49	0.33	0.00	
		14	0.39	75.0	58	14	75.0		0.61	0.39	0.00	
		16	0.44	87.6	61	16	87.6		0.70	0.44	0.00	
		19	0.53	100.1	64	19	100.1		0.78	0.53	0.00	
		21	0.58	112.6	69	21	112.6		0.93	0.58	0.00	
		24	0.67	125.0	72	24	123.8		0.99	0.65	0.01	
		26	0.72	137.6	75	25	136.0		1.08	0.68	0.01	
		28	0.78	150.0	79	26	148.3		1.21	0.71	0.01	
		30	0.83	162.6	83	27	160.1		1.31	0.75	0.02	
		32	0.89	175.0	86	28	172.0		1.40	0.78	0.02	
		35	0.97	187.5	88	28	184.0		1.46	0.76	0.02	
		37	1.03	200.1	94	28	196.5		1.60	0.76	0.02	
		39	1.08	212.6	97	28	208.1		1.69	0.76	0.02	
		41	1.14	225.3	100	28	219.2		1.78	0.76	0.03	
		43	1.19	237.7	102	28	231.3		1.84	0.76	0.03	
		46	1.28	250.1	106	28	241.8		1.95	0.76	0.03	
		48	1.33	262.5	109	28	253.9		2.04	0.76	0.03	
		50	1.39	275.0	112	28	265.7		2.10	0.76	0.03	
		52	1.44	287.4	114	28	274.1		2.16	0.76	0.05	
		55	1.53	300.0	116	28	285.6		2.22	0.76	0.05	
		58	1.61	312.6	117	28	294.8		2.25	0.76	0.06	
		60	1.67	325.0	117	28	304.6		2.25	0.76	0.06	

Table D.13: Result for $r_0 = 36\,\text{mm}$ with fixed frequency, increasing aspect ratio.

f	f_*	h_0	a	m_0	r_f	h_f	m_f	t_f	r_*	h_*	m_*	t_*
1.18	0.07	10	0.28	50.2	52	10	50.2	0.148	0.43	0.28	0.00	2.44
		12	0.33	62.5	55	12	62.5	0.167	0.52	0.33	0.00	2.75
		14	0.39	75.0	59	14	75.0	0.186	0.64	0.39	0.00	3.07
		16	0.44	87.6	62	16	87.6	0.210	0.73	0.44	0.00	3.46
		19	0.53	100.1	65	19	100.1	0.224	0.81	0.53	0.00	3.69
		21	0.58	112.5	71	21	112.5	0.233	0.96	0.58	0.00	3.85
		24	0.67	125.1	73	23	123.8	0.257	1.02	0.64	0.01	4.24
		26	0.72	137.6	76	24	134.5	0.276	1.11	0.67	0.02	4.56
		28	0.78	150.1	80	25	146.5	0.286	1.22	0.69	0.02	4.72
		30	0.83	162.6	84	27	157.8	0.295	1.34	0.75	0.03	4.87
		32	0.89	175.0	88	27	170.2	0.295	1.46	0.75	0.03	4.87
		35	0.97	187.5	92	28	180.4	0.338	1.54	0.76	0.04	5.58
		37	1.03	200.1	95	28	191.3	0.371	1.63	0.76	0.04	6.13
		39	1.08	212.5	98	28	202.4	0.414	1.72	0.76	0.05	6.84
		41	1.14	225.0	101	27	211.6	0.433	1.81	0.75	0.06	7.15
		43	1.19	237.5	104	27	223.4	0.467	1.89	0.75	0.06	7.70
		46	1.28	250.1	104	27	229.7	0.548	1.89	0.74	0.08	9.04
		48	1.33	262.8	105	27	234.8	0.624	1.92	0.74	0.11	10.30
		50	1.39	275.1	105	27	243.0	0.686	1.92	0.74	0.12	11.32
		52	1.44	287.7	105	27	249.4	0.724	1.92	0.74	0.13	11.95
		55	1.53	300.0	105	27	254.2	0.786	1.92	0.74	0.15	12.97
		58	1.61	312.5	105	27	258.7	0.833	1.92	0.74	0.17	13.76
		60	1.67	325.2	105	27	263.1	0.881	1.92	0.74	0.19	14.54
1.26	0.08	10	0.28	50.0	53	10	50.0		0.46	0.28	0.00	
		12	0.33	62.6	55	12	62.6		0.52	0.33	0.00	
		14	0.39	75.1	59	14	75.1		0.64	0.39	0.00	
		16	0.44	87.5	62	16	87.5		0.73	0.44	0.00	
		19	0.53	100.0	67	19	98.7		0.87	0.53	0.01	
		21	0.58	112.6	72	21	110.5		0.99	0.58	0.02	
		24	0.67	125.1	75	23	122.8		1.08	0.64	0.02	
		26	0.72	137.6	79	24	134.0		1.19	0.67	0.03	
		28	0.78	150.0	83	25	145.1		1.31	0.69	0.03	
		30	0.83	162.6	86	26	155.5		1.40	0.71	0.04	
		32	0.89	175.1	89	26	165.9		1.49	0.72	0.05	
		35	0.97	187.6	93	26	174.5		1.57	0.72	0.07	
		37	1.03	200.1	93	26	180.9		1.57	0.72	0.10	
		39	1.08	212.6	94	26	186.6		1.60	0.71	0.12	
		41	1.14	225.0	93	26	189.8		1.57	0.71	0.16	
		43	1.19	237.6	94	26	196.7		1.60	0.71	0.17	
		46	1.28	250.0	94	26	199.6		1.60	0.71	0.20	
		48	1.33	262.5	94	26	202.0		1.60	0.71	0.23	
		50	1.39	275.0	93	26	204.6		1.57	0.71	0.26	
		52	1.44	287.6	93	26	207.3		1.57	0.71	0.28	
		55	1.53	300.1	93	26	208.3		1.57	0.71	0.31	
		58	1.61	312.6	94	26	214.8		1.60	0.71	0.31	
		60	1.67	325.1	94	26	218.2		1.60	0.71	0.33	

Table D.14: Result for $r_0 = 36\,\mathrm{mm}$ with fixed frequency, increasing aspect ratio.

f	f_*	h_0	a	m_0	r_f	h_f	m_f	t_f	r_*	h_*	m_*	t_*
1.33	0.08	10	0.28	50.1	52	10	50.1		0.45	0.28	0.00	
		12	0.33	62.7	56	12	62.7		0.55	0.33	0.00	
		14	0.39	75.0	61	14	74.0		0.70	0.39	0.01	
		16	0.44	87.5	66	16	85.7		0.84	0.44	0.02	
		19	0.53	100.1	71	19	97.1		0.96	0.53	0.03	
		21	0.58	112.5	74	21	108.7		1.05	0.58	0.03	
		24	0.67	125.1	79	23	119.0		1.19	0.64	0.05	
		26	0.72	137.6	80	24	127.9		1.22	0.67	0.07	
		28	0.78	150.0	81	26	136.2		1.25	0.71	0.09	
		30	0.83	162.6	81	26	140.8		1.25	0.71	0.13	
		32	0.89	175.1	82	26	144.3		1.28	0.71	0.18	
		35	0.97	187.6	81	26	147.8		1.25	0.71	0.21	
		37	1.03	200.1	82	26	147.6		1.28	0.71	0.26	
		39	1.08	212.6	81	26	150.2		1.25	0.71	0.29	
		41	1.14	225.1	81	26	151.2		1.25	0.71	0.33	
		43	1.19	237.5	82	26	153.8		1.28	0.71	0.35	
		46	1.28	250.2	81	26	155.6		1.25	0.71	0.38	
		48	1.33	262.6	81	26	155.1		1.25	0.71	0.41	
		50	1.39	275.1	81	26	156.1		1.25	0.71	0.43	
		52	1.44	287.6	82	26	154.8		1.28	0.71	0.46	
		55	1.53	300.0	82	26	160.4		1.28	0.71	0.47	
		58	1.61	312.5	81	26	158.8		1.25	0.71	0.49	
		60	1.67	325.1	82	26	162.5		1.28	0.71	0.50	
1.41	0.09	10	0.28	50.0	53	10	48.9	0.167	0.46	0.28	0.02	2.75
		12	0.33	62.5	57	12	60.6	0.238	0.58	0.33	0.03	3.93
		14	0.39	75.0	60	14	72.4	0.257	0.67	0.39	0.04	4.24
		16	0.44	87.7	65	16	82.9	0.295	0.81	0.44	0.05	4.87
		19	0.53	100.1	69	19	92.1	0.476	0.93	0.53	0.08	7.86
		21	0.58	112.6	72	21	99.9	0.600	0.99	0.57	0.11	9.90
		24	0.67	125.1	73	23	104.7	0.662	1.02	0.63	0.16	10.93
		26	0.72	137.7	72	24	110.1	0.752	0.99	0.65	0.20	12.42
		28	0.78	150.0	73	24	111.6	0.786	1.02	0.65	0.26	12.97
		30	0.83	162.5	73	23	112.1	0.867	1.02	0.64	0.31	14.31
		32	0.89	175.0	72	23	111.9	0.919	0.99	0.64	0.36	15.17
		35	0.97	187.4	72	23	110.7	1.071	0.99	0.64	0.41	17.69
		37	1.03	200.0	72	23	111.2	1.119	0.99	0.64	0.44	18.47
		39	1.08	212.5	72	23	112.7	1.224	0.99	0.64	0.47	20.20
		41	1.14	250.0	72	24	116.6	1.300	0.99	0.65	0.53	21.46
		43	1.19	225.1	72	23	114.5	1.310	0.99	0.64	0.49	21.62
		46	1.28	237.6	72	24	113.7	1.333	0.99	0.65	0.52	22.01
		48	1.33	262.7	72	24	116.0	1.381	0.99	0.67	0.56	22.80
		50	1.39	275.1	72	24	118.1	1.419	0.99	0.67	0.57	23.43
		52	1.44	287.6	72	24	116.4	1.448	0.99	0.67	0.60	23.90
		55	1.53	300.2	72	24	116.2	1.500	0.99	0.67	0.61	24.76
		58	1.61	312.5	72	24	118.8	1.567	0.99	0.67	0.62	25.86
		60	1.67	325.2	72	24	118.8	1.629	0.99	0.67	0.63	26.88

Table D.15: Result for $r_0 = 36\,\mathrm{mm}$ with fixed frequency, increasing aspect ratio.

f	f_*	h_0	a	m_0	r_f	h_f	m_f	t_f	r_*	h_*	m_*	t_*
1.65	0.10	10	0.28	50.0	52	10	40.9	0.590	0.43	0.28	0.18	9.75
		12	0.33	62.6	52	12	44.9	0.657	0.43	0.33	0.28	10.85
		14	0.39	75.0	52	14	47.2	0.833	0.43	0.39	0.37	13.76
		16	0.44	87.6	52	16	48.9	0.886	0.43	0.44	0.44	14.62
		19	0.53	100.0	53	19	50.2	0.957	0.46	0.53	0.50	15.80
		21	0.58	112.6	52	20	48.3	1.052	0.43	0.54	0.57	17.37
		24	0.67	125.0	52	21	47.0	1.238	0.45	0.57	0.62	20.44
		26	0.72	137.7	52	21	48.5	1.238	0.43	0.58	0.65	20.44
		28	0.78	150.0	52	21	48.3	1.362	0.43	0.57	0.68	22.48
		30	0.83	162.5	51	20	47.4	1.443	0.42	0.56	0.71	23.82
		32	0.89	175.1	51	20	47.7	1.405	0.42	0.56	0.73	23.19
		35	0.97	187.7	52	20	48.0	1.400	0.43	0.56	0.74	23.11
		37	1.03	200.0	51	20	47.0	1.419	0.42	0.56	0.76	23.43

Table D.16: Result for $r_0 = 36\,\mathrm{mm}$ with fixed frequency, increasing aspect ratio.

r_0	h_0	a	f	f_*	m_0	r_f	h_f	m_f	r_*	h_*	m_*
36	16	0.44	0.00	0.000	87.4	54	16	87.4	0.49	0.44	0.00
			0.21	0.013	87.6	54	16	87.6	0.49	0.44	0.00
			0.33	0.020	87.5	54	16	87.5	0.49	0.44	0.00
			0.47	0.028	87.5	55	16	87.5	0.52	0.44	0.00
			0.55	0.033	87.5	55	16	87.5	0.52	0.44	0.00
			0.63	0.038	87.6	57	16	87.6	0.58	0.44	0.00
			0.71	0.043	87.5	58	16	87.5	0.61	0.44	0.00
			0.79	0.048	87.6	59	16	87.6	0.64	0.44	0.00
			0.86	0.052	87.6	60	16	87.6	0.67	0.44	0.00
			0.94	0.057	87.7	60	16	87.7	0.67	0.44	0.00
			1.02	0.062	87.6	61	16	87.6	0.70	0.44	0.00
			1.10	0.067	87.6	61	16	87.6	0.70	0.44	0.00
			1.18	0.071	87.6	62	16	87.6	0.73	0.44	0.00
			1.26	0.076	87.5	62	16	87.5	0.73	0.44	0.00
			1.33	0.081	87.5	65	16	85.7	0.81	0.44	0.02
			1.41	0.085	87.7	64	16	82.9	0.78	0.44	0.05
			1.49	0.090	87.6	63	16	75.7	0.74	0.44	0.14
			1.56	0.095	87.5	56	16	63.2	0.55	0.44	0.28
			1.65	0.100	87.6	52	16	48.9	0.43	0.44	0.44
36	26	0.72	0.00	0.000	137.5	66	26	137.5	0.84	0.72	0.00
			0.21	0.013	137.5	66	26	137.5	0.84	0.72	0.00
			0.33	0.020	137.5	66	26	137.5	0.84	0.72	0.00
			0.47	0.028	137.6	67	26	137.6	0.87	0.72	0.00
			0.55	0.033	137.6	67	26	137.6	0.87	0.72	0.00
			0.63	0.038	137.6	68	26	137.6	0.90	0.72	0.00
			0.71	0.043	137.8	69	26	137.8	0.93	0.72	0.00
			0.79	0.048	137.6	71	26	137.6	0.96	0.72	0.00
			0.86	0.052	137.6	72	26	137.6	0.99	0.72	0.00
			0.94	0.057	137.8	73	26	137.8	1.02	0.72	0.00
			1.02	0.062	137.6	74	25	137.6	1.06	0.69	0.00
			1.10	0.067	137.6	75	25	136.0	1.08	0.68	0.01
			1.18	0.071	137.6	76	24	134.5	1.11	0.67	0.02
			1.26	0.076	137.6	79	24	134.0	1.19	0.67	0.03
			1.33	0.081	137.6	80	24	127.9	1.22	0.67	0.07
			1.41	0.085	137.7	72	24	110.1	0.99	0.67	0.20
			1.49	0.090	137.6	64	23	86.7	0.78	0.64	0.37
			1.56	0.095	137.5	56	22	66.4	0.55	0.61	0.52
			1.65	0.100	137.7	52	21	48.5	0.43	0.58	0.65

Table D.17: Result for $r_0 = 36\,\text{mm}$ with fixed aspect ratio, increasing frequency.

r_0	h_0	a	f	f_*	m_0	r_f	h_f	m_f	r_*	h_*	m_*
36	35	0.97	0.00	0.000	187.6	76	31	187.6	1.11	0.86	0.00
			0.21	0.013	187.5	76	31	187.5	1.11	0.86	0.00
			0.33	0.020	187.5	77	30	187.5	1.13	0.83	0.00
			0.47	0.028	187.6	80	30	187.6	1.22	0.83	0.00
			0.55	0.033	187.5	80	30	187.5	1.22	0.83	0.00
			0.63	0.038	187.5	81	29	187.5	1.25	0.81	0.00
			0.71	0.043	187.7	82	30	187.7	1.28	0.82	0.00
			0.79	0.048	187.6	82	28	187.6	1.28	0.78	0.00
			0.86	0.052	187.5	83	28	187.5	1.31	0.78	0.00
			0.94	0.057	187.5	85	29	185.8	1.37	0.81	0.01
			1.02	0.062	187.7	87	29	184.9	1.43	0.79	0.01
			1.10	0.067	187.5	88	28	184.0	1.46	0.76	0.02
			1.18	0.071	187.5	92	28	180.4	1.54	0.76	0.04
			1.26	0.076	187.6	93	26	174.5	1.57	0.72	0.07
			1.33	0.081	187.6	81	26	147.8	1.25	0.71	0.21
			1.41	0.085	187.4	72	23	110.7	0.99	0.64	0.41
			1.49	0.090	187.5	62	22	85.7	0.73	0.61	0.54
			1.56	0.095	187.5	54	22	63.5	0.49	0.60	0.66
			1.65	0.100	187.7	52	20	48.0	0.43	0.56	0.74
36	43	1.19	0.00	0.000	237.0	86	32	237.0	1.40	0.89	0.00
			0.21	0.013	237.5	86	32	237.5	1.40	0.89	0.00
			0.33	0.020	237.5	87	31	237.5	1.43	0.86	0.00
			0.47	0.028	237.6	89	30	237.6	1.49	0.83	0.00
			0.55	0.033	237.5	89	30	237.5	1.49	0.83	0.00
			0.63	0.038	237.5	92	30	237.5	1.54	0.82	0.00
			0.71	0.043	237.6	93	30	237.6	1.57	0.82	0.00
			0.79	0.048	237.6	94	30	237.6	1.60	0.82	0.00
			0.86	0.052	237.5	95	29	237.5	1.63	0.81	0.00
			0.94	0.057	237.5	97	29	234.1	1.69	0.81	0.01
			1.02	0.062	237.6	100	29	233.4	1.78	0.79	0.02
			1.10	0.067	237.7	102	28	231.3	1.84	0.76	0.03
			1.18	0.071	237.5	104	27	223.4	1.89	0.75	0.06
			1.26	0.076	237.6	94	26	196.7	1.60	0.71	0.17
			1.33	0.081	237.5	81	26	153.8	1.25	0.71	0.35
			1.41	0.085	237.6	71	24	113.7	0.96	0.67	0.52
			1.49	0.090	237.6	62	23	86.3	0.73	0.64	0.64
			1.56	0.095	237.6	55	22	62.3	0.52	0.61	0.74

Table D.18: Result for $r_0 = 36\,\text{mm}$ with fixed aspect ratio, increasing frequency.

r_0	f	f_*	f_*^2	a_{cone}
20	0.00	0.000	0.0000	0.79
	0.47	0.021	0.0005	0.77
	0.71	0.032	0.0010	0.74
	0.94	0.042	0.0018	0.72
	1.02	0.046	0.0021	0.71
	1.10	0.050	0.0025	0.70
	1.18	0.053	0.0028	0.69
	1.26	0.057	0.0032	0.67
	1.33	0.060	0.0036	0.67
	1.41	0.064	0.0041	0.65
	1.65	0.075	0.0056	0.59
25	0.00	0.000	0.0000	0.78
	0.47	0.024	0.0006	0.76
	0.71	0.036	0.0013	0.74
	0.94	0.047	0.0023	0.71
	1.02	0.051	0.0027	0.69
	1.10	0.056	0.0031	0.68
	1.18	0.060	0.0035	0.65
	1.26	0.064	0.0040	0.65
	1.33	0.067	0.0045	0.63
	1.41	0.071	0.0051	0.62
	1.65	0.083	0.0069	0.56
30	0.00	0.000	0.0000	0.78
	0.47	0.026	0.0007	0.76
	0.71	0.039	0.0015	0.73
	0.94	0.052	0.0027	0.70
	1.02	0.056	0.0032	0.68
	1.10	0.061	0.0037	0.66
	1.18	0.065	0.0043	0.65
	1.26	0.070	0.0049	0.63
	1.33	0.074	0.0054	0.60
	1.41	0.078	0.0061	0.58
	1.65	0.091	0.0083	0.51
36	0.00	0.000	0.0000	0.78
	0.47	0.028	0.0008	0.75
	0.71	0.043	0.0018	0.72
	0.94	0.057	0.0032	0.68
	1.02	0.062	0.0038	0.66
	1.10	0.067	0.0044	0.64
	1.18	0.071	0.0051	0.61
	1.26	0.076	0.0058	0.59
	1.33	0.081	0.0065	0.58
	1.41	0.085	0.0073	0.55
	1.65	0.100	0.0100	0.47

Table D.19: Onset of the full conical shape at an aspect ratio a_{cone} as per discussion in Section 6.3.2.

r_0	f	f_*	Λ	ϵ	Λ_*
20	0.00	0.000	1.01	0.00	0.000
	0.47	0.021	1.01	0.04	0.000
	0.71	0.032	1.04	0.05	0.030
	0.94	0.042	1.08	0.06	0.069
	1.02	0.046	1.08	0.10	0.069
	1.10	0.050	1.12	0.10	0.109
	1.18	0.053	1.13	0.12	0.119
	1.26	0.057	1.17	0.10	0.158
	1.33	0.060	1.25	0.07	0.238
	1.41	0.064	1.33	0.00	0.317
25	0.00	0.000	1.06	0.00	0.000
	0.47	0.024	1.09	0.01	0.028
	0.71	0.036	1.15	-0.01	0.085
	0.94	0.047	1.20	0.00	0.132
	1.02	0.051	1.24	-0.01	0.170
	1.10	0.056	1.25	0.03	0.179
	1.18	0.060	1.30	0.02	0.226
	1.26	0.064	1.32	0.02	0.245
	1.33	0.067	1.37	0.03	0.292
	1.41	0.071	1.49	0.00	0.406
30	0.00	0.000	1.11	0.00	0.000
	0.47	0.026	1.13	0.02	0.018
	0.71	0.039	1.21	0.00	0.090
	0.94	0.052	1.29	0.00	0.162
	1.02	0.056	1.33	-0.01	0.198
	1.10	0.061	1.40	-0.01	0.261
	1.18	0.065	1.45	-0.01	0.306
	1.26	0.070	1.52	-0.01	0.369
	1.33	0.074	1.59	-0.02	0.432
	1.41	0.078	1.66	-0.03	0.495
36	0.00	0.000	1.14	0.00	0.000
	0.47	0.028	1.16	0.05	0.018
	0.71	0.043	1.23	0.06	0.079
	0.94	0.057	1.37	0.05	0.202
	1.02	0.062	1.44	0.04	0.263
	1.10	0.067	1.53	0.00	0.342
	1.18	0.071	1.59	0.00	0.395
	1.26	0.076	1.70	-0.03	0.491
	1.33	0.081	1.79	0.00	0.570

Table D.20: Evaluation of $r_* = \Lambda a + \epsilon$ as in Section 6.4.1.

r_0	f	f_*	f_*^2	h_f	a_h
20	0.00	0.000	0.0000	20.0	1.04
	0.47	0.021	0.0005	18.5	0.96
	0.71	0.032	0.0010	18.0	0.93
	0.94	0.042	0.0018	17.5	0.90
	1.02	0.046	0.0021	17.5	0.90
	1.10	0.050	0.0025	17.0	0.87
	1.18	0.053	0.0028	16.7	0.85
	1.26	0.057	0.0032	16.5	0.83
	1.33	0.060	0.0036	16.4	0.82
	1.41	0.064	0.0041	16.0	0.78
25	0.00	0.000	0.0000	22.5	0.90
	0.47	0.024	0.0006	22.0	0.88
	0.71	0.036	0.0013	21.5	0.86
	0.94	0.047	0.0023	20.8	0.83
	1.02	0.051	0.0027	20.4	0.81
	1.10	0.056	0.0031	20.0	0.79
	1.18	0.060	0.0035	19.0	0.75
	1.26	0.064	0.0040	19.0	0.75
	1.33	0.067	0.0045	18.6	0.73
	1.41	0.071	0.0051	18.5	0.72
	1.65	0.083	0.0069	17.3	0.69
30	0.00	0.000	0.0000	18.0	0.93
	0.47	0.026	0.0007	27.0	0.90
	0.71	0.039	0.0015	26.0	0.88
	0.94	0.052	0.0027	25.0	0.84
	1.02	0.056	0.0032	24.5	0.82
	1.10	0.061	0.0037	24.0	0.80
	1.18	0.065	0.0043	23.0	0.78
	1.26	0.070	0.0049	22.5	0.76
	1.33	0.074	0.0054	22.0	0.74
	1.41	0.078	0.0061	21.0	0.71
	1.65	0.091	0.0083	20.0	0.65
36	0.00	0.000	0.0000	31.5	0.89
	0.47	0.028	0.0008	30.5	0.87
	0.71	0.043	0.0018	29.5	0.85
	0.94	0.057	0.0032	29.0	0.83
	1.02	0.062	0.0038	28.5	0.83
	1.10	0.067	0.0044	27.5	0.83
	1.18	0.071	0.0051	26.5	0.81
	1.26	0.076	0.0058	26.0	0.79
	1.33	0.081	0.0065	25.5	0.77
	1.41	0.085	0.0073	23.5	0.72
	1.65	0.100	0.0100	20.0	0.63

Table D.21: Onset of stagnating h_f at an aspect ratio a_h as per discussion in Section 6.4.1.

f	t	r_1	r_2	r_3	r_{av}	$r_{*,av}$
0.00	0.0000	36	36	36	36.0	0.0000
	0.0143	37	39	38	37.9	0.0526
	0.0286	38	40	39	38.8	0.0789
	0.0429	43	43	40	41.7	0.1579
	0.0571	45	45	44	44.5	0.2368
	0.0714	46	47	45	46.4	0.2895
	0.0857	47	50	47	48.3	0.3421
	0.1000	51	54	50	51.8	0.4386
	0.1143	52	54	52	52.7	0.4649
	0.1285	53	55	53	53.7	0.4912
0.47	0.0000	36	36	36	36.0	0.0000
	0.0143	38	38	38	37.9	0.0526
	0.0286	39	39	40	39.2	0.0877
	0.0429	41	44	44	42.6	0.1842
	0.0571	45	46	45	45.5	0.2632
	0.0714	46	47	47	47.1	0.3070
	0.0857	48	51	52	50.5	0.4035
	0.1000	52	54	55	53.7	0.4912
	0.1143	54	55	56	54.9	0.5263
	0.1285	55	55	56	55.3	0.5351
	0.1429	55	56	57	55.9	0.5526
0.71	0.0000	36	36	36	36.0	0.0000
	0.0143	39	38	38	38.2	0.0614
	0.0286	40	40	39	39.5	0.0965
	0.0429	43	43	43	42.6	0.1842
	0.0571	45	45	45	45.5	0.2632
	0.0714	48	48	47	48.0	0.3333
	0.0857	51	52	52	51.8	0.4386
	0.1000	53	55	54	54.0	0.5000
	0.1143	54	56	56	55.3	0.5351
	0.1285	56	56	57	56.2	0.5614
	0.1429	57	56	58	56.8	0.5789

Table D.22: Temporal data for runout with $r_0 = 36\,\text{mm}$, $h_0 = 23\,\text{mm}$, $a = 0.61$ for $f = 0.00, 0.47, 0.71\,\text{Hz}$.

f	t	r_1	r_2	r_3	r_{av}	$r_{*,av}$
0.94	0.0000	36	36	36	36.0	0.0000
	0.0143	38	39	38	38.2	0.0614
	0.0286	39	40	40	39.5	0.0965
	0.0429	44	45	44	44.2	0.2281
	0.0571	46	47	46	46.7	0.2982
	0.0714	51	54	49	51.5	0.4298
	0.0857	56	57	53	55.3	0.5351
	0.1000	59	60	55	57.8	0.6053
	0.1143	61	62	58	60.0	0.6667
	0.1285	63	63	60	61.9	0.7193
	0.1429	64	64	62	63.5	0.7632
	0.1571	65	64	63	64.4	0.7895
	0.1714	65	64	63	64.4	0.7895
	0.1857	65	64	64	64.7	0.7982
1.18	0.0000	36	36	36	36.0	0.0000
	0.0143	38	38	39	38.2	0.0614
	0.0286	40	41	41	40.4	0.1228
	0.0429	44	44	45	43.9	0.2193
	0.0571	45	45	47	46.1	0.2807
	0.0714	47	49	52	49.6	0.3772
	0.0857	52	52	55	53.1	0.4737
	0.1000	55	55	58	55.9	0.5526
	0.1143	57	57	62	58.4	0.6228
	0.1285	61	60	62	60.6	0.6842
	0.1429	63	61	63	62.2	0.7281
	0.1571	64	63	64	63.8	0.7719
	0.1714	65	64	65	65.1	0.8070
	0.1857	66	65	66	66.0	0.8333
	0.2000	68	66	66	66.9	0.8596

Table D.23: Temporal data for runout with $r_0 = 36\,\text{mm}$, $h_0 = 23\,\text{mm}$, $a = 0.61$ for $f = 1.18, 0.94\,\text{Hz}$.

f	t	r_1	r_2	r_3	r_{av}	$r_{*,av}$
1.30	0.0000	36	36	36	36.0	0.0000
	0.0143	38	38	38	37.9	0.0526
	0.0286	41	41	41	40.7	0.1316
	0.0429	45	45	45	45.2	0.2544
	0.0571	47	48	48	48.0	0.3333
	0.0714	53	56	53	54.0	0.5000
	0.0857	56	60	58	57.8	0.6053
	0.1000	59	63	61	60.6	0.6842
	0.1143	63	64	63	63.5	0.7632
	0.1285	65	67	67	66.6	0.8509
	0.1429	67	68	69	68.2	0.8947
	0.1571	68	69	69	68.8	0.9123
	0.1714	70	72	71	71.1	0.9737
	0.1857	72	72	73	72.3	1.0088
	0.2000	74	74	75	74.2	1.0614
	0.2143	75	75	76	75.2	1.0877
	0.2286	76	75	76	75.5	1.0965
	0.3238	76	73	74	74.2	1.0614
	0.4190	71	68	72	70.4	0.9561
	0.5143	68	66	69	67.9	0.8860
1.41	0.0000	36	36	36	36.0	0.0000
	0.0143	38	38	38	37.9	0.0526
	0.0286	40	40	40	39.8	0.1053
	0.0429	45	45	45	44.5	0.2368
	0.0571	48	47	47	47.7	0.3246
	0.0714	53	52	52	52.4	0.4561
	0.0857	56	57	57	56.5	0.5702
	0.1000	62	61	60	60.6	0.6842
	0.1143	64	65	64	64.7	0.7982
	0.1285	67	69	68	68.2	0.8947
	0.1429	70	71	71	70.7	0.9649
	0.1571	73	73	73	72.9	1.0263
	0.1714	75	76	76	75.5	1.0965
	0.1857	76	77	77	76.4	1.1228
	0.2000	77	79	79	78.0	1.1667
	0.2143	80	81	81	80.2	1.2281
	0.2286	81	82	82	82.1	1.2807
	0.2429	84	82	82	83.1	1.3070
	0.2571	84	83	83	83.7	1.3246
	0.2714	84	84	84	84.3	1.3421
	0.3667	82	81	81	81.5	1.2632
	0.5095	68	70	70	69.5	0.9298
	0.6524	66	67	67	66.9	0.8596
	0.7952	63	63	63	63.5	0.7632

Table D.24: Temporal data for runout with $r_0 = 36\,\text{mm}$, $h_0 = 23\,\text{mm}$, $a = 0.61$ for $f = 1.30, 1.41\,\text{Hz}$.

f	t	r_1	r_2	r_3	r_{av}	$r_{*,av}$
1.53	0.0000	36	36	36	36.0	0.0000
	0.0143	38	38	38	37.9	0.0526
	0.0286	39	40	40	39.5	0.0965
	0.0429	44	45	45	44.5	0.2368
	0.0571	46	46	48	47.1	0.3070
	0.0714	50	50	52	50.8	0.4123
	0.0857	56	55	56	55.6	0.5439
	0.1000	59	58	60	58.7	0.6316
	0.1143	63	63	63	62.8	0.7456
	0.1285	66	66	68	66.9	0.8596
	0.1429	69	70	70	69.8	0.9386
	0.1571	74	75	75	74.5	1.0702
	0.1714	75	76	76	75.5	1.0965
	0.1857	77	78	78	77.4	1.1491
	0.2000	79	81	80	79.6	1.2105
	0.2143	81	83	82	82.1	1.2807
	0.2286	82	84	84	83.7	1.3246
	0.2429	84	85	86	85.3	1.3684
	0.2571	85	86	87	86.2	1.3947
	0.2714	85	88	87	86.8	1.4123
	0.3667	85	85	86	85.6	1.3772
	0.5095	79	80	81	79.6	1.2105
	0.6524	65	69	70	68.2	0.8947
	0.7952	63	66	65	64.7	0.7982
	0.9381	58	60	60	59.1	0.6404
	1.0810	56	55	56	55.6	0.5439
	1.2238	52	53	54	53.1	0.4737
	1.3667	49	49	52	50.2	0.3947

Table D.25: Temporal data for runout with $r_0 = 36\,\text{mm}$, $h_0 = 23\,\text{mm}$, $a = 0.61$ for $f = 1.53, 1.65\,\text{Hz}$.

f	t	r_1	r_2	r_3	r_{av}	$r_{*,av}$
1.65	0.0000	36	36	36	36.0	0.0000
	0.0143	39	38	39	38.5	0.0702
	0.0286	42	41	42	41.4	0.1491
	0.0429	45	45	45	45.2	0.2544
	0.0571	48	47	48	48.0	0.3333
	0.0714	54	52	53	53.1	0.4737
	0.0857	58	56	58	57.2	0.5877
	0.1000	63	63	63	63.2	0.7544
	0.1143	66	66	67	66.6	0.8509
	0.1285	70	71	71	70.7	0.9649
	0.1429	73	75	74	73.9	1.0526
	0.1571	76	78	77	76.7	1.1316
	0.1714	79	81	80	79.6	1.2105
	0.1857	81	83	82	82.4	1.2895
	0.2000	84	85	84	84.6	1.3509
	0.2143	85	87	86	86.2	1.3947
	0.2286	88	90	88	88.7	1.4649
	0.2429	91	93	90	91.3	1.5351
	0.2571	93	95	92	93.2	1.5877
	0.2714	93	95	94	93.8	1.6053
	0.2857	94	95	95	94.4	1.6228
	0.3000	95	95	96	95.1	1.6404
	0.4429	88	87	90	88.4	1.4561
	0.5381	78	80	79	78.6	1.1842
	0.6333	70	70	71	70.4	0.9561
	0.7524	63	65	63	63.8	0.7719
	0.8952	54	59	56	56.2	0.5614
	1.0381	51	54	52	52.4	0.4561
	1.1810	45	49	47	47.4	0.3158
	1.3238	41	44	42	42.0	0.1667

Table D.26: Temporal data for runout with $r_0 = 36\,\text{mm}$, $h_0 = 23\,\text{mm}$, $a = 0.61$ for $f = 1.65\,\text{Hz}$.

f	t	r_1	r_2	r_3	r_{av}	$r_{*,av}$
0.00	0.0000	36	36	36	36.0	0.0000
	0.0143	39	39	38	38.5	0.0702
	0.0286	39	39	40	39.2	0.0877
	0.0429	41	44	43	42.3	0.1754
	0.0571	45	46	45	45.5	0.2632
	0.0714	47	49	47	48.0	0.3333
	0.0857	53	55	50	52.7	0.4649
	0.1000	57	57	55	56.2	0.5614
	0.1143	62	61	58	60.0	0.6667
	0.1285	66	64	63	64.4	0.7895
	0.1429	67	66	64	66.0	0.8333
	0.1571	70	68	66	68.2	0.8947
	0.1714	73	70	68	70.4	0.9561
0.47	0.0000	36	36	36	36.0	0.0000
	0.0143	38	38	38	37.9	0.0526
	0.0286	41	40	40	40.1	0.1140
	0.0429	45	43	44	43.6	0.2105
	0.0571	46	45	45	45.8	0.2719
	0.0714	49	47	47	48.0	0.3333
	0.0857	56	55	51	54.0	0.5000
	0.1000	58	60	55	57.5	0.5965
	0.1143	64	64	59	62.5	0.7368
	0.1285	66	66	63	65.1	0.8070
	0.1429	71	68	64	67.9	0.8860
	0.1571	72	68	68	69.5	0.9298
	0.1714	73	70	70	71.1	0.9737
0.71	0.0000	36	36	36	36.0	0.0000
	0.0143	38	38	39	38.2	0.0614
	0.0286	40	41	41	40.4	0.1228
	0.0429	42	44	45	43.3	0.2018
	0.0571	45	46	46	46.1	0.2807
	0.0714	47	49	50	48.9	0.3596
	0.0857	53	55	56	54.6	0.5175
	0.1000	57	58	61	58.4	0.6228
	0.1143	61	65	64	63.5	0.7632
	0.1285	65	68	67	66.9	0.8596
	0.1429	67	72	73	70.7	0.9649
	0.1571	72	74	75	73.6	1.0439
	0.1714	74	75	76	74.8	1.0789
	0.1857	74	76	76	75.2	1.0877

Table D.27: Temporal data for runout with $r_0 = 36\,\text{mm}$, $h_0 = 39\,\text{mm}$, $a = 1.03$ for $f = 0.00, 0.47, 0.71\,\text{Hz}$.

f	t	r_1	r_2	r_3	r_{av}	$r_{*,av}$
0.94	0.0000	36	36	36	36.0	0.0000
	0.0143	38	38	40	38.5	0.0702
	0.0286	39	40	42	40.1	0.1140
	0.0429	44	45	45	44.5	0.2368
	0.0571	45	46	47	46.4	0.2895
	0.0714	49	49	53	50.5	0.4035
	0.0857	53	54	57	54.6	0.5175
	0.1000	57	58	63	59.4	0.6491
	0.1143	63	63	66	64.1	0.7807
	0.1285	65	66	73	68.2	0.8947
	0.1429	68	71	74	71.1	0.9737
	0.1571	71	73	78	73.9	1.0526
	0.1714	75	76	81	77.4	1.1491
	0.1857	78	78	82	79.3	1.2018
	0.2000	80	80	84	81.2	1.2544
	0.2143	81	81	85	82.4	1.2895
1.06	0.0000	36	36	36	36.0	0.0000
	0.0143	38	38	38	37.9	0.0526
	0.0286	39	39	39	38.8	0.0789
	0.0429	45	45	45	44.8	0.2456
	0.0571	46	46	46	46.4	0.2895
	0.0714	48	49	50	49.3	0.3684
	0.0857	54	55	54	54.3	0.5088
	0.1000	57	57	58	57.2	0.5877
	0.1143	61	63	63	62.2	0.7281
	0.1285	65	66	66	66.0	0.8333
	0.1429	68	73	71	70.7	0.9649
	0.1571	73	75	74	73.9	1.0526
	0.1714	75	76	76	75.5	1.0965
	0.1857	78	81	80	79.3	1.2018
	0.2000	81	84	82	82.4	1.2895
	0.2143	83	85	84	84.3	1.3421
	0.2286	85	85	85	85.3	1.3684

Table D.28: Temporal data for runout with $r_0 = 36\,\text{mm}$, $h_0 = 39\,\text{mm}$, $a = 1.03$ for $f = 0.94, 1.06\,\text{Hz}$.

f	t	r_1	r_2	r_3	r_{av}	$r_{*,av}$
1.18	0.0000	36	36	36	36.0	0.0000
	0.0143	38	38	38	37.9	0.0526
	0.0286	41	41	40	40.4	0.1228
	0.0429	45	45	44	44.2	0.2281
	0.0571	46	46	45	46.1	0.2807
	0.0714	51	51	48	50.2	0.3947
	0.0857	54	55	55	54.6	0.5175
	0.1000	58	60	58	58.4	0.6228
	0.1143	64	64	65	64.7	0.7982
	0.1285	67	69	71	69.2	0.9211
	0.1429	73	73	75	73.6	1.0439
	0.1571	77	76	76	76.1	1.1140
	0.1714	81	81	82	81.8	1.2719
	0.1857	84	84	84	84.3	1.3421
	0.2000	86	85	85	85.6	1.3772
	0.2143	88	89	88	88.4	1.4561
	0.2286	90	91	89	90.0	1.5000
	0.2429	90	92	91	90.9	1.5263
	0.2571	91	93	91	91.6	1.5439
	0.2714	92	93	92	92.2	1.5614
	0.4143	91	92	90	90.9	1.5263
	0.5571	87	87	85	86.5	1.4035
	0.7000	85	84	83	84.3	1.3421
	0.8429	83	82	83	83.1	1.3070

Table D.29: Temporal data for runout with $r_0 = 36\,\text{mm}$, $h_0 = 39\,\text{mm}$, $a = 1.03$ for $f = 1.18\,\text{Hz}$.

f	t	r_1	r_2	r_3	r_{av}	$r_{*,av}$
1.30	0.0000	36	36	36	36.0	0.0000
	0.0143	38	38	38	37.9	0.0526
	0.0286	41	41	40	40.4	0.1228
	0.0429	45	45	45	45.2	0.2544
	0.0571	47	47	47	47.4	0.3158
	0.0714	51	53	55	53.1	0.4737
	0.0857	56	57	57	56.5	0.5702
	0.1000	62	63	65	63.5	0.7632
	0.1143	65	67	67	66.6	0.8509
	0.1285	69	74	74	72.3	1.0088
	0.1429	75	77	79	76.7	1.1316
	0.1571	78	81	82	80.2	1.2281
	0.1714	81	85	85	84.0	1.3333
	0.1857	84	86	87	85.9	1.3860
	0.2000	86	90	88	88.1	1.4474
	0.2143	90	92	91	90.9	1.5263
	0.2286	93	95	94	93.8	1.6053
	0.2429	94	96	95	94.7	1.6316
	0.2571	95	97	97	96.0	1.6667
	0.2714	97	99	98	97.6	1.7105
	0.2857	99	100	99	99.8	1.7719
	0.3000	101	102	101	101.7	1.8246
	0.3143	103	104	101	102.9	1.8596
	0.3286	104	104	102	103.6	1.8772
	0.4238	104	103	105	104.2	1.8947
	0.5190	99	99	95	97.6	1.7105
	0.6143	91	94	88	90.9	1.5263
	0.7095	85	87	83	85.3	1.3684
	0.8048	81	82	78	80.5	1.2368
	0.9000	79	80	78	78.6	1.1842
	0.9952	76	76	76	75.8	1.1053
	1.0905	75	75	75	74.8	1.0789
	1.1857	74	75	74	74.2	1.0614
	1.2810	74	74	73	73.6	1.0439

Table D.30: Temporal data for runout with $r_0 = 36\,\text{mm}$, $h_0 = 39\,\text{mm}$, $a = 1.03$ for $f = 1.30\,\text{Hz}$.

f	t	r_1	r_2	r_3	r_{av}	$r_{*,av}$
1.41	0.0000	36	36	36	36.0	0.0000
	0.0143	38	38	38	37.9	0.0526
	0.0286	41	41	40	40.4	0.1228
	0.0429	45	45	44	44.5	0.2368
	0.0571	48	47	47	47.7	0.3246
	0.0714	54	51	52	52.4	0.4561
	0.0857	58	56	57	56.8	0.5789
	0.1000	65	60	63	62.8	0.7456
	0.1143	72	64	67	67.9	0.8860
	0.1285	76	69	75	73.3	1.0351
	0.1429	81	75	80	78.6	1.1842
	0.1571	84	80	84	82.7	1.2982
	0.1714	86	84	88	86.2	1.3947
	0.1857	91	87	92	90.0	1.5000
	0.2000	94	91	95	93.2	1.5877
	0.2143	96	95	98	96.0	1.6667
	0.2286	99	96	99	97.9	1.7193
	0.2429	103	99	100	101.1	1.8070
	0.2571	104	102	103	103.3	1.8684
	0.2714	106	104	104	104.8	1.9123
	0.2857	108	106	106	106.7	1.9649
	0.3000	112	106	109	108.9	2.0263
	0.3143	114	110	109	110.8	2.0789
	0.3286	114	113	111	112.4	2.1228
	0.3429	115	114	114	114.0	2.1667
	0.3571	117	114	114	114.6	2.1842
	0.5000	114	111	112	112.1	2.1140
	0.6429	102	102	95	99.8	1.7719
	0.7857	83	83	84	83.7	1.3246
	0.9288	74	74	73	73.6	1.0439
	1.0714	65	66	66	66.0	0.8333
	1.2143	64	63	64	64.1	0.7807
	1.3571	63	62	63	62.5	0.7368
	1.5000	61	60	59	59.7	0.6579
	1.6429	58	58	59	58.1	0.6140

Table D.31: Temporal data for runout with $r_0 = 36\,\text{mm}$, $h_0 = 39\,\text{mm}$, $a = 1.03$ for $f = 1.41\,\text{Hz}$.

f	t	r_1	r_2	r_3	r_{av}	$r_{*,av}$
1.53	0.0000	36	36	36	36.0	0.0000
	0.0143	38	39	38	38.2	0.0614
	0.0286	41	43	42	41.7	0.1579
	0.0429	45	45	46	45.5	0.2632
	0.0571	46	48	48	47.7	0.3246
	0.0714	50	55	54	53.1	0.4737
	0.0857	55	57	58	56.5	0.5702
	0.1000	60	63	63	62.2	0.7281
	0.1143	64	66	70	66.9	0.8596
	0.1285	69	74	74	72.3	1.0088
	0.1429	75	78	80	77.4	1.1491
	0.1571	79	83	83	81.8	1.2719
	0.1714	84	87	88	86.5	1.4035
	0.1857	87	91	92	90.0	1.5000
	0.2000	93	95	97	94.7	1.6316
	0.2143	95	97	98	96.3	1.6754
	0.2286	100	102	101	101.4	1.8158
	0.2429	103	102	105	103.6	1.8772
	0.2571	107	104	107	106.1	1.9474
	0.2714	110	109	112	110.2	2.0614
	0.2857	114	112	114	113.1	2.1404
	0.3000	115	114	116	114.6	2.1842
	0.3143	121	117	119	119.1	2.3070
	0.3286	123	119	122	121.6	2.3772
	0.3429	124	122	124	123.5	2.4298
	0.3571	130	124	127	126.9	2.5263
	0.5000	120	114	119	117.8	2.2719
	0.5952	106	104	108	106.1	1.9474
	0.6905	91	86	90	89.1	1.4737
	0.7857	78	77	80	78.0	1.1667
	0.8810	73	75	74	73.9	1.0526
	0.9762	66	71	69	68.8	0.9123
	1.0714	63	66	66	65.4	0.8158
	1.1667	61	63	63	62.5	0.7368
	1.2619	57	57	58	57.2	0.5877
	1.3571	55	55	56	55.3	0.5351
	1.5000	53	52	54	53.1	0.4737
	1.6429	53	51	52	52.1	0.4474
	1.7857	53	51	52	52.1	0.4474

Table D.32: Temporal data for runout with $r_0 = 36\,\text{mm}$, $h_0 = 39\,\text{mm}$, $a = 1.03$ for $f = 1.53\,\text{Hz}$.

f	t	r_1	r_2	r_3	r_{av}	$r_{*,av}$
1.65	0.0000	36	36	36	36.0	0.0000
	0.0143	38	38	38	37.9	0.0526
	0.0286	42	42	42	41.7	0.1579
	0.0429	46	45	46	46.1	0.2807
	0.0571	51	50	51	50.8	0.4123
	0.0714	57	56	57	56.5	0.5702
	0.0857	63	63	64	63.8	0.7719
	0.1000	70	71	71	70.7	0.9649
	0.1143	75	76	76	75.5	1.0965
	0.1285	83	84	84	84.0	1.3333
	0.1429	87	88	88	87.8	1.4386
	0.1571	92	93	93	92.5	1.5702
	0.1714	98	98	97	97.3	1.7018
	0.1857	101	102	101	101.7	1.8246
	0.2000	106	105	104	105.2	1.9211
	0.2143	109	108	107	108.0	2.0000
	0.2286	113	112	112	112.1	2.1140
	0.2429	116	114	114	114.3	2.1754
	0.2571	118	117	116	116.8	2.2456
	0.2714	121	120	120	120.6	2.3509
	0.2857	124	123	123	123.5	2.4298
	0.3000	126	126	125	125.7	2.4912
	0.3143	130	129	128	128.8	2.5789
	0.3286	134	132	132	132.3	2.6754
	0.3429	135	133	133	133.3	2.7018
	0.4857	128	127	129	127.9	2.5526
	0.6286	104	104	104	104.2	1.8947
	0.7714	68	70	68	68.8	0.9123
	0.9143	57	55	55	55.6	0.5439
	1.0571	51	50	50	50.5	0.4035
	1.2000	48	47	47	47.7	0.3246
	1.3429	46	45	47	46.4	0.2895
	1.4857	45	45	45	44.5	0.2368

Table D.33: Temporal data for runout with $r_0 = 36\,\text{mm}$, $h_0 = 39\,\text{mm}$, $a = 1.03$ for $f = 1.65\,\text{Hz}$.

r_0	f	f_*	K
20	0.00	0.000	3.4
	0.47	0.021	3.8
	0.71	0.032	4.0
	0.94	0.042	4.3
25	0.00	0.000	3.5
	0.47	0.023	3.8
	0.71	0.035	4.1
	0.94	0.047	4.5
30	0.00	0.000	3.6
	0.47	0.025	3.9
	0.71	0.039	4.1
	0.94	0.051	4.4
36	0.00	0.000	3.5
	0.47	0.028	4.0
	0.71	0.043	4.2
	0.94	0.056	4.6

Table D.34: Data for dependence of proportional coefficient K in the relation $t_* = K\sqrt{a}$ on f_*.

Appendix E

DEM script

In Chapter 7 the LIGGGHTS DEM code was implemented to perform the simulations. This language has a front end that performs like a mark-up language similar to HTML or Matlab. The following code was implemented alongside the meshes discussed within the section to perform the simulation.

Comments within the code are indicated with '#'. The particle/wall friction and rotation frequency was altered between simulations. The place where this can be altered is clearly indicated. Details on each keyword applied have been left to the reader where they can consult the documentation online (www.liggghts.com), but the code reads realitively simply for the layman.

```
    #initialise granular system with fixed boundaries
atom_style granular
boundary f f f
newton off
communicate single vel yes
units si

    #create simulation
region reg block -0.42 0.42 -0.42 0.42 -0.01 0.4 units box
create_box 2 reg

    #setup neighbor lists
neighbor 0.0005 bin
neigh_modify delay 0

    #set all material properties and pair style
#using hertz model. refer to documentation
fix m1 all property/global youngsModulus peratomtype 200.e7 200.e7
```

```
fix m2 all property/global poissonsRatio peratomtype 0.3 0.3
fix m3 all property/global coefficientRestitution peratomtypepair 2 0.6 0.6 0.6 0.6
#Alter m4 to alter alter friction.
#change the 2nd and 3rd values for particle/wall friction value
fix m4 all property/global coefficientFriction peratomtypepair 2 0.5 0.5 0.5 0.5
pair_style gran/hertz/history 1 0 #Hertz without cohesion
pair_coeff * *

        #define timestep
timestep 0.0000001

        #define integration type (volume/energy conserving integration)
fix 1 all nve/sphere

        #apply gravity
fix 2 all gravity 9.81 vector 0 0 -1

        #####IMPORTING MESHES######
#insert tank radius 40cm, depth 15cm
fix cadtank all mesh/gran tank.stl 2 1 0 0 0 0 0 0

        #insert cylinder so it sits directly on tank: radius 1cm depth 20cm
fix cadcyl all mesh/gran 2cmcyl.stl 2 1 0 0 0 0 0 0

        #make meshes granular walls with the material properties
fix granwall all wall/gran/hertz/history 1 0 mesh/gran 2 cadtank cadcyl

        #define region of insertion and put granules in
#region defined to be between 2cm-10cm of the cylinder
region incyl cylinder z 0 0 0.009 0.02 0.1 units box
group nve_group region incyl

        #10000 particles are 'poured' into the insertion region
#1mm particles, uniform
#density 8000kg/m3 (steel)
fix ins nve_group pour 10000 1 1 region incyl diam uniform 0.001 0.001 dens uniform
8000 8000

        #insert the first particles so dump isn't empty (work-around)
```

```
run 1

        #create dump of particle characteristics
#(id,displacement,velocity,force,rotation)
#dump every 40000 timesteps i.e. 0.004s
#run for just over 1 second to pour in particles
dump dmpins1 all custom 40000 ins1.liggghts id type type x y z ix iy iz vx vy vz fx
fy fz omegax omegay omegaz radius
run 2520000
undump dmpins1

        #rotate the tank and cylinder
#the first three values are the position of the
#centre of rotation axis
#next three values is the direction vector for the axis
#final value is the rotation frequency
fix movecadtank all move/mesh/gran rotate 0 0 0 0 0 1 1.0 cadtank
fix rotcadcyl all move/mesh/gran rotate 0 0 0 0 0 1 1.0 cadcyl

        #allow the particles to enter solid body rotation
#continue to create particle dumps every 0.004s which rotating
#for a total of 6 seconds
dump dmpsbr1 all custom 40000 sbr1.liggghts id type type x y z ix iy iz vx vy vz
fx fy fz omegax omegay omegaz radius
run 2520000
undump dmpsbr1
dump dmpsbr2 all custom 40000 sbr2.liggghts id type type x y z ix iy iz vx vy vz
fx fy fz omegax omegay omegaz radius
run 2520000
undump dmpsbr2
dump dmpsbr3 all custom 40000 sbr3.liggghts id type type x y z ix iy iz vx vy vz
fx fy fz omegax omegay omegaz radius
run 2520000
undump dmpsbr3
dump dmpsbr4 all custom 40000 sbr4.liggghts id type type x y z ix iy iz vx vy vz
fx fy fz omegax omegay omegaz radius
run 2520000
undump dmpsbr4
dump dmpsbr5 all custom 40000 sbr5.liggghts id type type x y z ix iy iz vx vy vz
```

```
fx fy fz omegax omegay omegaz radius
run 2520000
undump dmpsbr5
dump dmpsbr6 all custom 40000 sbr6.liggghts id type type x y z ix iy iz vx vy vz
fx fy fz omegax omegay omegaz radius
run 2520000
undump dmpsbr6

        #unfix cylinder and remove from simulation. ensure tank is still
#subject to material propeties
unfix rotcadcyl
unfix granwall
unfix cadcyl
fix granwall2 all wall/gran/hertz/history 1 0 mesh/gran 1 cadtank

        #dump how particles fall every 0.004s
#continue for 4 seconds
dump dmpfall1 all custom 40000 fall1.liggghts id type type x y z ix iy iz vx vy vz
fx fy fz omegax omegay omegaz radius
run 2520000
undump dmpfall1
dump dmpfall2 all custom 40000 fall2.liggghts id type type x y z ix iy iz vx vy vz
fx fy fz omegax omegay omegaz radius
run 2520000
undump dmpfall2
dump dmpfall3 all custom 40000 fall3.liggghts id type type x y z ix iy iz vx vy vz
fx fy fz omegax omegay omegaz radius
run 2520000
undump dmpfall3
dump dmpfall4 all custom 40000 fall4.liggghts id type type x y z ix iy iz vx vy vz
fx fy fz omegax omegay omegaz radius
run 2520000
```

Appendix F

Published papers

Results from stationary granular column collapse using laser scanning technology found in Chapter 4 has been published in *Granular Matter*. The reference is given in the bibliography Warnett et al. [2014a]. Attached here is the published paper.

Granular Matter (2014) 16:115–124
DOI 10.1007/s10035-013-0469-x

ORIGINAL PAPER

Scalings of axisymmetric granular column collapse

J. M. Warnett · P. Denissenko · P. J. Thomas · E. Kiraci · M. A. Williams

Received: 4 March 2013 / Published online: 7 December 2013

Abstract Experimental investigations into the collapse of granular columns are presented with dimensional results of the final deposit obtained using a 3D laser scanner. The high accuracy measurement method has found that the final pile radius is not only dependent on the aspect ratio of the initial geometry as previously thought, but also the initial column radius and hence the ratio of column radius to particle diameter. This was also observed to be true for the angle at the base of the deposit. Theoretical considerations coupled with obtained data have allowed the angle at summit for aspect ratios less than approximately 3 to be described entirely in terms of material parameters and aspect ratio—something desired for all length scalings but seemingly unobtainable due to the dynamic nature of the collapse. With the method being non intrusive, measurement of the summital radius was also made possible. The final height showed a dependence predominantly with aspect ratio in agreement with previous authors.

Keywords Granular collapse · Granular flow · Failure surface · Avalanches

1 Introduction

Granular flows have been the interest of much research due to their existence in many man made processes and natural phenomena. The handling of grains and powders is important to many civil engineering projects, such as the storage of grains and powders, and also to the pharmaceutical industry in the sorting of pills and medicines. Description of these flows have been offered by interpretation of the collapse of a granular column [1–8] and the failure of a granular step [9–11]. The avalanching flows observed in these experiments are analogous to some geophysical flows. Examples such as pyroclastic flows and avalanches are of particular interest for hazard management, but direct observation of these flows are rare and dangerous to undertake. Predictions of such deluges are based on the final deposits [12] and so the dynamics of collapse can be difficult to describe over specific geographic topologies with variability in the landscape.

The collapse of an axisymmetric granular column is an unsteady flow; there are phases of acceleration, steady flow and deceleration during the collapse. This dynamic is further complicated by the existence of static and flowing regions within the collapsing column. A general physical description of avalanching granular flows is given by Cates et al. [13] in terms of mechanisms behind the development of a sand pile. A sand pile can be seen as 'fragile' in that it cannot elastically support some infinitesimal loads. This fragility leads to avalanching and settles where grains have successfully jammed under the load of a granular force chain. A slight change in the direction of the force acting on a grain at the extremity (surface of the pile) can break this chain and results in further reorganisation of the previously jammed medium below and additional avalanching.

Theoretical models of granular flows have been developed using depth-averaged and Saint–Venant equations, applied with a varying degree of success dependent upon the flow regime [14–17]. This is due to the lack of a set of constitutive laws as in fluidic systems. The collapse of a granular column is a highly unsteady example of a granular flow and

J. M. Warnett (✉) · P. Denissenko · P. J. Thomas
School of Engineering, University of Warwick, Gibbet Hill Road, Coventry CV4 7AL, UK
e-mail: j.m.warnett@warwick.ac.uk

E. Kiraci · M. A. Williams
Warwick Manufacturing Group, University of Warwick, Gibbet Hill Road, Coventry CV4 7AL, UK

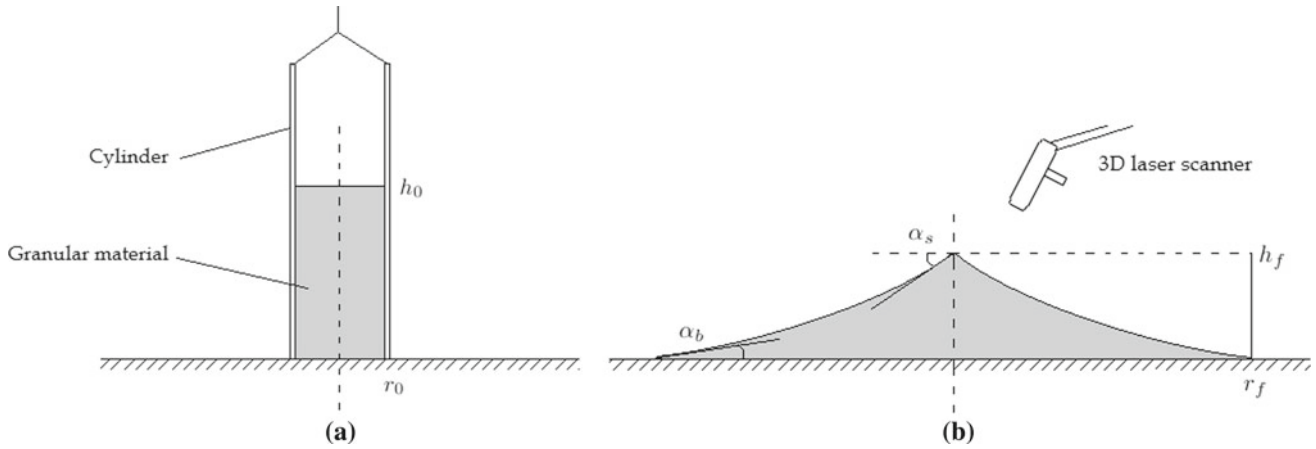

Fig. 1 Experimental setup. **a** Initial setup of granular column on rotating table. **b** Column after collapse with dimensions

applying these sets of equations struggled to recover the precise dynamic behaviour of the system [18]. Much progress has been made in this area with a different combination of models; for example Larrieu et al. [19] used a combination of shallow water depth-averaged equations with the regular timed addition of material to the flow. This model is in good agreement with the scalings already found experimentally up to an aspect ratio of $a < 10$, but requires an unphysical fricition coefficient. This is in addition to the evolution of the profile of the deposit often being exagerrated. Even greater progress has been made in the collapses' 2D counterpart, the failure of a granular step. This particular collapse while largely exhibiting similar flow regimes results in slightly different scalings, suggested to be due to the geometry dependent mechanism of side-ways mass ejection [4]. Doyle et al. [20] adapted the model proposed by Larrieu et al. by including an estimation for the interface between the static and flowing region which allow a more realistic coefficient of friction. Crosta et al. [21] used a Mohr–Coulomb yield rule with non associative flow that was in very good agreement with the physical experiments, although struggled with the tapering of the front of the flow. The most encouraging and accurate model to date, again in 2D, is the $\mu(I)$ rheology proposed by Lagree et al. [22] recovering the evolution of the flow with a greater accuracy. In the future it is hoped that the $\mu(I)$ rheology can be successfully applied to the 3D cylindrical column collapse case.

Computationally this collapse has been investigated by discrete-element modelling (DEM) simulations; in 2D by Staron and Hinch [4] and Zenit [5], and in 3D by Cleary and Frank [6]. Knowing that scalings achieved for the 2D collapse [9–11] display variations from its axisymmetric counterpart, comparison is best drawn from the 3D case. Cleary and Frank demonstrate that particle shape is a limiting factor in reproducing experimental results and achieve values obtained by both Lube et al. [1] and Lajeunesse et al. [2] for their singular test case. Non spherical particle models, particularly in 3D, consume a much larger amount of computational power and reasons why this investigation has not been taken further.

Several previous authors [1–3] have investigated the collapse of an axisymmetric column and have concluded several simple scaling laws based on the initial aspect ratio of the granular column. Lube et al. [1] used a vernier scale and laser pointer technique with a stated accuracy of ± 0.1 mm to dimensionalise the final column, where as Lajeunesse et al. [2] used a camera imaging technique with a spatial resolution of 0.4 mm. In this study a different experimental technique is applied where a 3D laser scanner with a substantially higher accuracy of ± 0.04 mm is employed for data acquisition with the added benefit of digitizing the result for analysis and further interrogation. Experiments performed using this technique with similar initial system sizes to those of previous authors have revealed a variation of previously proposed dimensional scalings with a dependence on this initial system size. The experimental method has also allowed investigation into the angular profile of the deposit and the rate at which the summit is consumed with an increase in aspect ratio.

2 Experimental setup

2.1 Apparatus

The apparatus was set up as in Fig. 1. A cylinder of radius r_0 was placed on a smooth perspex plane and partially filled with granular media of mass m_0 to a specified height h_0. The aspect ratio, $a = h_0/r_0$, was varied for a single cylinder radius r_0 by varying the mass of the particulate, m_0. A number of cylinder radii were used with a range of aspect ratios as outlined in Table 1. The experiments were performed in a randomised order to prevent systematic errors from affecting the final results.

In these experiments the granular media used was a limestone particulate with bulk density $\rho = 1.5\ \mathrm{g/cm^3}$ and a

Table 1 Range of aspect ratios a trialled for each cylinder of radius r_0 and associated r_0/d value

r_0 (mm)	r_0/d	a range
20	28	0.24–8.69
25	35	0.30–7.00
30	42	0.20–6.05
35	50	0.24–5.29
40	57	0.25–4.40
45	64	0.24–4.02
75	107	0.28–1.69

dynamic angle of repose of $\theta_r \approx 30°$. The angle of repose is the maximal angle to the horizontal sustained by a pile of granular material before the slope face begins to slide. This value was given by the manufacturer and was confirmed experimentally by slowly funneling the particulate onto a horizontal surface and finding the greatest slope of the resulting deposit.

To ensure repeatable initial conditions grains were sieved prior to filling to select grains of diameter $d = 0.6 - 0.8$ mm, which were then funneled into the cylinder and the top gently flattened. This results in a non-dimensional system size parameter defined as r_0/d. The mean packing density of the material in the cylinder is calculated $\phi = m_0/(\rho\pi r_0^2 h_0)$, and found to be 0.78–0.82.

The cylinder was connected to rope over a series of pulleys that was mounted above the table. The cylinder was removed quickly by pulling on the rope at a speed greater than the speed of collapse to ensure minimal interference with the collapse itself. An average speed of 1.8 ms^{-1} was found to be sufficient. After release, the material spreads across the table resulting in a final deposit.

A 3D scanner was then used to digitize the resulting deposit enabling precise dimensionalisation of the pile by use of the analysis software '*Geomagic Qualify*' (3D Digital 2002; Geomagic, Research Triangle Park, NC, USA). This enabled non-contact measurement with high accuracy and a greater amount of interrogation in comparison to previous studies.

2.2 Data capture and scanner calibration

The 3D laser scanner used in this study was the '*Nikon Metrology MCA 2400 M7*' articulated arm enabling complete detailed geometric scans of the sand piles. The scanner head produced a laser stripe that was made to traverse the deposit, capturing data points viewable in real time providing immediate feedback on the scanning pace, progress and scanned area. The scanner was able to scan areas as large as 470 mm × 470 mm which was a limitation in terms of allowable aspect ratio ranges shown in Table 1.

A typical scan path consisted of 1,000 measurement points per stripe. To maintain a consistent number of measurement points per scan path and reduce the level of data noise it is critical to sustain the optimum distance between the scanning head and deposit. The scanner produced a laser guide with the stripe enabling the laser user to maintain this distance and obtain quality data. With this level of precision, the obtained point cloud contained 800–900 points per cm^2. When using the equipment to scan objects with defined edges, numerous scans can be easily amalgamated to produce the final object. The software was found to struggle performing this task with granular heaps due to the largely uneven surface and so all scans were completed in a single motion of the articulated arm.

The laser intensity also has an impact on the quality of data achieved, and this is managed by the equipment itself to include adjustments according to lighting conditions. Once the system is fully calibrated the lighting levels were maintained and temperature controlled at ±5 °C relative to the temperature when calibrated. Single point and length accuracy of the scanner is 31 microns and 42 microns $\pm 2\sigma$ respectively. These values were determined by point repeatability and volumetric accuracy tests as outlined in the industrial standard ASME B89.4.22 [23,24].

2.3 Processing and accuracy

The point cloud generated was interpreted as a surface mesh as in Fig. 2 using '*Geomagic Qualify*'; industrial standard software used for the inspection of scanned objects and materials. On occasion particles can be ejected a measurable distance further from the edge of the resultant pile. These were easily identifiable and removed from the final mesh for evaluation.

The global coordinate system of the mesh was altered so the table that the deposit rested on aligned with the x-y plane. Four 2D cross sections were taken of the resultant mesh through the centre of the pile. The ability to take several 2D cross sections of the final deposit allowed evaluation of the initial setup and cylinder removal. The cross sections made it easy to find where the cylinder had not been raised vertically as the resultant pile would be asymmetric, so adjustments could be made to the equipment in trials before the main experiments were run.

The achieved cross sections were then used to retrieve several dimensions of the final deposit indicated in Fig. 1; the final pile radius, r_f, the final pile height, h_f, the summital angle, α_s, the angle at the base, α_b, and in the case of a truncated cone, r_s, the summit radius. In the case of all these measurements with the exception of the final pile height, an average was taken across all four 2D cross sections where there is known to be variability due to an uneven periphery.

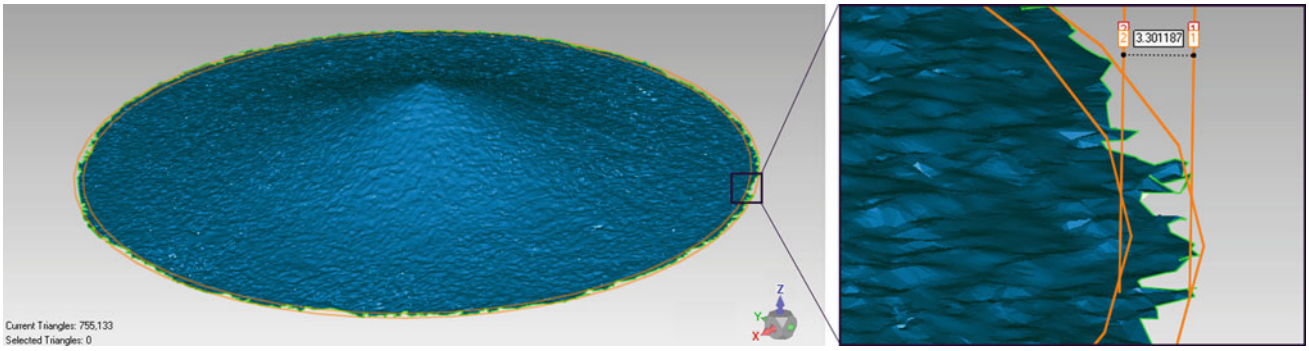

Fig. 2 Example surface mesh for $r_0 = 45$ mm $a = 1.87$ produced from point cloud achieved with laser scanning of the resultant deposit. Boundary effect demonstrated by two orange periphery lines formed from the inner most and outer most points. The distance between these boundaries is 3.30 mm, approximately $4.7d$

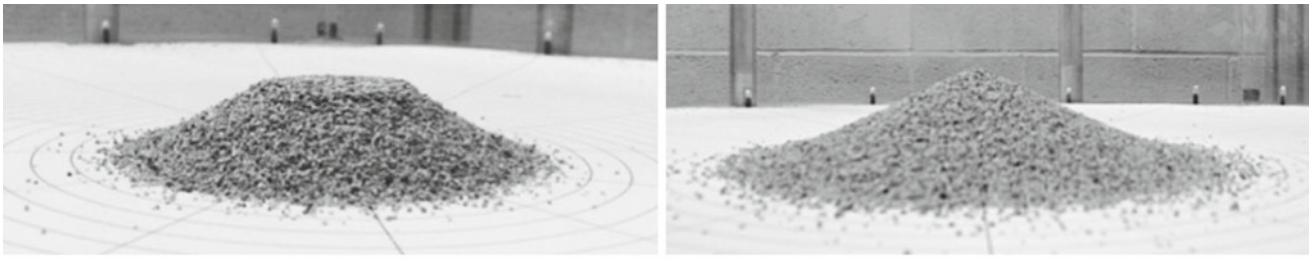

Fig. 3 Two distinct morphologies arise dependent upon aspect ratio a. **a** Truncated cone when $a < 0.90$. **b** Sloping conical shape when $a > 0.90$

Repeatability testing was performed on several initial aspect ratios and cylinder sizes to determine the maximal variation in dimensional quantities. The largest source of error within a single collapse can be observed at the periphery of the pile where grains do not fall into a clearly defined edge. Figure 2 highlights the smallest and largest possible boundaries in a particular example while displaying the deviation from the possible edges. Across varying aspect ratios this was observed to be $3d$ (± 1.1 mm) where $a < 0.50$ up to $5d$ (± 1.8 mm) for $a > 2$, confirmed by inspection of the resultant scans. Averaging across the four 2D cross sections in this way finds the mean periphery profile of the deposit. Results from the repeatability testing and accounting for the error due to the uneven rim of the deposit, dimensional quantities were found to vary as $r_f = \pm 1.6 - 2.3$ mm (aspect ratio dependent), $r_s = \pm 2.0$ mm, $h_f = \pm 0.5$ mm, and angular quantities $\pm 1°$. The material was measured to within ± 0.1 g, allowing only a variability in packing.

3 Experimental observations

3.1 Flow description and morphology

Qualitative descriptions of the collapse have been previously studied by other authors [1,2]. For $a \lesssim 3$ the periphery of the column crumbles vertically downwards resulting in a frontal flow to develop at the foot of the column that propagates radially outwards. Subsequently collapsing layers flow over the surface of the deposit continuing the flow in the radial direction. This results in a secondary front which separates the frontal flow and the currently static summittal region, which propagates inwards. This results in a circular discontinuity between the two regions, which is eventually consumed by the avalanche and the flow continues until stability is achieved in the summital region of the deposit.

In this range two distinct morphological deposits that can be seen in Fig. 3. For shallow columns where $a < 0.90$ the summit is never completely consumed by the avalanche and results in a truncated cone. Upon exceeding this aspect ratio the summit is entirely consumed and a full conical shape is left. Previous authors have found this critical aspect ratio to be $a = 0.74$ [1,2]. Without direct inspection with a 3D scanner, it can be difficult to determine where one geometric regime ends and the second begins as a summit may still exist but is small. It is for these reasons that a higher value is expected to be achieved, although this maybe compounded with the difference in granular material.

With the non-intrusive accurate measurement capabilities the rate of consumption of the summital plateau was also observed. The variation of the summit radius, r_s, with aspect ratio is shown in Fig. 4 where r_s is normalised against the initial radius as

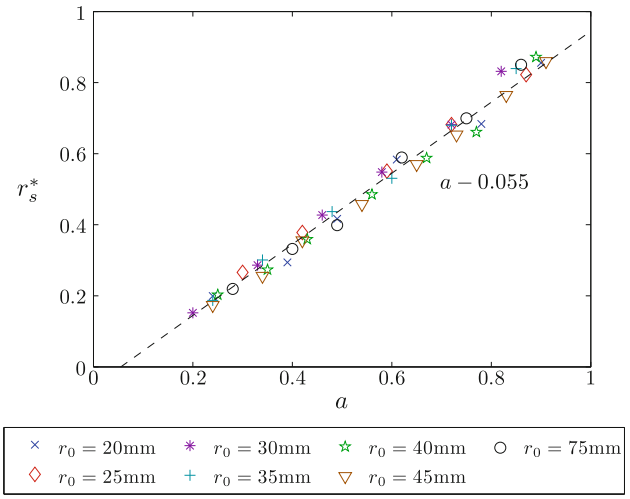

Fig. 4 Variation of normalised summital radius $r_s^* = (r_0 - r_s)/r_0$ against aspect ratio. *Dashed line* indicates linear fit given in Eq. (2)

$$r_s^* = \frac{r_0 - r_s}{r_0} \tag{1}$$

This shows a common linear relation across all cylinder sizes given by

$$r_s^* = a - 0.055 \tag{2}$$

valid for $a < 0.90$. Where $a > 0.90$ there is a sharp deceleration in the shrinking of the plateau with increasing aspect ratio as the peak becomes curved and the summital plateau becomes indistinguishable as it is of the order of a few grain sizes.

The direct proportionality observed is expected with consideration of geometric arguments. Under the first regime, the collapse results in a truncated cone. Hence

$$r_s = r_0 - h_0 \tan\bar{\theta} \tag{3}$$

for some mean angular profile of the slope of the deposit $\bar{\theta}$. Some rearrangement gives

$$r_s^* = a \tan\bar{\theta} \tag{4}$$

in agreement with the obtained data.

Where $a \gtrsim 3$ the collapse dynamic changes from that previously observed. In this case the whole upper surface of the column moves, initially retaining its horizontal profile. A frontal flow then develops at the base on the pile as before spreading radially outwards. Part way through the collapse the upper surface begins to dome while the frontal flow continues to spread. The end result is a deposit with a shallower angular profile than lower aspect ratios.

The evolution of the profile with increasing aspect ratio can be seen in Fig. 5a for $r_0 = 35$ mm. The height, $h(r)$ is given as a function of radius, r, and both values are normalised against r_0. It is evident that the angular profile not only becomes shallower with increasing a, but the nose of the deposit becomes less sharp and displays an increase in curvature. The relationship between defining dimensional values and aspect ratio are discussed in detail below to include the final deposit radius, r_f, final height, h_f, and angles at the summit, α_s, and base, α_b. This has previously been investigated by Lube et al. [1] and Lajeunesse et al. [2] but a further dependence has emerged; a dependence on the initial system size r_0/d.

Similar system sizes were used as in previous experimental works, but notable differences in the defining dimensional values were found and are presented in this study. An example of resultant deposit profiles for $a = 1.7$ is given in Fig. 5b for several cylinder sizes. In this particular case the final height and angle at the summit is largely the same. The difference occurs at the nose of the deposit where larger system sizes result in a greater final deposit radius and a shallower angle

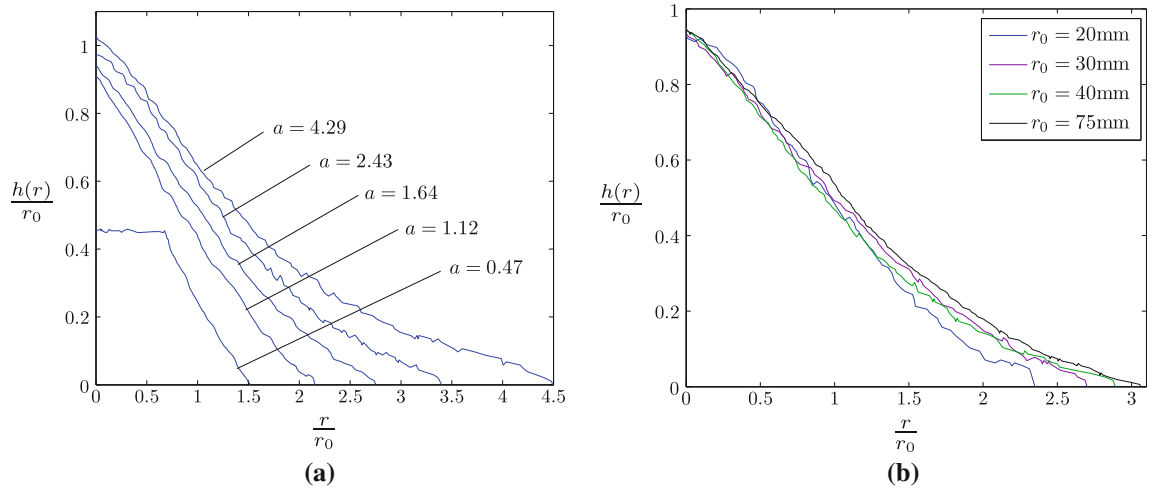

Fig. 5 Deposit profiles normalised against the cylinder radius r_0. **a** Evolution of the profile with increasing aspect ratio a for $r_0 = 35$ mm. **b** Difference in profiles for $a = 1.70$

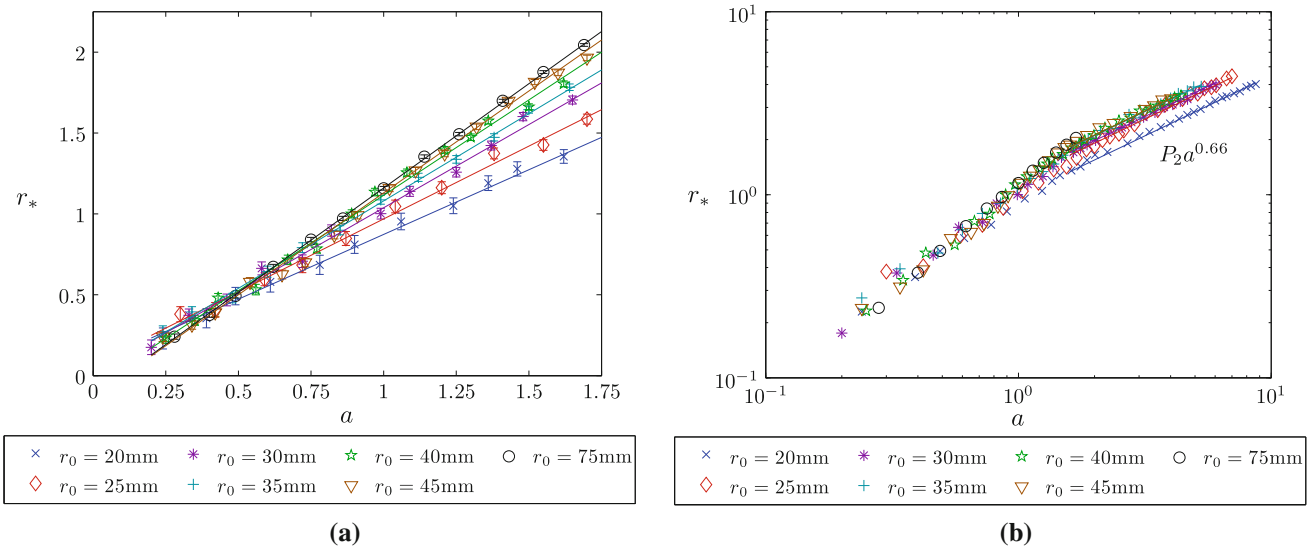

Fig. 6 Relationship between r_* and a for varying cylinder radii r_0 with coefficients given in Table 2. **a** $a < 1.7$ with errors displayed as discussed in Sect. 2.3. Linear fits for each r_0 satisfying Eq. (6) are shown. **b** $a \gtrsim 1.7$ following a power law relation as indicated by line fit

at the base. The impact of r_0/d is considered for each of the dimensional quantities and frequently displays an arresting value of this effect. Meso-scale interactions are known to occur across granular systems but in this case it has been previously overlooked.

3.2 Final pile radius

Previous results [1–3] suggested that the final deposit radius is independent of the initial system size. Final pile radius, r_f, against aspect ratio was considered for each cylinder radius, with r_f normalised against r_0 as

$$r_* = \frac{r_f - r_0}{r_0} \tag{5}$$

3.2.1 Low aspect ratios

First consider where $a < 1.7$ as shown in Fig. 6. A linear relation of the form

$$r_* = P_1 a + Q \tag{6}$$

where P_1 and Q are constants is observed, but there is a clear dependence of these coefficients on the initial cylinder size and inherently the system size. The gradient P_1 for each cylinder radii is given in Table 2. It evidently increases with cylinder radii although it indicates strong signs of arresting. For $r_0 = 20 - 45$ mm it follows a strongly linear relation given by:

$$P_1 = 0.013\frac{r_0}{d} + 0.45 \tag{7}$$

Table 2 Variation in proportional constants P_1 and P_2 for relationship between r_* and a given by Eqs. (6) and (9) and respectively

r_0 (mm)	r_0/d	P_1	P_2
20	28	0.79	1.00
25	35	0.88	1.21
30	42	1.02	1.25
35	50	1.06	1.33
40	57	1.18	1.34
45	64	1.26	1.34
75	107	1.29	–

and substituting this into Eq. 6 gives

$$r_* = 0.013\frac{h_0}{d} + 0.45a + Q \tag{8}$$

This reveals a secondary dependence on initial height h_0 while the system size $r_0/d \lesssim 70$. The increase in P_1 severly slows for the largest cylinder size and while limitations of the equipment prevent investigation of larger values of r_0/d, it is presupposed that this deceleration continues in strength with increases in P_1 being negligible. This disputes previous research by other authors [1–3] who conclude there is no such effect while investigating comparable values of r_0/d, although it is worth noting that the gradient for $r_0 = 75$ mm, $P_1 = 1.29$, is close to the value of 1.24 achieved by Lube et al. With previous experiments subject to greater inaccuracies in their measurement methods, differences in achieved data have previously been assumed to be due to experimental error. The high spatial resolution in the presented results and strong variation in P_1 indicates the existence of this dependence to be correct. Reasoning for this

difference in scaling can be given insight by consideration of the degree of mass flow and process of jamming and flowing layers as described by Cates et al. [13].

Consider a fixed aspect ratio $a = h_0/r_0$ for two different initial column radii r_0 with $r_0/d < 70$. The larger r_0 will initially contain more granular matter and so at the start of the avalanche, the larger r_0/d will have a greater initial deposit on the surface. The larger initial deposit has a greater amount of jammed grains under a larger amount of pressure and hence a longer granular force chain length. In both cases the subsequently avalanching layers will disturb the force chain but a smaller proportion of the force chain will be disturbed in the case of the larger deposit due to the stronger jamming effect and the grains being under a greater amount of pressure. This results in a smaller proportion of the flowing layer being entrained in the disturbed surface and hence a smaller proportional energy loss in the flowing layer. This allows for greater movement of the avalanching layer and overall a greater runout. Where we observe a saturation of the meso-scale effect and considering two different values of r_0/d, the proportion of the force chain that will be disturbed in the collapse will be small and comparable to other larger values of r_0/d. For this reason it is reasonable to expect to observe the arresting effect seen in the proportional constant P_1 of the final pile radius relation.

3.2.2 Larger aspect ratios

When $a \gtrsim 1.7$ a new relation begins to emerge with a good fit to a the power law

$$r_* = P_2 a^{0.66} \tag{9}$$

where P_2 varies for r_0/d as given in Table 2. Compared to the relation given in Eq. (6) this constant appears to arrest earlier having stagnated when $r_0 = 35$ mm, $r_0/d = 50$. The difference in P_2 can be attributed to the earlier discussion on jamming with its quicker cessation likely to be due to the greater amount of material involved in the collapse. The data is in agreement with Lube et al. in terms of the onset of Eq. (9), but the power 0.66 is higher than both Lube et al. and Lajeunesse et al. who agree with a square root fit. The variation in the precise value of the power could be due to different granular materials used to the other authors, but again they negate the effect of r_0/d as the data clearly shows.

3.3 Final height

The final height was normalised as $h_* = h_f/r_0$ and compared against a in Fig. 7. In the first geometric regime where $a < 0.90$ the deposit is a truncated cone and so $h_f = h_0$. This suggests that there is an internal conical surface over which the avalanche occurs, with the angle at the base of this internal cone to be $\theta = \tan^{-1}(0.90) = 42.0°$. This observation was concluded by Lajeunesse et al. [2] where layers of coloured sand were used in the prepared column and the resultant deposit was split to reveal a conical zone where there had been no movement of material.

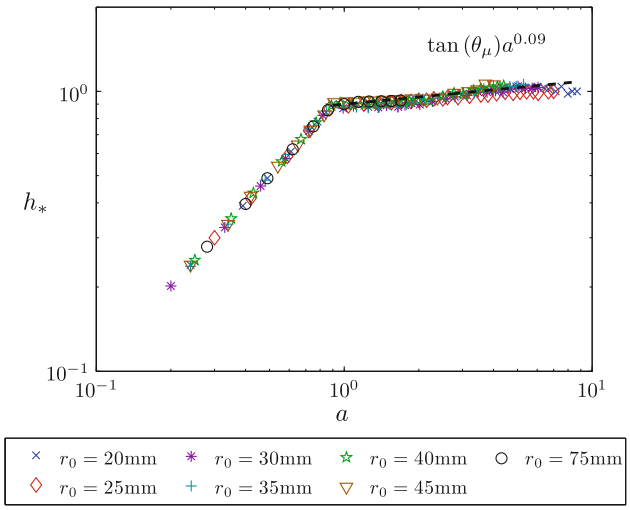

Fig. 7 Evolution of normalised height h_* with aspect ratio a. *Dashed line* indicates power law relation given by Eq. (10)

When entering the second geometric regime, the particulate above a height $0.90r_0$ avalanches over the currently deposited matter and the height minutely continues to increase. It argued that this increase is marginally smaller for $r_0 = 20$, 25 mm with exponents of 0.05 and 0.07 respectively, while for all other cylinder radii the relation

$$h_* = 0.90a^{0.09} \tag{10}$$

holds. In this case the meso-scale effect is observed for $r_0/d \lesssim 40$, likely to be arresting faster than the radial coefficient P_1 due to the greater amount of material as presupposed for the radial coefficient P_2. Lajeunesse et al. suggest that there is no increase in height while Lube et al. agree that there is, although proposing a higher exponent of 0.17.

Mohr-Coulomb theory states that the development of surface failure is due to the inability to sustain its composition under shear stresses and occurs along an envelope projected at an angle equal to the internal friction angle θ_μ. The data provided for the limestone based particulate used indicated an internal friction angle $\theta_\mu \approx 39°$. This would imply that the onset of the second geometic regime would occur at an aspect ratio of $a = 0.89$ which is in good agreement with the experimental data. This allows description of the height with known material parameters:

$$\begin{aligned} h_* &= a & a &< \tan\theta_\mu \\ h_* &= \tan(\theta_\mu)a^{0.09} & a &> \tan\theta_\mu \end{aligned} \tag{11}$$

where 0.09 is exchanged for a lower value for the smallest r_0/d. Obtaining scalings where constants are completely

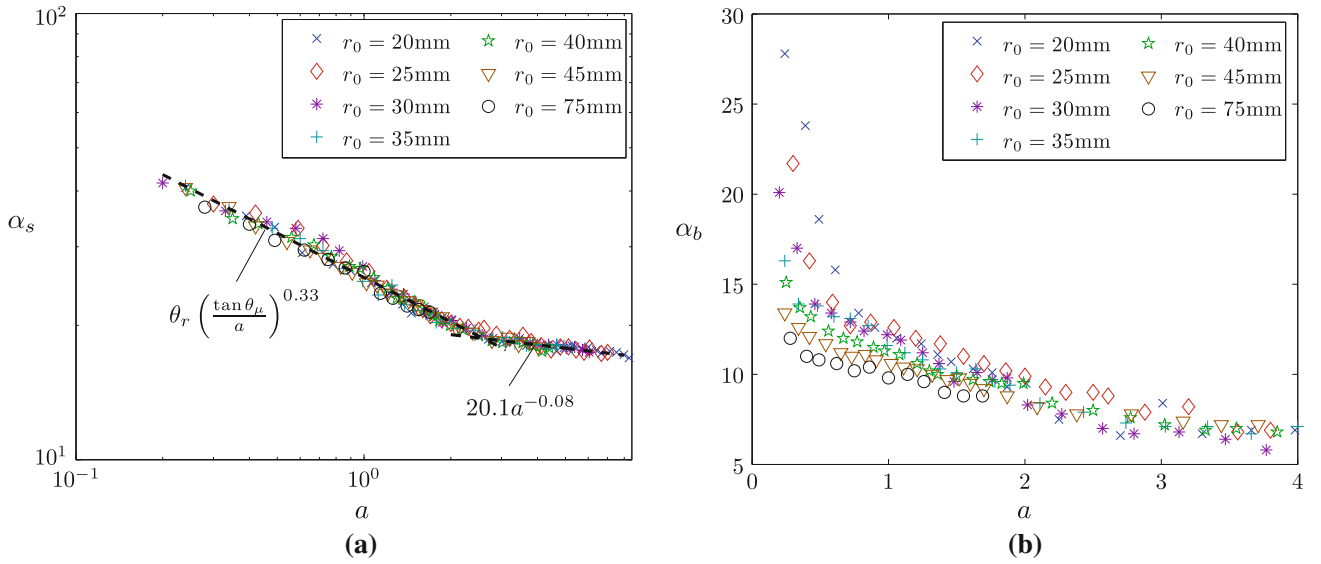

Fig. 8 Variation in angle against aspect ratio for **a** summital angle, **b** base angle

described by the material parameters is desirable for equivalence in other experimental setups with different granular materials. This is an encouraging step to a fuller description of the final deposit independent of seemingly arbitrary proportional constants.

3.4 Angular profiling

The surface of the deposit does not have a straight edge as a cone does, but it curved to some angular profile. Two characteristic angles of the profile are the angle at the summit, α_s, and the angle at the base, α_b. These values were obtained from the 3D meshes generated, so the method was not intrusive or destructive of the deposit. Where the first geometric regime exists and there is a flat summit, α_s was taken to be the angle of the slope directly below the flat surface.

For $a \lesssim 3$ the summital angle was found to vary with aspect ratio as in Fig. 8a, following a power relation:

$$\alpha_s = 25.6a^{-0.33} \tag{12}$$

While the aspect ratio is such that the resulting deposit is a truncated cone, the avalanching periphery is strongly dependent upon the internal friction angle rather than the angle of repose as discussed in Sect. 3.3 and so $\alpha_s > \theta_r$. The onset of the second geometric regime where the entirety of the summit is consumed corresponds to the aspect ratio where material exists above the conical failure envelope defined by the internal friction angle. At aspect ratios greater than this critical onset, the greatest sustainable angle of a deposit with a sharp peak is exactly the angle of repose by definition. Hence where this occurs $\alpha_s < \theta_r$. The continued decrease in the summital angle is due to increased avalanching over already deposited layers smoothing the steep sides.

Using the angular analysis of the onset of the second geometric regime and assuming the summital angle to be a function of aspect ratio, $\alpha_s(a)$, we have the condition

$$\alpha_s(\tan\theta_\mu) = \theta_r \tag{13}$$

Applying this condition to Eq. (12) the coefficient can be expressed in terms of the internal parameters:

$$\alpha_s = \theta_r \left(\frac{\tan\theta_\mu}{a}\right)^{0.33} \tag{14}$$

Enabled by the previous analysis via interpretation of Mohr–Coulomb theory, this is the second scaling with constants given in terms of known material parameters.

When $a \gtrsim 3$ a different relationship emerges coinciding with the change in collapse regime where the entire upper surface of the initial column falls retaining its horizontal profile. The angle at the summit continues to decrease but at a severely slower rate following the power law

$$\alpha_s = 20.1a^{-0.08} \tag{15}$$

The variation in the angle at the base with aspect ratio was found to be more complex and dependent upon the r_0 and hence the initial system size as shown in Fig. 8b. While $a \lesssim 3$ this follows a power law relation of the form

$$\alpha_b = Ea^{-F} \tag{16}$$

where E and F are constants dependent on r_0/d as given in Table 3. The dependence on r_0/d is initially linear up to $r_0 = 45$ mm, giving relations

$$E = 14.7 - 0.066\frac{r_0}{d} \tag{17}$$

$$F = 0.010\frac{r_0}{d} - 0.78 \tag{18}$$

Table 3 Constants fitting power law relation $\alpha_b = Ea^{-F}$ for given initial cylinder size

r_0 (mm)	r_0/d	E	F
20	28	12.94	0.52
25	35	12.33	0.45
30	42	11.69	0.32
35	50	11.42	0.25
40	57	10.98	0.23
45	64	10.53	0.17
75	107	9.76	0.16

For $r_0 = 75$ mm the F exponent evidently stagnates and it can be assumed that for $r_0/d > 100$ $F = 0.16$. With an error of $\pm 1°$ it is presupposed that $E \approx 10$ for $r_0/d > 100$. For $a \gtrsim 3$, α_b stagnates with $6° < \alpha_b < 8°$.

For a fixed aspect ratio, smaller system sizes have a distinctly higher base angle at least in the first geometric regime. This would be expected given a proportionally smaller radius of the deposit and equivalently low r_0/d as described in Sect. 3.2. After the end of the first geometric regime the variation in angle between cylinder sizes becomes small and approaches the stagnation point. Within this range, avalanching of the upper surface of the column flows over the already deposited layers that stretch beyond 0.75 cylinder radii and are of similar thickness at the extremity. $\alpha_b < \theta_r$ for all aspect ratios as expected or further avalanching would occur as per the definition of the angle of repose.

4 Conclusions

The methodology used in the experiments have allowed a substantially greater degree of accuracy than any previous research on the subject. Coupled with mesh generation of the deposits and the ability to obtain data non-intrusively, a deeper dependence on the scaling of granular collapse has been revealed. It was previously thought that in the absence of internal parameters, scalings of the collapse were uniquely describable in terms of the aspect ratio of the initial granular column. Given similar initial conditions to the previous studies, this analysis has shown that differences in data that were originally explained as experimental error are a demonstration of system size dependence calculated as r_0/d. While this dependence exists, it has demonstrated a saturation at the larger r_0/d with this particular point dependent on the scaling under consideration. Furthermore some relations are expressible in terms of internal parameters, desirable of all scalings for a full theoretical model of the collapse to exist.

It is well known that the final deposit radius has a linear dependence on aspect ratio, but results showed that the coefficient of this proportionality increased, at least initially, with the system size. For values $r_0/d \lesssim 70$ this proportionality was also linear, showing signs of abruptly saturating for $r_0/d = 107$. This behavior is mirrored in the angle at the base of the deposit; larger initial system sizes have a shallower base angle. Together these results support the idea that the initially deposited layers have an effect on the scalings of the resultant pile, with their deposition dependent upon the amount of initial mass collapse and the resultant jamming. For a fixed aspect ratio, a greater initial radius means a thicker initial deposit. The thicker deposit experiences greater jamming, and hence results in greater spreading of subsequently avalanching material and a shallower angle at the base of the resultant pile.

In the first geometric regime a summital plateau exists that shrinks with increasing aspect ratio. The continued contraction was directly proportional to aspect ratio, but had no relation to system size or rate of increase of the final pile radius. Within this first geometric regime the final height is exactly the initial height, but where $a > \tan\theta_\mu$ the increase in height significantly slows of the order $a^{0.09}$. It is argued that the height increases even slower in the smaller systems with $r_0/d = 28, 35$. The angle at the summit follows a power law relation with aspect ratio, independent of system size, and coupled with other analysis is shown to depend on the angle of repose and internal friction while $a \lesssim 1.7$.

In summary, dimensions r_f and α_b that result directly from material deposition depends strongly upon the initial system size r_0/d in addition to the aspect ratio and material parameters. Dimensions r_s, h_f and α_s which result from material loss to avalanching and not the history of the collapse have little or no secondary dependence and are subject only to aspect ratio and material parameters. This further fuels the necessity for any theoretical model of the collapse to incorporate internal dynamics such as those described by Cates et al. [13], particularly where investigations could contain a meso-scale effect.

Acknowledgments This research was funded by an EPSRC doctoral-training grant to whom we offer our gratitude.

References

1. Lube, G., Huppert, H.E., Sparks, R.S.J., Hallworth, M.A.: Axisymmetric collapses of granular columns. J. Fluid Mech. **508**, 175–199 (2004)
2. Lajeunesse, E., Mangeney-Castelnau, A., Vilotte, J.P.: Spreading of a granular mass on a horizontal plane. Phys. Fluids **16**, 2371–2381 (2004)
3. Thompson, E.L., Huppert, H.E.: Granular column collapses: further experimental results. J. Fluid. Mech **575**, 177–186 (2007)
4. Staron, L., Hinch, E.J.: Study of the collapse of granular columns using two-dimensional discrete-grain simulation. J. Fluid Mech. **545**, 1–27 (2005)
5. Zenit, R.: Computer simulations of the collapse of a granular column. Phys. Fluids **17**, 031703 (2005)

6. Cleary, P.W., Frank, M.: Three-dimensional discrete element simulations of axi-symmetric collapses of granular columns. Technical Report 44710, Technische Universitat Kaiserslautern (2006)
7. Lacaze, L., Phillips, J.C., Kersewell, R.R.: Planar collapse of a granular column: experiments and discrete element simulations. Phys. Fluids **82**, 063302 (2008)
8. Tapia-McClung, H., Zenit, R.: Computer simulations of the collapse of columns formed by elongated grains. Phys. Rev. E **85**, 061304
9. Lube, G., Huppert, H.E., Sparks, R.S.J., Freundt, A.: Collapses of two-dimensional granular columns. Phys. Rev. E **72**, 041301 (2005)
10. Balmforth, N.J., Kerswell, R.R.: Granular collapse in two dimensions. J. Fluid Mech. **538**, 399–438 (2005)
11. Siavoshi, S., Kudrolli, A.: Failure of a granular step. Phys. Rev. E **71**, 051302 (2005)
12. Mangeney, A., Heinrich, P., Roche, R., Boudon, G., and Chemine, J.L.: Modeling of debris avalanche and generated water waves: application to real and potential events in montserrat. Phys. Chem. Earth **25**, 741–745 (2000)
13. Cates, M.E., Wittmer, J.P., Bouchad, J.P., Claudin, P.: Jamming, force chains and fragile matter. Phys. Rev. Lett. **81**, 1841–1844 (1998)
14. Savage, S.B., Hutter, K.: The motion of a finite mass of granular material down a rough incline. J. Fluid. Mech. **199**, 177–215 (1989)
15. Kadanoff, L.P.: Built upon sand: theoretical ideas inspired by granular flows. Rev. Mod. Phys. **71**, 435–443 (1999)
16. Douady, S., Andreotti, B., Daerr, A.: On granular surface flow equations. Eur. Phys. J. B Cond. Matter **11**, 131–142 (1999)
17. Hadeler, K.P., Kuttler, C.: Dynamic models for granular matter. Granul. Matter **2**, 9–18 (1999)
18. Pouliquen, O., Forterre, Y.: Friction law for dense granular flows: application to the motion of a mass down a rough inclined plane. J. Fluid Mech. **453**, 133–151 (2002)
19. Larrieu, E., Staron, L., Hinch, E.J.: Raining into shallow water as a description of the collapse of a column of grains. J. Fluid. Mech. **554**, 259–270 (2006)
20. Doyle, E.E., Huppert, H.E., Lube, G., Made, H.M., and Sparkes, R.S.J.: Static and flowing regions in granular collapses down channels: Insight from a sedimenting shallow water model. Phys. Fluids **19**, 106601 (2007)
21. Crosta, G.B., Imposimato, S., Roddeman, D.: Numerical modelling of 2-d granular step collapse on erodible and nonerodible surface. J. Geophys. Res. **114**, 03020 (2009)
22. Lagreé, P.-Y., Staron, L., Popinet, S.: The granular column collapse as a continuum: validity of a two-dimensional Navier-Stokes model with a mu(I)-rheology. J. Fluid Mech. **686**, 378–408 (2011)
23. ASME.: American Society of Mechanical Engineers: B89.4.22-2004 Methods for performance evaluation of articulated arm coordinate measuring machines (2004)
24. Kiraci, E., Attridge, A., Williams, M.A.: The use of laser scanning technology to improve the design process. App. Mech. Mat. **110**, 4118–4122 (2012)

Bibliography

R. Al-Raoush. Microstructure characterization of granular materials. *Physica A*, 377(2), 2007.

E. Andò, S. A. Hall, G. Viggiani, J. Desrues, and P. Bésulle. Experimental micromechanics: Grain-scale observation of sand deformation. *Geotech. Lett.*, 2:107–112, 2012.

E. Andò, G. Viggiani, S. A. Hall, and J. Desrues. Experimental micro-mechanics of granular media studied by X-ray tomography: Recent results and challenges. *Geotech. Lett.*, 3:142–146, 2013.

ASME. *American Society of Mechanical Engineers: B89.4.22-2004 Methods for performance evaluation of articulated arm coordinate measuring machines.* 2004.

R. A. Bagnold. The shearing and dilation of dry sand and the 'singing' mechanism. *Proc. Roy. Soc. A*, 295:219–232, 1954.

N. J. Balmforth and R. R. Kerswell. Granular collapse in two dimensions. *J. Fluid Mech.*, 538, 2005.

S. Yu. Borovikov, L. A. Tarasova, and O. A. Troshkin. Movement of a granular material on a rotating disk in a bunker-spreader system. *Chem. Petrol. Eng.*, 38: 124–127, 2002.

J. F. Bruchon, J. M. Pereira, M. Vandamme, N. Lenoir, P. Delage, and M. Bornert. Full 3D investigation and characterisation of capillary collapse of a loose unsaturated sand using X-ray CT. *Granular Matter*, 15(6), 2013.

S. Carmignato. Accuracy of industrial computed tomography measurements: Experimental results from an international comparison. *CIRP Ann. Man. Tech.*, 61: 491–494, 2012.

S. Carmignato, D. Dreossi, L. Mancini, F. Marinello, G. Tromba, and E. Savio. Testing of X-ray microtomography systems using a traceable geometrical standard. *Meas. Sci. Tech.*, 20:084021, 2009.

M. E. Cates, J. P. Wittmer, J. P. Bouchad, and P. Claudin. Jamming, force chains and fragile matter. *Phys. Rev. Lett.*, 81:1841–1844, 1998.

R. Caulkin, X. Jia, C. Xu, M. Fairweather, R. A. Williams, H. Stitt, and P. Marchot. Simulations of structures in packed columns and validation by X-ray tomography. *Ind. Eng. Chem. Res*, 48(1), 2008.

P. W. Cleary and M Frank. Three-dimensional discrete element simulations of axi-symmetric collapses of granular columns. Technical Report 44710, Technische Universitat Kaiserslautern, 2006.

P. W. Cleary and M. L. Sawley. Discrete-element modelling and smooth particle hydrodynamics: Potential in the environmental sciences. *Phil. Trans. R. Soc. Lond. A*, 362:2003–2030, 2004.

D. C. Copley, J. W. Eberhard, and G. A. Mohr. Computed tomography part I: Introduction and industrial applications. *JOM*, 46:14–26, 1994.

P. A. Cundall and O. D. L. Strack. A discrete numerical model for granular assemblies. *Geotechnique*, 29:47, 1979a.

P. A. Cundall and O. D. L. Strack. A discrete numerical model for granular assemblies. *Geotechnique*, 29:47–65, 1979b.

F. da Cruz. Écoulements de grains secs: Frottement et blocagè (flows of dry grains: Friction and locking. *Thèse de l'Ecole Nationale des Ponts et Chaussees*, page http://pastel.paristech.org/archive/946, 2004.

A. Daerr and S. Douady. Sensitivity of granular surface flows to preparation. *Euro. Phys. Lett.*, 47:324–330, 1999.

DailyMail. The largest North American landslide ever that dropped 165 million tons more than half a mile down at copper mine in Utah. `http://www.dailymail.co.uk/news/article-2334139/`. Accessed June 3, 2013.

F. V. Donze, V. Richefeu, and S. A. Magnier. Advances in discrete element method applied to soil, rock and concrete mechanics. *E. J. Geotech. Eng.*, 44, 2009.

S. Douady, B. Andreotti, and A. Daerr. On granular surface flow equations. *Euro. Phys. J. B - Cond. Matter*, 11:131–142, 1999.

E. E. Doyle, H. E. Huppert, and G. Lube. Static and flowing regions in granular collapses down channels: Insights from a sedimenting shallow water model. *Phys. Fluids*, 19, 2007.

A. Dziugys and B. Peters. An approach to simulate the motion of spherical and non-spherical fuel particles in combustion chambers. *Granular Matter*, 3:231–265, 2001.

L. A. Feldkamp, L. C. Davis, and J. W. Kress. Practical cone-beam algorithm. *JOSA A*, 1:612–618, 1984.

J-F. Ferellec and G. R. McDowell. A method to model realistic particle shape and inertia in DEM. *Granular Matter*, 12:459–467, 2010.

F. Forsberg and C. R. Siviour. 3D deformation and strain analysis in compacted sugar using X-ray microtomography and digital volume correlation. *Meas. Sci. Tech*, 20(9), 2009.

Y. Forterre and O. Pouliquen. Flows of dense granular media. *Annu. Rev. Fluid Mech.*, 40:1–24, 2008.

X. Fu, M. Dutt, A. C. Bentham, B. C. Hancock, R. E. Cameron, and J. A. Elliott. Investigation of particle packing in model pharmaceutical powders using X-ray microtomography and discrete element method. *Powder tech.*, 167(3), 2006.

G.D.R-Midi. On dense granular flows. *Eur. Phys. J. E.*, 341, 2004.

I. Goldhirsch and G. Zanetti. Clustering instability in dissipative gases. *Phys. Rev. Lett.*, 70:1619, 1993.

I. Goldhirsch, M.-L. Tan, and G. Zanetti. A molecular dynamical study of gradular fluids I: The unforced granular gas in two dimensions. *J. Sci. Comp.*, 8:1–40, 1993.

C. Goniva, C. Kloss, A. Hagar, and S. Pirker. Models, algorithms and validation for opensource DEM and CFD-DEM. *Prog. Comp. Fluid Int. J.*, 12(2):140–152, 2012.

S. Hamel and W. Krumm. Near-wall porosity characteristics of fixed beds packed with wood chips. *Powder Tech.*, 188:55–63, 2008.

R. J. Hocken and P. H. Pereira. *Coordinate measuring machines and systems*. Taylor & Francis, 2012. ISBN 9781574446524.

H. E. Huppert, M. A. Hallworth, G. Lube, and R. S. J. Sparks. Granular column collapses. *Bull. Am. Phys. Soc.*, 48, 2003.

P. Jop, Y. Forterre, and O. Pouliquen. Crucial role of side walls for granular surface flows: Consequences for the rheology. *J. Fluid Mech.*, 541:167, 2005.

P. Jop, Y. Forterre, and O. Pouliquen. A constitutive law for dense granular flows. *Nature*, 441:727–730, 2006.

R. R. Kerswell. Dam break: A model for granular slumping. *Phys. Fluids*, 17, 2005.

R. A. Ketcham and W. D. Carlson. Acquisition, optimization and interpretation of X-ray computed tomographic imagery: applications to the geosciences. *Computers & Geosciences*, 27:381–400, 2001.

E. Kiraci, A. Attridge, and M . A. Williams. The use of laser scanning technology to improve the design process. *App. Mech. Mat.*, pages 110–116, 2012.

C. Kloss and C. Goniva. LIGGGHTs - a new open source DEM simulation software. *Proceedings of the 5th international conference on DEM*, 2010.

J. P. Kruth, M. Bartscher, S. Carmignato, R. Schmitt, L. De Chiffre, and A. Weckenmann. Computed tomography for dimensional metrology. *CIRP Ann. Man. Tech.*, 60:821–842, 2011.

J. Kumar, A-H. G. Abulrub, A. Attridge, and M. A. Williams. Effect of X-ray computed tomography scanning parameters on the estimated porosity of foam specimens. *International Conference MIMT 2011 proceedings*, 2011.

P-Y. Lagrée, L. Staron, and S. Popinet. Granular column collapse as a continuum: Validity of a two-dimensional Navier-Stokes model with a mu(i)-rheology. *J. Fluid Mech.*, 686:378–408, 2011.

E. Lajeunesse, A. Mangeney-Castelnau, and J. P. Vilotte. Spreading of a granular mass on a horizontal plane. *Phys. Fluids*, 16:2371–2381, 2004.

E. Lajeunesse, J. B. Monnier, and G. M. Homsy. Granular slumping on a horizontal surface. *Phys. Fluids*, 17, 2005.

E. Larrieu, L. Staron, and E. J. Hinch. Raining into shallow water as a description of the collapse of a column of grains. *J. Fluid Mech.*, 554:259, 2006.

P. Van Liedekerke, E. Tijskens, E. Dintwa, F. Rioual, J. Vangeyte, and H. Ramon. DEM simulations of the particle flow on a centrifugal disc spreader. *Powder Tech.*, 190:348–360, 2009.

J. J. Lifton, A. A. Malcolm, J. W. McBride, and K. J. Cross. The application of voxel size correction in X-ray computed tomography for dimensional metrology. *Singapore International NDT Conference*, 2013.

G. Lube, H. E. Huppert, R. S. J. Sparks, and M. A. Hallworth. Axisymmetric collapses of granular columns. *J. Fluid Mech.*, 508:175–199, 2004.

G. Lube, H. E. Huppert, R. S. J. Sparks, and A. Freundt. Collapses of two-dimensional granular columns. *Phys. Rev. E*, 72, 2005.

A. Mangeney, P. Heinrich, R. Roche, G. Boudon, and J. L. Chemine. Modeling of debris avalanche and generated water waves: Application to real and potential events in montserrat. *Phys. Chem. Earth*, 25, 2000.

A. Mangeney-Castelnau, J-P. Vilotte, M. O. Bristeau, B. Perthame, F. Bouchut, C. Simeoni, and S. Yerneni. Numerical modeling of avalanches based on Saint Venant equations using a kinetic scheme. *J. Geophys. Res.*, 108:2527, 2003.

A. Mangeney-Castelnau, F. Bouchut, J-P. Vilotte, E. Lajeunesse, A. Aubertin, and M. Pirulli. On the use of Saint Venant equations to simulate the spreading of a granular mass. *J. Geophys. Res.*, 110, 2005.

A. Mehta and G. C. Barker. The dynamics of sand. *Rep. Prog. Phys.*, 57:383, 1994.

J.-J. Moreau. Some numerical methods in multibody dynamics: Application to granular materials. *Eur. J. Mech. A*, 4:93–114, 1994.

R. D. Morrison and P. W. Cleary. Using DEM to model ore breakage within a pilot scale SAG mill. *Min. Eng.*, 17:1117–1124, 2004.

N. Otsu. A threshold selection method from gray-level histograms. *Automatica*, 11: 23–27, 1975.

O. Pouliquen and Y. Forterre. Friction law for dense granular flows: Application to the motion of a mass down a rough inclined plane. *J. Fluid Mech.*, 453:133–151, 2002.

PowerFarming. Vicon - superflow spreading system. `http://www.powerfarming.co.nz/`. Accessed June 3, 2013.

P. Richard, P. Philippe, F. Barbe, S. Bourlès, X. Thibault, and D. Bideau. Analysis by X-ray microtomography of a granular packing undergoing compaction. *Phys. Rev. E*, 68(2), 2003.

F. Rioual, E. Piron, and E. Tijskens. Rolling and sliding dynamics in centrifugal spreading. *App. Phys. Letters*, 90, 2007.

O. Roche, M. Attali, A. Mangeney, and A. Lucas. On the run-out distance of geophysical gravitational flows: Insight from fluidized granular collapse experiments. *Earth Plan. Sci. Lett.*, 311:375–385, 2011.

S. B. Savage and K. Hutter. The motion of a finite mass of granular material down a rough incline. *J. Fluid. Mech.*, 199:177–215, 1989.

S. B. Savage and K. Hutter. The dynamics of avalanches of granular material from initiation to runout. Part i: Analysis. *Acta Mechanica*, 86:201–223, 1991.

T. Shinbrot, N. H. Duong, M. Hettenbach, and L. Kwan. Coexisting static and flowing regions of a centrifuging granular heap. *Granular Matter*, 9:295–307, 2007.

S. Siavoshi and A. Kudrolli. Failure of a granular step. *Phys. Rev. E*, 71, 2005.

L. E. Silbert, D. Ertas, G. S. Grest, T. C. Halsey, D. Levine, and S. J. Plimpton. Granular flow down an inclined plane: Bagnold scaling and rheology. *Phys. Rev. E.*, 64:051302, 2001.

L. Staron and E. J. Hinch. Study of the collapse of granular columns using two-dimensional discrete-grain simulation. *J. Fluid Mech*, 545:1–27, 2005.

P. J. Thomas and F. Zoueshtiagh. Granular ripples under rotating flow: A new experimental technique for studying ripples in non rotating, geophysical applications? *Phil. Trans. Roy. Soc. A*, 363:1663–1676, 2005.

E. L. Thompson and H. E. Huppert. Granular column collapses: Further experimental results. *J. Fluid. Mech*, 575:177–186, 2007.

S. Torquato and Y. Jiao. Dense packings of the Platonic and Archimedean solids. *Nature*, 460:876–879, 2009.

J. M. Warnett, P. Denissenko, P. J. Thomas, E. Kiraci, and M. A. Williams. Scalings of axisymmetric column collapse. *Granular Matter*, 16(1):115–124, 2014a.

J. M. Warnett, P. Denissenko, P. J. Thomas, and M. A. Williams. Collapse of a granular column under rotation. *Powder Tech.*, 262:249–256, 2014b.

R. Zenit. Computer simulations of the collapse of a granular column. *Phys. Fluids*, 17, 2005.

F. Zoueshtiagh and P. J. Thomas. Wavelength scaling of spiral patterns formed by granular media underneath a rotating fluid. *Phys. Rev E.*, 61(5), 2000.

F. Zoueshtiagh and P. J. Thomas. Universal scaling for ripple formation in granular media. *Phys. Rev. E*, 67(031301), 2003.

F. Zoueshtiagh, P. J. Thomas, V. Thomy, and A. Merlen. Micrometric granular ripple patterns in a capillary tube. *Phys. Rev. Lett.*, 100(5), 2008.